Synthesis and characterisation of new transition metal complex anion phases

Wang, Qianlong

Award date:
2014

Awarding institution:
University of Bath

FACULTY OF SCIENCE
DEPARTMENT OF CHEMISTRY

SYNTHESIS AND CHARACTERISATION OF NEW TRANSITION METAL COMPLEX ANION PHASES

A thesis submitted for the Degree of Doctor of Philosophy

Qianlong Wang

University of Bath

Oct 2014

Signature Date

ABSTRACT

SYNTHESIS AND CHARACTERISATION OF NEW TRANSITION METAL COMPLEX ANION PHASES

A range of inorganic materials, with structures based on transition metal centred polyhedra linked through simple or polyatomic anions, has been synthesised and fully characterised. These materials were prepared using a variety of synthetic methods, including the direct high temperature, solid state reactions, and hydrothermal techniques in fluoride rich media. The materials produced were structurally characterised by powder (PXD) and single crystal (SXD) X-ray diffraction techniques with further analysis via infrared and UV/visible/near-infrared spectroscopies, thermogravimetric analysis and scanning electron microscopy.

Copper (II) phosphates and related materials have potential applications derived from their near-infrared (NIR) radiation absorbing properties. A range of complex copper phosphate phases in the Cu-P-O or A-Cu-P-O systems, where A is a Group 1 or 2 element, has been synthesised and characterised. The intensity and positions of absorptions in the NIR region found for these materials and derived from *d-d* transitions on copper, are dependent upon the copper ion coordination geometry and the ligand field produced by the surrounding anions. $K_2CuP_2O_7$ and the phases $A_3Cu_3(PO_4)_3$ (A = Sr, Ca) were all found to absorb strongly in the NIR region. The NIR absorbance spectrum could be modified further by introducing fluoride into the Cu(II) ligand environment and Cu_2PO_4F was shown to have a very strong, broad NIR absorption spectrum.

Hydrothermal synthesis techniques, in fluoride rich media, have been used to synthesise twenty two new inorganic framework, layer and chain materials whose structures have been determined using SXD. Mixed anion systems containing a transition metal (M = Mn, Fe, V) in combination with fluoride and phosphate or sulfate were investigated. The new materials have structures based on a variety of transition metal (M = Mn, Fe, V) centred polyhedra linked by simple (O^{2-}, F^-) and polyatomic (PO_4^{3-}, PO_3F^{2-}, $PO_2F_2^-$, SO_4^{2-}) anions; negatively charged polyhedral networks were found to incorporate a variety of inorganic and organic cations as extra-framework species. Fluorophosphate materials produced included $Li_3MnF_2(PO_3F)_2$, adopting a layered structure, and $(NH_4)Mn_3(PO_3F)_2(PO_2F_2)F_2$, a three-dimensional framework with channels containing NH_4^+ ions. Structures containing sulfate, such as the series $Na_3MF_2(SO_4)_2$ (M = V, Mn, Fe), form metal fluoride-sulfate layers separated by Na^+ cations, while $Li_3FeF_2(SO_4)_2 \cdot H_2O$, has a one-dimensional chain structure. With templating organic cations, $[H_2\text{-}(C_6H_{16}N_2)]\ Mn_2(SO_4)_2F_2$, was found to have an unusual layer-type structure and the one-dimensional structure determined for $[H_2\text{-}(C_6H_{16}N_2)]V(SO_4)_2F$ is an analogue of the mineral Tancoite. The incorporation of fluoride together with (fluoro-)oxoanions has thus enabled the synthesis of new types of functional materials and structure types. Li^+ or Na^+ templated materials were found to be good candidates for use as cathodes in rechargeable batteries.

TABLE OF CONTENTS

DECLARATION OF AUTHORSHIP

I, Qianlong Wang, declare that the thesis entitled 'Synthesis and characterisation of new transition metal complex anion phases' and the work presented in the thesis are both my own, and have been generated by me as the result of my own original research. I confirm that:

- This work was done wholly or mainly while in candidature for a research degree at this University;
- Where any part of this thesis has previously been submitted for a degree or any other qualification at this University or any other institution, this has been clearly stated;
- Where I have consulted the published work of others, this is always clearly attributed;
- Where I have quoted from the work of others, the source is always given, With the exception of such quotations, this thesis is entirely my own work;
- I have acknowledged all main sources of help;
- Where the thesis is based on work done by myself jointly with others, I have made clear exactly what was done by others and what I have contributed myself;
- Part of the work have been published as:

  Keates, A. C. Wang, Q. L. and Weller, M. T.
  Synthesis and structural characterisation of iron(II) and copper(II) diphosphates containing flattened metal oxotetrahedral.
  Journal of Solid State Chemistry, 10-14, 2014

  Wang, Q. L. Madsen, A. Owen, J. R. and Weller, M. T.
  Direct hydrofluorothermal synthesis of sodium transition metal fluorosulfates as possible Na-ion battery cathode materials.
  Chemical Communication, 2121-2123, 2013

Signed:……

Date:……

The work was preformed exclusively by the author, with the following exception: the electrometrical investigations of compound **XI**, presented in Chapter 5, were carried out by Alex Madsen from Prof. J. R. Owen's research group at the University of Southampton.

ACKNOWLEDGEMENTS

It's been a long road, but here I am at the end. I am grateful for everyone who has been there to support my journey towards the finished thesis. I am indebted to and grateful for the following people:

First and foremost, is a well-deserved thanks to my supervisor, Professor Mark Weller, for his guidance, patience, support and invaluable advice throughout my studies. The scene of my first interview in the University of Southampton remains fresh in my memory.

Many thanks to members of the Weller group both past and present, who have helped and supported me, especially to Dr. Edward Williams, you have been an excellent proof-reader and give me so much of your time.

I would like also to thank my friends both in Southampton and Bath, who made my life truly memorable. Special mention is due for Dr. Wenjian Zhang and Chun Borodzicz, I am truly thankful for their help to both my personal and academic developments.

A special thanks to my family. Words cannot express how grateful I am to my parents and my elder sisters; I know I've left home for too long. Thank you for all of the sacrifices that you've made on my behalf, and hope to be able to spend more time with you after this!

Finally, thank all people around the world, men, women, boys and girls, you guys are awesome! I am so grateful to have you all on the same planet! Last of the last, to all animal and plant life, a member part of this planet, we have this beautiful home called Earth!

I dedicate this thesis to my family for their constant support and unconditional love.

I love you all dearly.

CHAPTER ONE: INTRODUCTION

1.1 Inorganic materials

Inorganic material chemistry is an important branch of material science. It is concerned with the synthesis, structure, properties and application of inorganic materials. These materials can be categorised into a variety of different compound types, ranging from the open frameworks, such as zeolites, to the more densely packed structures of complex metal oxides. The increasing demand for functional inorganic materials is due to their widespread possible and actual applications in different fields, including use as catalysts, ion-exchangers, high-temperature superconductors and battery materials. However, these applications are ultimately determined by their chemical and physical properties, which in turn arise from the crystal structure of these materials. In order to exploit their properties for use in different areas, research into novel materials with either new properties, or improvements on existing properties is required. As such, synthesis of new functional inorganic materials remains an important research topic. Moreover, such work can also provide insights into the formation processes of these inorganic materials.

The structures of many inorganic materials can be described in terms of linked polyhedral units, commonly tetrahedra or/and octahedra. The polyhedral units are usually linked through corner-sharing, edge-sharing and face-sharing. For example, naturally occurring zeolites, with structures consisting of corner-sharing tetrahedral TO_4 (T = Al, Si) units, are commonly used as molecular sieves. Layered structures of some complex metal oxides like $LiCoO_2$, used in commercial batteries, can be built up from face-sharing CoO_6 octahedra.

1.1.1 Transition metals

Transition metals, also known as the transition elements, are classified as elements in the *d*-block of the periodic table. These usually include all elements in rows 4-6 and groups 3-12 of the periodic table. However, the elements in group 12 are often disputed as their electron shells are fully occupied by paired electrons in the d^{10} state. Characteristically, transition elements are all metals, so they are heat and electricity conductive and often paramagnetic, they usually form coloured compounds and most of them exhibit variable oxidation states. The maximum oxidation state attainable for the each transition metal varies depends upon their position in the series, for example, in the first row transition metals series, the number of oxidation states increases from Sc to Mn, where Mn exhibits the most oxidation states; thereafter it decreases from Mn to Zn as shown in Table 1.1.

Table 1.1: *Oxidation states of first row transition metals (TMs). The most common oxidation states are bolded and underline*

				+7					
			+6	+6	+6				
		+5	+5	+5	+5	+5			
	+4	**+4**	+4	**+4**	+4	+4	+4		
+3	**+3**	**+3**	**+3**	**+3**	**+3**	**+3**	+3	+3	
	+2	+2	+2	**+2**	**+2**	**+2**	**+2**	**+2**	**+2**
								+1	
Sc	Ti	V	Cr	Mn	Fe	Co	Ni	Cu	Zn
[Ar] $3d^1 4s^2$	[Ar] $3d^2 4s^2$	[Ar] $3d^3 4s^2$	[Ar] $3d^4 4s^2$	[Ar] $3d^5 4s^2$	[Ar] $3d^6 4s^2$	[Ar] $3d^7 4s^2$	[Ar] $3d^8 4s^2$	[Ar] $3d^{10} 4s^1$	[Ar] $3d^{10} 4s^2$

The first row transition elements exhibit multiple oxidation states, except Sc. This is due to the energy levels of the 4*s* and 3*d* electrons having similar energies, meaning that the transition metals can form various ions with roughly the same stability by losing different numbers of electrons. Therefore the transition elements from titanium to copper, exhibit two or more oxidation states. In general, there is an increase in the number of oxidation states from Sc to Mn as more *d*-electrons are available to be removed, then a decrease is observed after Mn, where the *d*-electrons become more tightly bound. This is likely to arise from the increased nuclear charge that binds the d-electrons more strongly in these elements.

Transition metals exhibit different oxidation states, along with their varying ionic radii, enabling them to form a wide range of complexes possessing various coordination geometries, such as octahedral, square pyramidal, tetrahedral and square planar, depending on the type of coordinated ligands and their steric requirements. Transition metal based complex as are usually coloured and this can be explained as being due to the partially filled *d* orbital, allowing the transition of electrons between *d* electronic states. The so called *d-d* transitions often occur in the visible part of the electromagnetic spectrum giving rise to partial absorption of light and the absorption of colour. An example is Egyptian blue, known as the earliest synthetic blue pigment, which contains copper. Many natural occurring minerals also reflect different colours based on the type of transition metals within them. Many materials containing transition metals are also found to display useful magnetic and catalytic properties. For example, the copper based layered structure of $YBa_2Cu_3O_{7-x}$, which is the first material to display superconductivity with T_c > 77 K, has been applied in a superconducting maglev vehicle.[1] As an example of a catalytic role, the transition metal nickel is often used in catalytic hydrogenation.[2]

1.2 Inorganic materials with solar near infrared absorbing properties

Infrared radiation is electromagnetic radiation with a wavelength longer than visible light, but shorter than that of microwaves. The infrared region spans from roughly 1 mm to 750 nm and can be divided into three parts: near-infrared (NIR), mid-infrared, and far-infrared. The NIR spectral region is typically recognised to be from 750 nm to 2500 nm. NIR materials can be described as substances that interact with NIR light, by means of absorption, reflection and transmission. NIR materials can either be organic or inorganic, each having their own advantages. Research on NIR materials and technology is motivated by their numerous practical applications such as bio-imaging, sensing, energy, communication and advanced optoelectronics.

Almost half of the solar radiation falls in the NIR spectral region (Figure 1.1). This radiation is effectively wasted and considered harmful as it is not needed by plants for photosynthesis, and contributes significantly towards the warming of the Earth's surface. The effect is particularly apparent in buildings and greenhouses, as this radiation only contributes to the ambient temperature. However, these problems could be solved by developing materials that can absorb or reflect such radiation. These materials can be used in coatings to reduce the heat gained inside buildings. Alternatively, if this radiation could be harvested, and used for solar-power generation, a potential reduction in global warming would be achieved. The applications of NIR absorbing materials are diverse and a few specific examples are described.

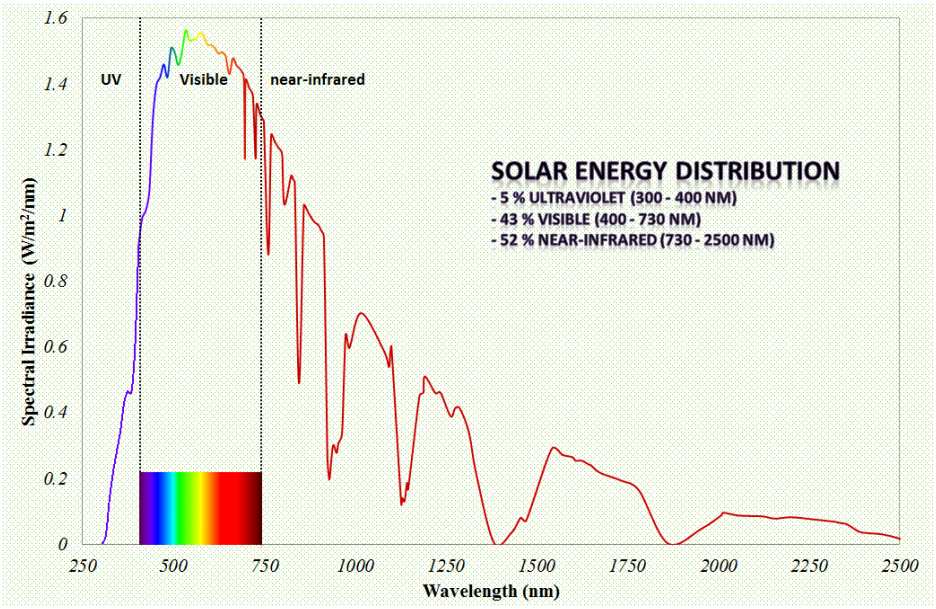

Figure 1.1: *The spectrum of sunlight with energy distribution*

1.2.1 Applications of NIR absorbers

Materials possessing strong NIR absorbing properties can be widely utilised. Most of these materials are organic compounds, usually exhibiting strong and tailored NIR absorbance, but have drawbacks such as weak thermal and chemical resistances. Therefore, the need for more robust NIR absorbing materials has driven some chemical companies such as Merck and BASF to develop inorganic equivalents. Applications for such NIR absorbing materials include: solar or laser filters, solar cells, and laser welding.

- Laser welding and marking

Welding is the sculptural process of joining materials through coalescence, traditionally used for metals. The process requires a source of heat in order to melt the interface of the metal pieces to be joined. Lasers are often used to provide a concentrated and continuous heat source. In the last few years, laser welding of plastics and polymers has been a growing field of research and development. The difficulty with plastic welding is that plastics or polymers are transparent to the operating wavelength of most laser beams. Since the discovery of low-cost semi-conducting diode lasers, the development of new NIR absorbing materials has become of more interest. The original absorber used was carbon black,[3] but this is unsuitable for clear plastics. New idealised NIR absorbers were developed that were either transparent to the visible light or absorbing a minimum amount. However, these materials are mainly organic dyes, typically cyanines,[4] which perhaps are the most widely studied and applied chemical class of NIR absorbers. Other organic candidates include squarylium and heptamethine dyes, which are structurally similar to cyanines. Inorganic NIR absorbers are much rarer than organic dyes, as most inorganic NIR absorbing materials contain transition metals, which can result in strongly coloured substances. Nevertheless, there are still examples of stronger NIR absorbing inorganic materials, such as the transition metal oxides and lanthanum hexaborides.[5] For example, iron oxide absorbs broadly into the NIR region, and consequently it is used in the application of laser welding of plastics and as a transparent pigment when a light colour is of importance.[6] Iron oxide can also be used as an infrared reflecting material for the prevention of solar heat gain in architecture and other structures, because of its broad absorption range in the NIR region.[7] Comparisons between the organic NIR absorbing dyes and inorganic pigments can be found in Table 1.2.

Table1.2: *Property comparison between inorganic/organic pigments or dyes*

Properties	Inorganic Pigments	Organic Pigments/Dyes
Particle size	0.5-1.1 mm	0.01-0.1 mm/dissolve
Colour strength	Low-moderate	High
Transparency	Generally opaque	Generally transparent
Heat resistance	High	Low to high
Light fastness	Moderate to excellent	Low to excellent
Weather fastness	Excellent	Low to excellent
Migration	Excellent	Moderate to excellent/low to moderate
Dispersion	Usually good	Soluble

- Photoelectric and photothermal conversions

Sunlight contains a significant portion of NIR radiation, which can be either useful or undesirable, depending on the environment on which it impinges. It is useful in solar-power generation for the production of electrical energy, but is unhelpful in generating heat in cars and other vehicles, causing excessive heating and hence a need for increased air-conditioning. Reflective coatings are the most common answer to this problem, but it is also possible to absorb the radiation and convert it to electrical or thermal energy. As shown in the table above, inorganic NIR absorbing materials have better photo-, thermo- and chemo- stability than those of organic pigments or dyes; as such they may be a better choice for use in electrical and thermal energy conversions. Alternatively, sunlight can also be absorbed by a solvent layer, such as water molecules in a material. Absorbed energy can then be circulated through heat exchangers and used to heat water for central heating or other domestic uses. The traditional solar water heaters use blackened metallic tubes as the absorbing component; however materials designed with good NIR absorbing properties are preferred coating materials, with greater spectral absorption abilities, resulting in thermal energy conversion being more efficient.

1.2.2 Electronic transitions

Materials selected and synthesised in this research all produce characteristic bands in the NIR spectra region. The materials contain a transition metal ion, that gives rise to the absorption features over approximately 800-1300 nm, with this observed spectra directly related to the electronic transitions within the *d* shell of the transition metal ion. In an isolated transition metal ion, the occupied *d* orbitals are split into five *d*-orbitals, which are all degenerate, given symbols of $d_{x^2-y^2}$, d_{z^2}, d_{xy}, d_{xz} and d_{yz} (Figure 1.2). Once the transition metal atom coordinates to ligands, the energies of the five *d* orbitals change due to the electronic repulsion that occurs within the complex.

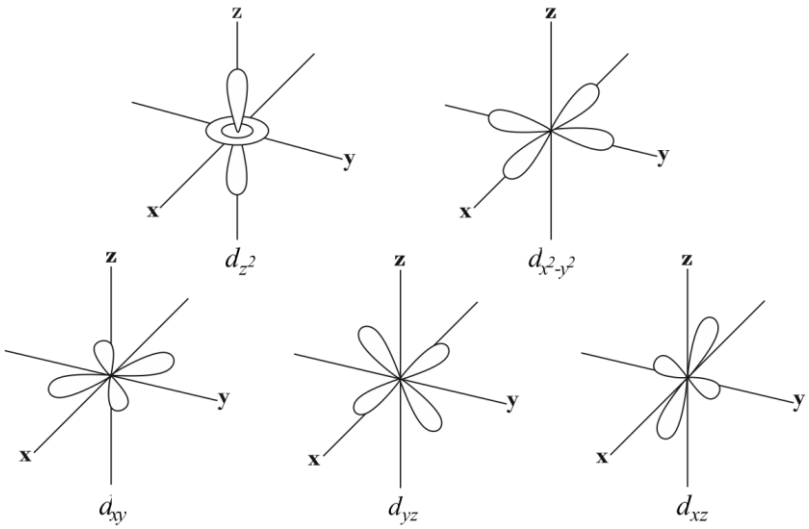

Figure 1.2: *d orbitals*

The energies of all five orbitals are raised as a result of the repulsion between the electron cloud surrounding the ligands and the metal *d* orbitals. The electronic repulsion causes the *d* orbitals to lose their degeneracy and split into different energies states, this is known as the crystal field splitting, where the energy difference between the states is denoted by Δ. The formation of diverse complexes causes the *d* orbitals to split into different energy levels. For example, in an octahedral complex with symmetry of O_h, the *d* orbitals are split into two sets, the t_{2g} set and the destabilised e_g set. The energy gap Δ can be significantly influenced by the type of ligand which coordinates to the metal centres, with π-donor ligands (weak field) reducing the energy gap, whilst π-acceptor ligands (strong field) result in large Δ.

The energy difference between *d* orbitals enables complexes to absorb specific frequencies of light. The *d-d* transition is explained as the occurrence of an electronic transition within the *d* orbitals, with an electron promoted by the incoming photon from one *d* orbital to another, usually from lower energy orbitals to higher energy orbitals. Within an octahedral complex, the only expected electronic transition is from $t_{2g} \rightarrow e_g$, the energy of which typically falls in the visible region of the electromagnetic spectrum.

The intensity of the absorption spectrum caused by the electronic transitions is governed by the selection rules, in particular the spin and Laporte selection rules. Fundamentally, the *d-d* transitions are spin allowed transitions as these involves no change in electron spin (or number of unpaired electron), but Laporte forbidden. In this research, the transitions are most affected by the latter selection rule, which states that *a transition is forbidden when it involves the redistribution of electrons having similar orbitals within a single quantum shell*.[8] Therefore the transitions from orbitals $p \rightarrow d$ or $d \rightarrow p$ is allowed, whilst the $d \rightarrow d$ is forbidden. Table 1.3 shows the approximate values for the intensities of the various transitions observed in the metal complexes.

Table 1.3: *Intensities of the different transitions*

Band type	Intensity ($dm^{-3}mol^{-1}cm^{-1}$)	Type of transition
spin forbidden	$\varepsilon_0 < 1$	*d-d* (e.g. Mn^{2+}, d^5)
Laporte-forbidden	20-100	*d-d* (e.g. O_h)
Laporte-allowed	ca. 250	*d-d* (e.g. T_d)
symmetry allowed	1000-5000	charge transfer

However, the Laporte selection rule only applies to the centrosymmetric molecules, thus examples such as those possessing tetrahedral symmetry are not subject to this rule. Indeed, a transition metal complex possessing a tetrahedral coordination with T_d symmetry can be described as having two types of hybridised orbitals. According to the principle of symmetry and group theory, the formation of a tetrahedron occurs not only though sp^3 hybridisation, but also though sd^3 (d^{3s}) hybridisation.[9] It is the appropriate combination of the *p* and *d* orbitals, resulting in $s(p\text{-}d)^3$ hybridisation, which therefore helps the *d-d* transitions to overcome the Laporte rule.

On the other hand, the Laporte rule can be removed by changing the centre of symmetry, through vibration or distortion of the perfect shape.[10] For a complex that has regular octahedral geometry, which has a centre of symmetry, transitions between *d*

orbitals are restricted. The subscript *g* of t_{2g} and e_g orbitals in an octahedral crystal field stands for the gerade, and represents the centrosymmetric nature of both orbitals. As a result, the predicted absorption for regular octahedral complexes is weak. However, molecules are vibrating at all times, and these vibrations may temporarily change the symmetry, thus resulting in a breakdown of the Laporte rule. The interaction between the electronic and vibrational modes is known as vibronic coupling.[10]

In another aspect, distortion from the regular symmetry is often encountered if the vibrational mode is not possible. The tetragonal distortion is a common distortion of octahedral symmetry, with two ligands along the *z* axis either closer or further away from the metal centre than the four equatorial ligands. This distortion is defined as the Jahn-Teller distortion (effect), which states that *a non-linear molecule in a degenerate electronic orbital state is unstable with respect to spontaneous distortion of the nuclear configuration that lowers the symmetry and removes the degeneracy*,[11] The Jahn-Teller distortion causes the O_h symmetry to be lowered along the *z* direction, removing the degeneracies of the e_g and t_{2g} sets. The d_{z^2} orbital becomes more stable than the $d_{x^2-y^2}$ orbital, due to the elongation of bonds, resulting in less repulsion, whilst the d_{xz}, d_{yz} orbitals are stabilised relative to the d_{xy} orbital.

1.2.3 Candidate materials

The desired candidate materials with NIR optical properties have to be cheap and have strong absorption properties, as well as low toxicity. Phosphate-based materials are usually a very good choice. NIR absorbing materials comprised of phosphate offer several advantages, including the ability to form stable structures. The phosphate-based materials also have low toxicity, which make them ideal as replacements for toxic materials. For example, zinc phosphate has replaced the most toxic lead and chromate pigments to become the most commonly used phosphate-based pigment.[12] As mentioned earlier, weak field ligands can reduce the energy gaps between *d*-orbitals, thus increasing the number of transitions. The ligands of most interest are oxygen and fluoride, as they all exhibit strong π-donor characteristics.

NIR absorbance can also be affected by the type of metal within the material, and one of the most desirable metals for making NIR absorbing materials is copper. Copper usually adopts a oxidation state of +2, resulting in a d^9 configuration for the Cu^{2+} ion. The copper with a d^9 configuration usually coordinates to six ligands to form an octahedral environment, which is frequently subject to a strong Jahn-Teller effect and becomes distorted. This is due to the distribution of the nine electrons within the five *d* orbitals of copper resulting in the d_{z^2} orbital only being occupied by one unpaired electron, whilst all other orbitals are filled with paired electrons. This causes the degenerated e_g set to be energetically unstable and further split between the half-filled d_{z^2} orbital and the fully filled $d_{x^2-y^2}$ orbital. This is reflected in the copper coordination with bond elongation along the axial axis and compression along the equatorial axis, leading to the formation of lower energy states (Figure 1.3).

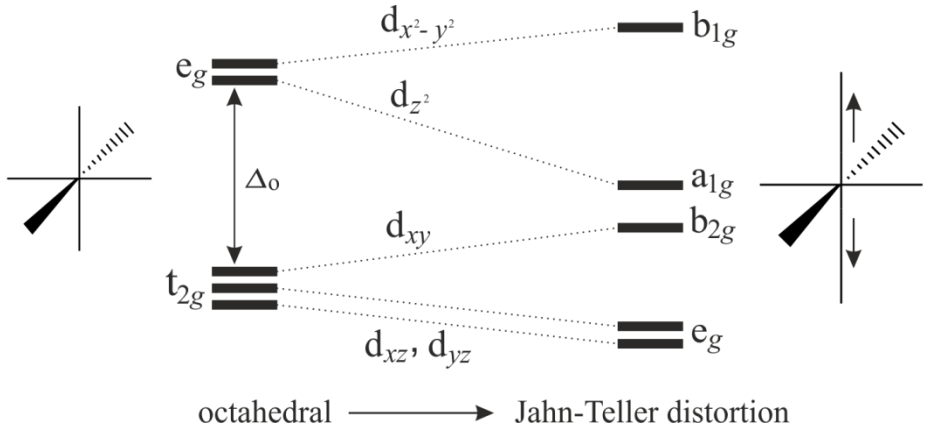

Figure 1.3: *Orbital correlation diagram showing Jahn-Teller distortion from a regular octahedral geometry*

1.3 Inorganic framework materials

Materials possessing open structures have always been of interest because of their many potential applications. Most of the earlier work in this field focused on aluminosilicate zeolites, followed by the discovery of nanoporous aluminophosphates in the 1980s by Flanigen and co-workers.[13] Since then research has been carried out into the aluminophosphate (AlPO) family extensively,[14] and the materials obtained show rich structural diversity, ranging from not only the zeolitic structures of three-dimensional frameworks, but also the one/two-dimensional structures of chains and layers.

In the mid-1980s, research into the open-framework materials was extended to bring other elements into focus, and for example, the gallophosphate (GaPO) family was subsequently reported.[14] The successful discovery of these extended zeotype species has given rise to the search for other elements which can be incorporated into frameworks. During the past 16 years, more than 25 suitable elements have been found to participate as main components of such frameworks, including most first row transition metals, and the number is still increasing.[14] Most of these materials are primarily phosphate-based, however similar materials based upon other anions have also been produced, including germanates, phosphites, arsenates or, rarer, sulfates.[15] Introducing other elements such as transition metals also added possibilities for the formation of new structural architectures. Unlike the zeolites and early aluminophosphates, which were all entirely based upon corner-sharing tetrahedra (AlO_4, SiO_4, PO_4), the transition metals can possess various coordination environments other than tetrahedral, such as octahedral, square-based pyramidal, tetrahedral and square planar. These in combination with their various chemical and physical properties, result in materials with even greater structural diversity, and also wider application prospects. For example, they can be used as battery materials or non-linear optical materials, and many of them also exhibit useful magnetic properties.

In general, metal framework materials are often prepared through the hydrothermal method, in the presence of water at temperatures between 80 and 200 ^{o}C. Water was employed as the main solvent in most of the early synthetic work. Later studies attempted to use different solvents, mainly alcohols, which indicated the significant influence of the solvent on the final outcome structures.[16] The utilisation of solvents and templating agents has also led to the discovery of new frameworks. The interaction

between the solvent and templating agents is not strong, so the templating molecules remain in isolation in the reaction mixture, and the solvent acts to facilitate the interactions between the framework species and the templating molecules. By far the most common templating agents are amines, and they often act as structure-directing and as cationic templates once being protonated, balancing a negative charge on the framework. However, the templating agents can also be inorganic species, thus the resulting structures can be organic-inorganic hybrid materials or pure inorganic structures. More recently, ionic liquids have been used in both inorganic and hybrid reactions, and have been shown to be effective as solvents.[17] They provide an ionic reaction environment and result in the formation of many new types of structures. For example, 1-ethyl-3-methylimidazolium bis(trifluoromethylsulfonyl) imide was used in the preparation of a highly promising electrode material $LiFeSO_4F$.[18]

The fluoride method is also widely used in metal framework material preparation. Fluoride ions introduced in the reactions were found to play a mineralising role, similar to the hydroxyl ions in alkaline conditions, but the difference is that the fluoride anions can assist with the crystallisation, leading to the formation of larger crystals.[19] This effect likely arises from the fluoride anions increasing the nucleation rate followed by shortening of the crystallisation time.[20] Fluoride anions can also have a catalytic role, which can be seen in the preparation of some zeolitic structures, such as aluminophosphate-14A ($AlPO_4$-14A),[21] where the fluoride anions are required for the formation of the material, but are not incorporated in the framework.

Alternatively, at high concentrations fluoride can be incorporated into the structures, through replacing oxide ions on metal or phosphate polyhedral units, thereby changing the structural and compositional aspects of the chemistry of the material. Fluoride anions shows a propensity for bridging some metal centres or occupying terminal sites within polyhedral units. For example, $Rb_3Mn_3(PO_4)(PO_3F)_2F_5$, formed in the presence of HPF_6 and RbF.[22] Its structure consists of fluoride anions acting as bridges between manganese centres, or as terminal sites on the phosphate tetrahedra. Recently, through the fluoride synthetic route, there has been great success in the synthesis of arsenate- and sulfate-based materials.[23]

The structure of a material can be described as being built-up from a variety of building units. A building unit is defined as the minimum assembly of atomic

condensations that have the same or different unit within a structure. In fact, the description of material structures relies upon the concept of the secondary building unit (SBU). A SBU is basically a selected grouping of different polyhedral units, for example, tetrahedral units AlO_4 and SiO_4 in zeolite structures. There are distinct advantages through using SBUs to describe material structures, as a whole family of related structures can be described sufficiently by using a few SBUs; they also provide an aid to imagining new structural topologies.

SBUs were initially developed and used for describing zeolitic structures; however the introduction of other periodic table elements, such as transition metals with more coordination environments than tetrahedral, has required the SBU concept to expand. Thus a new series of SBUs for mixed octahedral-tetrahedral structures has been developed by Férey,[24] e.g , the simplest SBU within a typical structure is made by linking one transition metal polyhedron and a tetrahedron, and other SBUs are based on further linking of this simplest SBU. For example, two metal polyhedra and two tetrahedra share vertices resulting in four-membered ring, or two metal polyhedra linked by sharing corner and bridged by two tetrahedra.

1.3.1 Iron phosphate and sulfate materials

Phosphate frameworks containing iron have been widely studied. Many iron phosphates occur naturally, and their structures have largely been characterised. Many of their structures adopt three-dimensional frameworks, containing pores and channels, and are important in the search for new open-framework metal phosphates. The most striking example of a natural mineral iron phosphate exhibiting a porous structure is the mineral cacoxenite, which exhibits pore sizes up to approximately 14 Å.[25] There are also many synthetic iron phosphates, which are novel or analogous to the natural species. The first synthetic iron phosphates were prepared hydrothermally and were found to be analogues of the minerals hureaulite and alluaudite.[26]

Iron phosphate materials with small channels have been of interest for many years, primarily due to their useful properties. For example, the iron based NASICON-type structures, exhibiting fast ion transport, have been considered for use as battery materials. Iron phosphates have also been reported as good catalysts for selective oxidation reactions,[27] in particular for the effective oxidative dehydrogenation of lactic acid to pyruvic acid, or of glycolic acid to glyoxylic acid.[28, 29] Iron phosphates have also been of interest in terms of their magnetic properties. Some of them possess porous frameworks and exhibit the dual functionality of porosity and long range magnetic effects.[30-33]

More recently, research on iron phosphates has focussed on their use in lithium batteries,[34, 35] where they can be used as either the cathode[36] or the anode[37]. $LiFePO_4$ was discovered in 1996,[38] and has been vigorously pursued as an alternative cathode for lithium ion rechargeable batteries. Compared to the traditional lithium cobalt oxides, this material offers many advantages, due to all of the elements being naturally abundant and inexpensive, as well as displaying low toxicity. $LiFePO_4$ demonstrates a cell voltage at 3.5 versus Li, and therefore quickly becomes the choice for a Li insertion and extraction cathode material.[36, 39] $LiFePO_4$ occurs naturaly as the mineral triphylite, which adopts an olivine-type crystal structure, built up of FeO_6 octahedra and PO_4 tetrahedra connected through shared vertices, with lithium cations residing in the created channels (Figure 1.4). This material can be easily obtained synthetically. Many research papers and patents have been filed with various synthetic procedures developed to prepare optimised $LiFePO_4$ powders; however the hydrothermal method is more

frequently used, compared to other methods. In a general synthetic procedure,[40] $FeSO_4$ and H_3PO_4 solutions are mixed first, LiOH solution added, and the solution heated in a Parr reactor for five hours.

All through the lithium ion battery materials dominate the commercial, portable rechargeable battery market at present, secondary cells based on sodium ion insertion/extraction address new requirements. The sodium ion based technologies have lower energy density and voltages compared to the lithium ion, but they can be focused on applications where the requirements on weight and footprint are less important, for example in electrical grid storage. The framework iron phosphates possessing olivine or NASICON structures have been also proposed for sodium ion batteries materials, with examples including $NaFePO_4$ and $Na_3Fe_2(PO_4)_3$.[41, 42]

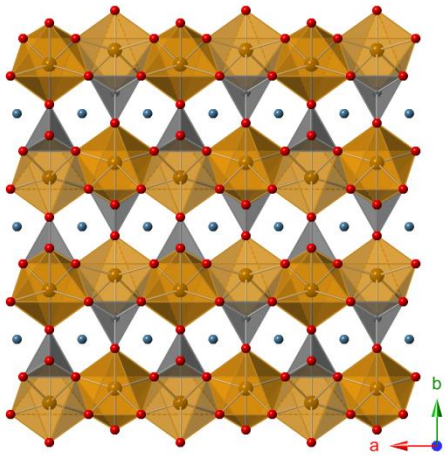

Figure 1.4: *The olivine structure of triphylite $LiFePO_4$ viewed down the c-axis, with the iron octahedra shown in yellow-brown, the phosphate tetrahedra shown in grey, oxygen atoms in red and lithium atoms in sky blue*

The phosphate based cathode class of compounds are also known as polyanionic compounds. These materials usually exhibit high operating potentials, due to the strong inductive effect of the PO_4^{3-} polyanion.[36] However the performance can be theoretically enhanced by incorporating fluoride into the structure. The electronegative fluorides, adopting the metal polyhedral through the forming of M-F bonds, exhibit high ionic character and thus result in the cell potential increasing. In order to exploit this feature, various fluorine based metal phosphate materials have been investigated.[43] One example is the Na_2FePO_4F, a potential multifunctional cathode, has been characterised by Nazar's group, and shows redox potentials situated at 3 and 3.5 V,[44] which is the first ever electrochemically feasible Fe-based fluorophosphate material with sodium. Its

derivative Li_2FePO_4F was also investigated soon afterwards. Both materials possess two-dimensional layered structures, with each layer consisting of pairs of face-sharing Fe-octahedra, each coordinated with four oxygen and two fluorine atoms. The pairs of bioctahedra are connected with other pairs of Fe-octahedra through sharing of fluorine atoms, forming Fe-based chains, whilst these chains are capped by phosphate tetrahedra.

Following the success of the polyanionic phosphate in the field of battery materials, many groups have turned their research direction to the polyanionic sulfate materials. The effect of substituting phosphate PO_4^{3-} for sulfate SO_4^{2-}, resulting in an improved electrode potential, has been investigated.[45, 46] The origin of such an improvement arises from the higher electronegativity of sulfur with respect to phosphorus. Examples of polyanionic sulfate materials include $Li_2Fe(SO_4)_2$, which shows a redox potential of 3.83 V, the highest recorded for fluorine-free and iron-based material.[47] Interestingly, many polyanionic materials initially designed and prepared for battery electrodes, are also of interest for their magnetic properties. $Li_2Fe(SO_4)_2$ has a structure built up from FeO_6 octahedra sharing corners with six sulfate tetrahedra, and each sulfate tetrahedron is linked with three adjacent FeO_6 octahedra through vertex-sharing of three oxygen. The fourth vertex within the SO_4 tetrahedron is terminated and pointed towards the large tunnels in the structure. The particular arrangement of these polyhedral units enables superexchange interactions within $Li_2Fe(SO_4)_2$ and leads to an antiferromagnetic ordering at 23 K with an effective moment μ_{eff} of 5.7 μ_B, and μ_{eff} of 5.8 μ_B at 71 K.[48] The antiferromagnetic properties have also been observed in other iron-based polyanionic compounds, such as $FePO_4$[49], $Fe_2(SO_4)_3$[50] and $AFe(SO_4)_2$ (A = K, Cs, Rb)[51], where the superexchange interactions between magnetic metal atoms are only possible through M-O-M pathways. Ferromagnetic properties can be observed in jarosite $NH_4Fe_3(SO_4)_2(OH)_6$, which possesses an exotic frustrated magnetic structure.[52] The antiferromagnetic materials can be used for making antiferromagnetic thin films,[53] and can be incorporated into data storage systems.

Fluorine-based battery materials exhibiting high cell voltages have been previously found for polyanionic phosphates. Intrinsically, the incorporation of fluoride to the sulfate materials should yield similar improvement in cell voltages. The first reported F-containing metal sulfate was $LiMgSO_4F$, but was found to be electrochemically inactive. Substituting magnesium with transition metals resulted in tavorite, $LiFeSO_4F$. This

fluorosulfate cathode material shows a cell potential of 3.6 V and a reversible capacity of 140 mAh/g, with good rate capability, which is unprecedented.[54] However, the synthesis of $LiFeSO_4F$ involves a complex route based on exchange of LiF for H_2O in macroporous $FeSO_4 \cdot H_2O$ in an ionic liquid or tetraethylene glycol. The structure of $LiFeSO_4F$ is built up from Fe-based chains linked by sulfate tetrahedra, forming a three-dimensional framework with channels filled by Li^+ cations (Figure 1.5). The Fe-chain is made up of Fe-octahedra connected via *trans*-fluorides.

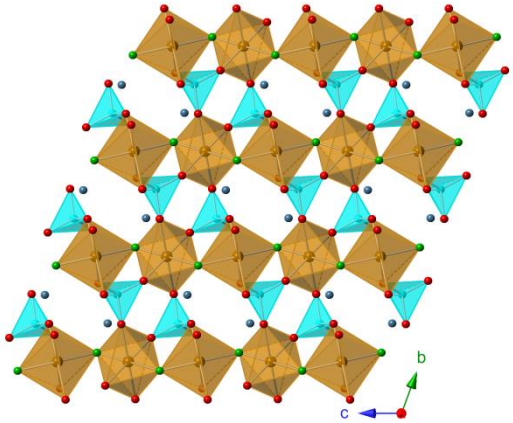

Figure 1.5: *Crystal structure of tavorite $LiFeSO_4F$ viewed down the a-axis, with the iron octahedra shown in yellow-brown, the sulfate tetrahedra shown in aqua blue, oxygen atoms in red and lithium atoms in sky blue*

For extended structures based on iron and sulfate, several examples have been studied by Rao's group.[55, 56] The materials were all organically templated and exhibit linear or layered structures. For example, $(H_3N(NH_2)_2NH_3)FeF_3SO_4$ formed in the presence of HF, whose structure comprises alternating connected FeF_3O_3 octahedra and sulfate tetrahedra, which form a ladder chain consisting of four-member rings as seen in Figure 1.3. It was the first structure showing an octahedral-tetrahedral (O-T) ladder in the metal sulfate family. The ladder-type chains are held together through hydrogen bonds formed by diprotonated ethylenediamine interactions with the framework oxygen and fluorine atoms. Thermal behaviour indicates the material is stable up to 280 ^oC. Other structures based on chains include $(C_2N_6H_{12})FeF(SO_4)_2$, built up from FeF_2O_4 octahedra and SO_4 tetrahedra. Where the Fe-octahedra are connected through corner-sharing of *trans*-fluoride to form a linear *zigzag* chain, sulfate tetrahedra are capped pairs of Fe-octahedra along the linear chain. Hydrogen bonding interactions exist between the protonated amine molecules and the framework oxygen atoms. $(C_4N_3H_{16})FeF(SO_4)_2$, is structurally similar to the $(C_2N_6H_{12})FeF(SO_4)_2$ but with a

different templating amine. $(C_4N_2H_{12})FeF_3SO_4$, produced hydrothermally, has a structure based on the Fe-chains, which are made up of corner-sharing FeF_4O_2 units linked via F-atoms. The sulfate tetrahedra are grafted onto the pair of Fe-octahedra along the chain and the individual chains are held together by hydrogen bonds. $(C_3N_3H_5)FeFSO_4 \cdot H_2O$ comprises a two-dimensional layered structure. Each layer is built up from corner-sharing FeF_2O_4 octahedra to produce linear chains, which are cross-bridged by sulfate tetrahedra as seen in Figure 1.6. Protonated amine molecules are located in the interlayer space and interact with framework oxygen to created hydrogen bonds.

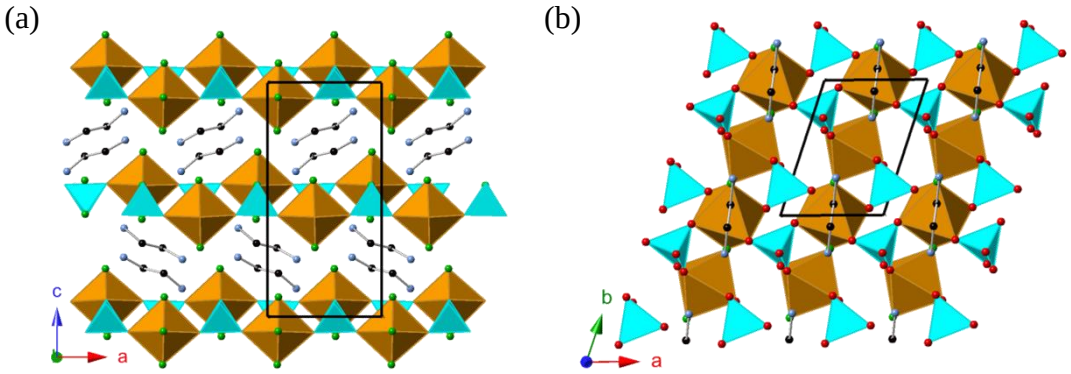

Figure 1.6: (a) *crystal structure of $(H_3N(NH_2)_2NH_3)FeF_3SO_4$ viewed down the b-axis, (b) structure of $(C_3N_3H_5)FeFSO_4 \cdot H_2O$ viewed down the c-axis, with the iron octahedra shown in yellow-brown, the sulfate tetrahedra shown in aqua blue, F-green sphere, N-sky blue sphere, C-black sphere*

1.3.2 Manganese phosphate and sulfate materials

Manganese is one of the transition elements with the most variety in oxidation states, and materials that have manganese with oxidation states of +2, +3 or +4, or even mixed valences are widely used in batteries[57] and catalytic processes[58]. For example, manganese phosphates as catalysts are commonly used for the oxidation of methyl mandelate[59] and adonitol to ribose[60]. Manganese phosphate can also be used as a coating material on mild steels in order to prevent corrosion,[61] or as an intermediate layer before automobile iron casting painting[62]. Furthermore, the electrochemical properties of manganese phosphates and sulfates have been shown recently to be of industrial interest.[63]

In terms of battery materials, many manganese phosphates have been studied due to their possible use as alternative cathode materials, including the three-dimensional olivine-type structure of $LiMnPO_4$.[64] Compared to the iron version, lithium manganese phosphates have several advantages. Firstly, the production of such materials is easier and secondly they store more energy and have a higher lifespan. The electro-chemical optimisation on $LiMnPO_4$,[65] has led to it being adopted in batteries used for powering electric vehicles. More recent research on olivine structure materials has been extended to the doped system $LiMn_{1-x}Fe_xPO_4$. Through substituting Mn for Fe, the energy density of the material was significantly increased compared with the non-doped olivine structure. The reason likely arises from the Jahn-Teller distortions of Mn^{3+} species, resulting in lattice interactions.[66] Manganese based phosphates for use in sodium ion batteries are also of great interest, for example the olivine structure of doped $NaMn_{1-x}M_xPO_4$ (M = Fe, Ca, Mg),[67] which can be prepared via a simple solid state reaction at less than 100 ^oC. As earlier mentioned, the energy density of battery materials can be improved through the introduction of electronegative fluorine. Thus promising manganese based fluorophosphate materials for use as positive-electrodes in lithium or sodium ions batteries include A_2MnPO_4F (Li, Na), which has been prepared and electrochemically investigated by Nazar's group.[43] Both materials possess two-dimensional layered structures, and each layer is built up from corner-sharing manganese octahedra and phosphate tetrahedra. Fluorosulfates such as $Na_3MnF_2(SO_4)_2$, consisting of a two-dimensional layered structure, have been prepared from hydrofluorothermal reactions, and are proposed as potential positive electrode materials for sodium ion batteries.[68]

In addition to applications in the field of battery materials, many Mn-based phosphates, possessing different crystal structures, also show interesting magnetic properties. For example, the three-dimensional porous $NH_4Mn^{II}_4(PO_4)_3$[69] has been prepared through a solvothermal method, using $MnCl_2{\cdot}4H_2O$, tributyl phosphate and 1,3-diaminopropane as reactants. Its structure is built up from MnO_6 octahedra, connected to MnO_5 square-based pyramids and trigonal bipyramids through sharing corners and edges. The Mn-polyhedra are further linked by PO_4 tetrahedra to form a continuous network, with NH_4^+ cations residing in the extra-framework spaces. This material was found to demonstrate ferromagnetic behaviour. Other three-dimensional frameworks include $NaMn^{II}_3(PO_4)(HPO_4)_2$,[70] built up from face- or corner-sharing MnO_6 and PO_4 polyhedral units. The two-dimensional layered structures $(C_2H_{10}N_2)Mn^{II}_3(HPO_4)_4$[71], $Ba(Mn^{II}_2PO_4)_2 \cdot H_2O$[72], $K_4Mn^{II}_3(HPO_4)_4(H_2PO_4)_2$[73] have all been produced hydrothermally, and their structures consist of Mn-polyhedra, with six coordinated octahedra as well as fivefold trigonal bipyramids linked with PO_4 tetrahedra, and cations occupying the inter-layer space. These two-dimensional manganese phosphates are antiferromagnetic at low temperature. The manganese in these major reported structures mainly shows the oxidation state of +2, and structures with Mn^{3+} are scarce, but a few examples are known, such as $Na_3Mn^{III}H(P_{0.9}O_4)_2$ and $MMn^{III}HPO_3O_{10}$ (M = Rb, Cs).[74-76] The reason for these dominating hydrothermally synthesised Mn^{II} materials, is the easy reduction of manganese from higher oxidation states to lower oxidation states at high temperatures in aqueous solution.[74]

Recently, it was found that by introducing fluoride anions into the hydrothermal reaction mixture, the resulting materials are primarily comprised of Mn^{III}-centred polyhedra.[22, 77] This likely arises as the fluoride anions, when coordinated to metal centres, can stabilise higher oxidation states on metals due to their excellent electron-withdrawing and σ-donor character. Examples include the three-dimensional $Na_4Mn^{III}_2F_6(P_2O_7)$, consisting of chains formed of MnF_2O_4 octahedra connected through *trans*-fluorides and bridged by corner-shared P_2O_7 units. These chains are further cross-linked by MnF_4O_2 octahedra with the channels filled with Na^+ cations (Figure 1.4). $Rb_2Mn^{III}F_2(H_2PO_4)(HPO_4)$ possesses a two-dimensional structure, and consists of MnF_2O_4 octahedra connected via corner-sharing of oxygen to four phosphate tetrahedra to form corrugated layers separated by Rb^+ ions.

Manganese based sulfate materials are also of interest for their magnetic behaviour. For example, $Li_2Mn(SO_4)_2$, is prepared via the solid state method, by heating a mixture of Li_2SO_4 and $MnSO_4$. Unlike $Li_2Fe(SO_4)_2$, the Mn-based sulfate is known to be electrochemically inactive, due to the Jahn-Teller distortions of Mn^{3+} species that could result in the de-lithiated structure being unstable.[78] Magnetic studies indicate this material shows antiferromagnetic behaviour, with Néel temperature $T_N = 6$ K.[48] Open-framework manganese sulfates are rare compared with manganese phosphates, possibly due to their poor hydro- and thermo-stability. A few organo-templated manganese sulfate structures have been reported. $(C_2H_6O_2)MnSO_4$, possessing a three-dimensional zeolite GIS framework, was produced through the solvothermal treatment of manganese acetate, ethylene glycol and piperazine sulfate. Its structure is constructed from the alternating MnO_6 octahedra and SO_4 tetrahedra. Each MnO_6 octahedron corner-shares with four SO_4 tetrahedra, and each sulfate tetrahedron links with four MnO_6 octahedra through vertex-sharing of four oxygen. The polyhedral units extend to form the continuous network, with the channels formed along the *c*-axis filled with ethylene glycol molecules. The observed Mn-O bond lengths suggest the manganese cations are divalent. Another example is the one-dimensional chain structure of $(C_4N_2H_{12})Mn(SO_4)_2{\cdot}H_2O$, also prepared solvothermally, with a structure consisting of infinite $[Mn(SO_4)_2(H_2O)]^{2-}$ chains. The diprotonated piperazinium ions occupy the inter-chain space and form strong hydrogen bonds to the adjacent chains in order to stabilise the structure (Figure 1.7). Magnetic studies indicated the two compounds are antiferromagnetic with θ = -9.33 K and -12.04 K respectively.[79]

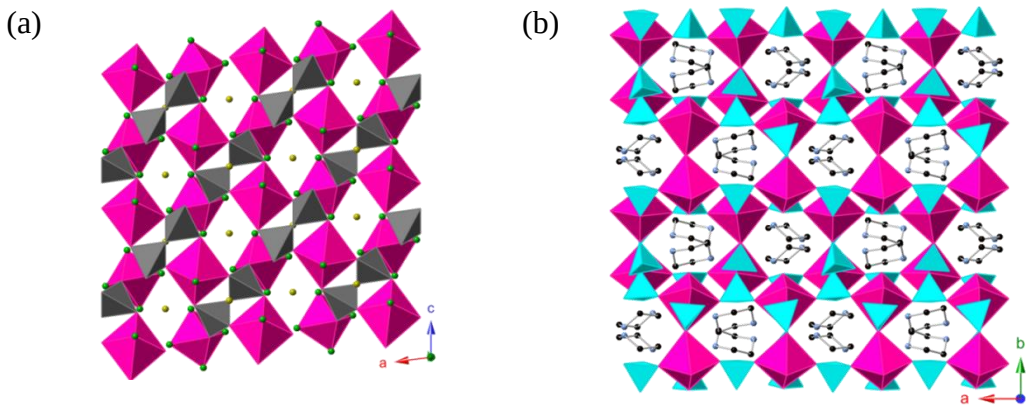

Figure 1.7: *(a) structure of $Na_4Mn^{III}{}_2F_6(P_2O_7)$ viewed down the b-axis, (b) structure of $(C_4N_2H_{12})Mn(SO_4)_2{\cdot}H_2O$ viewed down the c-axis, with Mn-octahedra in pink, P-tetrahedra in grey, S-tetrahedra in aqua blue, F^- - green sphere, Na^+ - yellow sphere, N – sky blue sphere, C – black sphere*

There is very limited information reported for manganese fluorosulfate materials. Much of the research work on manganese sulfates focused on mineral-like compounds that were primarily templated by alkali metals, such as the $MMnSO_4F$ (M = Li, Na or NH_4) and these have been suggested for use in the field of battery materials. Manganese fluorosulfates with templated open-frameworks have only been reported by Rao *et al.*[80] $(C_4N_2H_{12})(NH_4)_2Mn_3F_6(SO_4)_2$ was prepared solvothermally with $Mn(NO_3)_2 \cdot 4H_2O$, H_2SO_4, ethylene glycol ,piperazine and HF used as reactants, with heating at 150 ^oC for 3 days. This compound has a two-dimensional layered structure, with each layer consisting of six-membered rings, made up of alternating connected MnO_2F_4 octahedra and further capped by sulfate tetrahedra. The created rings are filled with NH_4^+ cations and the inter-layer space is occupied by diprotonated piperazine cations (Figure 1.8).

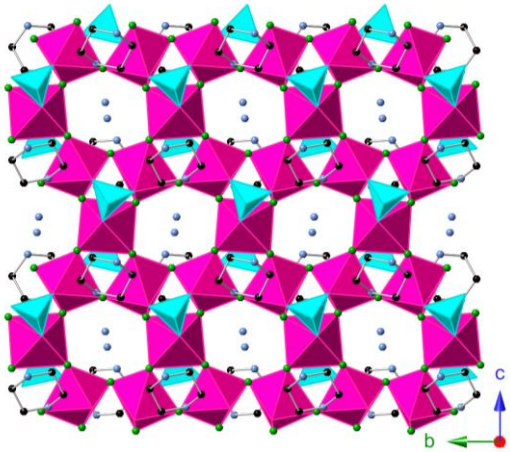

Figure 1.8: *Structure of $(C_4N_2H_{12})(NH_4)_2Mn_3F_6(SO_4)_2$ viewed down the a-axis, with Mn-octahedra in pink, S-tetrahedra in aqua blue, F-green sphere, N-sky blue sphere, C-black sphere.*

1.3.3 Vanadium phosphate and sulfate materials

Vanadium phosphate and sulfate materials have been broadly studied in respect of their rich structural diversities and applications. Vanadium based phosphates were originally investigated for their use in catalysis, particularly for the oxidation of *n*-butane, butane and pentane to maleic anhydride.[81] These are called V/P/O-based catalysts with examples such as $(VO)_2P_2O_7$ and alpha-$VOPO_4$.[82] Synthesis of vanadium phosphate materials can be achieved through both high temperature solid state or low temperature hydrothermal methods. The resulting materials, especially from the latter method, possess various structural dimensionalities, with vanadium adopting different oxidation states and coordinations environments including tetrahedral, square pyramidal and octahedral.

Layered vanadyl phosphates [$VOPO_4$] based on the unit form is an important class of low-dimensional phosphate structures, of interest due to their heterogeneous catalytic behaviour, and in intercalation chemistry as hosts to prepare functional materials.[83-86] For example, the intercalation of monovalent alkali metals leading to the $MVOPO_4$ (M = Li, Na, K) phases, where $KVOPO_4$ is of particular interest as it is isostructural with the well-known nonlinear optical material $KTiOPO_4$. $LiVOPO_4$ is also promising as a potential cathode material, showing a high redox potential of 3.95 V,[87] whilst $NaVOPO_4$ can be used in sodium ion batteries.[88] The series $MVOPO_4$ (M = Li, Na, K) can also be prepared from hydrothermal methods, with $LiVOPO_4$, Li_2O, V_2O_5 and H_3PO_4 used as starting materials. Within the structure of $LiVOPO_4$, the framework layers are built up from alternating connected VO_6 octahedra and PO_4 tetrahedra through corner-sharing. The VO_6 octahedron is extremely distorted, with one very long V-O bond and a characteristic short vanadyl V=O bond. Similar vanadium octahedral environments are also observed within other related vanadyl phosphates, where the long V-O bonds are usually in the range of 2.1-2.6 Å, whereas the short V=O bond is typically between of 1.55 Å and 1.75 Å.[89] The V-centres were determined to be in an oxidation state of +5 and Li^+ cations reside in the inter-layer spaces, as shown in Figure 1.5. Furthermore, through introducing the Cs^+ and Rb^+ ions into the vanadyl phosphate systems, the resulting structures were no longer layered, but formed of three-dimensional intersecting tunnel structures. The V-centres adopt the same oxidation states of +5, but exhibit five coordinated square pyramids, compared to the octahedral coordinations within the other related compounds.[90]

Fluoride incorporation into vanadium phosphates has been quite extensively studied, with most of the alkali metal templated vanadium fluorophosphates being synthesised due to their potential use as positive electrodes. The example of $LiVPO_4F$ was initially described by Barker et al,[91] as a material possessing a three-dimensional framework made up of vanadium octahedral chains bridged by PO_4 tetrahedra to form a continuous network. The fluoride anions occupy the *trans*-positions in the V-octahedra and form bridges between V centres. The V-octahedron is almost regular, adopting the +3 oxidation state and Li^+ ions were found to reside in the channels. Electrochemical performance of $LiVPO_4F$ indicated a high redox potential of 4 V with multivalent redox reactions (V^{2+} to V^{5+}). Soon after the $LiVPO_4F$ study, the sodium analogue was made through a similar method of combining VPO_4 and NaF at high temperature. Other examples of fluorides incorporated to the vanadium phosphate systems include $Na_3V_2O_2(PO4)_2F$,[92] which is structurally related to $Na_3Fe_2(PO_4)_2F_3$,[93] and possesses a three-dimensional lattice formed from layers of alternating linked VO_4F_2 octahedra and PO_4 tetrahedra through corner-sharing of oxygen. The layers are interconnected via F-bridging, and the channels filled with Na^+ ions. This material is of interest as being a potential positive electrode for sodium ion batteries. A further example is $Li_5V(PO_4)_2F_2$, produced via a solid state reaction method in the presence of LiF. It possesses a two-dimensional layered structure, where each layer is made of eight-membered rings consisting of corner-sharing VO_4F_2 octahedra and PO_4 tetrahedra. The fluoride anions occupy *trans*-positions within each V centred octahedron and are pointed toward the open space. Li^+ ions were found to reside within the rings as well as in between the layers (Figure 1.9). The layered and lithium containing nature of the structure makes this material a possible cathode for lithium-ion batteries. Electrochemical examination indicated the $Li_5V(PO_4)_2F_2$ exhibits a high redox potential greater than 4 V.[94]

In comparison with vanadium phosphate structures, the sulfate-based structures are very rare in the chemical structure database. However, one example is $NaV_3(SO_4)_2(OH)_6$ synthesised hydrothermally from VCl_4, Na_2SO_3 and H_2O. Its structure consists of VO_6 octahedral layers, cross-linked by SO_4 tetrahedra to form a three-dimensional framework with cavities occupied by Na^+ ions. This material demonstrates a strong ferromagnetic coupling between V-centres.[95] Amine-templated vanadium sulfate/fluorosulfate frameworks have been well studied by Rao *et al*.[56] Examples include $(C_6N_2H_{14})(VO)_2(SO_4)_2(OH)_2$ which can be prepared hydrothermally

using V_2O_5, $VOSO_4$ and DABCO, and whose structure is comprised of pairs of edge-sharing VO_5 square pyramids, and bridged by pairs of SO_4 tetrahedra to form the negatively charged chains. These chains are charge balanced by the diprotonated DABCO cations. $(C_4N_2H_{12})VF_3(SO_4)$, is produced hydrothermally in the presence of HF and its structure contains one-dimensional chains. The chains are built up from linked VO_2F_4 octahedral units through *trans*-fluoride, with SO_4 tetrahedra, bridging pairs of VO_2F_4 octahedra, alternating up and down along the vanadium chain. The adjacent chains interleave sulfate groups and are separated by diprotonated piperazine, held in place through hydrogen bonding interactions (Figure 1.10).

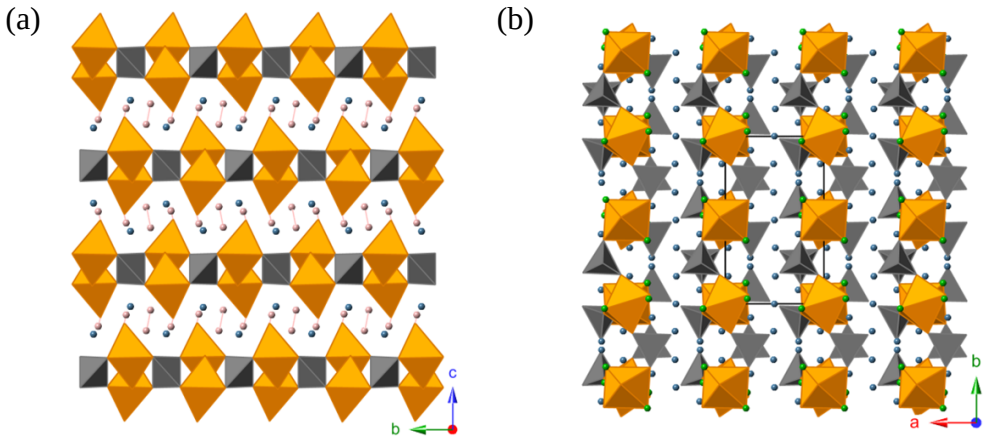

Figure 1.9*: (a) Structure of $LiVOPO_4$ viewed down the a-axis, (b) Structure of $Li_5V(PO_4)_2F_2$ viewed down the c-axis, with V-octahedra in orange, P-tetrahedra in grey, Li-sky blue, F-green, H-pale pink.*

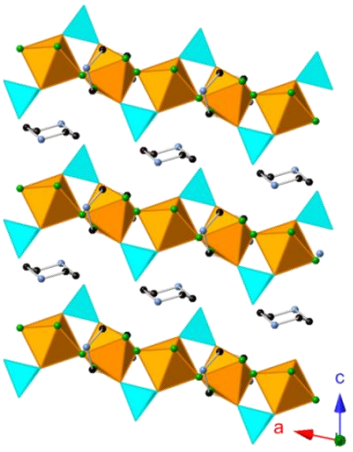

Figure 1.10: *Structure of $(C_4N_2H_{12})VF_3(SO_4)$ viewed down the b-axis, with V-octahedra in orange, S-tetrahedra in aqua blue, F-green sphere, N- blue sphere, C-black sphere.*

1.4 Scope of work

- 1.2 Inorganic materials with solar near infrared absorbing properties

The work includes the use of different synthetic techniques to prepare candidate materials with good NIR absorbing properties. These materials are all copper and phosphate based and their absorbing properties will be investigated. Preparations of these materials were all based on the methods from the literature, but other synthetic methods will be attempted in terms of making optimised materials. The products will be characterised using powder X-ray diffraction to determine the phase purities and the absorbance spectra will be investigated using a Perkin Elmer UV/Vis/NIR Lambda 19 spectrometer.

In this thesis, the inorganic materials with NIR absorbing properties are presented as follows.

Chapter Three describes a series of copper phosphate materials prepared through different synthetic methods, and their NIR absorbing properties were studied.

- 1.3 Inorganic framework materials

The aim of this project is to synthesis and characterise new transition metal phosphate and sulfate materials with potential for industrial applications such as battery materials, catalysis and ion exchange materials. The determined structures were found to be based on a variety of polyhedral building units, primarily octahedral and tetrahedral. The transition metals vanadium, iron and manganese form octahedral units, whereas the tetrahedral units will primarily be phosphate and sulfate anions. The different structural building units provide an aid to imagining the new structural topologies.

Results from synthetic work on new framework materials are covered in this thesis as follows.

Chapter Four describes seven novel phosphate-based structures produced from the developed hydrothermal method in fluoride-rich medium. Fluoride anions were successfully incorporated in every structure, and the resulting structural features were examined.

Chapter Five describes ten new sulfate-based structures with a variety of structural dimensionalities. Electrochemical studies have been carried out on two materials. Most of the structures incorporated fluoride anions.

Chapter Six summaries results on several templated metal sulfate structures with thermal investigations of these materials.

1.5 References

1. J. S. Wang, S. Y. Wang, Y. W. Zeng, H. Y. Huang, F. Luo, Z. P. Xu, Q. X. Tang, G. B. Lin, C. F. Zhang, Z. Y. Ren, G. M. Zhao, D. G. Zhu, S. H. Wang, H. Jiang, M. Zhu, C. Y. Deng, P. F. Hu, C. Y. Li, F. Liu, J. S. Lian, X. R. Wang, L. H. Wang, X. M. Shen and X. G. Dong, *Physica C-Superconductivity and Its Applications*, 2002, **378**, 809-814.
2. D. W. Goodman, R. D. Kelley, T. E. Madey and J. T. Yates, *J. Catal.*, 1980, **63**, 226-234.
3. *Joining Plastics 2006*, Rapra Technology Ltd, London, 2006.
4. J. O. Escobedo, O. Rusin, S. Lim and R. M. Strongin, *Curr. Opin. Chem. Biol.*, 2010, **14**, 64-70.
5. G. Cao and C. J. Brinker, *Annual Review of Nano Research*, World Scientific Publishing Co, 2008.
6. P. Bamfield, M. G. Hutchings and C. Phenomena, *Technological Applications of Colour Chemistry*, RSC Publising, Cambridge, 2010.
7. E. R. Dufresne, H. Noh, V. Saranathan, S. G. J. Mochrie, H. Cao and R. O. Prum, *Soft Matter*, 2009, **5**, 1792-1795.
8. P. Atkins, T. Overton, J. Rourke, M. Weller and F. Armstrong, *Inorganic Chemistry*, 5 edn., W.H. Freeman & Company, Oxford 2009.
9. K. V. Reddy, *Symmetry And Spectroscopy Of Molecules*, 2 edn., New Age Science Ltd, 2009.
10. G. S. Manku, *Theoretical Principles of Inorganic Chemistry*, McGraw-Hill Education, 1982.
11. I. B. Bersuker, *The Jahn–Teller Effect*, Cambridge University Press, Cambridge, 2006.
12. G. Buxbaum and G. Pfaff, *Industrial inorganic pigments*, 3 edn., Wiley, 2005.
13. S. T. Wilson, B. M. Lok, C. A. Messina, T. R. Cannan and E. M. Flanigen, *J. Am. Chem. Soc.*, 1982, **104**, 1146-1147.
14. A. K. Cheetham, G. Ferey and T. Loiseau, *Angew. Chem. Int. Ed.* , 1999, **38**, 3268-3292.
15. S. Natarajan and S. Mandal, *Angew. Chem. Int. Ed.*, 2008, **47**, 4798-4828.
16. R. E. Morris and S. J. Weigel, *Chem. Soc. Rev.*, 1997, **26**, 309-317.

17. E. R. Cooper, C. D. Andrews, P. S. Wheatley, P. B. Webb, P. Wormald and R. E. Morris, *Nature*, 2004, **430**, 1012-1016.
18. N. Recham, J. N. Chotard, L. Dupont, C. Delacourt, W. Walker, M. Armand and J. M. Tarascon, *Nat. Mater.*, 2010, **9**, 68-74.
19. M. Estermann, L. B. McCusker, C. Baerlocher, A. Merrouche and H. Kessler, *Nature*, 1991, **352**, 320-323.
20. H. Kessler, J. Patarin and C. Schottdarie, *Advanced Zeolite Science and Applications*, 1994, **85**, 75-113.
21. M. Goepper and J. L. Guth, *Zeolites*, 1991, **11**, 477-482.
22. J. A. Armstrong, E. R. Williams and M. T. Weller, *Dalton Trans.*, 2013, **42**, 2302-2308.
23. C. N. R. Rao, J. N. Behera and M. Dan, *Chem. Soc. Rev.*, 2006, **35**, 375-387.
24. G. Ferey, *Chem. Mater.*, 2001, **13**, 3084-3098.
25. P. B. Moore and J. Shen, *Nature*, 1983, **306**, 356-358.
26. D. R. Corbin, J. F. Whitney, W. C. Fultz, G. D. Stucky, M. M. Eddy and A. K. Cheetham, *Inorg. Chem.*, 1986, **25**, 2279-2280.
27. M. Ai and K. Ohdan, *J. Mol. Catal. A: Chem.*, 2000, **159**, 19-24.
28. M. Ai and K. Ohdan, *Appl. Catal., A*, 1997, **165**, 461-465.
29. M. Ai and K. Ohdan, in *3rd World Congress on Oxidation Catalysis*, eds. R. K. Grasselli, S. T. Oyama, A. M. Gaffney and J. E. Lyons, Elsevier Science Publ B V, Amsterdam, 1997, vol. 110, pp. 527-534.
30. J. R. D. DeBord, W. M. Reiff, C. J. Warren, R. C. Haushalter and J. Zubieta, *Chem. Mater.*, 1997, **9**, 1994-1998.
31. J. R. D. DeBord, W. M. Reiff, R. C. Haushalter and J. Zubieta, *J. Solid State Chem.*, 1996, **125**, 186-191.
32. M. Cavellec, D. Riou and G. Ferey, *J. Solid State Chem.*, 1994, **112**, 441-442.
33. M. Riou-Cavellc, D. Riou and G. Ferey, *Inorg. Chim. Acta*, 1999, **291**, 317-325.
34. P. P. Prosini, M. Lisi, S. Scaccia, M. Carewska, F. Cardellini and M. Pasquali, *J. Electrochem. Soc.*, 2002, **149**, A297-A301.
35. Y. N. Song, S. F. Yang, P. Y. Zavalij and M. S. Whittingham, *Mater. Res. Bull.*, 2002, **37**, 1249-1257.
36. A. K. Padhi, K. S. Nanjundaswamy and J. B. Goodenough, *J. Electrochem. Soc.*, 1997, **144**, 1188-1194.

37. M. S. Whittingham, Y. J. Li, J. Chen and W. Hurng, *U.S. Patent*, 1996, **490**, 5514.
38. K. S. Nanjundawamy, A. K. Padhi, J. B. Goodenough, S. Okada, H. Ohtsuka, H. Arai and J. Yamaki, *Solid State Ionics*, 1996, **92**, 1-10.
39. J. M. Tarascon and M. Armand, *Nature*, 2001, **414**, 359-367.
40. S. F. Yang, P. Y. Zavalij and M. S. Whittingham, *Electrochem. Commun.*, 2001, **3**, 505-508.
41. C. Masquelie, C. Wurm, J. Rodriguez-Carvajal, J. Gaubicher and L. Nazar, *Chem. Mater.*, 2000, **12**, 525-532.
42. S. M. Oh, S. T. Myung, J. Hassoun, B. Scrosati and Y. K. Sun, *Electrochem. Commun.*, 2012, **22**, 149-152.
43. B. L. Ellis, W. R. M. Makahnouk, W. N. Rowan-Weetaluktuk, D. H. Ryan and L. F. Nazar, *Chem. Mater.*, 2010, **22**, 1059-1070.
44. R. Tripathi, S. M. Wood, M. S. Islam and L. F. Nazar, *Energy Environ. Sci.*, 2013, **6**, 2257-2264.
45. A. K. Padhi, V. Manivannan and J. B. Goodenough, *J. Electrochem. Soc.*, 1998, **145**, 1518-1520.
46. A. K. Padhi, K. S. Nanjundaswamy, C. Masquelier and J. B. Goodenough, *J. Electrochem. Soc.*, 1997, **144**, 2581-2586.
47. S. Islam, C. Eames, J. Clark, J.-M. Tarascon, G. Rousse, J.-N. Chotard and M. Reynaud, *J. Mater. Chem. A*, 2014.
48. M. Reynaud, G. Rousse, J. N. Chotard, J. Rodriguez-Carvajal and J. M. Tarascon, *Inorg Chem*, 2013, **52**, 10456-10466.
49. P. D. Battle, A. K. Cheetham, G. J. Long and G. Longworth, *Inorg. Chem.*, 1982, **21**, 4223-4228.
50. G. J. Long, G. Longworth, P. Battle, A. K. Cheetham, R. V. Thundathil and D. Beveridge, *Inorg. Chem.*, 1979, **18**, 624-632.
51. H. Serrano-Gonzalez, S. T. Bramwell, K. D. M. Harris, B. M. Kariuki, L. Nixon, I. P. Parkin and C. Ritter, *J. Appl. Phys.*, 1998, **83**, 6314-6316.
52. A. S. Wills, *Can. J. Phys.*, 2001, **79**, 1501-1510.
53. J. S. White, M. Bator, Y. Hu, H. Luetkens, J. Stahn, S. Capelli, S. Das, M. Döbeli, T. Lippert, V. K. Malik, J. Martynczuk, A. Wokaun, M. Kenzelmann, C. Niedermayer and C. W. Schneider, *Phys. Rev. Lett.*, 2013, **111**, 037201.

54. P. Barpanda, M. Ati, B. C. Melot, G. Rousse, J. N. Chotard, M. L. Doublet, M. T. Sougrati, S. A. Corr, J. C. Jumas and J. M. Tarascon, *Nat. Mater.*, 2011, **10**, 772-779.
55. G. Paul, A. Choudhury and C. N. R. Rao, *Chem. Mater.*, 2003, **15**, 1174-1180.
56. J. N. Behera and C. N. R. Rao, *Chem. Asian J.*, 2006, **1**, 742-750.
57. M. M. Thackeray, *Prog. Solid State Chem.*, 1997, **25**, 1-71.
58. V. V. Krishnan and S. L. Suib, *J. Catal.*, 1999, **184**, 305-315.
59. R. K. Malkani, K. S. Suresh and G. V. Bakore, *J. Indian Chem. Soc.*, 1978, **55**, 215-219.
60. A. G. Fadni and S. K. Kulshrestha, *React. Kinet. Catal. Lett.*, 1982, **19**, 267-269.
61. T. E.-M. A, A. M. Hassib and S. M. Farid, *Met. Finish.*, 1988, **86**, 29.
62. G. Y. Li, J. S. Lian, L. Y. Niu and Z. H. Jiang, *ISIJ Int.*, 2005, **45**, 1326-1330.
63. C. V. Subban, M. Ati, G. Rousse, A. M. Abakumov, G. Van Tendeloo, R. Janot and J. M. Tarascon, *J. Am. Chem. Soc.*, 2013, **135**, 3653-3661.
64. G. H. Li, H. Azuma and M. Tohda, *Electrochemical and Solid State Letters*, 2002, **5**, A135-A137.
65. G. H. Li, H. Azuma and M. Tohd, *J. Electrochem. Soc.*, 2002, **149**, A743-A747.
66. A. Yamada, Y. Kudo and K. Y. Liu, *J. Electrochem. Soc.*, 2001, **148**, A747-A754.
67. K. T. Lee, T. N. Ramesh, F. Nan, G. Botton and L. F. Nazar, *Chem. Mater.*, 2011, **23**, 3593-3600.
68. Q. L. Wang, A. Madsen, J. R. Owen and M. T. Weller, *Chem. Commun.*, 2013, **49**, 2121-2123.
69. S. Neeraj, M. L. Noy and A. K. Cheetham, *Solid State Sciences*, 2002, **4**, 397-404.
70. F. Leroux, A. Mar, C. Payen, D. Guyomard, A. Verbaere and Y. Piffard, *J. Solid State Chem.*, 1995, **115**, 240-246.
71. S. Fernandez, J. L. Mesa, J. L. Pizarro, L. Lezama, M. I. Arriortua, R. Olazcuaga and T. Rojo, *Chem. Mater.*, 2000, **12**, 2092-2098.
72. J. Escobal, J. L. Mesa, J. L. Pizarro, L. Lezama, R. Olazcuaga and T. Rojo, *J. Mater. Chem.*, 1999, **9**, 2691-2695.
73. D. Feng, C. Wang, W. Cheng, G. Li, S. Tian, F. Liao, M. Xiong and J. Lin, *Solid State Sciences*, 2009, **11**, 845-851.

74. S. Ferdov, A. M. L. Lopes, Z. Lin and R. A. S. Ferreira, *Chem. Mater.*, 2007, **19**, 6025-6029.
75. A. J. Wright and J. P. Attfield, *J. Solid State Chem.*, 1998, **141**, 160-163.
76. A. J. Wright and J. P. Attfield, *Inorg. Chem.*, 1998, **37**, 3858-3861.
77. J. A. Armstrong, E. R. Williams and M. T. Weller, *J. Am. Chem. Soc.*, 2011, **133**, 8252-8263.
78. M. M. Thackeray, W. I. F. David, P. G. Bruce and J. B. Goodenough, *Mater. Res. Bull.*, 1983, **18**, 461-472.
79. G.-W. Ge, Z.-Y. Qi, Y.-R. Miao, H.-B. Du and X.-Z. You, *CrystEngComm*, 2013, **15**, 435-438.
80. J. N. Behera and C. N. R. Rao, *Dalton transitions* 2007, 669-673.
81. E. Bordes, *Catal. Today*, 1993, **16**, 27-38.
82. G. J. Hutchings, *Applied Catalysis*, 1991, **72**, 1-32.
83. A. J. Jacobson, J. W. Johnson, J. F. Brody, J. C. Scanlon and J. T. Lewandowski, *Inorg. Chem.*, 1985, **24**, 1782-1787.
84. M. Roca, M. D. Marcos, P. Amoros, J. Alamo, A. BeltranPorter and D. BeltranPorter, *Inorg. Chem.*, 1997, **36**, 3414-3421.
85. H. Nakajima and G. E. Matsubayashi, *J. Mater. Chem.*, 1995, **5**, 105-108.
86. N. Dupre, J. Gaubicher, T. Le Mercier, G. Wallez, J. Angenault and M. Quarton, *Solid State Ionics*, 2001, **140**, 209-221.
87. T. A. Kerr, J. Gaubicher and L. F. Nazar, *Electrochemical and Solid State Letters*, 2000, **3**, 460-462.
88. J. Song, M. W. Xu, L. Wang and J. B. Goodenough, *Chem. Commun.*, 2013, **49**, 5280-5285.
89. P. Y. Zavalij and M. S. Whittingham, *Acta Crystallogr., Sect. B: Struct. Sci*, 1999, **55**, 627-663.
90. K.-H. Lii and W.-C. Liu, *J. Solid State Chem.*, 1993, **103**, 38-44.
91. J. Barker, M. Y. Saidi and J. L. Swoyer, *J. Electrochem. Soc.*, 2003, **150**, A1394-A1398.
92. F. Sauvage, E. Quarez, J. M. Tarascon and E. Baudrin, *Solid State Sciences*, 2006, **8**, 1215-1221.
93. A. C. Keates, J. A. Armstrong and M. T. Weller, *Dalton Trans.*, 2013, **42**, 10715-10724.

94. Y. Makimura, L. S. Cahill, Y. Iriyama, G. R. Goward and L. F. Nazar, *Chem. Mater.*, 2008, **20**, 4240-4248.

95. D. Grohol, D. Papoutsakis and D. G. Nocera, *Angew. Chem. Int. Ed.*, 2001, **40**, 1519-1524.

CHAPTER TWO: EXPERIMENTAL TECHNIQUES

2.0 Introduction

The research work included in this thesis focussed on the synthesis and characterisation of known and new inorganic materials, due to their wide-ranging potential and current applications, these including as catalysts, as cathodes in rechargeable batteries, and in non-linear optical devices. The synthetic methods employed within this research include general solid state reactions, chemical co-precipitation and the hydrothermal (solvothermal) method for synthesis of new inorganic materials.

Resulting products were characterised using a variety of techniques commonly used in solid state chemistry, such as the powder X-ray diffraction (PXD) used to assist in the determination of phase purity of the reaction products. Near-infrared spectroscopy (NIR) was used to investigate the IR absorption bands of the products and any changes arising from physical processes, utilising a detection range of 900-2500 nanometers in addition to investigating the characteristic vibrational modes of the functional groups, in particular the hydroxide group. Single crystal X-ray diffraction (SXD) was used in the characterisation of any new crystal structures produced; this technique was the primary characterisation method used for identifying the products of hydrothermal reactions. Thermogravimetric analysis was used to study the thermal behaviour of selected products, e.g. the weight loss during the exo/endothermic processes. This technique is a useful analysis method for those products containing water molecules, ammonium cations and any amine templated structures. Scanning electron microscopy (SEM) was used to study the morphology of microcrystals, and was combined with energy dispersive X-ray microanalysis (EDX), used to identify the elemental composition of a sample.

2.1 Synthetic methods

The choice of method used to prepare a solid material is of considerable significance. Different synthetic methods may result in products with different forms, such as powders, single crystals, solid monoliths *etc*. The starting materials involved in preparation of inorganic materials are commonly inert; thereby for any reaction to take place, adequate energy input is required to drive the reaction forward, for example, reactions at very high temperature. Many methods have been developed based on a final high reaction temperature condition including the traditional solid state reaction, co-precipitation method, and the sol-gel processes. Materials prepared from those methods are usually classified as the thermodynamic products.

The hydrothermal or solvothermal routes are also well known in material chemistry, and have been commonly used in the synthesis of many functional inorganic materials with *meta*-stable structures (kinetic products), such as zeolites, other porous materials and many other composite materials.

2.1.1 Solid state reactions

The solid state reaction is one of the most commonly used methods in the preparation of inorganic materials, such as pigments and semiconductors. This method can be described as the direct reaction of a mixture of solid starting reagents,[1] and can also be called the "dry method". The reaction is undertaken at a high temperature due to the slow diffusion of ions within the inorganic starting materials at normal temperatures. In order to speed up reaction rates, the temperature used is as high as possible. Temperatures employed in the research presented herein were typically in the range of 500 °C to 1200 °C.

The general procedure for the solid state reaction employs stoichiometric mixtures of solid starting materials, which are usually in the form of a fine powder thereby yielding high contact surface areas. Metal oxides, carbonates, nitrates as well as oxalates are typically used at starting materials, as these decompose at the reaction temperature to yield small highly reactive particles. The mixtures are initially ground with an agate pestle and mortar to further reduce the particle sizes. Smaller particle sizes have a larger contact surface, which results in a faster reaction rate. A ball mill may be used to achieve extremely finely ground materials. The grinding stage is aimed at reducing the diffusion limitations of the solid starting materials as far as possible. The

finely ground mixture is then transferred to a suitable crucible, typically high density alumina. However, since alumina crucibles are not always chemically inert, platinum or gold crucibles can also be used.

The solid state reaction does not always produce pure homogeneous products; possible reasons are based on several factors, such as the solid reaction mixture cannot be uniformly heated during the reaction, and lack of sufficient heating may also result in unfinished reaction. In order to improve product purity, an intermediate regrind as well as pelletisation of the reaction mixture are essential, in order to obtain pure phase products. In addition, environmental control during a reaction can be crucial in controlling metal oxidation states present in the final product. Therefore the ability to keep the reaction in some cases under oxygen, nitrogen, argon, or hydrogen atmosphere is important.

2.1.2 Chemical co-precipitation

The chemical co-precipitation can be referred as the "wet method" and is also commonly used for preparation of inorganic materials. In contrast to the solid state dry method, the initial preparation of the starting materials for a co-precipitation synthesis is carried out in solution.

For a typical synthesis using the co-precipitation method, all starting materials are dissolved in solution and mixed, then precipitated together from a common solution by adding a precipitating reagent.[2] The precipitate obtained is subsequently heated to the required temperature under the desired reaction atmosphere to yield the product. The initial precipitated fine powder from a common solution is a solid solution[2], which contains mixed ions on an atomic scale with a high degree of homogenisation and large contact surface areas. This enhances the reaction rate, and results in a decrease of the reaction temperature and time, compared to a traditional solid state method. However, chemical synthesises always require specific reaction conditions, and these are greatly dependent on the nature of the materials used. The drawback of the wet method is that all reactants used for reactions are preferred to have similar solubilities and precipitation rates. Therefore the wet method is sometimes even more complex than the direct dry method.

2.1.3 Hydrothermal synthesis

Despite the fact that the hydrothermal synthetic technique has demonstrated significant improvements in material chemistry, there is no unanimity about its definition. The term *hydrothermal* usually refers to any heterogeneous chemical reaction occurring under high pressure and temperature conditions in water to dissolve and recrystallise materials that are relatively insoluble under normal conditions.[3] The hydrothermal reaction is typically carried out in a closed system to create ambient reaction conditions, for the synthesis in this work, hydrothermal vessels (autoclaves) are used to create such reaction atmospheres. The stainless steel autoclave design to use is a Parr acid digestion bomb manufactured by the Parr Instrument Company. The reaction vessel contains a removable Teflon liner with an internal volume of 23 mL and possesses a maximum operating temperature and pressure of 250 ℃ and 1800 psi. The hydrothermal vessel consists of a spring-loaded, broad flanged closure that is sealed by a bomb screw cap (Figure 2.1). For a typical hydrothermal synthesis, the reactants are placed in the Teflon-liner filled with water and well-sealed in an autoclave, autogenous pressure will be generated to drive the reaction, while heating the autoclave in an oven at desired temperature.

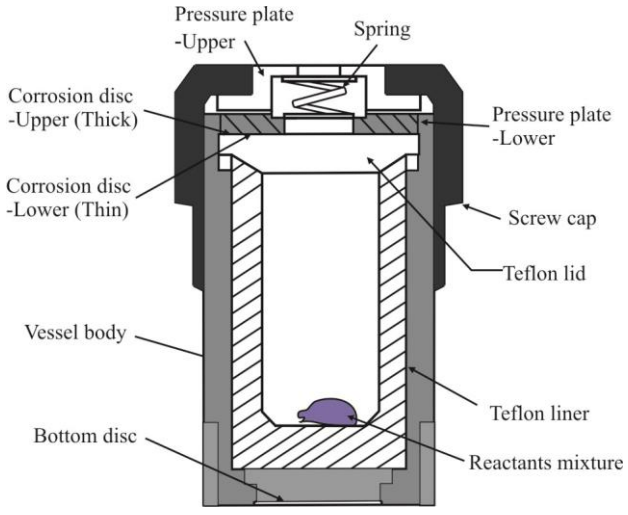

Figure 2.1: *Parr acid digestion vessel model 4749*

The hydrothermal method can also be referred to as solvothermal if a solvent is being used in the synthesis other than water. Solvents such as alcohols and many other organic solvents have all been used in preparation of new inorganic materials with varying degrees of success. This method employed in this research is primarily for growth of single crystals and preparation of new *meta-stable* materials. The principle

behind the solvo/hydrothermal synthesis is that the rate of reaction between solids can be increased when the solvent is above its usual boiling point under pressure, through heating the autoclave.[1] The solvent has two forms, as a liquid or a vapour, which serves as the pressure transmitting medium, allowing the practically insoluble reactants to become more soluble and reactive.

Although the solvothermal route is considered to be a high temperature method, in reality the temperatures operated are much lower than the traditional melt techniques. The solvothermal method offers many advantages over the traditional solid state methods. Within a solvothermal reaction, the mixture of starting materials is in a liquid transmitting medium, like water, which gives greater ion mobility between reagents compared to a solid mixture phase. As a result of the rapid diffusion process, this allows for fast growth of crystals. Whereas within a direct solid state reaction, reactions can only occur at much higher temperatures and longer reaction times in order for the reagents to overcome the considerable diffusion barriers. The high temperature solid state reaction method is good in preparation of thermodynamic materials of interest, such as oxides. Whilst the low reaction temperature applied for solvothermal syntheses often lead to formation of kinetic phases, such as the zeolites. Control of the size, shape distribution and crystallinity of the final product can be achieved via the solvothermal technique. An example of this is, the *meta-stable* layered structure of nano-scaled vanadium oxide,[4] prepared through the hydrothermal route for use in rechargeable batteries as a cathode material. However, the crystallisation process of materials in solvothermal synthesis does not necessarily take place in solution,[5] it may also occur on the surface of a reagent mixture.

Solvothermal synthesis does exhibit some disadvantages. The most noticeable of these is that the reaction mechanism is difficult to determine as the reaction is undertaken in a closed system. A large number of factors can influence the reaction which cannot be recorded and regulated readily. Factors such as the reaction temperature and time, as well as the pH and concentration of the initial prepared starting materials, may all play significant roles during the reaction process.

2.2 X-ray diffraction

During this research work, two X-ray diffraction techniques have been used to study the produced crystalline materials. These include the structural determination of any potential new materials synthesised in soluble form using single crystal X-ray diffraction. The second diffraction technique used to study the materials produced was powder X-ray diffraction. This technique was primarily used for phase identification, through comparing the collected diffraction pattern of the analysed material to the standard pattern in a database by the Joint Committee on Powder Diffraction Standards (JCPDS) using the EVA program.[6] The powder technique was also used for quick phase purity checks of any new materials produced. This can be done by comparing the collected diffraction patterns to those generated from the single crystal diffraction data.

2.2.1 Diffraction theory

The phenomenon of X-ray diffraction by crystals was first noted by Max von Laue in 1912,[7] after the discovery of X-rays which have wavelengths of the same order of magnitude of the interatomic spacing of crystals (d ≅1 Å). The subsequently proposed Laue equations described the diffraction of the incident radiation by a crystal. The work had been further advanced and simplified by W. H. Bragg and W. L. Bragg, who explained that incident X-rays can be scattered by a crystal from specific directions.

Crystals are solid materials consisting of regularly arranged atoms extending in three spatial dimensions. The arrangement can be represented by a smallest three dimensional repeating unit called the unit cell. The unit cell is a symmetric parallelepiped, characterised by lattice parameters including three non-coplanar directions *a (x), b (y), c (z),* which represent the cell edges and the interaxial angles α, β and γ (Figure 2.2). An infinite crystal is simply built up from a repetition of the unit cell along the *a (x), b (y), c (z)* directions.

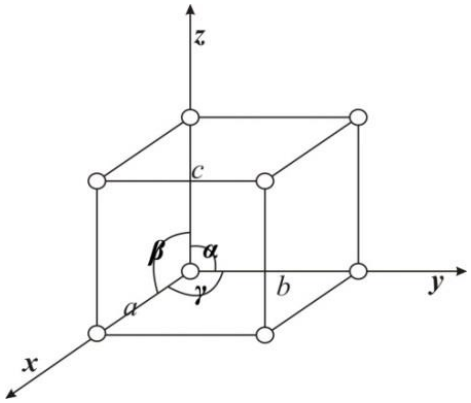

Figure 2.2: *The unit cell defined by lattice parameters a (x), b (y), c (z) and α, β, γ*

The unit cell geometry is constrained by the internal symmetry of the crystal lattice. A crystal lattice is the symmetrical arrangement of atoms in a regular repeating pattern or a regular array of points within the unit cell. Different kinds of symmetry provide unique characteristics that give rise to unit cell geometries for each of the seven crystal systems, as outlined in Table 2.1. The seven crystal systems can be divided further into fourteen Bravais lattices with four distinct Bravais lattice types; these are: Primitive (P), with lattice points on the unit cell corners only; Body centred (I), with one additional lattice point at the centre of the unit cell; and Face centred (F), with one additional lattice point at the centre of each face of the unit cell or selected points at one of the faces (A, B or C). The unit cell, in combination with different symmetry operations pass through a fixed single point, can be arranged into 32 possible combined symmetry elements. These are the 32 crystallographic point groups, also called the macroscopic symmetry elements,[8] which determines the properties of a crystal. The combination of point and translational symmetry operations result in a total of possible 230 space groups.

Crystal with three dimensional structure can be regarded as an assembly of equidistant parallel planes separated by an equivalent spacing. Each plane intersection with a regular periodic arrangement of lattice points is called the lattice plane. The separation distance is referred as the *d*-spacing. The orientation of the lattice plane is determined by connecting at least three lattice points. Due to the periodicity of the lattice, there will be a series of lattice planes parallel passing through these lattice points. A convenient way to specify the orientation of any planes in the series is defined as the Miller Indices; with the form of *h, k, l.* The Miller indices are the reciprocals of the plane intercepts in a unit cell of *a/h*, *b/k* and *c/l*.

Table 2.1: *The seven crystal systems, 14 Bravais lattices, and point groups*

Crystal System	Lattice Parameters	Point group	Bravais lattices
Triclinic	$a \neq b \neq c$ $\alpha \neq \beta \neq \gamma \neq 90°$	1, $\bar{1}$	P
Monoclinic	$a \neq b \neq c$ $\alpha = \gamma = 90° \ \beta \neq 90°$	2/*m*, *m*, 2	P C
Orthorhombic	$a \neq b \neq c$ $\alpha = \beta = \gamma = 90°$	*mmm*, *mm*2, 222	P C I F
Tetragonal	$a = b \neq c$ $\alpha = \beta = \gamma = 90°$	4/*mmm*, $\bar{4}$2*m*, 4*mm*, 422,4/*m*, -4, 4	P I
Trigonal/ Rhombohedral	$a = b = c$ $\alpha = \beta = \gamma \neq 90°$	$\bar{3}$*m*, 3*m*, 32, $\bar{3}$, 3	P
Hexagonal	$a = b \neq c$ $\alpha = \beta = 90° \ \gamma = 120°$	6/*mmm*, $\bar{6}$m2, 6*mm*, 622, 6/*m*, $\bar{6}$, 6	P
Cubic	$a = b = c$ $\alpha = \beta = \gamma = 90°$	*m*$\bar{3}$*m*, $\bar{4}$3*m*, 432, *m*$\bar{3}$, 23	P I F

The short wavelength of X-rays is well suited for studying inter-planar atomic spacing, and the approximate energy of a quantum of X-ray is equivalent to the energy of electrons in their orbitals. This similar energy leads to interactions where the incident X-rays can be scattered by electrons of atoms in crystals. The scattered waves can interfere constructively, causing the diffraction effect, and the resulting diffraction pattern reflects the internal arrangement of atoms in the crystal.

As the atoms are periodically arranged in a crystal lattice, the scattered X-rays from all atoms in a set of planes is in phase, thus they interfere constructively. However, the interference of X-rays are restrained by Bragg's law,[9] which defines the indispensable conditions to be met in order for constructive interference to occur. Figure 2.3 illustrates the incident X-ray beam scattered by a set of adjacent parallel lattice planes separated by a distance of d_{hkl}. The two incoming X-ray beams inclined at an angle θ with the lattice plane and are scattered at the same angle. If scattered beams are from different lattice points on the same plane, they are in phase. On the other hand, when the beams are scattered from two adjacent planes, the beam hitting a lower plane must travel additional distances (highlighted in orange on Figure 2.3), in order to remain in phase with the first beam. The distance travelled by the beam must be equal to an integral multiple of the wavelength that can be expressed in following equation:

$$n\lambda = 2d_{hkl}sin\theta \tag{2.01}$$

This is known as Bragg's equation (2.01), where d_{hkl} represents the *d*-spacing between adjacent planes where *n* is the diffraction order and λ is the X-ray wavelength. Thereby for constructive diffraction to occur, Bragg's conditions must be satisfied.

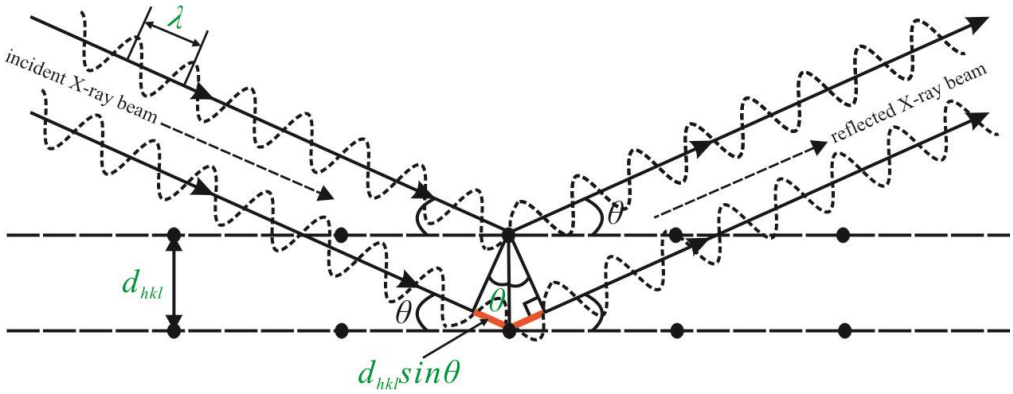

Figure 2.3: *Schematic representation of Bragg's Law*

The lattice spacing d_{hkl} can be expressed with regards to the crystal system lattice parameters and Miller indices *h, k, l*, and, when combined with Bragg's equation, it is possible to deduce the unit cell parameters. Table 2.2 summarises the relationships between the d_{hkl} and the lattice parameters.

Table 2.2: *d-spacing expressions in terms of lattice parameters and Miller indices.*

Crystal system	Expressions for d_{hkl}
Cubic	$\frac{1}{d^2} = \frac{h^2+k^2+l^2}{a^2}$
Tetragonal	$\frac{1}{d^2} = \frac{h^2+k^2}{a^2} + \frac{l^2}{c^2}$
Orthorhombic	$\frac{1}{d^2} = \frac{h^2}{a^2} + \frac{k^2}{b^2} + \frac{l^2}{c^2}$
Monoclinic	$\frac{1}{d^2} = \frac{1}{sin^2\theta}\left(\frac{h^2}{a^2} + \frac{k^2 sin^2\theta}{b^2} + \frac{l^2}{c^2} - \frac{2hlcos\beta}{ac}\right)$
Triclinic	Complex expression
Hexagonal	$\frac{1}{d^2} = \frac{4}{3}\left(\frac{h^2+hk+k^2}{a^2}\right) + \frac{l^2}{c^2}$

The lattice type of the crystal and the symmetry elements present are responsible for some of the systematic absences in the diffraction pattern, and therefore systematic absences are very useful for the determination of the Bravis lattice of a crystal. These absences impose restrictions on the reflections observed. In X-ray diffraction, the disappearance of some reflected intensities from certain planes are usually referred to as systematic absences. The systematic absence is a condition that applies to the class of

reflections specified. These systematic absences arise in centred lattice types with additional lattice points or due to the presence of symmetry elements from glide planes and screw axes. For example, for a body-centred cubic lattice, X-rays diffracted from the (100) plane have zero intensity, and therefore are systematically absent. This is because X-rays diffracted at the Bragg angle for the (100) plane get nullified due to the destructive interference from X-rays diffracted from the body-centred lattice point lying halfway between adjacent (100) planes. X-rays diffracted from the (200) plane give rise to a strong reflection and ascribe to constructive interference. For the same reasons described above, reflections from (111) planes are systematic absences, whilst reflections from (110) planes in a body-centered cubic lattice are observed. The condition for reflections to be observed in a body-centered cubic lattice is $h + k + l = 2n$, i.e. when $(h + k + l)$ is odd the reflections are absent, and *h, k, l* must be all odd or all even for reflections to be observed in face-centred crystal lattices.

The full determination of further structural information (atom positions/types etc.) for either a powder or single crystal sample requires much more information. It is very difficult to solve a structure from a powder diffraction data due to the problems arising from the overlapping of diffraction peaks. However, since the quantity of data collected from single crystal diffraction is much greater than from powder diffraction, thus to make the single crystal X-ray diffraction becomes the most popular analytical technique for crystal structure determination. Single crystal diffraction data is collected as huge number of diffraction spots, from whose positions and intensities of further structural information can be determined. The occurrence of diffractions spots can be explained by the means of Ewald's sphere, which is shown in Figure 2.4.

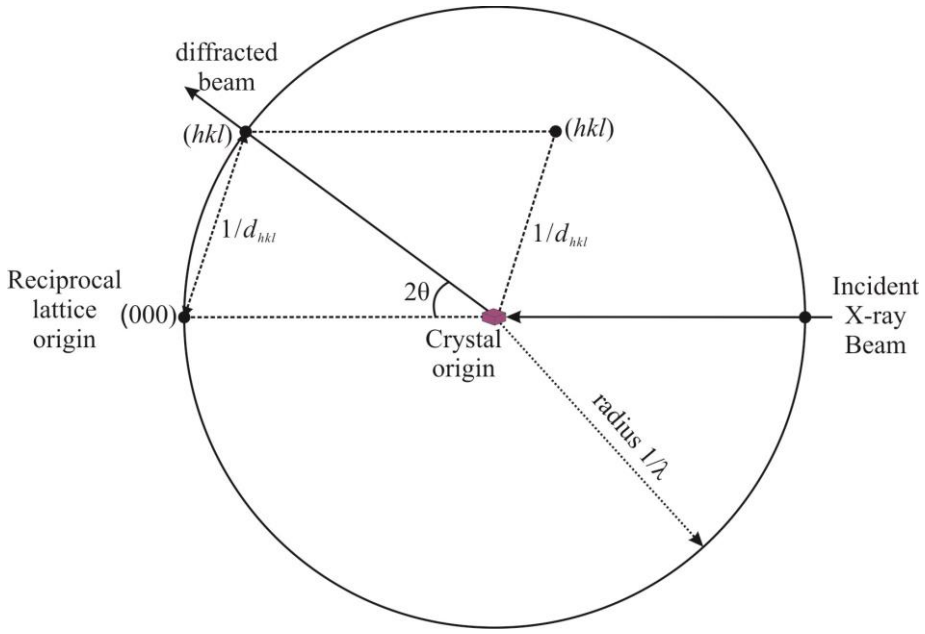

Figure 2.4: *Ewald's sphere for a set of planes (hkl) at the correct Bragg angle θ*

In a diffraction experiment, the concept of reciprocal lattice is used to give a physical picture of diffraction geometries in the studied crystal.[10] The reciprocal lattice was rediscovered by Ewald and Laue and is identical to the real crystal lattice, but where the representation of each lattice point in a reciprocal lattice is associated with a particular set of planes in the original lattice.[11] Whilst the real crystal lattice describes the lattice periodicity, the reciprocal lattice is described in terms of the reciprocal space vectors. When an incident X-ray beam hits a crystal, positioned at the centre of sphere with radius of 1/λ (Ewald's sphere), the unaffected X-ray beam passes straight through and it has the lattice point (000) on the surface of Ewald's sphere. Any other diffraction spots observed are due to scattering from atoms in the real lattice plane (*hkl*). However this forms a reciprocal lattice with unit cell translations of a^*, b^*, c^*, where $a^* = 1/a$, *etc*. The distance of the *hkl* reciprocal lattice points from the reciprocal lattice origin on the surface of a sphere is given by $1/d_{hkl,}$ where d_{hkl} is the inter-planar spacing of the (*hkl*) planes.

Rotation of the crystal during diffraction experiments allows further reciprocal lattice points to intersect the surface of the sphere, and thereafter to be recorded. This allows for the full characterisation of the crystal structure. The collection of diffraction spots is very dependent on the symmetry of the studied crystal. For example, crystals with no symmetry requires the recording of the full surface of Ewald's sphere, since the detector used for recording only covers a limited proportion of the sphere, whilst cubic

crystals only require 1/16th of the whole sphere to be recorded for full structural characterisation, due to the same diffraction pattern generated from all six equivalent faces. Therefore, increasing the unit cell symmetry of a crystal reduces the quantity of data required.

The understanding of diffraction intensity from a set of (*hkl*) planes is vital for the determination of the complete crystal structure. The observed intensity of a diffracted beam is dependent on atomic scattering factors, f_n, also known as atomic form factors, which are defined as the scattering power of an atom exposed to X-rays. As the X-rays are scattered by the electrons within an atom, the atomic scattering factor is proportional to the atomic number of an atom. The X-ray scattering for a hydrogen atom is very weak, due to its small atomic number. Thus to accurately locate hydrogen atom through X-ray diffraction is difficult. The atomic scattering factors can also be influenced significantly by the diffraction angle θ and the incident X-ray wavelength λ. In reality, atoms within a crystal are in motion at all times, even at absolute zero point. They vary with temperature in a different vibration states, but are also affected by the surrounding chemical environment. The vibration of atoms means they displace from their original places on a lattice plane. The smaller the *d*-spacing between lattice planes, the greater displacement of atoms (recorded as *u*), which results in a bigger phase angle differences (phase factor) and eventually leads to greater impact on X-ray scattering. Assuming that the thermal vibrations of all atoms on a lattice plane are the same (isotropic), the average vibration amplitude is u^2, then the atomic scattering factor f can be calculated using the equation 2.02.

$$f_n = f \cdot exp\left\{\frac{-8\pi^2 u^2 sin^2\theta}{\lambda^2}\right\} = f \cdot exp\left\{\frac{-2\pi^2 U}{d^2}\right\} \quad (2.02)$$

The u^2 is known as the "atomic displacement parameter (ADP)", denoted as *U*, The value of *U* increases with increase in temperature, thus it also simply interpreted as the atomic temperature factor. From the equation 2.02, it can be determined that the smaller the value of *U*, the greater the value of atomic scattering factor, and therefore the diffraction intensity is improved.

However, the chemical environment surround each atom is different, thus the thermal vibrations of atoms are different (anisotropic). The anisotropic vibrations of atoms within a crystal can be represented by using ellipsoid of three main axes U_{11}, U_{22}

and U_{33}, which the ellipsoid shape and orientation can be determined by the interceptions of U_{11}, U_{22} and U_{33}. The equation 2.02 then rewritten as:

$$f_n = f \cdot exp[2\pi^2(U_{11}h^2a^{*2} + U_{22}k^2b^{*2} + U_{33}l^2c^{*2} + 2U_{23}klb^*c^* + 2U_{13}hla^*c^* + 2U_{12}hka^*b^*)] \quad (2.03)$$

Where, *hkl* are Miller indices, a^*, b^*, c^* are reciprocal lattice parameters.

Many publications also use "equivalent isotropic atomic displacement parameters $U_{eq} = [(U_{11} + U_{22} + U_{33})/3]$" to report atomic displacement parameters.

The combination of the atomic scattering factor and phase factor lead to the structure factor, F_{hkl} (equation 2.04), which represents the total intensity of radiation scattered by a unit cell. If a crystal structure is centrosymmetric, then the structure factor expression can be simplified as shown in equation 2.05, due to atoms at positions (*x*, *y*, *z*), there must be same atoms at (-*x*, -*y*, -*z*) positions.

$$F_{hkl} = \sum f_n[\cos 2\pi(hx_n + ky_n + lz_n) + i\sin 2\pi(hx_n + ky_n + lz_n)] = F_{(hkl)}e^{i\emptyset_{hkl}} \quad (2.04)$$

$$F_{hkl} = 2\sum_n f_n \cos 2\pi(hx_n + ky_n + lz_n)] \quad (2.05)$$

where F_{hkl} is the structure factor, f_n is the scattering factor for *n* atoms, x_n, y_n, z_n are the fractional coordinates with respect to the unit cell edges, and $\emptyset_{hkl}$ is the phase angle, which is equal to $2\pi(hx_n + ky_n + lz_n)$.

If the structure factor and phase factor are known, then the electron density distribution in the unit cell can be calculated through Fourier transforms (FT) by using equation 2.06., and thus the atomic positions can be determined, and the crystal structure resolved.

$$\rho_{xyz} = \frac{1}{V}\sum_{h,k,l}|F_{hkl}| \cdot [\cos 2\pi(hx_n + ky_n + lz_n) + i\sin 2\pi(hx_n + ky_n + lz_n)] \quad (2.06)$$

where ρ is the electron density, $|F_{hkl}|$ is the modulus of the structure factor.

A problem arises as the measured intensity of a reflection I_{hkl} is proportional to the square modulus of the structure factor F_{hkl}, thus, the sign of F_{hkl} is not distinguishable. It is even more complex when considering non-centrosymmetric unit cells, because the

structure factor can be expressed as the complex number $F_{(hkl)}e^{i\emptyset_{hkl}}$ (equation 2.04). Where the value of F_{hkl} can be obtained easily, as it is equal to the square root of the measured intensity, but $\emptyset_{hkl}$, the phase angle cannot be calculated from the intensity. This is known as the phase problem,[12] which has been a continual problem in the field of crystallography.

The phase problem can be solved in two ways, the direct method, which is the most common way to overcome this problem, and the Patterson method, which is one of the first mathematical tools developed by crystallographers, described in 1934.[13] The Patterson function (equation 2.07) forms a Patterson map from the Fourier transformation of the obtained intensities, is proportional to F^2 and does not require phase information, with the values of F_{hkl}^2 and intensities of the *hkl* reflections available experimentally. The function is therefore solvable.

$$P_{xyz} = \frac{1}{V}\sum_{h,k,l}|F_{hkl}^2| \cdot [\cos 2\pi(hx_n + ky_n + lz_n) + i\sin 2\pi(hx_n + ky_n + lz_n)] \quad (2.07)$$

Rather than producing an electron density map, whereby peaks represent sites of electron density, in the Patterson map, the peaks correspond to interatomic vectors, with peak sizes proportional to the product of the scattering factors of the paired atoms. These peaks are similar to those in electron density maps, but much broader in size. The main drawback of this method is the overlapped peaks produced by the large number of similar atoms in a crystal structure, which cannot be resolved. As a result, the Patterson method is of greatest use in locating a small number of heavy atoms in a unit cell, which is so called the 'Heavy Atom' method.

Due to the limitations of the Patterson method, this method has been largely replaced by the 'direct methods' technique to overcome the phase problem. The direct methods techniques rely on the established statistical relationships between the phases of the Fourier Transform of the strong reflections and the corresponding amplitudes. The very important step in the development of direct methods is based on electron density functions, which has two important assumptions: that electron density can never have a negative value, and the electron density is concentrated in well-defined maxima (atomicity). With these two assumptions, the use of direct methods, through a trial and error approach, can solve the phase problem. For direct methods, the possible initial phases are calculated by statistical techniques from certain reflections (*hkl*). The

combination of all possible starting set phases are used, along with many additional phases, before a normalised electron density map is generated with an estimation of atomic positions for each set of possible initial phases. Hydrogen atoms many not be observed due to their weak and diffuse X-ray scattering. After initial positions of atoms are located in the electron density map, further estimated atomic positions can be obtained by least squares refinement, including atomic positions and anisotropic temperature factors, of the function 2.08.

$$D = \sum w\,(|F_o| - |F_c|)^2 \tag{2.08}$$

where *w* is the weight factor of the observation, can be calculated from,

$$w = 1/[\sigma^2 F_o^2 + (aP)^2 + bP] \tag{2.09}$$

where *a* and *b* are constants, *P* is $[2\mathrm{F}_c^2 + \mathrm{Max}(F_o^2, 0)]/3$.

During the model refinement, the accuracy of the model is described by a residual factor (R_1-factor) given in equation 2.10. In crystallography, the standard R_1-factor is used to indicate the level of agreement between the amplitudes of the structure factors F_c calculated from a crystallographic model and those observed structure factor F_o from the original X-ray diffraction data. It is calculated during each cycle of least-squares refinement, and the value is typically shown as percentage. The final R_1-factor is one measure of refinement quality, with the value below 5% generally accepted as publishable quality. For structure refinement accuracy consideration, an alternative residual factor of wR_2 is commonly included in many publications; this is due to the occasional low sensitivity of the R_1-factor to errors, particularly in specific cases, such as low resolution data sets. For such reasons, the weighted *R*-factor, wR_2 shown in equation 2.11, and the Goodness of Fit, *GooF* or *S* shown in equation 2.12, will often be included, along with the R_1-factor, in many publications. As wR_2 is based on F_o^2, as is the *GooF*, the value of wR_2 is generally higher than R_1, providing a significant description of the deviation of the calculated model from the observed data. The value of *GooF* should approach values of 1 for the model to be considered being a good fit.

$$R_1 = \frac{\sum||F_o| - |F_c||}{\sum|F_o|} \tag{2.10}$$

where R_1 is residual factor, F_o is the observed structure factor, F_c is the calculated factor.

$$wR_2 = \sqrt{\frac{\sum w\left(F_o^2 - F_c^2\right)^2}{\sum w\left(F_o^2\right)^2}} \tag{2.11}$$

where wR_2 is the residual factor by weight.

$$S = \frac{\sum w\sqrt{\left(|F_o^2| - |F_c^2|\right)}}{\sqrt{(m-n)}} \tag{2.12}$$

where *S* is the goodness of fit, *m* is the number of observed structures, *n* is the number of parameters.

2.2.2 Powder X-ray diffraction

Powder X-ray diffraction is a rapid analytical technique commonly used in the study of solid state chemistry. It is primarily used for the phase identification of crystalline materials. The fundamental principle of the powder diffraction technique relies on monochromatic X-ray scattering from a powdered sample and generating a diffraction pattern related to the sample information.

A powdered sample contains an enormous number of very small crystallites, typically 10^{-7}-10^{-4} nm in size and will adopt all possible orientations randomly. When the incident X-rays strike the powdered sample, the interaction between the incident X-rays and crystallites results in constructive interference and thereby produces diffraction to satisfy Bragg's law. Each set of lattice planes in a crystallite will give rise to a diffraction cone, and each diffraction cone contains a large number of closely spaced spots, which represent the diffraction maxima from a single crystallite. By scanning the sample through a range of 2θ angles, all possible diffraction maxima of the lattice should be attained. These diffracted X-rays are detected, processed and diffraction peaks generated, related to the unique *d*-spacing of the sample, allowing for the identification of the sample by comparison to *d*-spacing of standard reference patterns. During this research work, the Siemens D5000 and Bruker D8 diffractometers were used to obtain the diffraction patterns of all samples produced in the powdered form. A schematic diagram of a typical diffractometer is shown in Figure 2.5.

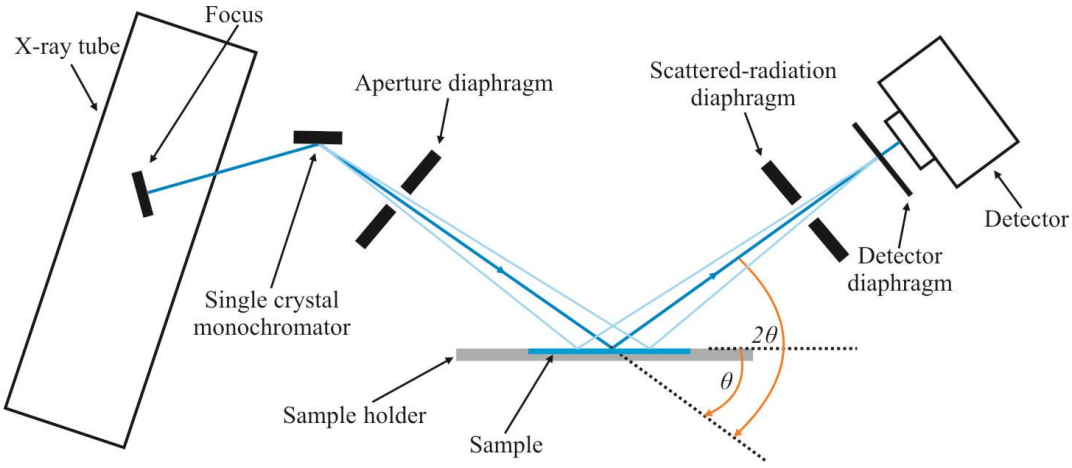

Figure 2.5: *Schematic diagram of a powder X-ray diffractometer*

Both Siemens and Bruker diffractometers use a copper source, combined with germanium single crystal monochromator, to generate a monochromatic beam with a

wavelength of λ = 1.54056 Å. The incident beam is collimated through an aperture diaphragm and directed onto sample which is normally placed in an aluminium or plastic sample holder. The sample rotates at a constant angular velocity and the detector moves correspondingly, with a fixed angle of 2θ to the incident beam around the sample, recording the number of X-rays observed. The incident beam, sample and detector are set up according to the *Bragg Brentano* geometry. After the diffraction pattern has been obtained, the Diffrac^{plus} evaluation program[6] can be used to view and identify the phase purity by comparing the observed pattern to standard patterns from a database.

A further application of the powder X-ray diffraction technique is the variable-temperature (VT) diffraction process. Since some of the materials were produced as potential battery materials, whilst other frameworks contain amine templates, studying the thermal stability properties of such materials are of important. The investigation of structural changes at elevated temperatures (up to 1200 °C) was undertaken. For a typical VT experiment, Diffrac^{plus} was used to create a job associated with the temperature range in different set points; the sample may be held under vacuum and exposed to Cu $K_{\alpha 1}$ radiation and heated to a chosen temperature. Subsequently, a diffraction pattern, including phase changes or structure collapse, is obtained which is corresponds to this temperature.

2.2.4 Structure refinement

In comparison with the SXD technique, which aims for the absolute crystal structure determination of a uniform crystalline compound, the powder techniques are used primarily for structural refinements. The purpose of structural refinement is to make the referenced crystal model as close possible to the experimental PXD data. The method requires a good starting model, usually in the form of crystallographic information file (CIF), which can be obtained either from the Inorganic Crystal Structure Database (ICSD) or from the SXD technique. Refinement takes the standard model in combination with collected PXD data, and attempts to minimise the difference between them.

Rietveld refinement

The Rietveld refinement method was developed by Hugo M. Rietveld and was first reported in 1967.[14,15] This method is utilised to refine the structure of crystalline materials by means of powder diffraction data. The drawback of the PXD method is the overlapping diffraction peaks, which are very difficult to separate, and therefore prevent the determination of structures with ease, compared to the SXD technique. However, Rietveld's theory uses the realisation that although many diffraction peaks overlap, they may still be modelled using simple peak shape parameters, through calculating the diffraction intensity of the overlapped peaks. The principle of the Rietveld refinement is based on the fitting of data between the data collected experimentally, and the data calculated from a referenced model structure.

The standard procedure described below lists the most important variables that are refined during a structure refinement, using the Rietveld method:

- Determination of a good starting model structure, providing lattice parameters, space group and atomic positions.
- The overall scale factor and background parameters are refined initially.
- Followed by refining the lattice parameters and zero point error in order to align any Bragg reflections.
- At this stage, a preliminarily peak shape refinement would carried out, through the peak shape parameters, including Gaussian and Lorentzian functions.
- The location of accurate atomic positions can then be refined by varying fractional coordinates *x*, *y* and *z*. The refinement affects the peak intensities and allows future improvement of the peaks shapes.
- The last parameters to be refined are the thermal motions of atoms, achieved by varying the isotropic temperature factors, further improving the refinement. In addition, the peak shapes may be further refined, including terms describing the asymmetry of the peak shapes, and preferred orientation of peaks.

At this point, the refinement is complete with all atoms accounted for.

The refinement was carried out through using the software package called Generalised Structure Analysis Suite (GSAS),[16] in combination with the EXPGUI graphical interface.[17] The programme uses the Rietveld method to carry out a least squares minimisation between the obtained and calculated pattern profiles, this is shown in equation 2.13 for the minimisation of refinement as a function of M.

$$M = \sum_i w_i \left(y_i^{obs} - y_i^{calc}\right)^2 \tag{2.13}$$

where w_i is a weighting factor equal to $1/y_i^{obs}$, y_i^{obs} and y_i^{calc} are the observed and calculated intensities, for each data point *i*, corresponding to $2\theta_i$ for PXD. The y_i^{calc} can be obtained from the following equation 2.14.

$$y_i^{calc} = S_p \sum_{k=1}^{N\ peaks} m_k L_k |F_k|^2 \Phi(\Delta\theta_{ik}) P_k A + y_i^{bkg} \tag{2.14}$$

where S_p is the scale factor, $m_k L_k$ are Lorentz Polarisation and multiplicity factors, F_k is the structure factor, $\Phi(\Delta\theta_{ik})$ is the reflection profile function, P_k is the function of the preferred orientation, A is an absorption factor and y_i^{bkg} is the background intensity at the point of *i*.

It is necessary to accurately describe the peak shape of each Bragg reflection for the construction of the calculated profile. The pseudo-Voigt function (equation 2.15) is used to approximate the peak shape, described as a combination of the Gaussian (G) and Lorentzian (L) components, which are represented by the equations 2.16 and 2.17.

$$P_{pseudo-Voigt} = \eta L + (1 - \eta) G \tag{2.15}$$

where L and G represent the Lorentzian and Gaussian component respectively, η is a mixing parameter that can be refined as a linear function of 2θ, and has value range of $0 \leq \eta \leq 1$.

$$G = \frac{2\sqrt{\ln 2}}{H_k\sqrt{\pi}} exp\left[-4 \ln 2 \left(\frac{\Delta\theta_{ik}}{H_k}\right)^2\right] \tag{2.16}$$

$$L = \frac{2}{H_k \pi}\left[1 + 4\left(\frac{\Delta\theta_{ik}}{H_k}\right)^2\right]^{-1} \tag{2.17}$$

where H_k is the full-width-at-half-maximum (FWHM) of the k^{th} Bragg reflection, and is of a Gaussian or Lorentzian peak varying with the scattering angle $2\theta_k$.[18] The H_k can be expressed as below, for the Gaussian component:

$$H_k^2 = Utan^2\theta_k + Vtan\theta_k + W \tag{2.18}$$

for the Lorentzian component:

$$H_k = Xtan\theta_k + \frac{Y}{\cos\theta_k} \tag{2.19}$$

Where the terms *U*, *V*, *W*, *X* and *Y* are refinement parameters, and θ_k is the scattering angle. The formula takes into account of the peak broadening resulting from the particle size effect, which in turn the average particle size can be extrapolated from the data.

At low scattering angles, the peaks exhibit asymmetric characteristics due to the finite sample heights and slit width, which may cause peak maxima to shift to lower angles than expected angles, whilst the integrated peak area remain the same. This can be modelled by introducing a semi-empirical correction factor (Equation 2.20).

$$k' = 1 - sP\frac{(\Delta\theta_k)^2}{tan\theta_k} \tag{2.20}$$

where *P* is the asymmetry parameter, $s = \pm 1, 0, -1$ when $\Delta\theta_k$ is positive, zero or negative respectively.

In the Rietveld method, through the use of these described parameters, as well as the initial crystallographic model, the theoretical diffraction patterns for any crystalline material may calculated. By refining the various parameters, including the unit cell, atomic and thermal parameters, and full structural characterisation of a crystalline material can be achieved.

Criteria of fit

In the refinement, there are different criteria of fit values which are used to quantitatively describe the degree of agreement between observed and calculated data. These values are known as the reliability factors or *R*-factors, and are defined as $R_{profile,}$ $R_{expected}$ and $R_{weighted\ profile}$. These values can be expressed as follows:

$$R_{profile} = R_p = 100\left[\frac{\sum_i \left|y_i^{obs} - y_i^{calc}\right|}{\sum_i y_i^{obs}}\right] \tag{2.21}$$

$$R_{expected} = R_{exp} = 100\left|\frac{(N-P+C)}{\sum_i w_i (y_i^{obs})^2}\right|^{1/2} \tag{2.22}$$

Where *N* is the number of observations, *P* is the number of refinable parameters and *C* is the number of constraints. Here the R_{exp} is a value defined by the statistics of the refinement. From a mathematical or statistical point of view, the $R_{weighted\ profile}$ is the most meaningful of the three criteria of fit values, because the residual being minimised is a numerator, it directly reflects the progress of a refinement and is given by:

$$R_{weighted\ profile} = R_{wp} = \left[\frac{\sum_i w_i \left(y_i^{obs} - y_i^{calc}\right)^2}{\sum_i w_i (y_i^{obs})^2}\right]^{1/2} \tag{2.23}$$

The last criterion to be considered is the reduced chi-squared, or goodness of fit that can be expressed relative to R_{exp} and R_{wp} as follows:

$$\chi^2 = \left[\frac{1}{N-P+C}\right]^2 \sum_i w_i \left[y_i^{obs} - y_i^{calc}\right]^2 = \left[\frac{R_{wp}}{R_{exp}}\right]^2 \tag{2.24}$$

The value is minimised during the refinement. A ‘good profile fit’ is achieved with R_{wp} approaching R_{exp}, leading to an idealised χ^2 value close to 1.0.

2.2.3 Single crystal X-ray diffraction

The single crystal X-ray diffraction measurements were all carried out at the University of Southampton, where the EPSRC National Crystallography Service operate two Rigaku FR-E+ diffractometers, the Ultra High Flux (UHF) SXD, the world's most powerful laboratory-based diffractometer and the Very High Flux (VHF) SXD. Both instruments run from a FR-E SuperBright^{TM} High-Brilliance rotating anode X-ray generator with a molybdenum target (λ = 0.71703 Å). The UHF diffractometer is equipped with VariMax VHF (Very High Flux) optics, which provides a highly focused monochromatic X-ray beam (70 μm), whilst the VHF diffractometer is equipped with VariMax HF (High Flux) optics with the achieved X-ray beam slightly de-focused (100 μm), thus crystal data collection on the UHF diffractometer requires a shorter collection time, but can only be used for small crystals. Both devices are completed with an AFC12 goniometer and an enhanced sensitivity Saturn 724+ 18 bit CCD detector. All data collection was completed at 120 K with the aid of Oxford Cryosystems Cobras, in order to reduce the thermal vibrations of a crystal studied. A typical diffraction experiment would involve isolating a single crystal from the sample bulk under an optical microscope with polarised light. The isolated crystal is then mounted using viscous oil on an amorphous thin film that is attached to a brass pip before mounting the pip onto the goniometer head, centred in the X-ray path. The photograph of Figure 2.6 shows the Rigaku FR-E+ UHF SXD system.

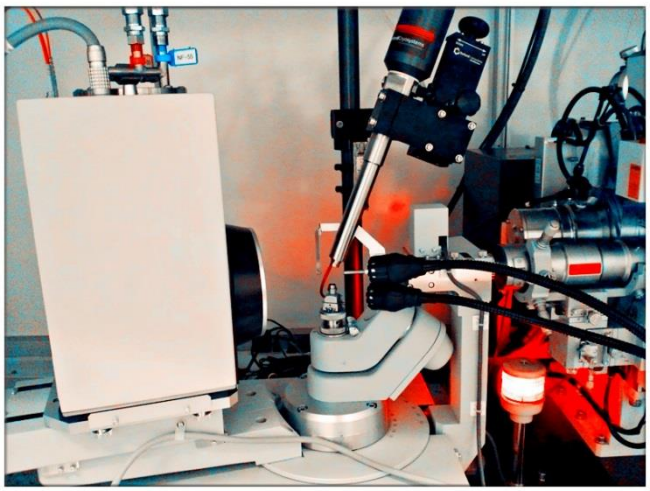

Figure 2.6: *Photograph of Rigaku FR-E+ UHF diffractometer*

During the data collection stage, a 'quick image collection' is necessary to check that the crystal produces well-defined diffraction spots without any smearing or twinning spots. Amorphous samples will not produce any diffraction spots, whilst rings of diffraction spots in the image suggest the sample is powdered rather than a single crystal. Weak diffraction spots can be improved through longer data collection periods. Crystals checked for high quality data collection will reduce time required for analysis and eventually result in a better structural solution.

As long as the quick image collection suggests a quality crystal has been mounted, a further collection of 15 diffraction images will be set up in order to identify the crystal unit cell. The unit cell is calculated through the programme CrystalClear-SEM 2.0 r5,[19] developed by Rigaku, and offers an idea of how well the data fits with a number associated with accepted and rejected reflections. In general, a percentage of less than 10% of rejected reflections suggests the crystal is of sufficient quality for future full data collection. The unit cell measurements provide an understanding of the type of crystal, and probable unit cell dimensions, which can be used in comparison against all known unit cell parameters from a database in order to check whether a full dataset collection is required.[20]

Once the unit cell dimensions have been confirmed, the CrystalClear programme will move to the full data collection strategy, suggesting the number of frames and collection time required. This is very dependent on the symmetry of the crystal. The programme aims to obtain data with high completeness of nearly 100% in all and further redundancies to improve the data accuracy. Once the data collection is completed, it undergoes an absorption correction, either through the use of the d*TREK[21] or FS-Process[22] software suits. The obtained final data sets, in HKLF format with a list of *hkl* values and the related F_o^2 and $\sigma(F_o^2)$, were analysed using the WinGX[23] suite of programme, including the XPREP[24] and SHELX-97[25] packages. To solve a crystal structure, the direct method was initially used, followed by Fourier transform, and the electron densities of different elements represented by Q peaks were obtained (electron density map). These Q peaks can be assigned by determining the distances (bond lengths) between them. A few cycles of refinements are required unless the obtained residual values are below 10 %. The final 'solved' structure was checked using the publCIF programme.[26]

2.3 UV-Visible Near-Infrared spectroscopy

UV-Visible-Near-Infrared spectroscopy (UV/VIS/NIR) is used to study the optical properties of materials, such as reflectance, transmittance and absorbance. In this thesis, inorganic materials were designed and produced due to their interesting near-infrared (NIR) absorbing properties, with potential for specific applications. The measurements of NIR absorption as a function of wavelength (800 nm to 2500 nm) for all samples were carried out on a PerkinElmer Lambda 750s UV/VIS/NIR spectrometer.

The fundamental principle of the absorption mechanism involves the interaction between the incident light and the sample. In the case of a sample in solution, the technique is usually carried out in transmission mode. Within the electromagnetic region of the spectrum, molecules absorb specific radiation and undergo electronic transitions. The absorbance behaviour of materials obeys the *Beer-Lambert* law, which states the absorbance is proportional to the concentration and path length of the sample. (Equation 2.25)

$$\mathrm{A} = -\log_{10}\left(\frac{I}{I_0}\right) = \varepsilon \mathrm{cl} \tag{2.25}$$

Where A is the absorbance, I is the intensity of incident light, I_0 is the transmitted intensity, ε is the molar absorptivity, c is the concentration of absorbing species, and l is the path length through the sample.

However, the transmission mode is impractical for powdered sample measurements. Solid samples, as fine powders, have high surface areas, and transmission can become very low. Hence, instead of measuring the transmitted light, an alternate way is to measure the reflected light in order to extract the absorption properties of a solid sample. The *Schuster-Kubelka-Munk* (SKM) model allows for the use of a diffuse reflectance mode to obtain the absorption spectrum of a powdered sample in the mid-IR and NIR spectral ranges.

Diffuse reflectance relies upon the analysis of multiple reflections at surfaces of the measured sample. When the incident spectrometer beam is directed onto the sample, it can be reflected, scattered and transmitted through the sample material. The part of beam scattered within the sample material and returned to the surface is considered to be a diffuse reflection, and emerges in a broad range of directions. This reflected light is then collected by a diffuse reflection accessory. Samples to be analysed by diffuse

reflectance are usually ground and diluted with a non-absorbing matrix such as KBr or $BaSO_4$, this ensures a deeper penetration of the incident beam into the sample, increasing the proportion of the diffuse reflection component while minimising the specular reflection component. This is desirable as the specular reflection component may cause changes in the band shapes in diffuse reflectance spectra.

The *Kubelka-Munk* theory is used for the analysis of diffuse reflectance spectra, providing a correlation for the spectral intensity of a measured spectrum relative to sample concentration.

The *Kubelka-Munk* function is expressed as follows:

$$f(R) = \frac{(1-R)^2}{2R} = \frac{k}{s} \tag{2.26}$$

where R is the absolute reflectance of sampled layer, k is the absorption coefficient, s is the scattering coefficient.

In NIR spectroscopy, the Tungsten-Halogen lamp in the spectrometer is used to produce the desired wavelength. The detector in the spectrometer used to collect absorption data under the diffuse reflectance mode was a Lead-Sulphide cell (PbS). Solid samples were ground uniformly and mixed with barium sulfate (5% by weight), before the sample was then loaded in a plastic sample holder and mounted. A barium sulfate plate was used as a reference to obtain the background. Sample absorption data was collected in the range of 200 to 2500 nm.

2.4 Electron Microscopy and Energy Dispersive Spectroscopy

Electron microscopy is a powerful analytical technique usually used for imaging samples. It provides much higher magnifications and greater resolving power than a light microscope. The scanning electron microscopy (SEM) introduced in this research work was used to study the morphology of samples, and was often used in conjunction with energy dispersive X-ray spectroscopy (EDS) for sample composition analysis.

In SEM, a high-energy electron beam is generated from an electron gun, which then travels a vertical path through the microscope, and is focused by electromagnetic condensers and objective lenses. Finally the beam passes through a series of scanning coils, which deflects the beam scans in a raster fashion across a rectangular area of the sample surface. A schematic instrumentation is shown in Figure 2.7.

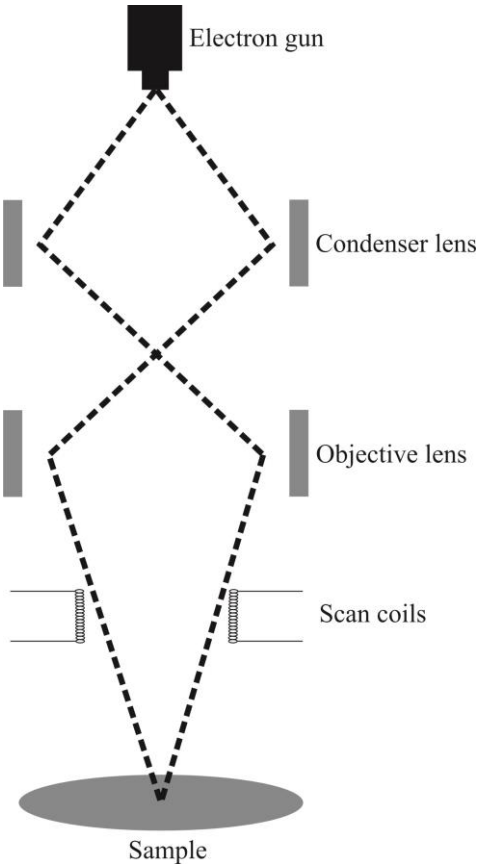

Figure 2.7: *Schematic of the JEOLSEM6480LV Scanning Electron Microscope*

Conventional SEM techniques require samples to be imaged under vacuum, this is to prevent the attenuation of the electron beam by the rapid spreading of gases within the sample chamber. Once the beam hits the sample, the electrons interact with atoms within the sample either elastically, where the scattered electrons retain the same energy,

or in-elastically, where the scattered electron energy is changed. With energy loss, inelastic scattering is responsible for a multitude of signal types: backscattered electrons, secondary electrons, X-rays, and Auger electrons. The signals of backscattered and secondary electrons are used for imaging purposes, and X-rays can provide information of use for sample elemental composition analysis.

Backscattered electrons arise when the elastically scattered electron beam is deflected back by atoms in the sample. The primary beam electrons interact with the sample atoms, resulting in a directional change in the electron beam, but without significant change in the energy of the beam electrons. The contrast depends on the atomic numbers of the elements, with stronger backscatters having greater atomic numbers. This means it is possible to show the elemental distribution present in the sample. However, the potential resolution of the resulted image is very low, compared to secondary electrons. This is likely due to the different maximum escape depths of electrons within the sample analysed; and lead to the energy differences. The greater escape depths of the electron the lower potential resolutions, where the backscattered electrons can be scattered from a depth of a hundred times greater than the secondary electrons.

Secondary electrons are electrons emitted from the atoms on the surface of the sample, during inelastic scattering. The electron beam interacts with the surface atom, resulting in an energy transfer to the sample atom and a potential electron expulsion from that atom. The secondary electrons are usually defined as low energy electrons, less than 50 eV.

When an electron of the sample atom is expulsed by the primary electron beam, a secondary electron is emitted. If the vacancy is filled by an outer shell electron, an X-ray photon, characteristic of the energy transition and the specific element, is emitted. These X-rays, with their energies detected and collected, allow for an elemental analysis of the sample, known as the EDS. The detection of emitted X-rays can also be of use for mapping the elemental distribution across the sample surface. The limitation of this technique is that the fairly weakly emitted X-rays from light elements, such as Li and B, cannot be detected. Another limitation is that overlapping signal peaks can be observed, due to elements such as O and F may generate similar X-ray energies.

Since SEM utilises vacuum conditions and uses electrons to image, special preparation are required. All water must be removed from the sample in order to prevent its vaporisation in the vacuum. Whilst conductive samples require no further preparation, samples that are non-conductive need to be made conductive by covering with an ultra-thin layer of conductive material, usually carbon. This is to avoid the sample become negatively charged when scanned by the electron beam, which may lead to the scanning faults. The coating process can be done by using a low-vacuum sputter coating device.

The study of SEM and EDS of samples was carried out on a JEOL SEM Scanning Electron Microscope and attached with a high speed, high sensitivity Oxford Instruments INCA X-Act Energy-Dispersive X-ray Spectrometry analysis system.

2.5 Thermogravimetric analysis

Thermogravimetric analysis (TGA) is a technique used to measure the weight of a sample as a function of temperature or time, and is typically used for the determination of thermostability of samples, for example, in the study of water loss from a sample. The sample may be heated to a specified temperature at a desired heating rate and held for a specified period of time, whilst the sample weight changes with increasing temperature will be recorded. Species such as water molecules will be lost during the heating, and can be clearly observed. In this work, this technique is also used to observe the loss of organic templating agents in framework materials. Any weight loss can be calculated as a percentage and then compared to the expected loss calculated from the empirical formula of the sample, thus confirming the lost species present within the crystal structure.

Differential thermal analysis (DTA) is usually carried out simultaneously with TGA. This technique is used to study how the temperature changes within a sample corresponding to an inert reference sample, typically alumina powder. Both samples in DTA and TGA studies are heated in identical conditions, with any temperature differences between the two samples recorded, such as those due to the occurrence of thermal events. For example, in the case of an exothermic event, a faster increasing temperature of the studied sample than that of reference sample will be obtained, whilst the opposite is true in the case of an endothermic event. This technique is helpful to identify whether a change in sample mass is caused by the thermal events. For example, a sample may have phase changed due to the thermal events, but without a change in total mass, therefore it is not possible to observe this type of change using TGA.

Both the TGA and DTA experiments were carried out on a Polymer Laboratories STA 1500 Simultaneous Thermogravimetric Analysis System. A schematic diagram of a TGA is shown in Figure 2.8. In a typical TGA experiment, approximately 10 mg of a homogeneous sample was placed in an alumina crucible, which was then heated from room temperature up to 500 ^{o}C at rate of 2 ^{o}C per minute, with data points collected every 2 seconds.

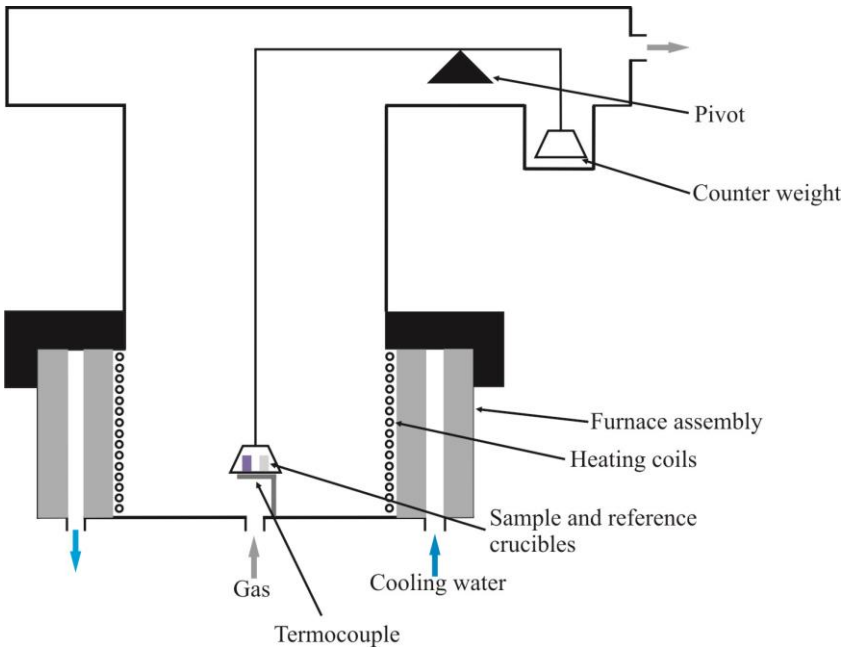

Figure 2.8: *Schematic of a PL-STA 1500 TGA/DTA*

2.6 Bond valence calculations

Bond valence calculations[27] were performed on the new materials presented in this work. The primary aim for the use of bond valence calculations on new crystal structures was to predict the charges of identified elements through quantitative calculations of the bond valence value for each atom in a crystal, thus giving an indication of whether the suggested empirical formula of a crystal structure is correct. The method was used initially in attempts to resolve possible O/F sites, followed by determining the elemental charges, as well as the occupancy factors within the suggested structural formulae.

The bond valence sum of each individual atom may be calculated using the equation 2.27. The bond valence method states that the atomic valence is equal to the sum of the bond valences at each atom. Pauling was first to notice that the bond strength correlates empirically with the bond length, with greater bond strengths having shorter bond lengths. A following study by Brese and O'Keefe[27] parameterised this relationship very effectively for ionic compounds, and almost 1000 pairs of atoms with their bond valence parameters have been estimated in this study.

$$V_i = \sum_j v_{ij} \tag{2.27}$$

$$v_{ij} = exp\left[\frac{(R_{ij} - d_{ij})}{b}\right] \quad (2.28)$$

where v is the valence of two bonds between i and j, R is the quoted bond valence parameter, d is the bond length, b is a 'universal' constant 0.37 Å.[28]

2.7 Infrared spectroscopy

Fourier Transform Infrared Spectroscopy was carried out on some samples within the work, and essentially used to identify the presence of water molecules, ammonium cations as well as the organic species within the materials. Collections of sample spectra were completed on a PerkinElmer Instruments Spectrum 100 FT-IR spectrometer within the range of 4000-450 cm^{-1}. The fundamental principle for the infrared spectroscopy is based on molecular vibrations. When characteristic energy is being absorbed by a functional group, it can vibrate in a stretching or bending mode, and this energy is specific for this vibrational mode, which is then reported in wavenumbers. All samples collected within the 4000-450 cm^{-1} range will include the N-H and O-H stretches, N-H bend as well as P-O, S-O, M-O and M-F stretches. The resulting spectrum for each sample was examined with Spectrum software to assign the expected peaks.

2.8 References

1. A. R. West, *Solid State Chemistry and Its Applications*, John Wiley & Sons, 1984
2. U. Schubert and N. Hüsing, *Synthesis of Inorganic Materials*, Third Edition edn., Wiley-VCH, 2012.
3. K. Byrappa and M. Yoshimura, *Handbook of Hydrothermal Technology*, Noyes Publications, United States of America, 2001.
4. J. Livage, *Materials*, 2010, **3**, 4175-4195.
5. J. Čejka, A. Corma and S. Zones, *Zeolites and Catalysis: Synthesis, Reactions and Applications*, Wiley-VCH 2010.
6. I. Sun Microsystem, Regents of the University of California, 2004.
7. W. L. Bragg, *Nature*, 1912, **90**, 410.
8. A. A. Kelly and K. M. Knowles, *Crystallography and Crystal Defects*, Second Edition edn., John Wiley & Sons, 2012.
9. W. L. Bragg, *Proceedings of the Cambridge Philosophical Society*, 1913, **17**, 43-57.
10. D. B. Williams and C. B. Carter, *Transmission Electron Microscopy: A Textbook for Materials Science*, second edn., USA, 2009
11. R. J. D. Tilley, *Understanding Solids: The Science of Materials*, John Wiley & Sons Ltd., England, 2004
12. R. J. D. Tilley, *Crystals and Crystal Structures*, John Wiley & Sons, 2006.
13. A. L. Patterson, *Phys. Rev.*, 1934, 372-376.
14. H. M. Rietveld, *Acta Cryst*, 1967, **22**, 151.
15. H. M. Rietveld, *J. Appl. Cryst*, 1969, **2**, 65.
16. A. C. Larson and R. B. Von Dreele, *Los Alamos National Laboratory Report LAUR*, 1994, 86-748.
17. B. H. J. Toby, *Appl. Crystallogr*, 2001, 210-213.
18. G. Caglioti, A. Paoletti and F. P. Ricci, *Nuclear Instruments & Methods*, 1958, **35**, 223-228.
19. Rigaku, *CrystalClear-SM Expert 2.0 r5*, 2010.
20. D. A. Fletcher, R. F. McMeeking and D. Parkin, *J. Chem. Inf. Comput. Sci.*, 1996, **36**, 746-749.

21. J. W. Pflugrath, *Acta Crystallographica Section D-Biological Crystallography*, 1999, **55**, 1718-1725.
22. T. Higashi, *FS-Process*, 2001.
23. L. J. Farrugia, *J. Appl. Crystallogr.*, 1999, **32**, 837-838.
24. G. Sheldrick, *XPREP. Space Group Determination and Reciprocal Space Plots*, 1991.
25. G. M. Sheldrick, *Acta. Cryst. A*, 1990, **46**, 467-473.
26. S. P. Westrip, *J. Appl. Crystallogr.*, 2010, **43**, 920-925.
27. N. E. Brese and M. O'Keefe, *Acta. Cryst. B*, 1991, **B47**, 192.
28. I. D. Brown and D. Altermatt, *Acta. Cryst. B*, 1985, **B41**, 244-247.

CHAPTER THREE: INORGANIC MATERIALS WITH NEAR INFRARED ABSORBING PROPERTIES

3.0 Introduction

The initial aim of this research was to produce inorganic materials that have the desired optical property of absorbing radiation in the near infrared region. Idealised materials are those which have good absorption ability, but also exhibit excellent chemical and thermal stability, as well as low toxicity and cost. Candidate materials investigated through this research include copper(II) complexes with preferred ligand types being phosphates and fluorophosphates. Some compounds were produced according to methods described in the literature as, although they are all known compounds, their optical properties, especially the absorption in the near infrared region, were not reported. The primary method used to prepare these materials was solid state reactions, at high temperatures. Compounds produced through this method typically have good thermodynamic stability. Other methods such as the co-precipitation or sol-gel routes were also investigated, where the initial preparation was in solution in order to increase homogeneity, but the resulting precursor still needed to be heated at high temperature to obtain the final product. However, the temperatures required in these methods are much lower in comparison to solid state reaction. Hydrothermal synthesis was also attempted for sample preparations. Products prepared by this method benefited from reduced reaction temperatures and times, while maintaining good phase purity. All samples produced via solid state reactions employed the use of carbonate, oxide, hydroxide and phosphate materials as starting materials. For the co-precipitation or sol-gel methods, nitrate starting materials are preferred, owing to their increased solubility. In a typical hydrothermal reaction, starting regents were mixed and combined in a 23 mL Teflon© autoclave liner, then sealed in a closed vessel. Autogenous pressure was generated during the reaction; resulting in a reduced reaction temperature and time, typically below than 200^{o}C and with the complete reaction lasting a few hours.

The materials presented in the chapter were characterised using different techniques. The powder X-ray diffraction technique was frequently used to check sample purity, which can be achieved through comparing the experimental patterns of interrelated materials to the standard patterns from a database. Structural refinements were carried out on samples in order to obtain model structure from the experimental data. The optical properties of prepared materials were investigated on a UV-Vis-NIR spectrometer. The absorption spectra obtained can then be interpreted with the material crystal structures.

The series of copper(II) phosphates (Cu-P-O system), complex copper(II) phosphates (A-Cu-P-O system, where A = group 1, 2 elements) and copper(II) fluorophosphates were all studied. These candidate materials are relatively easy to prepare, some of them show very good NIR absorption properties. They are potentially inorganic materials which can be widely used in applications such as solar cells and laser marking.

3.1 Copper phosphates

Some of the easily synthesised copper(II) phosphates were selected as a starting point; these materials are all known compounds, with their synthetic routes published in the literatures. Although some physical or chemical properties of these simple copper(II) phosphates have been investigated, their ability to absorb radiation in the near infrared region have only been recently studied by Norindr.[1] Some of the syntheses and investigations have been repeated in this work to build up a systemic library which details the relationships between copper(II) based phosphate materials and their NIR absorption properties.

3.1.1 Synthesis

$Cu_2P_2O_7$ and $Cu_2P_4O_{12}$ were produced following the methods reported in the literature,[2, 3] with other synthetic routes also attempted, such as co-precipitation. Both compounds, made through these two methods, were near pure phase. For the co-precipitation route, copper nitrate $Cu(NO_3)_2$ (0.623g for $Cu_2P_2O_7$ and 0.4234g for $Cu_2P_4O_{12}$) , and ammonium hydrogen phosphate, $(NH_4)_2HPO_4$ (0.4387g for $Cu_2P_2O_7$ and 0.5962g for $Cu_2P_4O_{12}$) , were employed as starting materials, with reaction ratio 1:1 for $Cu_2P_2O_7$ and 1:2 for $Cu_2P_4O_{12}$, respectively. They were separately dissolved in distilled water. The $(NH_4)_2HPO_4$ solution was then added slowly to the $Cu(NO_3)_2$ solution, with a precipitate formed as a precursor. This was filtered, transferred into an alumina crucible and heated slowly to 450 ℃ in air at a rate of 5 ℃/min; at this stage of the reaction the aim was to decompose ammonium moiety within the precursor. The solid product was then reground intermittently to reduce diffusion pathways during the heating and facilitate complete reaction. The reground mixtures were thereafter heated up to 700 ℃ for two days before cooling to room temperature. Several cycles of heat treatments as well as pelletisation were carried out in order to obtain pure phase products (form PXD). $Cu_2P_2O_7$ and $Cu_2P_4O_{12}$ as produced had a very light green colour.

3.1.2 Structural refinement

High quality PXD data with scan speed of 1°/min were collected for $Cu_2P_2O_7$ and $Cu_2P_4O_{12}$ overnight on a Siemens D5000 diffractometer. The Rietveld refinement was performed as outlined in Section 2.2.4. The trial models of $Cu_2P_2O_7$ and $Cu_2P_4O_{12}$ were taken from Inorganic Crystal Structure Database (ICSD).[2, 3] Resulting profile fits are shown in Figure 3.1 and 3.2, and refined crystallographic data are given in Table 3.1 and 3.2.

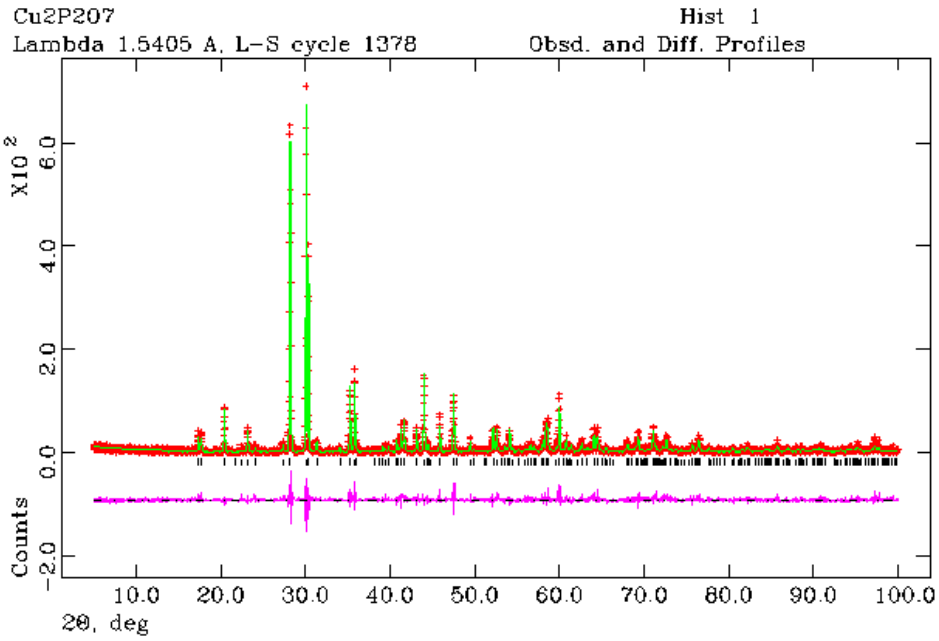

Figure 3.1: *Profile fit to PXD data for $Cu_2P_2O_7$. Experimental data shown as red crosses, continuous green line represented the calculated data from refinement. Pink line represented the difference. Allowed diffraction peaks are represented by black tick marks.*

- $Cu_2P_2O_7$: Monoclinic unit cell with space group *C*2/*c*. Cell parameters: a = 6.876(5) Å, b = 8.113(5) Å, c = 9.162(5) Å, β = 109.54(6)°

Table 3.1: *Refined crystallographic data of $Cu_2P_2O_7$*

Atom labels	*x*	*y*	*z*	U_{iso}/Å^{2*}100
Cu1	-0.0121(5)	0.3127(7)	0.5047(2)	4.70(5)
P1	0.1965(4)	0.0028(2)	0.2051(2)	2.44(5)
O1	0	0.0341(3)	0.25	4.51(3)
O2	0.3733(3)	0.0030(5)	0.3603(6)	1.01(8)
O3	0.2158(5)	0.1545(2)	0.1130(3)	4.20(1)
O4	0.1742(3)	-0.1542(6)	0.1258(1)	4.78(4)

R_p = 11.34%, R_{wp} = 16.87%, χ^2 = 2.53

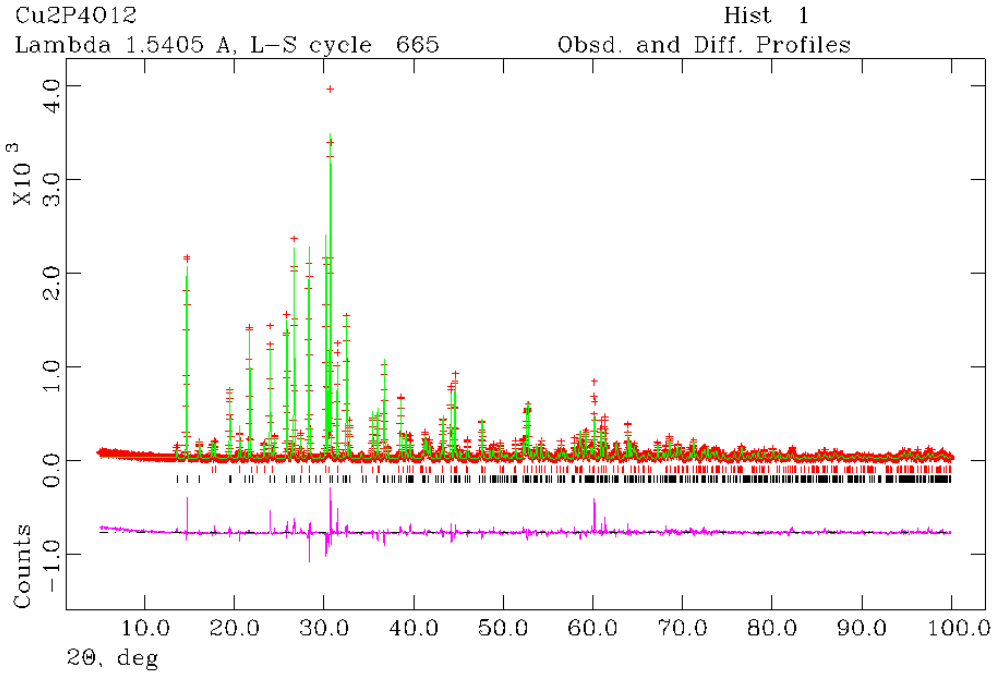

Figure 3.2: *Profile fit of joint structural refinements of $Cu_2P_4O_{12}$ and $Cu_2P_2O_7$. Experimental data are shown as red crosses, continuous green line represented the calculated data from refinement. Pink line represented the difference. Allowed diffraction peaks are represented by black ($Cu_2P_4O_{12}$) and red ($Cu_2P_2O_7$) tick marks.*

- $Cu_2P_4O_{12}$: Monoclinic unit cell with space group *C*2/*c*. Cell parameters: a = 12.5472 (7) Å, b = 8.0803(1) Å, c = 9.5679(7) Å, β = 118.57(9)^o

Table 3.2: *Refined crystallographic data of $Cu_2P_4O_{12}$*

Atom labels	*x*	*y*	*z*	U_{iso}/Å^{2*}100
Cu1	0.25	0.25	0	0.92(1)
Cu2	0	0.5537(4)	0.25	0.85(3)
P1	0.3124(8)	0.5037(7)	0.3032(5)	0.89(2)
P2	0.5113(6)	0.7457(6)	0.4801(6)	2.50(3)
O1	0.4207(3)	0.6228(9)	0.3443(3)	1.56(8)
O2	0.3725(6)	0.3722(9)	0.4402(7)	2.17(2)
O3	0.2755(2)	0.4217(6)	0.1485(4)	1.31(4)
O4	0.2148(2)	0.5947(9)	0.3316(6)	1.41(7)
O5	0.5385(7)	0.2282(6)	0.4098(5)	2.76(5)
O6	0.4579(5)	0.1158(6)	0.5902(6)	2.98(4)

R_p = 16.67%, R_{wp} = 23.34%, χ^2 = 4.248

3.1.3 UV-Vis-NIR spectroscopy

The absorption spectra of $Cu_2P_2O_7$ and $Cu_2P_4O_{12}$, collected on a Lambda 19 spectrometer, are shown in Figure 3.3. The spectrum of $Cu_2P_2O_7$ only displays a single absorption peak, whilst, the spectrum of $Cu_2P_4O_{12}$ shows two absorption maxima. Both spectra have an absorption peak at around 850 nm, and in addition, a second peak is observed at 1100 nm for $Cu_2P_4O_{12}$. It is well known that the mechanism of the NIR absorption is largely dependent on the electronic transitions within the *d* orbitals of the metal ion,[4] and the absorption coefficient is closely related to the metal coordination symmetry.[5] In consequence, the copper(II) coordination environments within the material structures are responsible for the observed absorption behaviours in the corresponding spectral region.

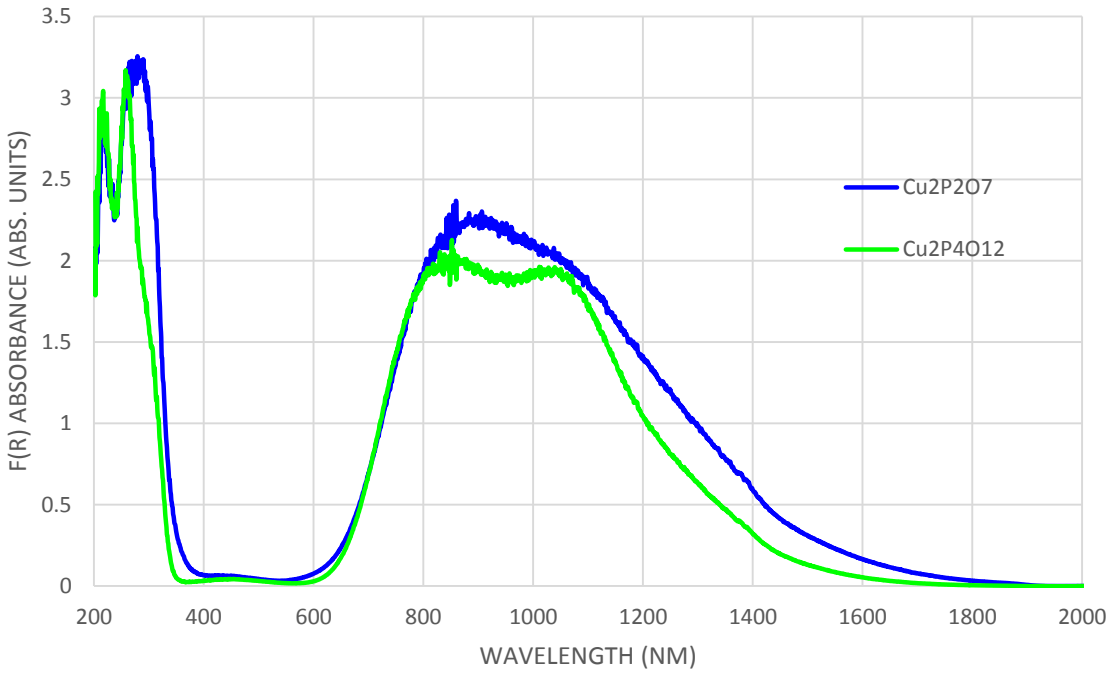

Figure 3.3: *Absorption spectra of copper phosphates between 200 and 2000nm*

3.1.4 Results and discussion

As mentioned above, the difference in absorption behaviours is directly related to the differing copper(II) coordination geometries. The energy level splitting of the *d* orbitals can be described through Crystal Field Theory within the copper(II) coordination sphere, the energies of *d* orbitals that point towards the ligands are raised as the negative charges of the anionic ligands approach the copper ion, owing to the repulsions between

the *d* orbitals electrons and the negative charge on the ligands. Since the negative charge associated with specific ligands is not spherically distributed and only occupy specific positions, thereby each *d* orbital is affected differently, depending on the metal ion geometry. The resulting effect is the splitting of the energy levels of the five *d* orbitals. Standard energy splitting diagrams can be calculated for different coordination geometries of a metal ion. Due to the energy difference between *d* orbitals, electrons in *d* orbitals at low energy levels can be excited to higher energy levels. The energy required has a corresponding wavelength, which is used to excite electrons between orbitals and can be observed in an absorption spectrum.

The crystal structures of many materials described in this thesis can be depicted in terms of linked polyhedral units of different types. For the copper(II) phosphates, their structures are comprised of linked copper polyhedra and phosphate tetrahedra. The tetrahedral phosphate geometries are very similar in all the samples studied and therefore the descriptions on the NIR absorbing properties of the two copper(II) phosphates focus on the comparison of their copper(II) coordination geometries.

The structure of $Cu_2P_2O_7$, viewed down the crystallographic *a*-axis, is depicted in Figure 3.4. Within the structure, the copper polyhedra are connected through edge-sharing and alternate up and down to form a chain running parallel to the *a*-axis. The oxygen atoms, bridging between adjacent copper polyhedra, also link to the phosphate tetrahedra. The PO_4 tetrahedra are further linked together through corner-sharing to form P_2O_7 groups, which bridge between the copper polyhedra chains via apical oxygen atoms. These alternating polyhedra extend to form the three-dimensional structure. The copper(II) atoms are found in an unusual five-fold coordination. By consideration of the bond lengths and angles summarised in Table 3.3, it can be seen that one Cu-O distance (2.409(7) Å) is significantly elongated compared to the other Cu-O bonds which all lie in the range 1.869(3)-2.015(3) Å. Such copper(II) coordination can be regarded as a strongly distorted square pyramid.

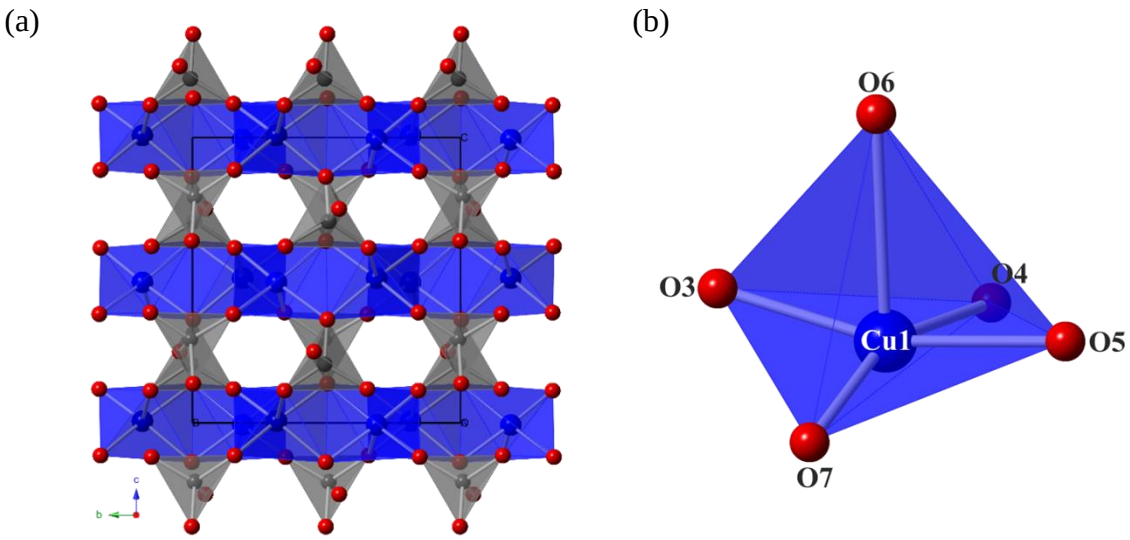

Figure 3.4: *(a) structure of $Cu_2P_2O_7$, viewed down the a-axis. Copper polyhedra are shown in blue, phosphate tetrahedra in grey and oxygen atoms in red. (b) single copper polyhedral unit within the structure*

Table 3.3: *Selected bond lengths and angles within CuO_5 polyhedra extracted from the Rietveld refinements.*

Bond	Bond length/Å	Bond angle	Degree/^{o}
Cu1-O3	2.015(3)	O3-Cu1-O3	78.23(3)
Cu1-O4	1.993(5)	O3-Cu1-O4	94.35(2)
Cu1-O5	1.956(2)	O3-Cu1-O5	160.19(5)
Cu1-O6	2.409(7)	O3-Cu1-O6	163.85(3)
Cu1-O7	1.869(3)	O3-Cu1-O7	93.63(6)
		O4-Cu1-O4	95.55(8)

Within the distorted copper(II) site, the d_{xz} and d_{yz}, orbitals remain near degenerate, and in a regular square based pyramid, these two orbitals have the lowest energy. However, in the distorted geometry as seen in Figure 3.4 (b), the four Cu-O bonds at equatorial positions in base plane are displaced, the d_{xz} and d_{yz} orbitals expected to have lowest energy in a regular square based pyramid, are raised in energy in the distorted geometry, which are slightly higher than the d_{xy} orbital. The $d_{x^2-y^2}$ orbital maintains the highest energy level, and the energy of the d_{z^2} orbital is slightly lowered owing to the elongated axial Cu-O bond, which results in less electronic repulsion between the *d* orbital electrons and the surrounding charge along the *z*-axis. In the NIR absorption spectrum for $Cu_2P_2O_7$, there is a peak centred at 900 nm, arising from the electronic transitions $b_1+b_2 \rightarrow a_1$, $a_2 \rightarrow b_1$ and $a_1 \rightarrow a_1$ respectively. However, the energy differences between *d* orbitals are very close, which is reflected in the absorption

spectrum only shows a single, broad peak. A correlation diagram of electric transition between *d* orbital energy levels is shown in Figure 3.5.

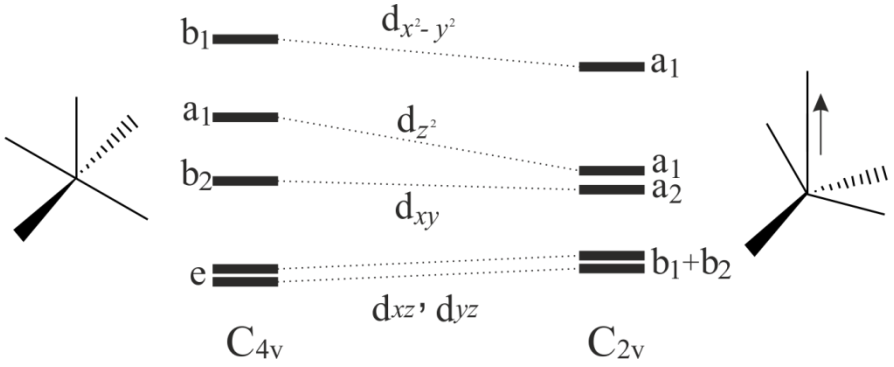

Figure 3.5: *The schematic energy levels of a regular square pyramid (C_{4v}) and a distorted square pyramid (C_{2v})*

The crystal structure of $Cu_2P_4O_{12}$ is formed of copper polyhedra that edge-share via four μ^3-bridging oxygen to form a quintet linkage. The μ^3-bridging oxygen atoms also form part of the phosphate coordinations, which are connected to form four-membered rings through sharing apical oxygen atoms. The polyhedral ring can be seen to build up from two structurally unique P_2O_7 groups. The phosphate tetrahedra and copper centred polyhedra alternate, forming a three-dimensional structure containing channels running down the *c*-axis. There are two crystallographic independent copper(II) geometries present within the structure, Cu1 and Cu2 (Figure 3.6). The copper centres are coordinated with six oxygen atoms form two distorted octahedral environments, with key bond lengths summarised in Table 3.4. Within the copper(II) centred octahedra, two axial bonds in both octahedra are noticeably elongated, compared to the equatorial bonds, due to the Jahn-Teller effect.

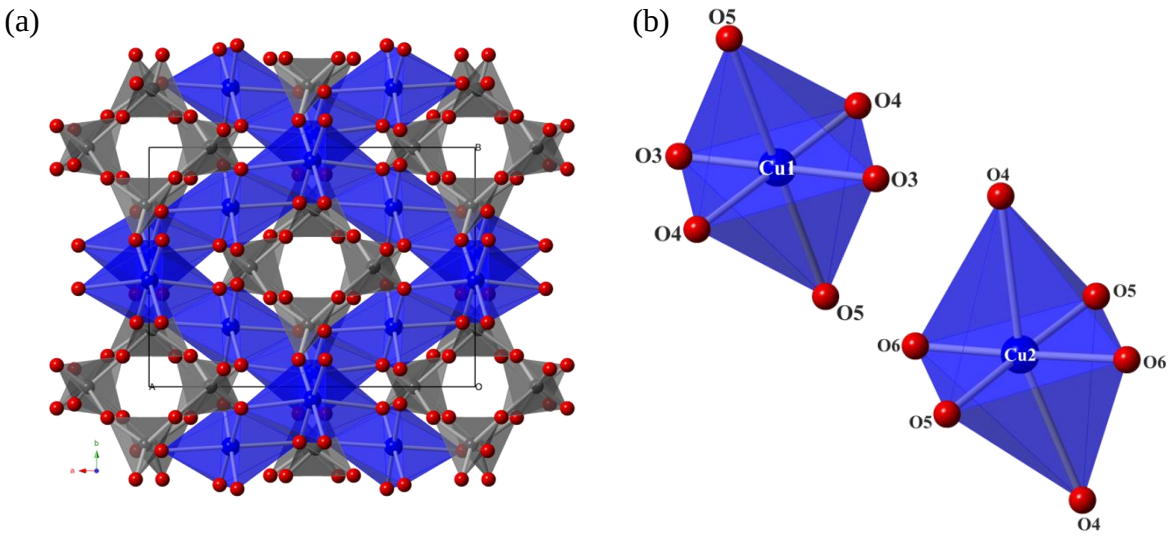

Figure 3.6: *(a) structure of $Cu_2P_4O_{12}$ viewed at c-axis. Copper polyhedra are shown in blue, phosphate tetrahedra in grey and oxygen in red. (b) shows two distorted copper polyhedra within the structure, Cu1 upper left, Cu2 bottom right*

Table 3.4: *Selected bond lengths within CuO_6 polyhedra*

Bond in Cu1	Bond length/Å	Bond in Cu2	Bond length/Å
Cu1-O3	1.937(7) × 2	Cu2-O4	2.471(7) × 2
Cu1-O4	1.971(6) × 2	Cu2-O5	1.982(6) × 2
Cu1-O5	2.370(7) × 2	Cu2-O6	1.913(6) × 2

According to the crystal field theory, for a regular copper(II) octahedral geometry with O_h symmetry, the *d* orbitals are split into two energy sets, the e_g set, rising in energy, and the t_{2g} set, of low energy (effectively not changed), thus creating an energy gap between the two sets of *d* orbitals. The e_g orbitals point directly at the ligands, whilst the t_{2g} orbitals point between ligands, and thus the t_{2g} set is more stabilised than the e_g set. However, the copper(II) geometries within the $Cu_2P_4O_{12}$ structure are distorted due to the Jahn-Teller effect. The Cu1-O5 bond in Cu1 site, and Cu2-O4 bond in Cu2 site are noticeably longer than other bonds. The elongation of bonds caused by the Jahn-Teller effect led to the symmetry of the copper(II) sites lowered to D_{4h}. As a result, the crystal field splitting energy for such distorted geometry was further split into more energy levels than derived from a regular octahedron. Within the distorted octahedral geometry, the $d_{x^2-y^2}$ orbital remains the highest energy level, but is slightly higher than that in a regular octahedron, due to Jahn-Teller distortion; the equatorial bonds may be shortened, causing the ligands to move closer to the copper centre, thus resulting in stronger electronic repulsion. For similar reasons, the d_{xy} orbital moves to a

higher energy level. As the axial bonds are significantly elongated, electronic repulsion is reduced, lowering the d_{xy}, d_{xz} and d_{z^2} energy levels. It should be noted that the Cu2 octahedron is slightly bent, with an O-Cu-O angle observed between the elongated Cu-O bonds of ~164.40°. This causes the d_{xy} orbital to have a higher energy than d_{z^2} orbital (Figure 3.7).

The $Cu_2P_4O_{12}$ product contained a small level of $Cu_2P_2O_7$ as a secondary phase, making it more difficult to distinguish whether the two distinct absorption peaks are caused by the distinct copper(II) geometries or are a result of the $Cu_2P_2O_7$ impurity. Assuming pure phase $Cu_2P_4O_{12}$, and according to the expression $\Delta E = hc/\lambda$, the absorption band centred at 900 nm is associated with the $e_g \rightarrow b_{1g}$ electronic transition and is assigned to the Cu2 environment, due to the strongest distortion leading to the greatest energy gap Δ. The absorption band with a peak centre at 1100 nm is attributed to the $e_g \rightarrow b_{1g}$ electronic transition of the Cu1 environment, in addition to possibly the $b_{2g} \rightarrow b_{1g}$ and $a_{1g} \rightarrow b_{1g}$ transitions of the Cu2 geometry. Since the exact information of the crystal field splitting energy is not known, especially for these distorted geometries, a definitive assignment of absorption wavelength with specific electronic transition is not possible. A correlation diagram of *d-d* electronic transitions is shown in Figure 3.7.

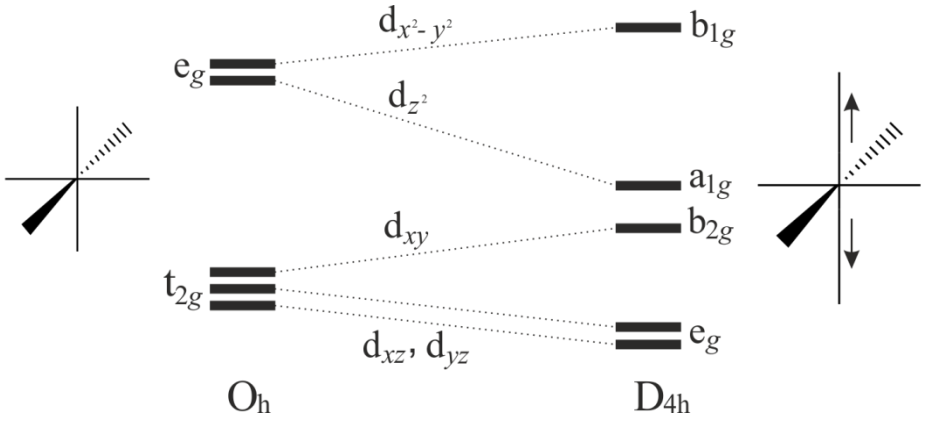

Figure 3.7: *The schematic energy levels of a regular octahedron (O_h) and a tetragonally distorted octahedron (D_{4h})*

3.1.5 Conclusions

The initial investigation carried on these copper phosphates concerned their synthesis followed by a powder X-ray diffraction study, which was used for structural refinements. Their NIR absorption behaviours were also investigated. It was concluded that the NIR absorption spectra of the candidate materials are closely linked to the metal

ion coordination geometries within their structures, as the absorption mechanism is based on *d-d* electronic transitions, and the transitions involved are symmetry forbidden according to the Laporte selection rule. In order to overcome the Laporte selection rule the metal ion should adopt unsymmetrical coordination geometry. Generally, the copper(II) geometry is subject to the Jahn-Teller effect and so becomes distorted. The centre of symmetry of the copper(II) coordination geometry is not necessarily removed through Jahn-Teller distortion, and thus Jahn-Teller effect does not account for absorption behaviour significantly. However, the Jahn-Teller distortion can be accompanied by vibrational modes resulting in bond angle variations from regular symmetry.[6] Bond angle vibrations within the copper(II) geometry can lead to a temporary geometric distortion, which is enough to partially relax the Laporte selection rule, and giving rise to absorption.

3.2 Monovalent cation incorporated copper phosphates

In order to improve the NIR absorption abilities of the copper(II) phosphates, it may be possible to tune the shape of the copper(II) coordination, for example, through introducing a second cation to produce a complex copper(II) phosphate. For this reason some monovalent cation copper(II) phosphates $A_2CuP_2O_7$ (A = Li, Na, K) were investigated. This Section describes the synthesis and characterisation of these complex copper(II) phosphates with monovalent cations. An iron based compound $K_2FeP_2O_7$ was also included in order to make comparison with the $K_2CuP_2O_7$ in regards to their characteristic structures as well as the NIR absorbing properties. Synthesis of $K_2FeP_2O_7$ was based on the method described by Keates.[7]

3.2.1 Synthesis

The syntheses of all candidate materials were carried out with the use of both conventional solid state and co-precipitation methods. For the solid state method, as the name suggests, the reactants are all solids. The ideal starting materials used to produce $A_2CuP_2O_7$ (A = Li, Na, K) are metal carbonates, oxides or hydroxide, combined with ammonia hydrogen phosphate.

The general procedure used was: all starting materials were weighed out and ground with pestle and mortar or a ball mill. The advantage of using a ball mill for grinding was to obtain smaller particles and help increase the contact surface area and thus facilitating a complete reaction. The ground mixture was then transferred to an alumina crucible and heated in air to the desired temperature (Table 3.5). Several intermediate regrinding stages as well as pelletisation were required in order to obtain pure phase products. For the co-precipitation method, water soluble materials were used as starting materials; the method is outlined in section 2.1.2. Both methods used produced pure phase products. $K_2FeP_2O_7$ was synthesised via the solid state method. Iron(II) oxalate dihydrate, potassium carbonate and ammonia phosphate dibasic were mixed at stoichiometric ratio, and finely ground. The mixture was then placed in a tube furnace and fired to 300 ^oC for 12 hours under a reductive atmosphere (5 % H_2 balance N_2). An intermediate regrind was required, and the reactants mixture finally heated to 600 ^oC for 24 hours in order to obtain pure phase product.

Table 3.5: *Reaction conditions of candidate materials*

Compound	Starting materials	Ratio	Temp./time
$Li_2CuP_2O_7$	Li_2CO_3(0.294g)+CuO(0.316g)+$NH_4H_2PO_4$(0.915g)	1:1:2	400℃-30 hrs
$Na_2CuP_2O_7$	Na_2CO_3(0.374g)+CuO(0.281g)+$NH_4H_2PO_4$(0.812g)	1:1:2	670℃-30 hrs
$K_2CuP_2O_7$	K_2CO_3(0.438g)+CuO(0.252g)+$NH_4H_2PO_4$(0.729g)	1:1:2	640℃-60 hrs
$K_2FeP_2O_7$	K_2CO_3(0.449g)+$Fe(C_2O_4)_2{\cdot}2H_2O$(0.87g)+ $(NH_4)_2HPO_4$(0.858g)	1:1:2	640℃-24 hrs

3.2.2 Structural refinement

The PXD data of compounds $Li_2CuP_2O_7$ and $K_2CuP_2O_7$ were collected on a D5000 diffractometer overnight, and confirmed the pure phases have been produced. The data were employed for structural refinements, and the standard refinement detail is outlined in section 2.2.4. The initial crystal structure model was taken from ICSD.[7, 8] The resulting profile fits are shown in Figure 3.8 and 3.9, and the refined crystallographic data are given in Table 3.6 and 3.7

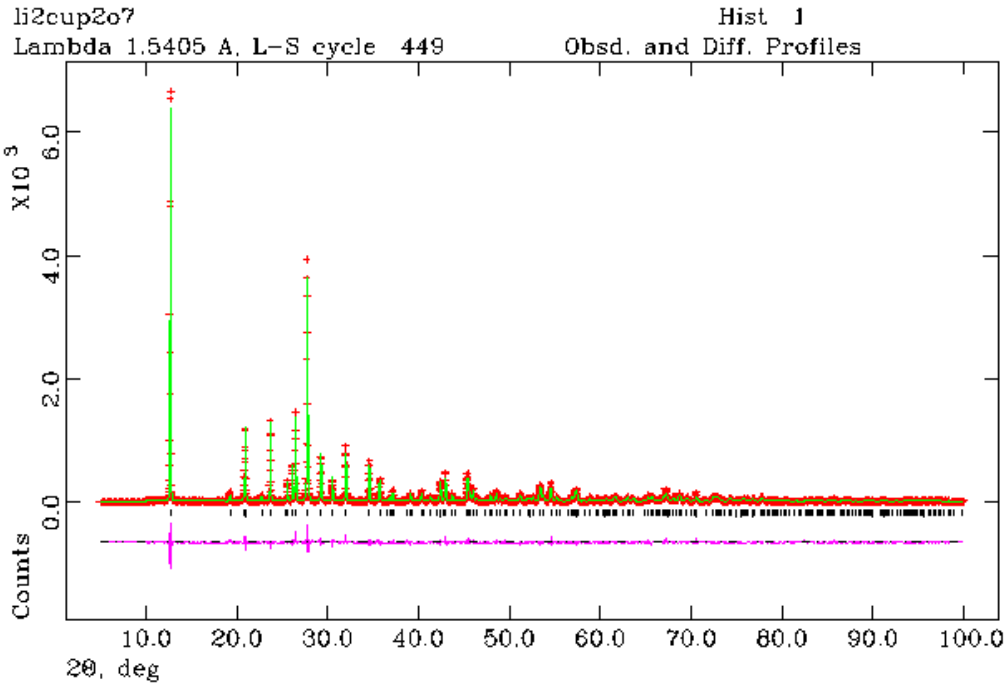

Figure 3.8: *Profile fit to PXD data for $Li_2CuP_2O_7$. Experimental data are shown as red crosses, continuous green line represented the calculated data from provided SXD file. The difference is shown underneath as pink line. Allowed diffraction peaks are represented by black tick marks.*

- $Li_2CuP_2O_7$: Monoclinic unit cell with space group *C*2/*c*. Cell parameters: a = 15.3360(1) Å, b = 4.8733(1) Å, c = 8.6216(6) Å, β = 114.8(1)°

Table 3.6: *Refined crystallographic data of $Li_2CuP_2O_7$*

Atom labels	*x*	*y*	*z*	U_{iso}/Å^{2*}100
Cu1	0	0	0	2.05(4)
O1	-0.1007(9)	0.2241(2)	-0.1509(6)	2.51(5)
O2	0.0992(8)	0.1534(7)	-0.0571(2)	3.12(9)
O3	0.1788(9)	-0.5741(2)	0.3882(7)	1.97(1)
O4	0	-0.5412(9)	0.25	1.86(3)
P1	0.1026(1)	-0.3651(6)	0.3142(8)	2.04(2)
Li1	0.3147(3)	-0.6474(1)	0.4481(6)	1.94(2)

R_p=11.16%, R_{wp}=16.37%, χ^2=3.099.

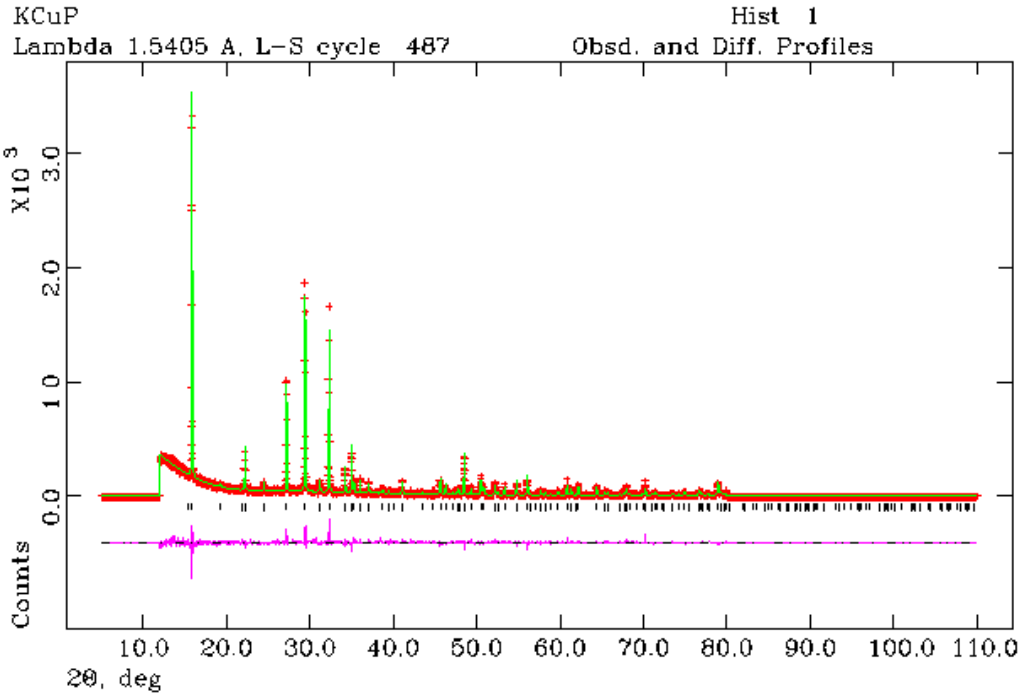

Figure 3.9: *Profile fit to PXD data for $K_2CuP_2O_7$. Experimental data are shown as red crosses, continuous green line represented the calculated data from SXD file. The difference is shown underneath as pink line. Allowed diffraction peaks are represented by black tick marks*

- $K_2CuP_2O_7$: Tetragonal unit cell with space group $P\bar{4}2_1m$. Cell parameters: a = 8.0560(2) Å, b = 8.0560(2) Å, c = 5.4600(1) Å, $\alpha = \beta = \gamma = 90^o$

Table 3.7: *Refined crystallographic data of $K_2CuP_2O_7$*

Atom labels	*x*	*y*	*z*	U_{iso}/Å^{2*}100
Cu1	0	0	0	3.36(3)
K1	0.1676(3)	0.3323(7)	0.5025(8)	3.34(6)
O1	0.8579(9)	0.3578(9)	0.7403(2)	3.28(5)
O2	0	0.5	0.1064(3)	1.13(3)
O3	0.9230(4)	0.2075(8)	0.1361(2)	2.61(6)
P1	0.8682(1)	0.3682(2)	0.0129(1)	3.89(1)

R_p=10.35%, R_{wp}=14.06%, χ^2=1.532

3.2.3 UV-Vis-NIR spectroscopy

The NIR absorption spectra for the series of compounds $A_2CuP_2O_7$ (A = Li, Na, K) were collected on a Lambda 19 spectrometer in the region between 200 nm and 2500 nm. Figure 3.10 shows the absorption spectra of the $A_2CuP_2O_7$ (A = Li, Na, K) series of samples. The spectrum for $K_2FeP_2O_7$ is also included for comparison. The first impression from the optical spectra is the strong absorption bands observed for the compounds $K_2FeP_2O_7$ and $K_2CuP_2O_7$. The latter compound indicates three independent absorption peaks, centred at 900 nm, 1200 nm and 1500 nm. For compound $K_2FeP_2O_7$, there is an intense absorption band with peak centred at 1300 nm, and a weaker peak at around 2340 nm. The strong absorption bands of the two samples indicate that the Laporte selection rule has been removed and electronic transitions between the *d* orbitals became more "allowed" on this basis. Moreover, the weak absorption in the visible region are consistent with the very light colouration of the samples , which would make them more favourable in many application fields, such as solar cells, paints or laser marking *etc*.

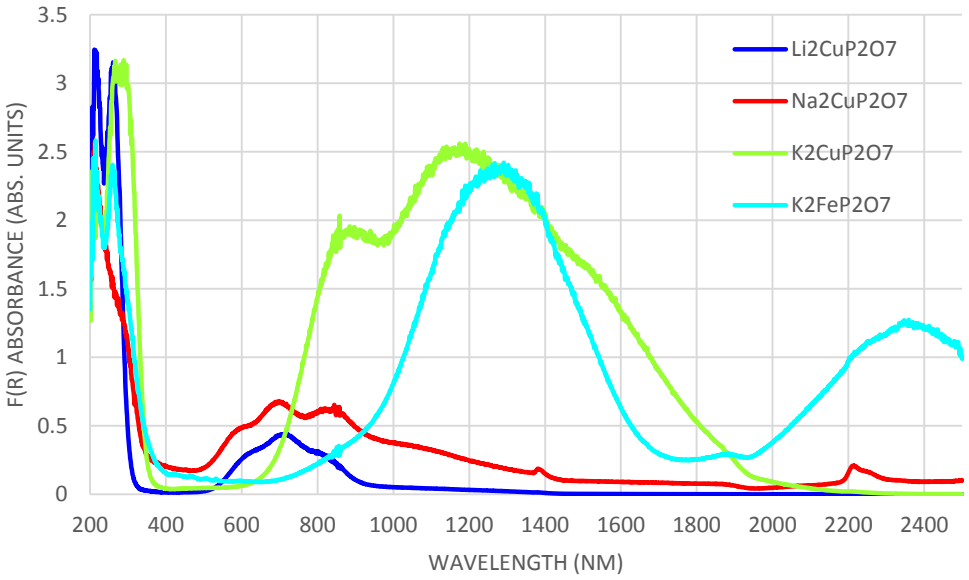

Figure 3.10: *NIR absorption spectra of $A_2CuP_2O_7$ (A = Li, Na, K) series samples, plus spectrum of $K_2FeP_2O_7$*

3.2.4 Results discussion for $A_2CuP_2O_7$ (A = Li, Na)

$Li_2CuP_2O_7$ and $Na_2CuP_2O_7$ are both weak NIR absorbers (Figure 3.10). The two samples have similar absorption band shapes, with strong absorption in the visible region. The crystal structures of $Li_2CuP_2O_7$ and $Na_2CuP_2O_7$ are similar but with differing cation arrangements, Figure 3.11. The compounds possess two-dimensional layered structures. Each layer is made up of alternating connected copper polyhedra and phosphate tetrahedra that running parallel to the crystallographic *c*-axis. Two PO_4 tetrahedra corner share to form a P_2O_7 pyrophosphate group, and these bridge between the neighbouring copper(II) sites in the chain. Li^+ or Na^+ cations reside in the inter-layer space but with different arrangements. The copper atoms within the two structures adopt nearly perfect square planar coordination, with four Cu-O bonds of nearly equal length. The highly symmetric D_{4h} copper(II) coordinations indicate the *d-d* transitions are inhibited by the Laporte selection rule, thus giving rise to the weak NIR absorption bands. The stronger absorption of these two compounds in the visible region is due to the splitting energy between the *d* orbitals, where the energy absorbed for *d-d* electronic transitions occurred in the visible regions.

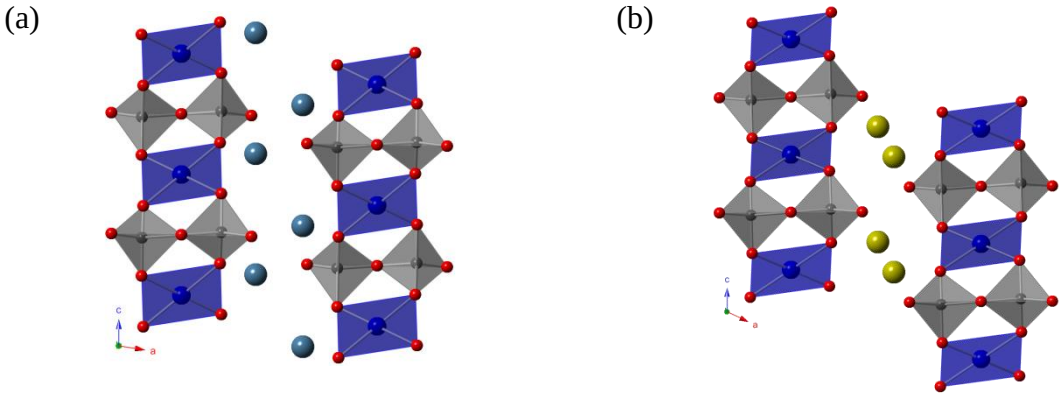

Figure 3.11: *(a) structure of $Li_2CuP_2O_7$ view down b-axis, (b) structure of $Na_2CuP_2O_7$ viewed down b-axis, copper square planar in blue, phosphate tetrahedra in grey, lithium in sky blue, sodium in yellow.*

3.2.4 Results discussion for $K_2MP_2O_7$ (M = Cu, Fe)

The samples of $K_2MP_2O_7$ (M = Cu, Fe) show strong absorptions in the NIR region, reflecting the unusual transition metal ion geometries within their structures. The spectrum of $K_2CuP_2O_7$ shows a very broad absorption feature between 650-2000 nm with several maxima and shoulders, whilst the absorption spectrum for $K_2FeP_2O_7$ displays two well separated broad absorption peaks. The structures of the compounds $K_2MP_2O_7$ (M = Cu, Fe) with the copper and iron coordination environments are depicted in Figure 3.12.

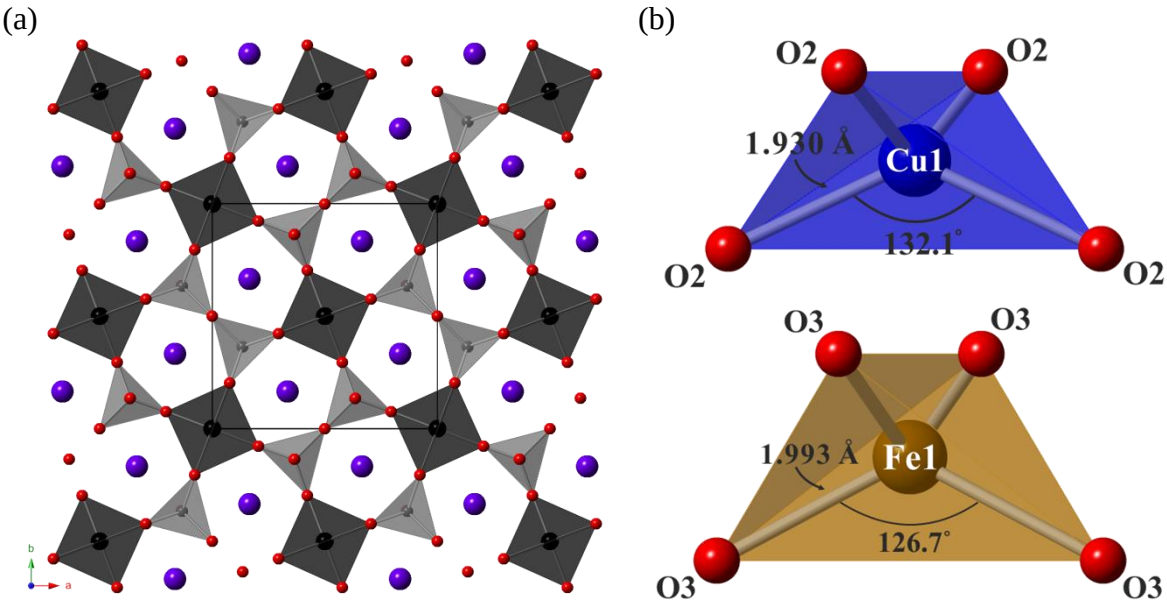

Figure 3.12: *(a) isostructural $K_2MP_2O_7$ (M = Cu, Fe) viewed at c-axis, copper or iron polyhedra is shown in blue, PO_4 tetrahedra in grey, oxygen in red and potassium in purple (b) shows the Cu (upper) and Fe (lower) coordination geometries in $K_2MP_2O_7$(M = Cu, Fe)*

The two compounds $K_2MP_2O_7$ (M = Cu, Fe) are isostructural, having a tetragonal crystal system with the space group of $P\bar{4}2_1/m$. The compounds are structurally related to $Na_2CoP_2O_7$,[9] forming two-dimensional structures, which consist of layers that are built up of MO_4 polyhedra and PO_4 tetrahedra running parallel to the *a*- and *b*-axis. Each layer is made up of flattened MO_4 tetrahedra and PO_4 tetrahedra connected through corner-sharing. The PO_4 tetrahedra are linked together by one vertex to form a pyrophosphate group of $P_2O_7^{4-}$, and further bridge between the MO_4 tetrahedra form five-membered rings in the *ab*-plane (Figure 3.10). Potassium cations are located in between the layers, in narrow channels, created by alignment of the five-membered rings, of diameter ~4 Å, along the *c*-axis.

Two PO_4 units are connected by sharing an apical oxygen from the $P_2O_7^{4-}$ anion with P-O-P angles in the ~138.7–141.9^o range. The bond lengths in the $P_2O_7^{4-}$ groups are very similar to those usually observed.[10] Each contributing PO_4 tetrahedron has one long and three short P-O bonds, with the long P-O bond to the oxygen atom forming the bridge between two PO_4 units. The shortest P-O bond is to the oxygen atom forming the terminal site and is directed into the inter-layer space. This also forms part of the potassium coordination.

Of most interest in the isostructural $K_2MP_2O_7$ (M = Cu, Fe) compounds are the unusual M^{II} environments, with four oxygen atoms forming strongly distorted tetrahedral co-ordinations (Figure 3.10 b). Such geometries are uncommon for both Cu(II) and Fe(II) coordination, in particular the latter. For materials containing Fe(II) in networks, the Fe(II) species normally adopts octahedral geometry. Only a few examples are known to possess Cu(II) and Fe(II) exclusively in tetrahedral or nearly tetrahedral geometry, including $RbCuPO_4$[11] and $KFePO_4$[12]. The bond lengths and angles of the unusual MO_4 tetrahedral geometries within the isostructural $K_2MP_2O_7$ (M = Cu, Fe) are summarised in Table 3.8.

The M-O bond lengths found in both distorted MO_4 geometries are markedly shorter than those in typical metal phosphates and pyrophosphates containing octahedral metal centres, due to their lower coordination numbers. In $K_2CuP_2O_7$, the Cu-O bonds in CuO_4 are 1.930(3) Å, whereas in $K_2FeP_2O_7$, the Fe-O bonds are 1.993(2) Å in FeO_4. Comparing the distortion of the two MO_4 geometries indicates the geometry around copper is strongly distorted; the O-Cu-O angels ranging between ~99^o and ~133^o, which

results in the copper(II) geometry being almost midway between the tetrahedral and more commonly found square planar geometry. The distortion level of the tetrahedron can be quantified by calculating the root mean square deviation($\sqrt{1/n \sum_{i=0}^{n}(\theta_i - \theta_0)^2}$), where θ_i is the determined bond angle and θ_0 is the standard 109.4° for a regular tetrahedron. The value calculated for CuO_4 is 15.4, and for FeO_4 11.8°. In addition, the high spin d^6 electronic configuration of Fe^{II} and d^9 electronic configuration of Cu^{II} are often encountered with strong Jahn-Teller distortions. There is less information reported for distorted FeO_4 sites, relating to the Jahn-Teller effect. However, it has been suggested that in the CuO_4 geometry, the distortion may be stronger, producing a flattened tetrahedron due to the involvement of the *4s* and *4p* orbitals in the highest occupied molecular orbital (HOMO) and the second-order Jahn-Teller effect may further enhance the flattening.[11] The results of the the isostructural $K_2MP_2O_7$ (M = Cu, Fe), containing flattened metal oxotetrahedra, has been published.[7]

Table 3.8: *Selected bond lengths and angles within MO_4 (M = Cu, Fe)*

Bond/Angle	M = Fe	M = Cu
M-O × 4	1.993(2)	1.930(3)
O-M-O × 4	101.62(6)	99.47(6)
O-M-O × 2	126.66(2)	132.14(2)

As discussed previously, the metal ions in $K_2MP_2O_7$ (M = Cu, Fe) adopt strongly distorted tetrahedral MO_4 sites. Such geometries offer materials that have good optical properties with strong absorption in the NIR region. The metal centre sites in both samples possess D_{2d} symmetry, which can be explained as the lowered symmetry from the T_d for a regular tetrahedron. A correlation diagram of the *d* orbital energy levels, associated with the D_{2d} symmetry, is shown in Figure 3.13. In $K_2CuP_2O_7$, the copper atom has the electronic configuration of d^9 with the free ion state term symbol ^2D. Due to the energy difference between *d* orbitals, the ^2D state of the copper ion in tetrahedral crystal fields splits into the T_2 and E energy levels. In a regular tetrahedral geometry, only the E $\rightarrow$ T_2 electronic transition is possible, and would be expected to show as a single absorption band in the spectrum. In the spectrum of $K_2CuP_2O_7$, three distinct absorption peaks are observed; this indicates there are at least three energetically different *d-d* transitions. However, in this compound the tetrahedral geometry is distorted, which lowers the symmetry to D_{2d}, leading to further energy level splitting into b_1 and a_1, derived from the E ground state (regular tetrahedron), and b_2 and e,

derived from the T_2 state. Therefore, three electronic transitions can now be expected. The absorption peak at 850 nm is attributed to the electronic transition from $a_1 \rightarrow b_2$, whilst the absorption peak at 1200 nm is believed to arise from the $b_1 \rightarrow b_2$ transition. A small shoulder at 1590 nm may arise from the transition from $a_1 \rightarrow b_1$. The lowered symmetry of D_{2d} allows the *d-d* transitions to overcome the selection rule associated with a centre of symmetry, and thus results in good absorption intensity. For $K_2FeP_2O_7$, the iron centre site is less distorted. The symmetry of this site is assumed to be the same as the copper(II) site, D_{2d}. Even so, the split energy levels of the *d* orbitals may be smaller than that of the copper(II) site, due to the reduction in distortion. The absorption spectrum shows an intense peak located at 1300 nm which is likely to arise from the sum of $a_1 \rightarrow e$ and $a_1 \rightarrow b_2$ electronic transitions, and an absorption peak at 2390 nm which may correspond to the $a_1 \rightarrow b_1$ transition.

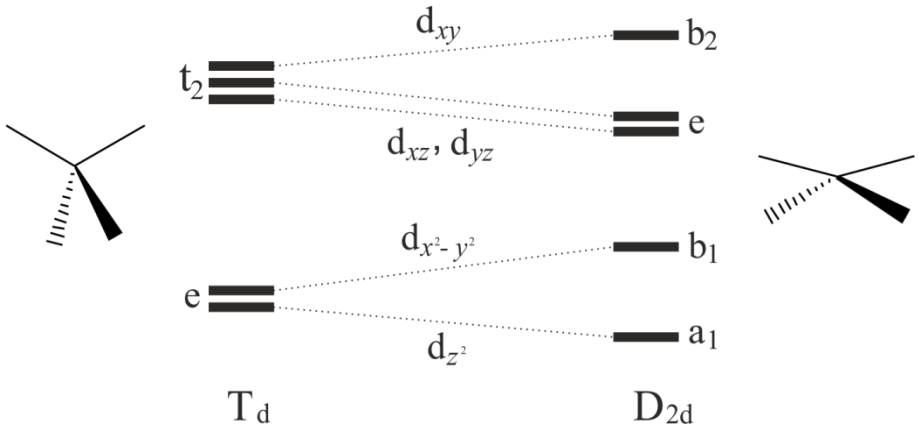

Figure 3.13: *The schematic energy levels of a regular tetrahedron (T_d) and a flattened tetrahedron (D_{2d})*

3.2.5 Conclusions

The series of $A_2CuP_2O_7$ (A = Li, Na, K) and $K_2MP_2O_7$ (M = Cu, Fe) materials had been investigated. It was hoped that introducing different cations into the copper phosphate system would change the copper(II) coordination geometries. The $K_2MP_2O_7$ (M = Cu, Fe) materials were found to be structurally related to $Na_2CoP_2O_7$. The transition metal coordination environments within these materials all form the unusual distorted tetrahedra. However, the copper(II) geometry is the most distorted. Divalent high spin cobalt 2+ ion would not be expected to demonstrate Jahn-Teller effect, and thus is the least distorted. Electron configurations of high spin d^6 of iron and d^9 of copper would be expected to undergo strong Jahn-Teller distortions, splitting the *e* levels and stabilising the overall structures. The distortion will be further reinforced by a second order Jahn-

Teller effect of the copper(II) geometry. Absorption spectra corresponding to the asymmetric transition metal geometries within the $K_2MP_2O_7$ (M = Cu, Fe) samples were therefore very intense.

3.3 Divalent cation incorporated copper phosphates

Following the study of complex copper(II) phosphates incorporating monovalent cations, which suggested that monovalent cations can be used to change and control the coordination environments of the copper ions. The UV-Vis-NIR absorption behaviours are determined by the derived metal geometries and a series of copper(II) phosphates incorporated with bivalent cations in the $A_3Cu_3(PO_4)_4$ (A = Sr, Ca) system have been prepared and their optical properties were investigated.

3.3.1 Synthesis

Compounds $A_3Cu_3(PO_4)_4$ (A = Sr, Ca) were prepared from the solid state reactions at high temperatures. Table 3.9 shows the reaction conditions of materials prepared from solid state reactions. All starting materials were mixed and ground sufficiently with pestle and mortar. The reaction mixtures of both samples were then heated slowly to 600 ^oC for 15 hours, to decompose the ammonium moiety within the reaction precursors. The samples were then reground intermediately and finally heated up to 900 ^oC for 30 hours before cooling to room temperature. Few cycles of heat treatments were carried out in order to obtain pure phase products.

Table 3.9: *Reaction conditions of $A_3Cu_3(PO_4)_4$ (A = Sr, Ca) synthesis*

Compound	Starting materials	Ratio	Temp./time
$Sr_3Cu_3(PO_4)_4$	$SrCO_3$(0.531g)+CuO(0.286g)+$NH_4H_2PO_4$(0.552g)	3:3:4	900℃-30 hrs
$Ca_3Cu_3(PO_4)_4$	$CaCO_3$(0.435g)+CuO(0.345g)+$NH_4H_2PO_4$(0.666g)	3:3:4	900℃-30 hrs

3.3.2 Structural refinement

PXD patterns were collected for all compounds and used in Rietveld structure refinements. The standard refinement procedure was outlined in Section 2.2.4. The initial crystal models of the two compounds were taken from ICSD,[13, 14] and the resulting profile fits for these two compounds are shown in Figures 3.14 and 3.15, with final extracted structural parameters summarised in Table 3.10 and 3.11.

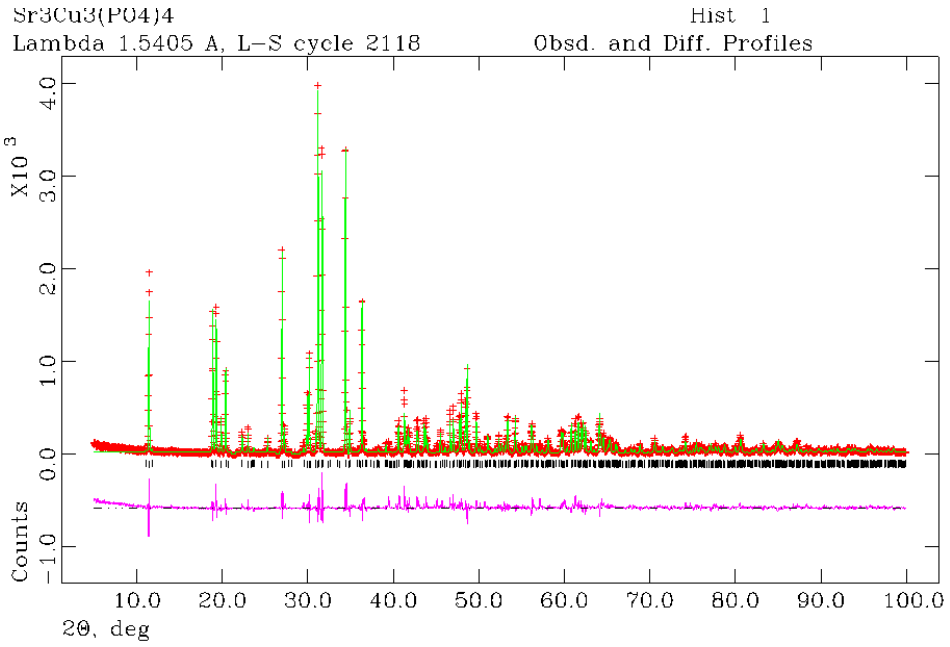

Figure 3.14: *Profile fit to PXD data for $Sr_3Cu_3(PO_4)_4$. Calculated data are shown in solid green line, observed data shown in red crosses. The difference displayed as pink line. Diffraction peaks are represented by black tick marks.*

- $Sr_3Cu_3(PO_4)_4$: Monoclinic unit cell with space group $P2_1/c$. Cell parameters: a = 9.2010(1) Å, b = 4.9410(4) Å, c = 17.8998(3) Å, β = 122.89(9)°

Table 3.10: *Refined crystallographic data of $Sr_3Cu_3(PO_4)_4$*

Atom labels	*x*	*y*	*z*	U_{iso}/Å^{2*}100
Sr1	0	0.2426(8)	0.25	1.23(8)
Sr2	0.3465(5)	0.2490(7)	0.8605(6)	1.59(9)
Cu1	0.25	0.25	0	3.16(2)
Cu2	0.3970(9)	0.2692(3)	0.5284(8)	1.51(6)
P1	0.2177(1)	0.2177(1)	0.3794(3)	2.89(7)
P2	0.5178(6)	0.2949(3)	0.1078(2)	4.35(7)
O1	0.2891(2)	0.0580(4)	0.4547(6)	1.23(1)
O2	0.1297(2)	0.2483(2)	0.3755(9)	1.23(1)
O3	0.2515(5)	0.5063(7)	0.4151(3)	1.23(1)
O4	0.2258(3)	0.2362(4)	0.2983(2)	1.23(1)
O5	0.5034(7)	0.5941(7)	0.1236(9)	1.23(1)
O6	0.5772(8)	0.1965(2)	0.0702(9)	1.23(1)
O7	0.4426(2)	0.1485(2)	0.0399(3)	1.23(1)
O8	0.5476(8)	0.0730(3)	0.1740(5)	1.23(1)

R_p = 15.31%, R_{wp} = 21.51%, χ^2 = 6.168.

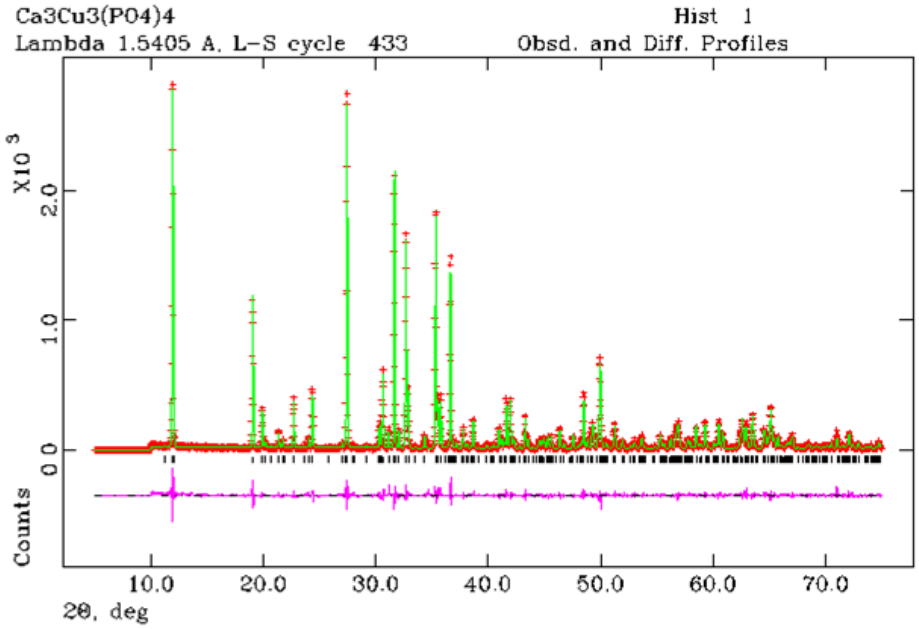

Figure 3.15: *Profile fit to PXD data for $Ca_3Cu_3(PO_4)_4$. Calculated data are shown as solid green line, observed data shown in red crosses. The difference displayed as pink line. Diffraction peaks are represented by black tick marks.*

- $Ca_3Cu_3(PO_4)_4$: Monoclinic unit cell with space group $P2_1/a$. Cell parameters: a = 17.6215(8) Å, b = 4.9021(2) Å, c = 8.9222(5) Å, β = 124.07(3)°

Table 3.11: *Refined crystallographic data of $Ca_3Cu_3(PO_4)_4$*

Atom labels	*x*	*y*	*z*	U_{iso}/Å^{2*}100
Cu1	0	0	0	2.34(9)
Cu2	0.1200(6)	0.4762(9)	0.9430(3)	2.17(6)
Ca1	0.5	0	0.5	1.94(8)
Ca2	0.2644(9)	0.4606(3)	0.7235(6)	2.38(3)
P1	0.5930(5)	-0.0068(9)	0.2484(3)	2.51(5)
P2	0.8414(2)	0.0155(3)	0.2169(2)	1.13(4)
O1	0.6823(9)	-0.1043(2)	0.4279(8)	1.04(6)
O2	0.0093(8)	0.5441(2)	0.2571(3)	1.04(6)
O3	0.6010(9)	0.2885(5)	0.2000(7)	1.04(6)
O4	0.5838(5)	-0.1957(3)	0.0935(9)	1.04(6)
O5	0.8986(9)	-0.1462(8)	0.3909(3)	1.04(6)
O6	0.8558(2)	-0.0748(3)	0.0676(2)	1.04(6)
O7	0.3577(7)	0.1735(5)	0.2482(2)	1.04(6)
O8	0.7394(2)	-0.0348(2)	0.1495(8)	1.04(6)

R_p = 11.51%, R_{wp} = 16.35%, χ^2 = 2.212.

3.3.3 UV-Vis-NIR spectroscopy

The NIR absorption spectra were collected for the two compounds $A_3Cu_3(PO_4)_4$ (A = Sr, Ca), and are depicted in Figure 3.16. In general, the NIR absorption spectra of the two compounds look similar, with broad absorption bands and two distinct absorption peaks centred at 900 nm and 1100 nm. Both samples exhibit very good NIR absorbing properties. However, $Ca_3Cu_3(PO_4)_4$ shows a greater NIR absorbance towards the NIR region than $Sr_3Cu_3(PO_4)_4$. It can be seen that, the absorption caused by *d-d* electronic transitions are no longer restricted by the Laporte selection rule, therefore leading to the absorbing maxima. The spectra of the two compounds also show weaker, but noticeable absorbance in the visible region, as expected for the coloured products obtained.

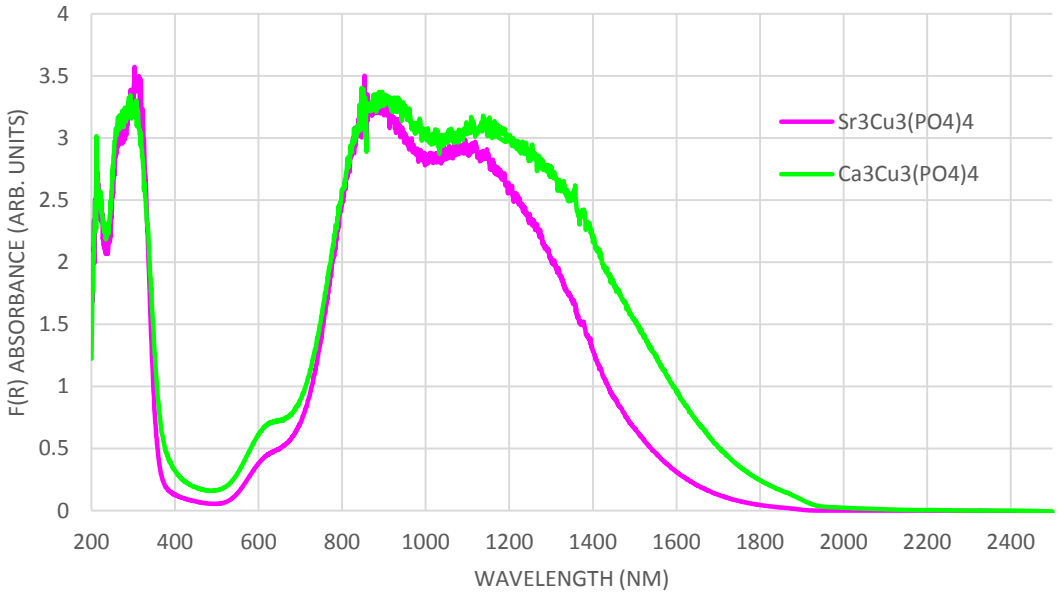

Figure 3.16: *NIR absorption spectra of $Sr_3Cu_3(PO_4)_4$ and $Ca_3Cu_3(PO_4)_4$*

3.3.4 Results discussion for $A_3Cu_3(PO_4)_4$ (A = Sr, Ca)

The structures $A_3Cu_3(PO_4)_4$ (A = Sr, Ca) all consist of two-dimensional layers, as shown in Figure 3.17. The layers within the two compounds are formed of linked polyhedra running parallel to the *ab*-plane, and separated by Sr^{2+} or Ca^{2+} ions respectively. Each layer is made up from copper triplets linked through corner-sharing, and bridged by phosphate tetrahedra. Within the copper triplets, two square-based pyramidal copper(II) sites are bridged by a square planar copper(II) site, with the apical oxygen in each square-based pyramid oriented up and down. The phosphate units are also involved in bridging, between pairs of square-base pyramidal copper(II) sites

forming four membered rings. The phosphate groups found within the two structures are quite regular, with similar P-O lengths observed. For $Sr_3Cu_3(PO_4)_4$, two distinct copper environments are present within the structure. The square planar species possess nearly perfect D_{4h} symmetry, whilst the square-based pyramidal species deviate from its ideal geometry with an apical elongation of Cu-O bond observed (~2.19 Å), compared to other equatorial bond lengths ranging from ~1.96 Å to ~2.05 Å. The $Ca_3Cu_3(PO_4)_4$ also contains two distinct copper(II) sites, similar to the $Sr_3Cu_3(PO_4)_4$, but the square-based pyramidal copper(II) site within the $Ca_3Cu_3(PO_4)_4$ deviates even greater from its ideal symmetry in contrast with such in $Sr_3Cu_3(PO_4)_4$. These two compound structures containing distorted copper(II) coordination sites of low symmetric configurations are responsible for their strong absorbing properties in the NIR regions.

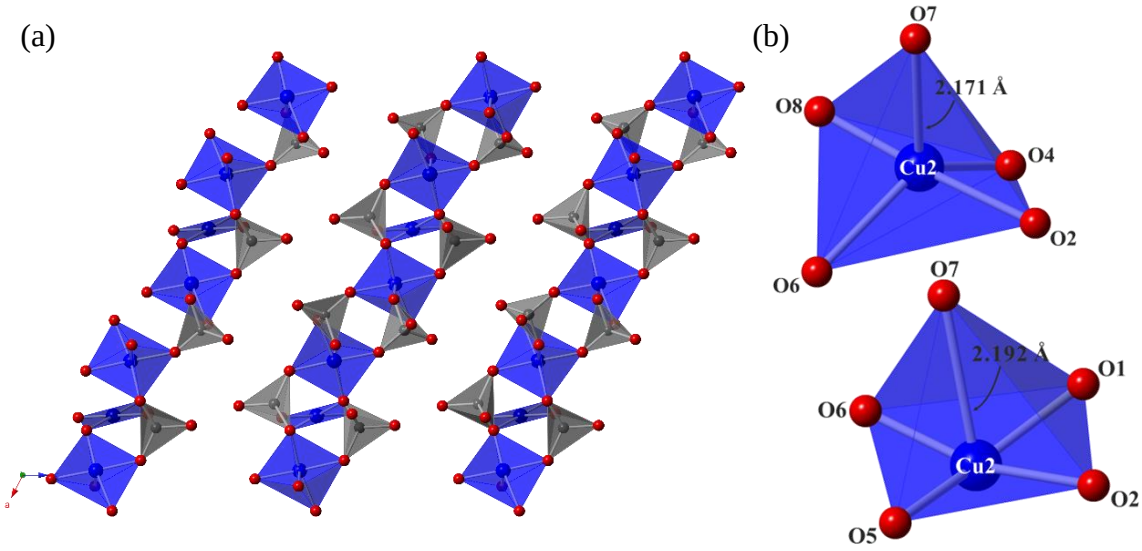

Figure 3.17: (a) *layers constituted by copper triplets and phosphate tetrahedra are similar in $A_3Cu_3(PO_4)_4$ (A = Sr, Ca). (b) Two strongly distorted copper sites within the two samples, upper geometry for $Ca_3Cu_3(PO_4)_4$, and lower geometry for $Sr_3Cu_3(PO_4)_4$*

The strong and broad NIR absorption bands of the two compounds are based on the electronic transitions occurred within the distorted square pyramidal copper(II) sites. Due to the lack of symmetry at these two copper(II) sites, the Laporte selection rule was no longer applied, therefore electronic transitions between *d* orbitals became allowed, and resulted in intense and broad absorption spectra. The second copper(II) sites within the two compounds have square planar geometries, with centre of symmetries. Thus the *d-d* transitions within such copper(II) sites are forbidden. Although the transitions are Laporte forbidden, and they may not contribute to the absorption behaviours in the NIR regions, but absorptions in the visible regions (550 - 700 nm) are observed, these are

presumably due to the *d-d* transitions within the square planar copper(II) sites occurred in the visible regions, resulting in coloured compounds obtained. Correlation diagrams of electronic transitions between *d* orbital energy levels of the two compounds are outlined in Figure 3.18. The copper centre with distorted square-based pyramidal geometry deviates significantly from its ideal geometry, with the local symmetry lowered to C_{2v} from C_{4v} for $Cu_3Cu_3(PO_4)_4$ and copper site geometry within the $Sr_3Cu_3(PO_4)_4$ remain the symmetry of C_{4v}. Because of this distortion, the d_{xz}, d_{yz} orbitals with their energy levels are elevated in energy, and the d_{z^2} orbital is lowered in energy, due to the elongation of the apical Cu-O bond causes less electronic repulsion. The d_{xy} orbital becomes the most stable, and the $d_{x^2-y^2}$ energy level is slightly lower in energy though the distortion for similar reasons.

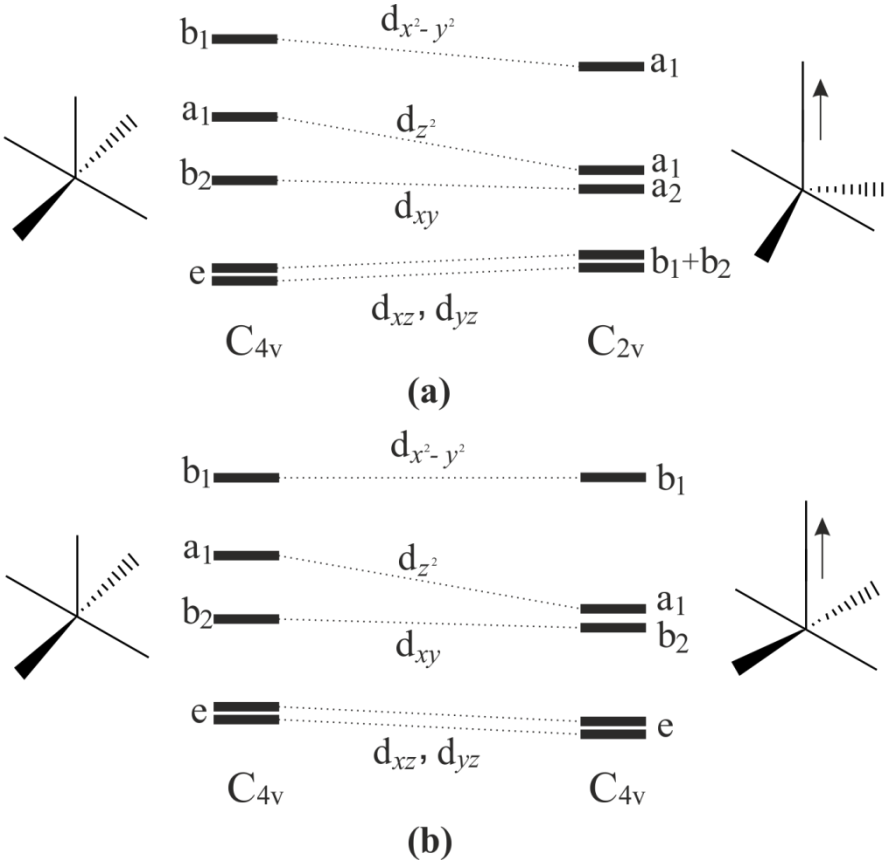

Figure 3.18: *The schematic energy levels of copper square pyramids within the two compounds, (a) Cu site within $Ca_3Cu_3(PO_4)_4$ (b) Cu site within $Sr_3Cu_3(PO_4)_4$*

In the absorption spectrum (Figure 3.16) of $Ca_3Cu_3(PO_4)_4$, the absorption peak centred at 900 nm is ascribed to the electronic transitions $b_1+b_2 \rightarrow a_1(d_{x^2-y^2})$ and, perhaps, $a_2 \rightarrow a_1(d_{x^2-y^2})$ of the C_{2v} distorted square pyramidal geometry. The absorption

peak at 1200 nm, is attributed to the $a_1(d_{z^2}) \rightarrow a_1(d_{x^2-y^2})$ transition. For $Sr_3Cu_3(PO_4)_4$, the spectrum looks very similar to $Ca_3Cu_3(PO_4)_4$, but has a slightly narrower absorption band in the NIR region. The strong absorption behaviour is believed to be caused by the *d-d* transitions occurred in the distorted square pyramidal geometry. The symmetry of this distorted copper(II) site is closer to C_{4v} than C_{2v}, with only an elongated axial Cu-O bond observed, whilst the base plane is almost square planar. In comparison with a regular square pyramid which has C_{4v} symmetry, the d_{z^2} orbital in the distorted site is more stabilised due to the elongated axial Cu-O bond, while the $d_{x^2-y^2}$ orbital is slightly destabilised. The d_{xy}, d_{xz} and d_{yz} orbitals have energy levels unchanged. Accordingly, the absorption peak in the $Sr_3Cu_3(PO_4)_4$ spectrum centred at 900 nm is ascribed to the $e \rightarrow b_1$ and $b_2 \rightarrow b_1$ transitions, whilst the shoulder at 1100 nm corresponds to the $a_1 \rightarrow b_1$ transition.

3.3.5 Conclusions

Samples of $A_3Cu_3(PO_4)_4$ (A = Sr, Ca) were successfully synthesised and characterised, and their absorption properties were also investigated. The copper(II) ion in five-fold sites gives rise to strong NIR absorption, due to its lowered site-symmetry. It is clear that the copper(II) coordination sphere within the structure has a significant impact on the optical absorption properties of a sample. However, the second cations (Sr and Ca) within the materials may also influence the absorption behaviours. Though their coordination environments are formed by sharing oxygen atoms with the neighbouring copper octahedra and phosphate tetrahedra. Due to their strong ionic characters, the Sr^{2+} and Ca^{2+} cations may form strong ionic bonds to the oxygen atoms, and influence the neighbouring copper centred units that help tune absorption band shifts.

3.4 Copper fluorophosphate

Based on the research of simple copper(II) phosphates and their derivatives, some candidate materials were found to demonstrate good NIR absorption properties. Following on from this, simple copper(II) fluorophosphates were identified as another readily synthesised target material. The crystal structure of Cu_2PO_4F was reported in 1976,[15] but its optical properties have not been investigated. The synthesis of this copper(II) fluorophosphate involved a low temperature hydrothermal method, compared with traditional solid state method at high temperature. Its NIR absorbing property has been studied and described.

3.4.1 Synthesis

Cu_2PO_4F was prepared hydrothermally, with CuF_2 (0.0584 g, 0.05751 mmol), H_3PO_3 (85% wt. H_2O. 0.04 ml, 0.0288 mmol) and NH_4F (0.0107 g, 0.0288 mmol) employed as starting materials. These reactants were mixed together in a 23mL Teflon liner and the mixture was subsequently left under a fume hood for HF evolution. The liner was then transferred to a stainless steel autoclave and sealed tightly. A three day heat treatment of the autoclave, at 175 ^oC, was carried out in a laboratory oven. The reaction vessel was allowed to cool down to room temperature naturally and the reaction products filtered under vacuum, before washing with deionised water to remove possible impurities. The collected solid product was left to dry overnight in oven at 80 ^oC. A light purple coloured crystalline product was obtained.

3.4.2 Structural refinement

PXD data from Cu_2PO_4F were collected on a D5000 diffractometer overnight, and proved a single phase product was produced. These data were then used for structural refinement, and the standard refinement detail is outlined in section 2.2.4. The initial trial crystal model was taken from ICSD.[15] The resulting profile fit shown in Figure 3.19 and final extracted structural parameters summarised in Table 3.12.

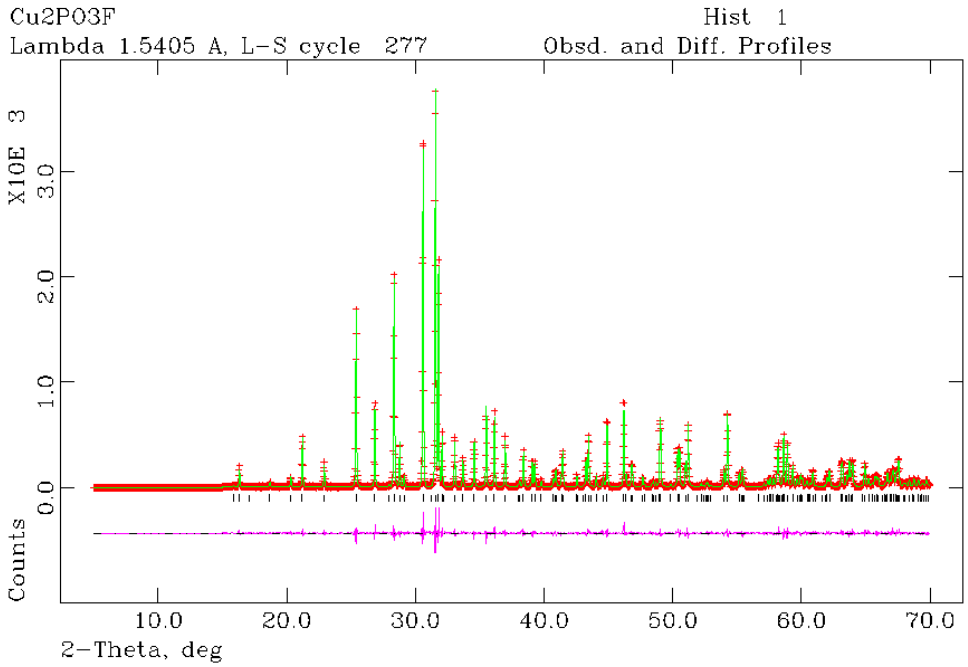

Figure 3.19: *Profile fit to PXD data for Cu_2PO_4F. Calculated data shown in solid green line, observed data shown in red crosses. The difference displayed as pink line. Diffraction peaks are represented by black tick marks.*

- Cu_2PO_4F: Monoclinic unit cell with space group *C*2/*c*. Cell parameters: a = 12.737(3)Å, b = 6.182(1) Å, c = 9.962(2) Å, β = 119.15(2)^o

Table 3.12: *Refined crystallographic data of Cu_2PO_4F*

Atom labels	*x*	*y*	*z*	U_{iso}/Å^{2*}100
Cu1	0.0619(3)	0.2616(1)	0.0026(6)	2.47(7)
Cu2	0.3464(6)	0.3835(8)	0.6483(1)	2.44(9)
P1	0.1728(2)	0.3913(6)	0.8020(8)	1.22(3)
O1	0.3167(7)	0.0819(5)	0.5965(3)	1.02(1)
O2	0.2054(3)	0.1541(4)	0.1886(4)	0.39(5)
O3	0.4221(1)	0.0716(7)	0.3645(8)	1.26(3)
O4	0.3634(5)	0.3056(1)	0.1320(5)	0.39(5)
F1	0.0236(3)	0.1184(7)	0.4022(6)	0.08(4)

R_p=9.84%, R_{wp}=13.31%, χ^2=1.620.

3.4.3 UV-Vis-NIR spectroscopy

The UV-Vis-NIR absorption spectrum was recorded at room temperature using a Lambda 750s spectrometer in the region 200-2500 nm, and is shown in Figure 3.20. The spectrum of Cu_2PO_4F shows a strong absorption in the NIR region, which can be interpreted as the result of an asymmetric copper(II) geometry, where the Laporte selection rule has been broken and the symmetry-forbidden *d-d* transitions become allowed and lead to the maximum absorption. The spectrum shows two independent absorption peaks with centres at 900 and 1300 nm, and a shoulder near 1500nm. The spectrum also shows weak absorbance in the visible region, as expected for the light coloured products obtained.

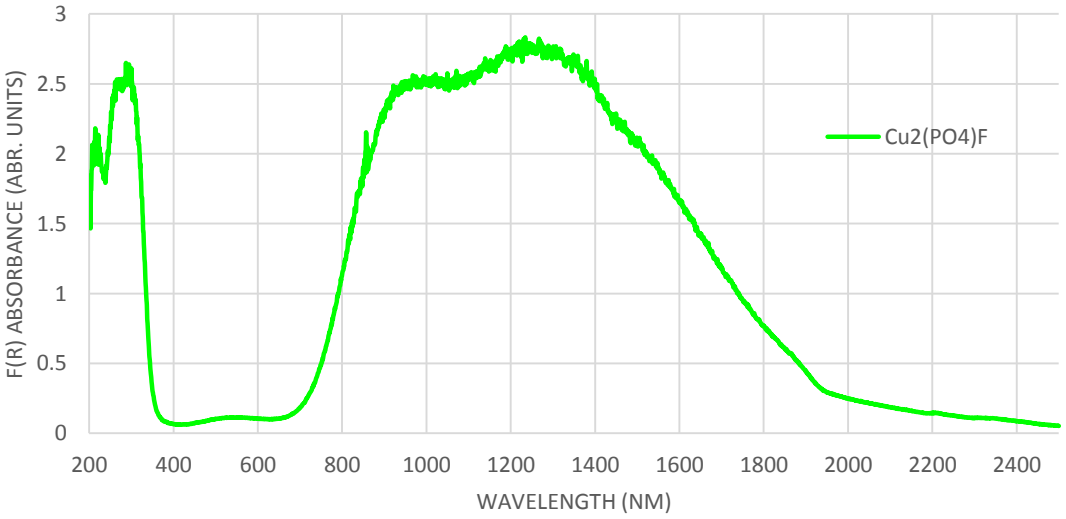

Figure 3.20: *NIR absorption spectrum of Cu_2PO_4F*

3.4.4 Results discussion for Cu_2PO_4F

Cu_2PO_4F possesses a three-dimensional structure consisting of copper polyhedra and phosphate tetrahedra which are alternated, through sharing corners. The crystallographic view along the *a*-axis of Cu_2PO_4F structure is depicted in Figure 3.21. The structure contains two distinct copper(II) environments Cu1 and Cu2; both exhibit distorted octahedral geometries. The bond lengths and angles within these copper(II) environments are summarised in Table 3.07. For Cu1 coordination, the four equatorial bonds consist of three Cu-O bonds and one Cu-F bond, which have similar bond lengths; the average of the four bonds is 1.98 Å. The two axial bonds Cu-O and Cu-F are clearly elongated, with lengths of 2.293(7) Å and 2.509(7) Å respectively. For the Cu2 site, the four equatorial bonds also have similar bond lengths lying between 1.925(8) Å and

2.044(8) Å, with an average of 1.965 Å, The two axial Cu-O and Cu-F bonds are elongated, with lengths of 2.335(8) Å and 2.431(7) Å respectively compared with the equatorial bonds. Fluoride ions in both the copper coordinations occupy positions *cis* to each other. The elongations of the axial bonds within the two copper(II) sites (Cu1 and Cu2) were attributed to the strong Jahn-Teller effect. The two copper(II) sites have no centre of symmetries, thus the Laporte selection rule is broken. As a result, Cu_2PO_4F demonstrates a strong and broad NIR absorption band.

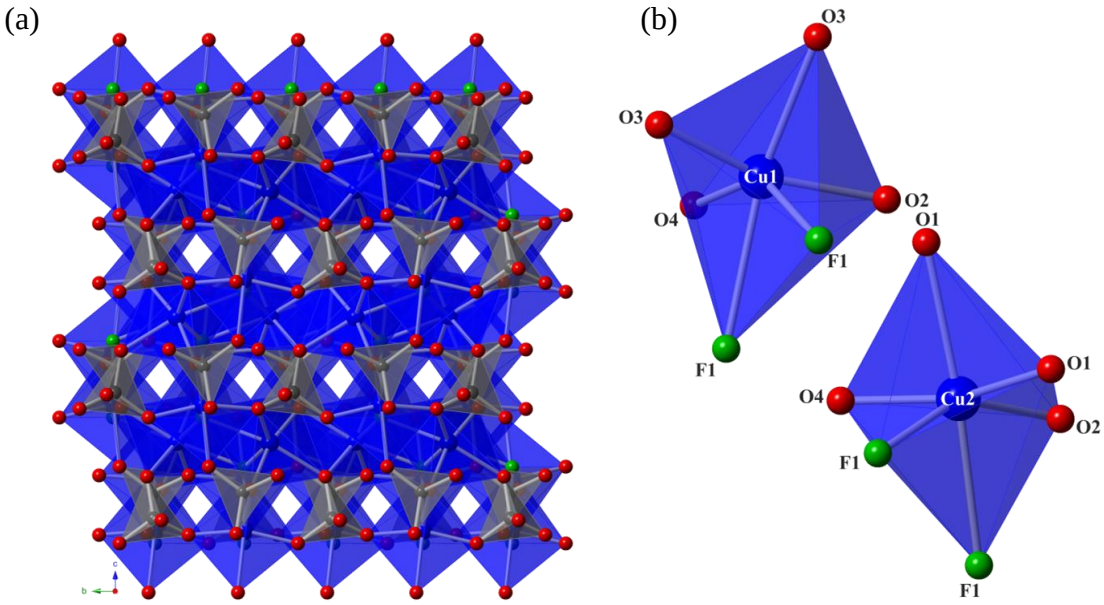

Figure 3.21: (a) *structure of Cu_2PO_4F close packed viewed at a-axis. (b) two strongly distorted copper ion sites within the sample, upper shows the Cu1 octahedron, and lower shows the Cu2 octahedron*

Table 3.07: *Selected bond lengths and angles within the two CuO_3F_2 octahedra*

Bonds	Length/Å	Angles	Degree/^{o}
Cu1-O3	2.293(7)	O2_Cu1_O3	163.02(3)
Cu1-O3	1.944(8)	O2_Cu1_O4	92.10(3)
Cu1-O2	1.988(8)	O2_Cu1_F1	82.43(3)
Cu1-O4	2.025(8)	O3_Cu1_O4	101.56(3)
Cu1-F1	1.978(7)	O3_Cu1_F1	92.96(3)
Cu1-F1	2.509(7)	O4_Cu1_F1	140.86(3)
Cu2-O1	1.925(8)	O1_Cu2_O2	90.18(3)
Cu2-O1	2.335(8)	O1_Cu2_O4	161.7(4)
Cu2-O2	2.044(8)	O1_Cu2_F1	90.49(3)
Cu2-O4	2.025(8)	O2_Cu2_O4	105.82(3)
Cu2-F1	1.956(7)	O2_Cu2_F1	148.02(3)
Cu2-F1	2.431(7)	O4_Cu2_F1	80.67(3)

The copper ions in the structure adopt two strongly distorted octahedra, as mentioned previously. The symmetry of a regular octahedron is O_h, however within the two distorted copper(II) coordinations; the axial Cu-O and Cu-F bonds within both geometries are elongated, in particular the latter ones. Thus the expected symmetries of the two copper(II) sites are close to C_{2v}. The $d_{x^2-y^2}$ orbitals in both distorted copper(II) sites are destabilised and remain the highest energy level, whilst the d_{z^2} orbitals become more stable due to elongated axial Cu-O and Cu-F bonds, as a result of reduction in electronic repulsion. The energy levels of the d_{xz}, d_{yz} orbitals are elevated, and d_{xy} orbital remains the most stable. The energy level distributions are approximately the same in both copper(II) sites, but the energy gaps between levels are likely to be slightly different. A correlation diagram of the *d* orbital energy levels associated with the C_{2v} symmetry is shown in Figure 3.22. In the spectrum of Cu_2PO_4F, the absorption peaks centred at 900 nm and 1300 nm correspond to the transitions $b_1+b_2 \rightarrow a_1(d_{x^2-y^2})$ and $a_2 \rightarrow a_1(d_{x^2-y^2})$ respectively. A small shoulder at 1500 nm is attributed to the $a_1(d_{z^2}) \rightarrow a_1(d_{x^2-y^2})$ transition. In addition, fluorine is the most electronegative element, thus a weak electron donor, and consequently a weak field ligand. According to the spectrochemical series, weak field ligands result in reduction of transition energy between *d* orbitals, and thus may enhance the absorption behaviour caused by *d-d* transitions in NIR region.

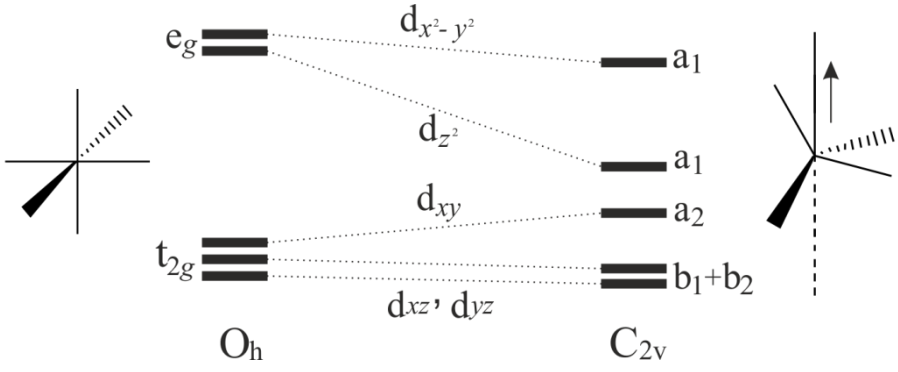

Figure 3.22: *The schematic energy levels of a regular octahedron with O_h symmetry and a distorted geometry with symmetry C_{2v}*

3.4.5 Conclusions

The synthesis of Cu_2PO_4F was successfully carried out using the hydrothermal method. The PXD pattern of Cu_2PO_4F was collected and its structure was refined using the Rietveld profile fitting method. The optical spectrum of Cu_2PO_4F displays a strong absorption band in the NIR region, which is attributed to the *d-d* transitions within the noncentrosymmetric copper(II) sites, where the Laporte selection rule is not applied. Cu_2PO_4F, is pale mauve in colour with weak absorption in the visible region, but exhibits strong NIR absorption property. These advantages make Cu_2PO_4F very interesting for further study regarding applications, which require strong NIR absorption but visible region transparency such as optical coatings on glass, solar heating, and laser marking.

3.5 Overall conclusions

For applications such as laser marking and thermal solar energy harvesting, the materials desirable are those having strong absorption behaviours in the near-infrared region (900-1600 nm) of the electromagnetic spectrum with no or weak visible colour. Additional properties such as high chemical and thermal stability, and non-toxicity are preferred. Throughout this research, a number of copper(II) phosphates with these properties have been synthesised. These materials produced were structurally characterised in order to relate their physical properties to their optical properties.

The preliminary results indicate that the absorption behaviours derived from *d-d* transitions are mainly dependent on the copper(II) coordination geometry and the ligand field produced by the surrounding anions within the structures. A low symmetry for a copper(II) site geometry within a structure gives rise to a strong NIR radiation absorbing property of material. Copper(II) phosphates have a rich structural chemistries, due to the flexible and versatile bonding with distorted (Jahn-Teller effect) CuO_{6-x} (x = 0, 2) polyhedra and the diverse coordination possible with PO_4 tetrahedra. For example, in the compound $Cu_2P_2O_7$, the copper ion adopts a distorted square pyramid, resulting in a significant absorption band in the NIR region. In $K_2CuP_2O_7$, the copper(II) coordination exhibits a strongly distorted, flattened tetrahedral geometry, which has no centre of symmetry. Hence, the absorption spectrum obtained for $K_2CuP_2O_7$ shows strong and intense absorption band.

The copper(II) geometries can be affected by incorporation of different cations within the compositions and as mentioned, the structure of $K_2CuP_2O_7$ contains a strongly distorted copper(II) site that gives rise to the strong absorption in the NIR region. For compounds $ACuP_2O_7$ (A = Li, Na), their spectra only demonstrate weak absorption bands, which is due to the fact that copper ions within the two structures are situated in symmetric square planar geometries. By considering the Laporte selection rule, electronic transitions between *d* orbitals within centrosymmetric symmetry are forbidden, thus weak absorption bands obtained. The structures of copper(II) phosphate materials can be altered through incorporation of different cationic species. Thus the NIR absorbing properties of copper(II) phosphates can be systematically studied and fine-tuned by exploring their rich structural chemistries.

Candidate NIR absorbing materials of the $A_3Cu_3(PO_4)_4$ series (A = Sr, Ca) were prepared and characterised. Their strong and broad NIR absorption spectra were the result of the presence of some distorted unsymmetrical copper(II) sites that broke the Laporte selection rule, leading to stronger electronic transitions between *d* orbitals. The second copper(II) sites within the two compounds adopt perfect square planar geometries with centre of symmetry, and thus the transitions within such copper(II) site are Laporte forbidden. These compounds $A_3Cu_3(PO_4)_4$ (A = Sr, Ca) have intense colours, but they can also be used for applications, where colour is not of importance.

Cu_2PO_4F was produced hydrothermally and shows broader absorption band compared to many materials produced. According to the spectrochemical series, the incorporation of the weak field ligand fluoride into a material structure can minimise the energy gaps between energy levels, and thereby decrease the transition energy. In addition, such a material can be readily synthesised at low temperature with a short reaction time, which would be more advantageous for commercial applications.

The best NIR absorbing material produced throughout this research is $K_2CuP_2O_7$, due to its strong NIR absorbing properties with a desired absorption peak in the spectrum, as well as its very light colour. These are ideal features for being as a transparent additive used for laser welding or marking plastics. However, other materials prepared with strong NIR absorption behaviours can also be used as coating materials for photo-electrical or photo-thermal energy conversions.

3.6 References

1. F. Norindr, University of Southampton, 2009.
2. H. Effenberger, *Acta Crystallogr. Sect. C-Cryst. Struct. Commun.*, 1990, **46**, 691-692.
3. M. Laugt, G. Bassi, I. Tordjman and J. C. Guitel, *Acta Crystallogr. Sect. B-Struct. Sci.*, 1972, **B 28**, 201-&.
4. H. Yersin, *Electronic and Vibronic Spectra of Transition Metal Complexes II*, Springer, Berlin, 1997.
5. E. Moore and R. Janes, *Metal-Ligand Bonding*, RSC Publishing, Cambridge, 2004.
6. G. L. Miessler and D. A. Tarr, *Inorganic Chemistry*, second edn., Engle-wood Cliffs: Prentice Hall, Inc., 1998.
7. A. C. Keates, Q. L. Wang and M. T. Weller, *J. Solid State Chem.*, 2014, **210**, 10-14.
8. M. R. Spirlet, J. Rebizant and M. Liegeoisduyckaerts, *Acta Crystallogr. Sect. C-Cryst. Struct. Commun.*, 1993, **49**, 209-211.
9. F. Erragh, A. Boukhari, B. Elouadi and E. M. Holt, *J. Cryst. Spectrosc.*, 1991, **21**, 321-326.
10. G. S. Gopalakrishna, M. J. Mahesh, K. G. Ashamanjari and J. S. Prasad, *Mater. Res. Bull.*, 2008, **43**, 1171-1178.
11. P. F. Henry, R. W. Hughes, S. C. Ward and M. T. Weller, *Chem. Commun.*, 2000, 1959-1960.
12. O. V. Yakubovich, W. Massa and O. V. Dimitrova, *Z. Anorg. Allg. Chem.*, 2005, **631**, 2445-2449.
13. H. Effenberger, *J. Solid State Chem.*, 1999, **142**, 6-13.
14. J. B. Anderson, E. Kostiner and F. A. Ruszal, *J. Solid State Chem.*, 1981, **39**, 29-34.
15. J. R. Rea and E. Kostiner, *Acta Crystallogr., Sect. B: Struct. Sci.*, 1976, **32**, 1944-1947.

CHAPTER FOUR: TRANSITION METAL FLUOROPHOSPHATES

4.0 Introduction

As previously introduced in Chapter 1, transition metal phosphate materials have attracted significant recent interest due to their widespread applications. Research on metal phosphates has focused on their excellent electrochemical performance which can be exploited in the positive-electrode materials of secondary batteries, such as $LiFePO_4$.[1] The metal phosphate structures usually consist of linked polyhedral units, including metal units of MO_n and PO_4 tetrahedra. The introduction of other anions such as fluoride into structural systems may lead to the formation of different polyhedral units, thus changing the morphology of the structures. This may enhance the physical properties of the materials, for example the electrochemical performance may improve by introducing the F^- ion, due to its electron-withdrawing character.[2]

Many metal phosphates have been produced through utilising solid-state reactions at high temperatures. However, the hydrothermal method offers a direct route for producing these materials without such extreme reaction conditions. For incorporation of fluoride into the final product, the traditional method uses hydrofluoric acid as fluorine source; however, due to safety issues, a hydrofluorothermal method was employed. The reactions were completed in fluoride-rich medium, through use of metal fluorides as alternatives to provide fluorine. The recent synthesis of metal fluoro-phosphate or –arsenate materials via a hydrothermal method showed successful incorporation of fluoride by using metal fluorides as starting regents including CeF_4, CuF_2, HfF_4 or ZrF_4.[3, 4] Starting materials involved in this synthetic work to produce the metal fluorophosphates were MnF_3, FeF_2 and VF_3. Hexafluorophosphoric acid (HPF_6 65 wt. % in H_2O) was also used as a fluorine provider in the reactions for the purpose of increasing fluorine content, as well as a source of phosphorous and oxygen through reaction with water.

For the hydrothermal method, water may be an important reaction medium, but the level of water used in this research work was minimised. The aim was to decrease the ratio between oxygen and fluorine within the reaction mixture, and thus increase the chance of incorporation of fluoride into the final products. The method used here can thus be redefined as a ‘hydrofluorothermal’ method.

Table 4.1 summaries the reaction conditions of new metal fluorophosphates produced including starting materials, reaction temperature and time, and observations

of final products. A wide range of reaction conditions was attempted during the research work, with more than 400 experiments carried out. However, other materials produced were either known compounds or amorphous materials or non-reacted starting materials, and thus were not studied further in this work.

The typical hydrofluorothermal reactions were carried out in 23 mL Teflon-lined Parr autoclaves. The resulting crystalline materials were primarily analysed via SXD, supporting techniques such as BV, PXD, IR, EDS and TGA were also conducted on the products to clarify the results where possible. Successful reactions resulted in production of single crystals of new phase and are discussed in detail in this Chapter.

Table 4.1: *Synthetic conditions for all transition metal fluorophosphate materials*

Starting regents	**Temp (^{o}C)**	**Time (hours)**	**Crystal morphology and purity**	**Product(s)**	**Thesis section**
MnF_3 (0.475 mmol , 0.0532 g); H_3PO_4 (0.95 mmol, 0.0652 ml); BaF_2 (0.95 mmol, 0.1667 g)	175	72	Dark brown block Single phase	$Ba_2Mn_2F_5(PO_4)(PO_3F)\cdot 2H_2O$	4.1 (I)
MnF_3 (0.536 mmol, 0.0603 g); H_2PO_3F (1.072 mmol, 0.0841 ml); NaF (1.072 mmol, 0.0452 g)	175	48	Dark brown plate Single phase	$Na_2MnF_2(PO_3OH)(PO_2F_2)$	4.2 (II)
MnF_3 (0.536 mmol, 0.0603 g); HPF_6 (1.075 mmol, 0.15 ml); $LiPF_6$ (1.075 mmol, 0.1712 g)	220	48	Brown hexagonal plate Single phase	$Li_3MnF_2(PO_3F)_2$	4.3 (III)
FeF_2 (0.639 mmol, 0.06 g); HPF_6 (1.918 mmol, 0.26 ml); NaF (1.918 mmol, 0.08 g)	175	48	Brown yellow column Multi-phases, Unknown impurity	$NaFe(PO_3F)_2$	4.4 (IV)
MnF_3 (0.475 mmol, 0.0532 g); H_3PO_4 (0.475 mmol, 0.0326 ml); NH_4OH (0.475 mmol, 0.0541 ml); HCl (0.0475 mmol, 0.039 ml)	150	72	Pink needle Multi-phases, Unknown impurity	$(NH_4)_2Mn_2F(PO_3F)_2Cl_2$	4.5 (V)
MnF_2 (0.476 mmol, 0.0442 g); H_3PO_4 (0.475 mmol, 0.0326 ml); NH_4F (0.475 mmol, 0.0176 g)	175	48	Pink column Single phase	$(NH_4)Mn_3(PO_3F)_2(PO_2F_2)F_2$	4.6 (VI)
VF_3 (0.4 mmol, 0.0432 g); H_3PO_4 (0.8 mmol, 0.055 ml); LiAc (1.2 mmol, 0.1225 g)	175	96	Dark green plate Multi-phases Unknown impurity	$Li_5(VOF)_3(PO_4)_3\cdot 3H_2O$	4.7 (VII)

4.1 Compound I: $Ba_2Mn_2F_5(PO_4)(PO_3F)\cdot 2H_2O$

The product crystallised as brown block crystals. A suitable crystal was selected for a single crystal X-ray diffraction study on a Rigaku FR-E+ Ultra High Flux Diffractometer at the University of Southampton. Data were collected at 120K with resulting crystallographic information summarised in Table 4.2. The structure of the title compound possesses monoclinic unit cell with space group $P2_1/c$ and forms a two-dimensional layered structure, which comprises manganese centred octahedra and phosphate tetrahedra (Figure 4. 1), key bond lengths are summarised in Table 4.3.

Within the structure of compound **I**, one *trans*-MnO_4F_2 and two MnO_2F_4 octahedra are linked to form a triplet. Each triplet consists of two MnO_2F_4 octahedra bridged by a central *trans*-MnO_4F_2 octahedron through corner-sharing of μ^2-bridging *trans*-fluoride within the central Mn based octahedron and forming Mn-F-Mn linkages, with an observed Mn-F-Mn angle around 121.35° (Figure 4.1). The Mn-polyhedral triplets are capped by phosphate tetrahedra to form a tancoite-type topology.[5] Each phosphate tetrahedron bridges two connected Mn octahedra resulting in three membered rings. This arrangement of the polyhedral building units can also be observed in other metal phosphates and phosphate minerals.[6, 7] The Mn based polyhedral triplets are further cross-linked by *trans*-MnO_4F_2 octahedra via sharing four equatorial oxygen atoms within each *trans*-MnO_4F_2 octahedron and produce the two-dimensional layers in the *ac*-plane. The inter-layer space is filled with barium ions, and water molecules.

The EDS data confirmed the presence of fluorine within the material. The presence of fluorine within the structure was deduced during the refinement using the atomic displacement parameters (ADPs) values (provided in cif). Use of oxygen atom scattering power yields non-positive or very small ADP values and reassignment of this site as fluoride produces an ADP value that is similar to all other anion sites. Correct assignment also led to a reduction in data fitting residual values. Subsequent bond valence calculations in combination with the overall charge-balancing of the structure also provide judgement of whether a fluoride site has been assigned correctly, where the bond valence value for an oxygen atom is expected to be approximately of 2, for fluorine is approximately of 1. The bond valence values are given in Table 4.4.

Table 4.2: *Crystal and diffraction information of compound I*

Empirical formula	$Ba_2Mn_2F_6P_2O_9H_4$
Formula weight ($gmol^{-1}$)	708.49
Temperature (K)	120(2)
Appearance	Brown block
Crystal size (mm)	0.5 × 0.025 × 0.05
Crystal system	Monoclinic
Space group	$P2_1/n$
Unit cell dimensions	a=7.365(3) Å, b=18.147(8) Å c=8.916(4) Å, β=91.309(7)^o
λ/Å	0.71073 Å (Mo K_α)
Volume ($Å^3$)	1189.18(7)
Z	4
Density (gcm^{-3})	3.61
Reflections collected	15831
Unique reflections	2330
R_1 (all)	0.0614
wR_2 (all)	0.1167
GooF	1.230

Three independent manganese octahedral environments were found within the structure and represented as Mn1, Mn2 and Mn3. Within the MnO_2F_4 (Mn1) octahedral site, the two oxygen atoms occupying the *cis*-position are all involved in bridging to the phosphate units, one of the *trans*-fluoride forms bridge to the neighbouring Mn centre, and the other three F-atoms are terminal. Bond lengths summarised in Table 4.3 show, bonds formed between the *trans*-fluoride and Mn centre are significantly longer than the *cis*-bridging Mn-O bonds and *cis*-terminal Mn-F bonds, which is suggested to be due to the Jahn-Teller effect of d^4 high-spin configuration of Mn^{III}. This leads to a strong elongation of the axial Mn-F bonds with mean length of 2.10 Å, compare to the equatorial Mn-O and Mn-F with average lengths of 1.87 Å and 1.90 Å. The BV sums of Mn1 with value of 3.02 also support the assigned oxidation state of the Mn ion as +3, as shown in Table 4.4.

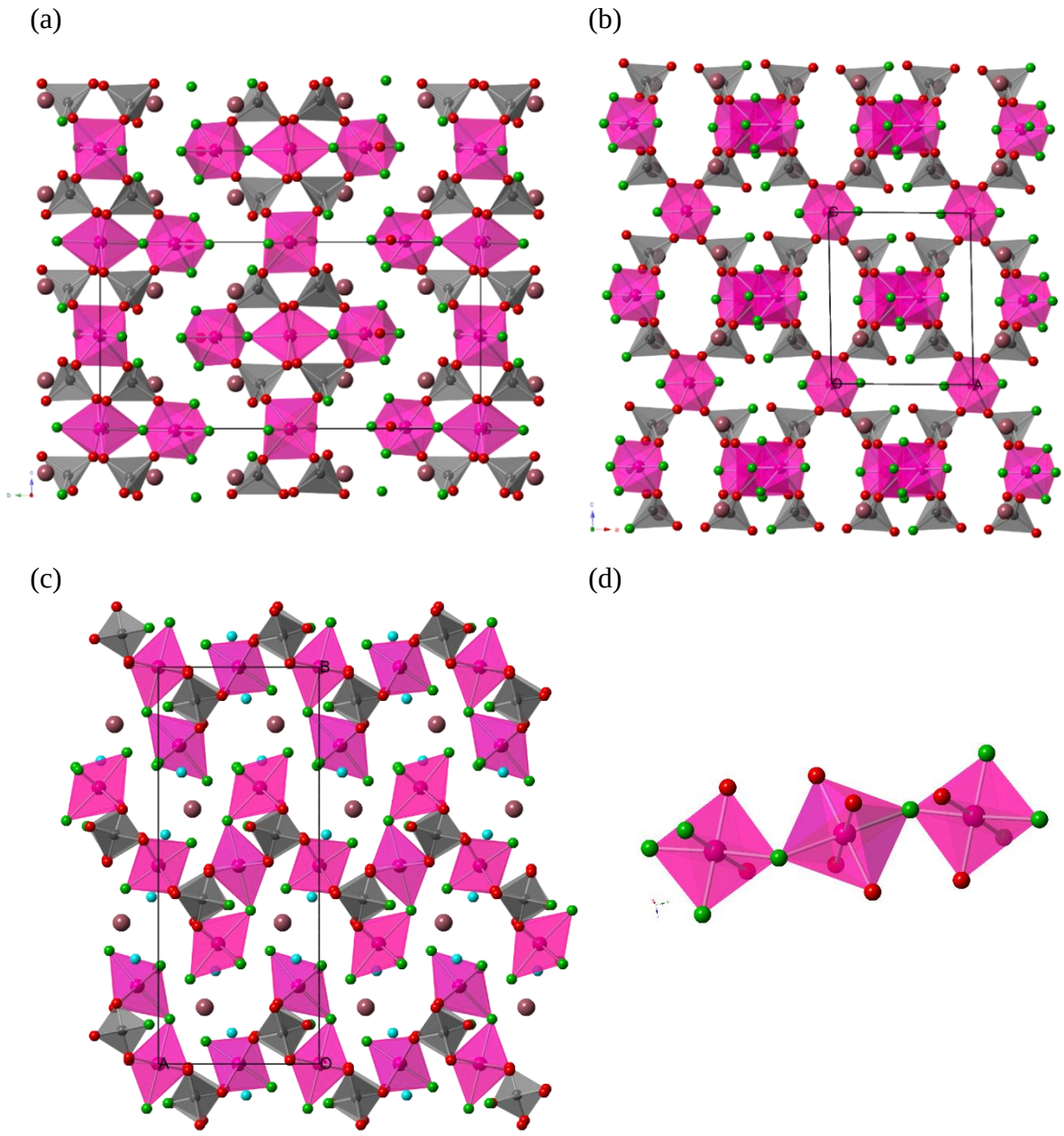

Figure 4.1*: The structure of $Ba_2Mn_2F_5(PO_4)(PO_3F)\cdot 2H_2O$ viewed down the (a) a-, (b) b-, (c) c-crystallographic axes, where the manganese octahedra are in pink, phosphate tetrahedra in grey, oxygen atoms in red, fluorine atoms in green, Ba^{2+} cations in rose colour, water molecule shown in sky blue. (d) the triplets form from three linked Mn centred octahedra.*

The +3 oxidation state for Mn ions in Mn2 and Mn 3 sites was also confirmed by BV calculations. Both Mn2 and Mn3 sites are six-coordinate and form the MnO_4F_2 octahedral environments. The four oxygen atoms within both octahedra are involved in bridging to the phosphate units, the two fluoride anions in Mn2 site are terminal and point toward the inter-layer space, whilst the *trans*-fluoride in Mn3 site are bridged between Mn centres. Similar to the Mn1 site, the Mn2 and Mn3 sites are all distorted

from the regular octahedral geometry due to the Jahn-Teller effect. For Mn2 site, there is a clear elongation of the axial Mn-O bond with an average length of 2.126(8) Å, compared to the equatorial Mn-O and Mn-F bonds (1.917(8) Å and 1.839(6) Å). Within the Mn3 site, the bridging Mn-F bonds were observed to be elongated with average length of 2.117 Å, and in comparison with the equatorial Mn-O bonds which have mean length of 1.944 Å. The axial elongation can be attributed to a Jahn-Teller distortion, which is commonly observed in octahedral Mn^{III} species, also known as the tetragonal distortion.

Table 4.3: *Bond lengths between selected atoms*

Bond	Bond length (Å)	Bond	Bond length (Å)
Mn1-O3	1.906(9)	Mn3-O7	1.946(8) × 2
Mn1-O5	1.888(8)	Mn3-F4	2.117(6) × 2
Mn1-F1	1.870(7)	P1-O4	1.503(8)
Mn1-F2	1.874(7)	P1-O5	1.538(9)
Mn1-F3	2.074(6)	P1-O7	1.538(9)
Mn1-F4	2.124(6)	P1-F6	1.559(8)
Mn2-O1	1.917(8) × 2	P2-O1	1.538(8)
Mn2-O4	2.126(8) × 2	P2-O2	1.566(8)
Mn2-F5	1.839(6) × 2	P2-O3	1.562(9)
Mn3-O2	1.943(8) × 2	P2-O6	1.515(8)

There are two crystallographically independent phosphate groups (P1 and P2) present within the structure of compound **I**, and each of them is four-coordinate. Within the P1 unit, three oxygen atoms are involved in bridging to the neighbouring Mn-octahedra, the fourth vertex being terminal site and assigned as a fluoride anion. One oxygen atom involved in bridging to Mn2 octahedron at axial position show short P-O bond lengths of 1.503(8) Å, and 1.538(9) Å for other two P-O bonds with oxygen atoms bridging to the M1 and M2 sites at their equatorial positions. The terminal P-F bond is elongated and displays a length of 1.559(8) Å. Within the P2 unit, the trend of the bond length of the bridging P-O bonds is similar to those in the P1 unit, where the P-O bonds involved in bridging to the Mn1 and Mn3 sites display longer lengths compared to that to the Mn2 site. The terminal site was refined as oxygen and produces a BV value of 1.55, which is smaller than the expected value of 2; the low bond valence value maybe due to undetermined hydrogen bonds formed between the terminal oxygen and the lattice water molecule or possibly some fluoride substitution. The created terminal P2-

O6 bond in P2 tetrahedron shows a very short length of 1.515(8) Å compared to other bridging P-O bonds, through this value would be consistent with some double bond character.

Table 4.4: *Bond valence calculations for selected atoms*

Atom label	Bond valence	Atom label	Bond valence
O1	2.03 -	Mn3	2.97 +
O2	1.91 -	F1	0.88 -
O3	1.86 -	F2	0.95 -
O4	1.95 -	F3	0.87 -
O5	1.95 -	F4	1.09 -
O6	1.55 -	F5	1.06 -
O7	1.92 -	F6	1.05 -
Mn1	3.02 +	O8	0.48 -
Mn2	3.16 +	O9	0.54 -

The oxygen atoms O8 and O9 were assigned as non-bonded water molecules; hydrogen atoms of these water molecules could not be assigned during structural refinement, due to their low scattering power. Thus the oxygen atoms only were used to represent the water molecules. The two oxygen atoms forming of the water molecules are both involved in the formation of barium coordination environment, and the hydrogen atoms attached to O8 and O9 are likely to be involved in bonding interactions to the framework anionic species. The observed low bond valences for O8 and O9 suggest additional electron densities are required to form fully bonded water molecules. Barium cations are found to form two distinct coordination environments. One of them is ten-coordinate, with six fluorine and four oxygen atoms forming an irregular geometry. The second one is coordinated with five fluorine and four oxygen atoms forming a ninefold site. The observed bond lengths are lying within the ~2.675-2.944 Å range, and the separation distance between barium cations is around 4.43 Å.

The FT-IR spectrum (Appendix.1) of compound **I** shows a broad absorption at around 3300-3100 cm^{-1}, which is assigned to the stretching mode of O-H in a water molecule. The TGA data (Figure 4.2) reveals a two-step weight loss. A gradual weight loss of 5.3 % was observed within the temperature range of 300-420 ^{o}C and is considered to be the 2 moles of the lattice water molecules being removed from the crystal structure, and the value is comparable to that calculated from the composition of

5.1 %. Further weight loss should correspond to the loss of fluorine containing species from the structure. The DTA trace shows exothermic peaks at 400 ^{o}C and 580 ^{o}C, which suggest the loss of water molecules and fluorine in a two-step process, with simultaneous structural changes occurring.

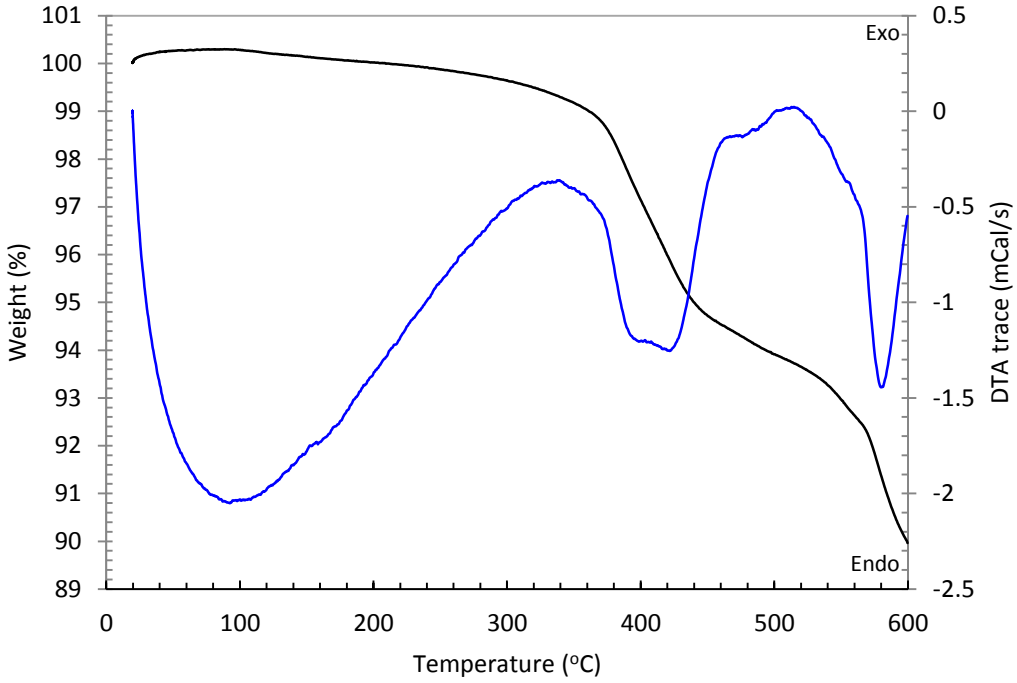

Figure 4.2: *TGA plot for the thermal decomposition of $Ba_2Mn_2F_5(PO_4)(PO_3F)\cdot 2H_2O$ Black and blue lines represented the TGA and DTA data as a function of temperature.*

EDS analysis showed the presence of Ba (9.3 %), Mn (8.2 %), P (8.7 %), F (36.5 %) and O (37.3 %), gives an experimental atomic ratio of 1.14:1:1.06:4.4:4.5, which is in approximate agreement with the theoretical ratios of 1:1:1:3:4.5. An SEM image of the compound **I** block crystals was recorded and is shown in Figure 4.3.

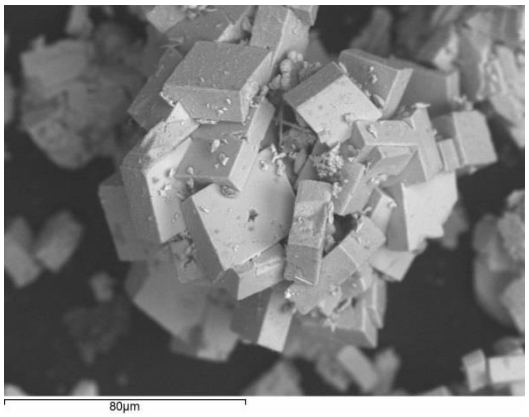

Figure 4.3: *SEM image of $Ba_2Mn_2F_5(PO_4)(PO_3F)\cdot 2H_2O$ rectangular block crystals*

4.2 Compound II: $Na_2MnF_2(PO_3OH)(PO_2F_2)$

The product crystallised as brown platy crystals. A suitable crystal was selected for a single crystal X-ray diffraction study. The data were collected at 120 K with the resulting crystallographic information summarised in Table 4.5. Compound **II** shows structural similarities with $Ba_{1.5}FeF_2(PO_2(OH,F)_2)_2 \cdot H_2O$,[8] which has been recently reported. The structure of compound **II** possesses a triclinic unit cell with space group *P*1 and forms a one-dimensional structure (Figure 4.4). Key bond lengths are summarised in Table 4.6.

The structure of compound **II** consists of one-dimensional chains, aligned parallel to the crystallographic *a*-axis. The type of chain can be seen as double-stranded based on four-membered rings, which are made up of alternating connected Mn centred octahedra and phosphate tetrahedra. Within in the polyhedral chain, the neighbouring Mn centred octahedra are bridged by two phosphate units through sharing corners of two μ^2-bridging oxygen atoms per phosphate unit. Adjacent chains interleave phosphate group positions in the *ac*-plane are separated by Na^+ ions. Compound **II** is also structurally related to the $K_2MnF_2(PO_2\ (O,OH,F)_2)_2$,[9] but the linear chains within the two compounds are arranged differently. In $K_2MnF_2(PO_2\ (O,OH,F)_2)_2$ the identical chains are interleaved in a herring-bone manner, while in the compound **II** the chains lie in rows perpendicular to the *b*-axis.

EDS data confirmed the presence of fluorine within the material. During structural refinement, the correct assignment of fluoride site produces an ADP value (provided in cif file) that is similar to all other anion sites as well as a reduction in data fitting residual value. BV calculations were used to verify whether a fluoride site has been assigned correctly, incorrect assignment of oxide ion to fluoride ion would result in a low BV value, the BV calculations for oxygen is expected to be approximately of 2, for fluorine is 1.

Only one crystallographically independent manganese coordination environment exists in compound **II**. The Mn site is six-coordinate, with four oxygen atoms at equatorial positions bridging to phosphate groups, and two terminal fluoride anions at axial positions, which also form part of the sodium ion coordination. The bond lengths indicate the Mn coordination is subjected to the Jahn-Teller effect, resulting in tetragonal distortion with the axial Mn-O bonds being elongated; the observed bond

lengths for the axial Mn-O bonds has an average value of 2.183 Å, which is noticeably longer than the equatorial Mn-O and Mn-F bonds, which have average lengths of 1.943 Å and 1.832 Å. The relative short terminal Mn-F bond maybe due to the great electronegativity of fluorine resulting in smaller covalent radius compared to oxygen. The BV calculation (Mn1 = 3.04) indicates the Mn centre adopts an oxidation sate of +3, as seen in Table 4.7.

Table 4.5: *Crystal and diffraction information of compound II*

Empirical formula	$Na_2MnF_4P_2O_6H$
Formula weight ($gmol^{-1}$)	335.86
Temperature (K)	120
Appearance	Brown plate
Crystal size (mm)	0.5 × 0.05 × 0.01
Crystal system	Triclinic
Space group	*P*1
Unit cell dimensions	a=4.694(5) Å, b=6.003(6) Å, c=7.771(7) Å α=102.44(1)^o, β=99.75(4)^o, γ=107.71(2)^o
λ/Å	0.71073 Å (Mo K_α)
Volume ($Å^3$)	197.07(2)
Z	1
Density (gcm^{-3})	2.64
Reflections collected	2176
Unique reflections	1597
Flack parameter	0.21(5)
R_1 (all)	0.0252
wR_2 (all)	0.0628
GooF	1.049

Table 4.6: *Bond lengths between selected atoms*

Bond	Bond length (Å)	Bond	Bond length (Å)
Mn1-O1	1.940(8)	P1-O2	1.513(8)
Mn1-O2	2.147(9)	P1-O5	1.553(8)
Mn1-O3	2.218(9)	P1-F3	1.529(7)
Mn1-O4	1.946(7)	P2-O3	1.487(8)
Mn1-F1	1.815(7)	P2-O4	1.506(7)
Mn1-F2	1.850(7)	P2-F4	1.609(8)
P1-O1	1.537(7)	P2-F5	1.525(7)

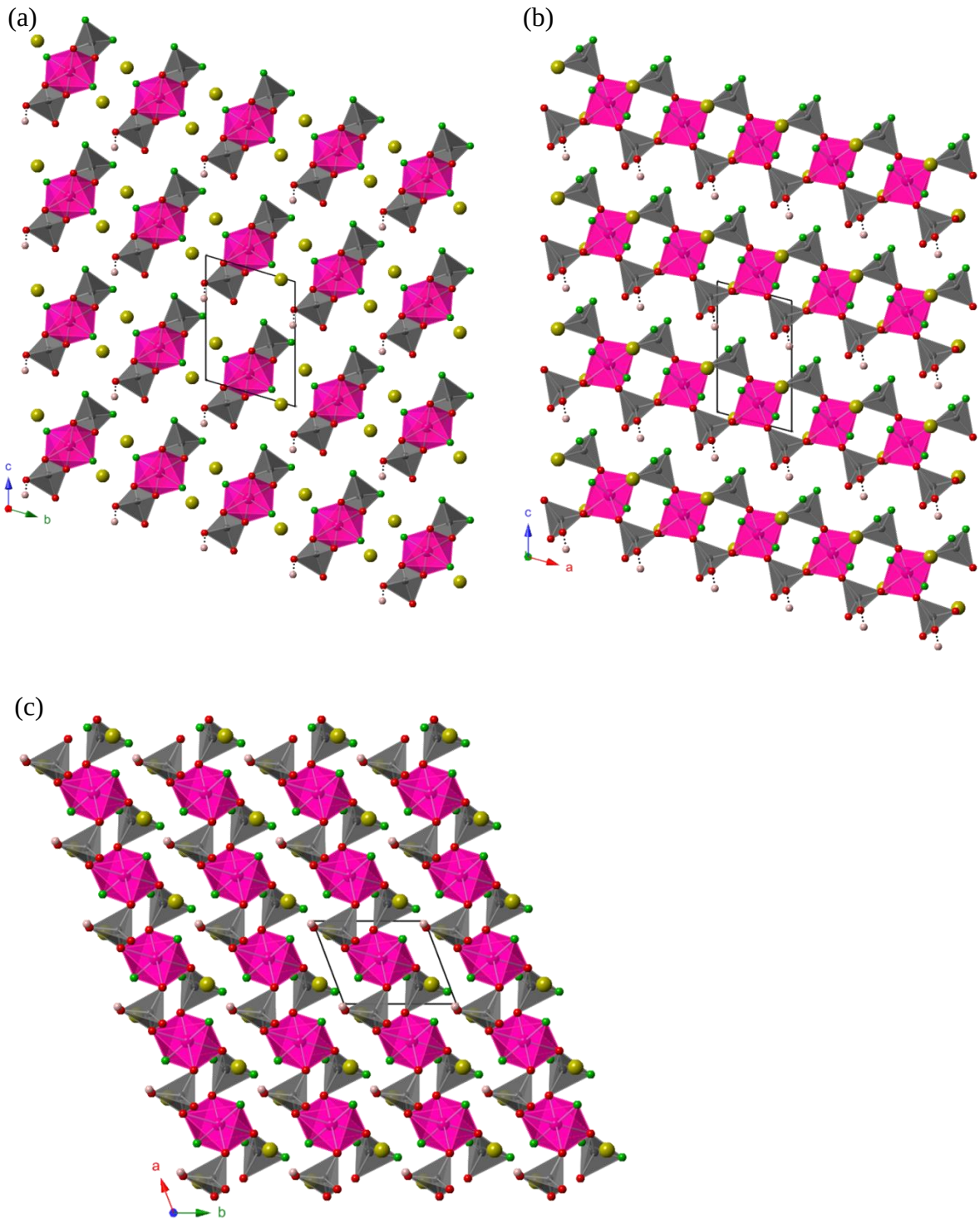

Figure 4.4*: The structure of $Na_2MnF_2(PO_3OH)(PO_2F_2)$ viewed down the (a) a-, (b) b-, (c) c-crystallographic axes, with the Mn^{III} octahedra are shown in pink, phosphate tetrahedra in gray, oxygen atoms in red, fluorine in green, hydrogen in pale pink and Na^+ cations in yellow*

There are two independent phosphate tetrahedral environments (P1 and P2) present within the structure. Each of them bridges between two MnO_4F_2 octahedra via two μ^2-bridging oxygen atoms. Both phosphate tetrahedra have two terminal sites which

protrude into the inter-chain space. For the P1 unit, two terminal sites are occupied by one oxide and one fluoride ion, whilst in the P2 unit; the sites are all terminated by fluoride or hydroxide groups. Bond lengths for the two phosphate tetrahedra are shown in Table 4.6, two bridging P-O bonds exhibit very different lengths, 1.513(8) Å for P1-O2 bond, and 1.553(8) Å for P1-O5 bond; the elongation of the P1-O5 bond is possibly due to the tetragonally distorted Mn-octahedron, as the corner-sharing oxygen O2 and O5 are found to occupy the neighbouring Mn-octahedra at their equatorial and axial positions. The two terminal bonds P1-O1 and P1-F3 show similar bond lengths (1.537(7) Å and 1.529(7) Å). For the P2 unit, one of the terminal P-F bonds is elongated significantly (1.609(8) Å), compared to one that is similar in the P1 unit. The two bridging P-O are found to have similar lengths with average of 1.497 Å.

Table 4.7: *Bond valence calculations for selected atoms*

Atom label	Bond valence	Atom label	Bond valence
O1	2.02 -	F2	0.96 -
O2	1.88 -	F3	0.99 -
O3	1.92 -	F4	0.86 -
O4	2.09 -	F5	1.10 -
O5	1.41 -	Mn1	3.04 +
F1	1.00 -		

There are two crystallographically distinct sodium ion coordination environments present within the structure, including the NaO_3F_2 and NaO_4F_2, form irregular geometries. All Na-F and Na-O bonds within the two Na^+ sites are less than 3 Å, in the range of 2.34-2.86 Å respectively. The shortest Na-Na separation distance is 3.72 Å. An SEM image of the compound **II** crystals was recorded and is shown in Figure 4.5.

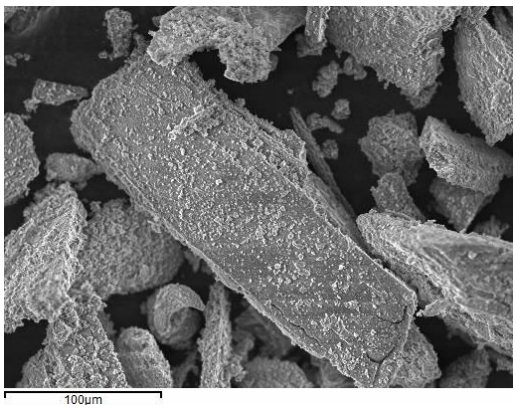

Figure 4.5: *SEM image of $Na_2MnF_2(PO_3OH)(PO_2F_2)$ crystals*

4.3 Compound III: $Li_3MnF_2(PO_3F)_2$

The product crystallised as brown coloured hexagonal shaped crystals. One suitable crystal was selected for a single crystal X-ray diffraction study and data were collected at 120 K, with the resulting crystallographic information summarised in Table 4.8. The structure of compound **III** possesses a monoclinic unit cell with space group $P2_1/c$ and forms a two-dimensional structure. The key bond lengths are summarised in Table 4.9.

The structure of compound **III** can be described as comprising two-dimensional layers running parallel to the *b*- and c-axis. Each layer is built up from alternating manganese centred octahedra and phosphate tetrahedra (Figure 4.6). Manganese centred octahedron within the polyhedral layer shares all four oxygen atoms with four phosphate units, with the two terminal sites being assigned as fluoride anions and oriented toward the inter-layer regions. Each phosphate tetrahedron bridges a pair of octahedra through corner-sharing two μ^2-bridging oxygen atoms. Full tetrahedral coordination is completed by terminal oxide and fluoride ions, with the oxide ion being orientated into the interlayer space. The polyhedral layer can also be seen as made up of eight-membered rings, based on four Mn-centred and P-centred polyhedra (Figure 4.6 b). The layers are separated by Li cations with inter-layer distance around 3 Å.

Only one independent manganese coordination environment exists in the structure of compound **III**. Each Mn-octahedron is six-coordinate, with four bridging oxygen atoms to the phosphate groups, and two terminal fluorine atoms. The Mn coordination, as expected, shows a Jahn-Teller distortion, resulting in bond elongation of axial Mn-O bonds, with a mean length of 2.168 Å. The equatorial Mn-O and Mn-F bonds display shorter bond lengths with averages of 1.91 Å and 1.863 Å. Again the terminal Mn-F bond has the shortest bond length, this fits the trend observed previously with regards to Mn-X (X = O, F) bond lengths within the manganese coordinations. BV analysis has been carried out on the Mn cation yielding a calculated value of 3.1 (Table 4.10), which supports the +3 oxidation state of the Mn ion.

Table 4.8: *Crystal and diffraction information for compound III*

Empirical formula	$Li_3MnF_4P_2O_6$
Formula weight ($gmol^{-1}$)	309.70
Temperature (K)	120
Appearance	Brown hexagon
Crystal size (mm)	0.13 × 0.03 × 0.02
Crystal system	Monoclinic
Space group	$P2_1/c$
Unit cell dimensions	a=6.333(5) Å, b=7.395(5) Å c=7.575(5) Å, β=90.947(11)^o
λ/Å	0.71073 Å (Mo K_α)
Volume ($Å^3$)	354.69 (4)
Z	2
Density (gcm^{-3})	2.900
Reflections collected	3914
Unique reflections	1183
R_1 (all)	0.0305
wR_2 (all)	0.0726
GooF	1.058

Table 4.9: *Bond lengths between selected atoms*

Bond	Bond length (Å)	Bond	Bond length (Å)
Mn1-O3	2.168(3) × 2	P1-O2	1.481(3)
Mn1-O1	1.910(3) × 2	P1-O3	1.507(3)
Mn1-F2	1.863(2) × 2	P1-O1	1.534(3)
		P1-F1	1.567(3)

Table 4.10: *Bond valence calculations for selected atoms*

Atom label	Bond valence	Atom label	Bond valence
O1	2.07 -	F2	1.05 -
O2	1.88 -	F1	1.03 -
O3	1.92 -	Mn1	3.10 +

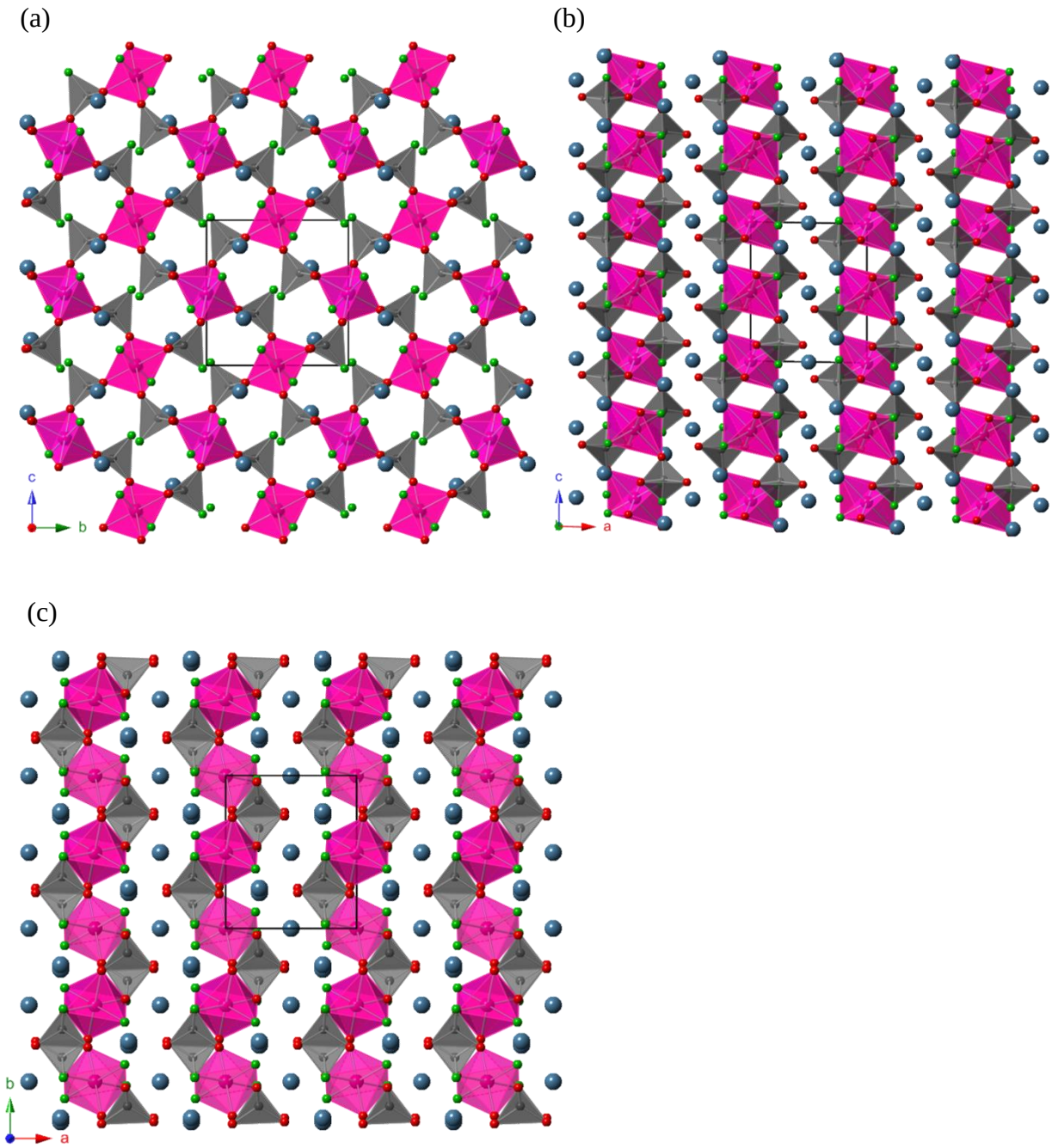

Figure 4.6*: The structure of $Li_3MnF_2(PO_3F)_2$ viewed down the (a) a-, (b) b-, (c) c-crystallographic axes, with the Mn^{III} octahedra in pink, fluorophosphate tetrahedra in grey, oxygen atoms in red, fluorine atoms in green, Li^+ cations in blue colour.*

There is one crystallographically unique phosphate tetrahedral unit (P1) present within the structure of compound **III**, which bridges a pair of Mn centred octahedra through two μ^2-bridging oxygen atoms, with two vertexes terminated and orientated into the inter-framework space. Within the phosphate tetrahedron, the P-F bond is clearly elongated and shows a bond length of 1.567(3) Å, whilst the terminal P-O bond is the shortest (1.481(3) Å). The two bridging P-O bonds fit the trend observed for

previously described compound **II**, the longer bond of P1-O1 (1.534(3) Å) than the P1-O3 bond (1.507(3) Å) is due to the arrangement of linked polyhedral units. The bond angles within the phosphate tetrahedron do not deviate substantially from the expected tetrahedral value of ~109.28^{o}, with all angles are found in the range around103.2^{o}-116.3^{o}.

The lithium cations which reside in the channels have two distinct environments including: LiO_3F_2 and LiO_4F_2. The former one forms a distorted square-based pyramid, with two long Li-F and Li-O bonds and three short bonds. The latter, LiO_4F_2, forms a distorted octahedral geometry, again with two elongated Li-O bonds compared to others. The observed Li-O and Li-F bond lengths within the two Li-coordinations are between of ~1.86 Å to ~2.27 Å, and Li^+ ion separations are at ~2.83 and ~3.39 Å respectively. An SEM image was collected for compound **III** and is shown in Figure 4.7.

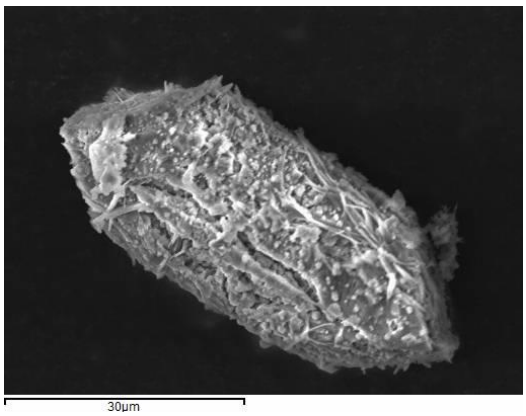

Figure 4.7: *SEM image of $Li_3MnF_2(PO_3F)_2$ single crystal, with fibrous surface*

4.4 Compound IV: $NaFe(PO_3F)_2$

The product crystallised as brown columnar crystals. One suitable crystal was selected for a single crystal X-ray diffraction study and data were collected at 120 K, with resulting crystallographic information summarised in Table 4.11. The structure of the compound **IV** possesses monoclinic unit cell with space group $P2_1/c$ and forms a three-dimensional framework, (Figure 4.8). Key bond lengths are summarised in Table 4.12.

The structure of the compound **IV** can be described as built up from four- and eight-membered rings. Each four membered ring is made up with two FeO_6 octahedra and two PO_3F tetrahedra, which are linked through corner-sharing of four μ^2-bridging oxygen atoms to produce a ladder topology. The PO_3F tetrahedra are orientated such that the ring spaces are lined by F-atoms. The assignment of the terminating fluorine atom is confirmed by BV calculations (Table 4.13). Each eight membered ring is based on four Fe-octahedra and four PO_3F tetrahedra. These polyhedral rings then extend along the three crystallographic axes resulting in the three-dimensional framework, with channels created down the *a*-axis, and filled with sodium cations.

The iron cation site in the structure of compound **IV** only possesses a single crystallographic octahedral environment. Within the FeO_6 octahedron, all six oxygen atoms bridge to form part of the neighbouring phosphate groups. BV calculation (Fe = 3.06) indicates that the oxidation state of the Fe centre within the FeO_6 octahedron is +3. Closer examination of the Fe coordination environment showed the octahedron can be regarded as almost regular. The O-Fe-O angles observed within the octahedron are close to 90^o, and all six Fe-O bonds very similar bond lengths, with an average of 2.004 Å, which is in good agreement with the sums of the Shannon crystal radii (Fe-O = 1.95 Å).[10]

There are two crystallographically independent phosphate tetrahedral environments present within the structure, represented as P1 and P2. Each of the phosphate tetrahedra bridges to three adjacent FeO_6 octahedra, through corner-sharing three μ^2-bridging oxygen atoms. The fourth terminal vertex in each phosphate tetrahedron is assigned as fluoride anions. The bond lengths within both P1 and P2 tetrahedral units show a noticeably elongation of the P-F bonds with lengths in the range of 1.596(1)-1.556(2) Å, compared to bridging P-O bonds which are all similar, lying within the 1.490(1)-1.512(1) Å range. The observed bond angles within the P1 unit are between ~105.7 ^{o} to

~116.1°, for the P2 unit the angles lie in the range of ~106.3-114.8°; in contrast with the idealised tetrahedral 109.28°, the P1 and P2 units are distorted from the regular geometry.

Table 4.10: *Crystal and diffraction information of compound IV*

Empirical formula	$NaFeP_2O_6F_2$
Formula weight ($gmol^{-1}$)	274.78
Temperature (K)	120
Appearance	Brown column
Crystal size (mm)	0.12 × 0.08 × 0.03
Crystal system	Monoclinic
Space group	$P2_1/c$
Unit cell dimensions	a=6.474(3) Å, b= 14.238(8) Å c=5.476(3) Å, β=95.86(14)°
λ/Å	0.71073 Å (Mo K_α)
Volume ($Å^3$)	593.79(1)
Z	2
Density (gcm^{-3})	1.76
Reflections collected	6129
Unique reflections	3340
R_1 (all)	0.1011
wR_2 (all)	0.2623
GooF	1.23

Table 4.11: *Bond lengths between selected atoms*

Bond	Bond length (Å)	Bond	Bond length (Å)
Fe1-O1	2.021(1)	P1-O5	1.509(1)
Fe1-O2	2.040(2)	P1-O6	1.495(1)
Fe1-O3	2.081(3)	P1-F2	1.596(1)
Fe1-O4	1.983(1)	P2-O1	1.490(1)
Fe1-O5	1.956(1)	P2-O2	1.496(1)
Fe1-O6	1.946(3)	P2-O4	1.505(1)
P1-O3	1.512(1)	P2-F1	1.556(2)

.

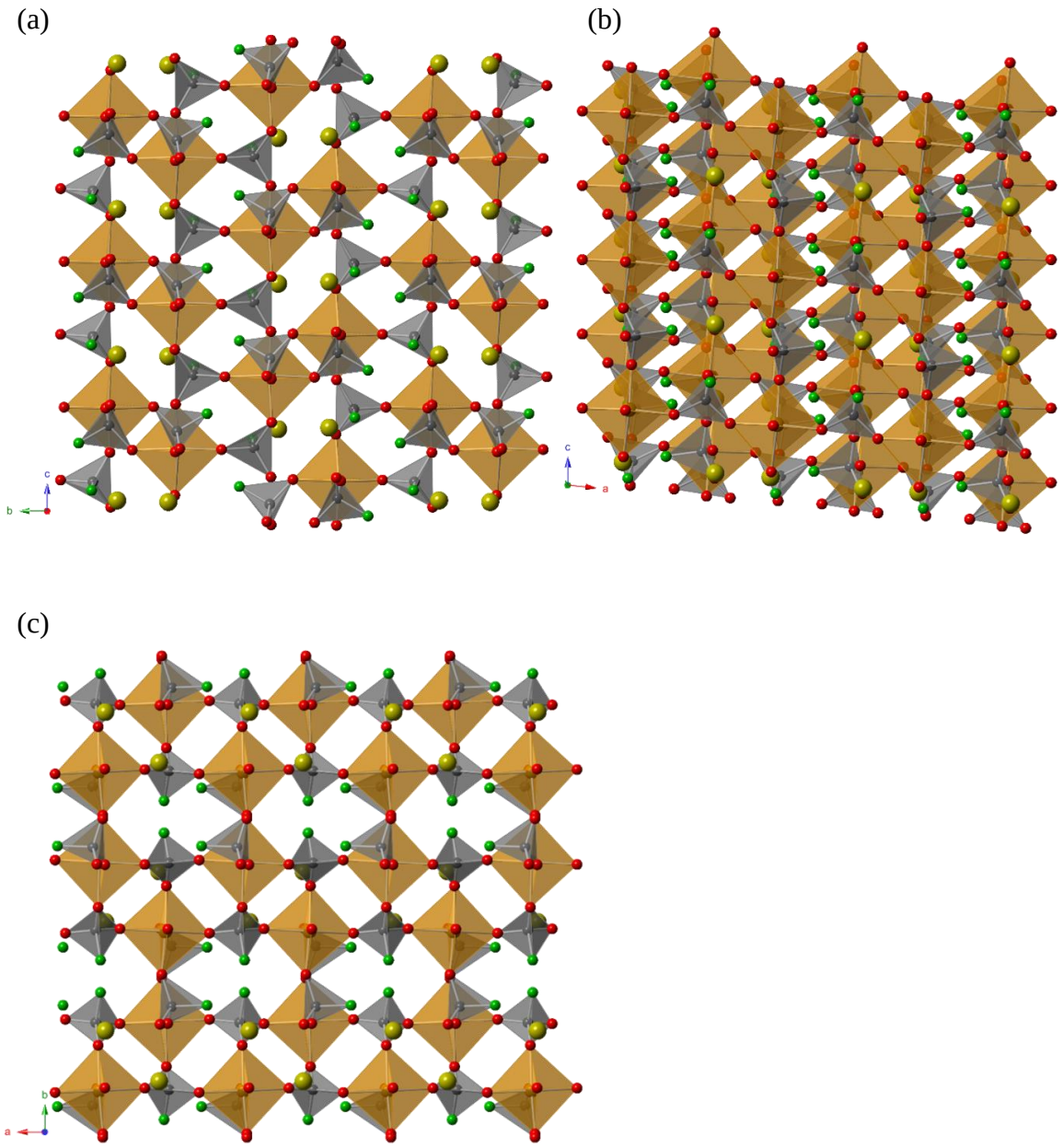

Figure 4.8*: The structure of $NaFe(PO_3F)_2$ viewed down the (a) a-, (b) b-, (c) c-crystallographic axes, with the Fe octahedra are shown in yellow-brown, phosphate tetrahedra in grey, oxygen atoms in red, fluorine in green and sodium cations in yellow.*

Table 4.12: *Bond valence calculations for selected atoms*

Atom label	Bond valence	Atom label	Bond valence
O1	2.07 -	O6	1.97 -
O2	2.05 -	F1	0.96 -
O3	1.99 -	F2	1.04 -
O4	1.91 -	Fe1	3.06 +
O5	1.96 -		

One Na^+ ion coordination is present within the Compound **IV**, consisting of $Na(O_4F_1)$ with an irregular geometry. The bond lengths found in the range of ~2.32-2.83 Å, which are typical Na-X (X=O, F) bond lengths. The sodium ion separation is 3.312 Å. An SEM image was recorded during the EDS data collection and is shown in Figure 4.9. EDS analysis showed the presence of Na (8.8 %), Fe (8.9 %), P (17.1 %), F (18.7 %), O (46.5 %), gives an experimental atomic ratio of 0.98:1:1.9:2.1:5.2, that is in approximate agreement with the theoretical ratios of 1:1:2:2:6.

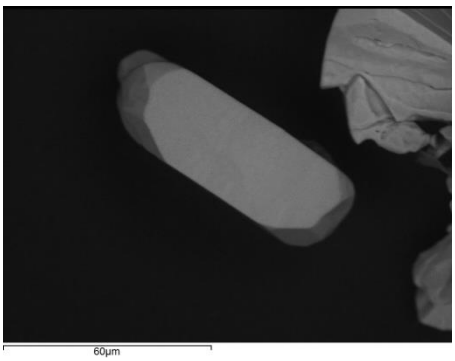

Figure 4.9: *SEM image of $NaFe(PO_3F)_2$ single crystal*

4.5 Compound V: $(NH_4)_2Mn_2F(PO_3F)_2Cl_2$

Single crystal X-ray diffraction of a suitable crystal of Compound **V** was carried out on a Rigaku FR-E+ VHF Diffractometer. The selection of a suitable crystal for the diffraction study was performed with the sample under oil using a stereo microscope. SXD data were collected at 120 K, with the resulting crystallographic information summarised in Table 4.13. Compound **V** crystallised as pink needle crystals and is isostructural to the $(NH_4)_2Fe_2(PO_3F)_2FCl_2$,[8] whose structure has previously been published. The structure contains mixed valence manganese, and it is the first reported framework structure containing both Cl^- and F^- anions. The structure of compound **V** has an orthorhombic unit cell with space group *Pba*2, which is built up of manganese centred octahedra and phosphate tetrahedra to form a three-dimensional framework with narrow channels (Figure 4.10). Key bond lengths are summarised in Table 4.14.

The structure of compound **V** shows the features of mixed valence manganese, and contains both chloride and fluoride anions in the framework. The structure is made up of manganese-centred octahedral sheets and chains bridged by phosphate groups resulting in a tightly packed three-dimensional network along all three axes. Small cavities are visible along the *a* and *c* crystallographic axes. Within the structure, $Mn^{II}O_2Cl_4$ octahedra are linked together through corner-sharing of four chloride ions to form an infinite sheet consisting of four-membered rings running along the *ab*-lattice plane, while the *trans*-$Mn^{III}O_4F_2$ octahedra are connected to each other through *trans*-fluoride and form "*zig-zag*" chains running parallel to each other along the *b*-axis (Figure 4.10). These sheets and chains are then linked through phosphate tetrahedra via three μ^2-bridging oxygen atoms and each phosphate tetrahedron has one terminal group that is orientated towards the open regions of the framework. The octahedra and tetrahedra alternate as corner-sharing units and form five-membered rings running along the *b*-axis. The cavity created by the ring has a maximum diameter of ~4.8 Å. NH_4^+ cations occupy the narrow channels formed between the $Mn^{II}O_2Cl_4$ octahedra based sheet and the bridging $Mn^{III}O_4F_2$ octahedral chains.

Table 4.13: *Crystal and diffraction information of compound V*

Empirical formula	$N_2H_8Mn_2P_2O_6F_3Cl_2$
Formula weight ($gmol^{-1}$)	431.4
Temperature (K)	120
Appearance	Pink needle
Crystal size (mm)	0.175 × 0.025 × 0.025
Crystal system	Orthorhombic
Space group	*Pba*2
Unit cell dimensions	a=14.630 (1) Å, b=7.150(3) Å c=10.698 (5) Å, $\alpha=\beta=\gamma=90^o$
λ/Å	0.71073 Å (Mo K_α)
Volume ($Å^3$)	1118.95(2)
Z	4
Density (gcm^{-3})	2.563
Reflections collected	3753
Unique reflections	1728
Flack parameter	0.59(3)
R_1 (all)	0.0319
wR_2 (all)	0.0899
GooF	1.039

Table 4.14: *Bond lengths between selected atoms*

Bond	Bond length (Å)	Bond	Bond length (Å)
Mn1-O2	2.006(5)	Mn2-O5	2.058(5)
Mn1-O3	1.983(5)	P1-O1	1.501(5)
Mn1-O6	1.970(4)	P1-O2	1.519(4)
Mn1-O7	1.960(4)	P1-O3	1.521(4)
Mn1-F1	1.965(3) × 2	P1-F3	1.591(2)
Mn2-Cl1	2.531(8)	P2-O5	1.485(5)
Mn2-Cl2	2.590(2) × 2	P2-O6	1.519(4)
Mn2-Cl3	2.542(9)	P2-O7	1.523(4)
Mn2-O1	1.989(5)	P2-F2	1.585(5)

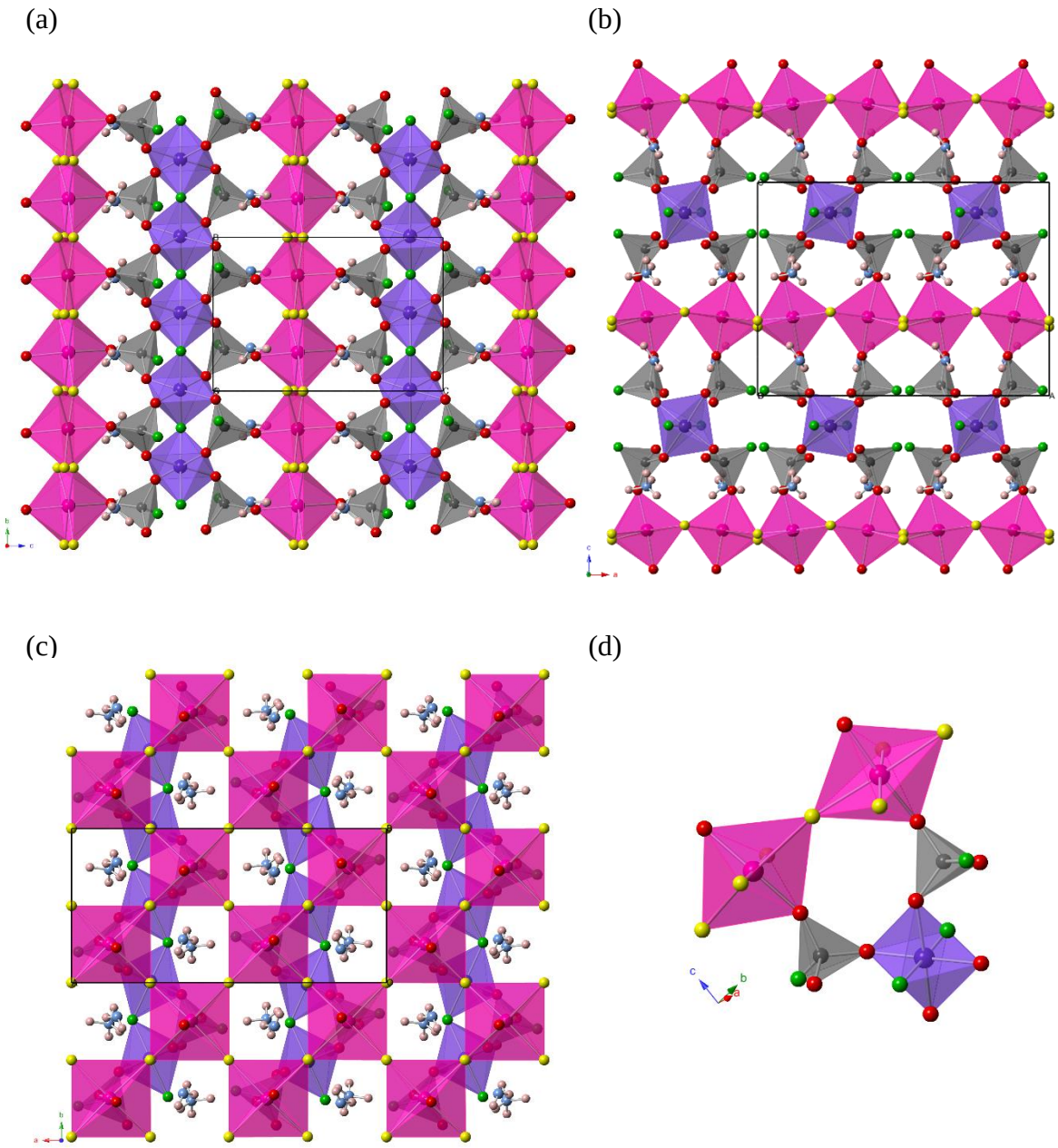

Figure 4.10*: The structure of $(NH_4)_2Mn^{(II)}Mn^{(III)}(PO_3F)_2FCl_2$ viewed down the (a) a-, (b) b-, (c) c-crystallographic axes, with the Mn^{II} octahedra are in pink, Mn^{III} octahedra are in purple, phosphate tetrahedra in grey, oxygen in red, fluorine in green, chlorine in yellow, nitrogen in sky blue, hydrogen in pale pink. (d) shows the five membered ring formed by two Mn^{II} octahedra, two phosphate tetrahedra and one Mn^{III} octahedron.*

The two manganese coordinations found within the structure are $Mn^{II}O_2Cl_4$ and $Mn^{III}O_4F_2$, each of them forms a crystallographically unique octahedral environment. In the $Mn^{II}O_2Cl_4$ site, the manganese centre coordinates with four chlorines at equatorial positions and two oxygen at axial positions to form a distorted octahedral coordination geometry. The bond lengths within the $Mn^{II}O_2Cl_4$ octahedron are given in Table 4.14.

The observed bond lengths are similar for all Mn-Cl bonds, lying in the range of 2.531(8)-2.590(2) Å, which in a good agreement with the sum of the Shannon crystal radii (Mn^{II}-Cl = 2.48 Å).[10] The lengths of the axial Mn-O bonds are quite typical with an average length of 2.024 Å. Within the *trans*-$Mn^{III}O_4F_2$ octahedron, the manganese centre coordinates to six anion sites and forms an almost regular octahedral geometry. The lengths for Mn-O and Mn-F bonds are close in value, the average bond length of all six bonds within the $Mn^{III}O_4F_2$ octahedron is 1.975 Å. The deduced oxidation states for manganese in the $Mn^{III}O_4F_2$ octahedron is +3 and for $Mn^{II}O_2Cl_4$ octahedron is +2, this was established by the consideration of bond lengths within each octahedron and in combination with BV calculations shown in Table 4.15. Although the manganese ion adopts +3 oxidation state in the $Mn^{III}O_4F_2$ octahedron, such coordination is not, or only weakly, subject to the Jahn-Teller effect, unlike the previously observed Mn^{III} octahedral species. Both Mn octahedra within the structure are fully coordinated to the neighbouring units through sharing of their apical chloride, oxide or fluoride anions.

Compound **V** contains two independent phosphate tetrahedral environments. Each of them bridges two adjacent MnO_4F_2 octahedra and one MnO_2Cl_4 octahedron through three μ^2-bridging oxygen atoms. Two of the μ^2-bridging oxygen occupy an equatorial position of MnO_4F_2 octahedra and one at the axial position of MnO_2Cl_4 octahedron. The fourth vertex within each tetrahedron is terminated by a fluoride group, and point into the open space. Consideration of the bond lengths given in Table 4.14 shows that, the terminal P-F bonds within in the two tetrahedral units are noticeably elongated with lengths of 1.585(5) Å and 1.591(2) Å. The bridging P-O bonds within the two tetrahedral units are close in length, being in the 1.485(5)-1.523(4) Å range.

Table 4.15: *Bond valence calculations for selected atoms*

Atom label	Bond valence	Atom label	Bond valence
O1	1.91 -	F2	0.96 -
O2	1.92 -	F3	0.90 -
O3	1.86 -	Mn1	2.91 +
O4	1.89 -	Mn2	2.13 +
O5	1.89 -	Cl1	1.01 -
O6	1.90 -	Cl2	1.02 -
F1	1.02 -	Cl3	0.98 -

As mentioned above, there are ammonium cations present in the narrow channels of the structure. The ammonium hydrogen atoms within the NH_4 were only partly found from the SXD data, due to the very low electron density of hydrogen. Although all oxygen atoms within the structure are fully coordinated, there are still hydrogen-bonding interactions between the NH_4^+ cations and the inorganic framework oxygen atoms. The distances found for O…N donor-acceptor are in the range of ~2.95-3.04 Å, which are reasonable lengths for N-H…O bonds. This suggests weak N-H…O hydrogen bonds are present within the framework.

4.6 Compound VI: $(NH_4)Mn_3(PO_3F)_2(PO_2F_2)F_2$

A single crystal diffraction study of the compound **VI** was carried out on a Rigaku FR-E+ UHF diffractometer. The SXD data were collected at 280 K. Compound **VI** crystallised as pale pink column crystals and is structurally related to the $AMn_3(PO_3F)_2(PO_2F_2)F_2$ (A=K, Rb).[4] The crystallographic information is summarised in Table 4.16. The structure of compound **VI** possesses monoclinic unit cell with space group *C2/c*, forming three-dimensional framework with channels (Figure 4.11). Key bond lengths are summarised in Table 4.17.

The structure contains triplets of manganese-centred octahedra linked by PO_3F tetrahedra, through corner-sharing of $1 \times \mu^3$- and $2 \times \mu^2$-bridging oxygen atoms to form a two-dimensional layer running along the crystallographic [010] direction. The polyhedral layers are further cross-connected by PO_2F_2 tetrahedra over sharing of apical oxygen with neighbouring manganese centred octahedra to constitute the three-dimensional framework with pores in the *ab*-plane and occupied by ammonium cations. The triplet building unit consists of a central *trans*-MnO_4F_2 octahedron that shares two adjacent faces with another two identical *trans*-MnO_4F_2 octahedra. The *trans*-MnO_4F_2 octahedra at both ends of the triplets are corner-sharing with other octahedra through *trans*-fluoride in the same plane to form chains along the *c*-axis. Two adjacent chains are bridged by face-sharing MnO_4F_2 octahedra that make up the triplets.

The structure of compound **VI** comprises two crystallographic distinct manganese coordination environments, both of them form common octahedral geometry with manganese coordinating to four oxygen and two fluorine atoms. As mentioned previously the manganese octahedra form a triplet building unit through sharing faces. Within the triplet, the central MnO_4F_2 octahedron has six bridging Mn-X (X=O, F) bonds of very similar in length (2.136(2)-2.185(2) Å). The O-O, O-F distances along the edges of the shared faces of this octahedron are much shorter (~2.74-2.78 Å) than the corresponding distances along the unshared edge (~3.27 Å), therefore the octahedron is strong trigonally distorted with a local symmetry of D_{3d}. The two octahedra at the ends of the triplets are identical. The geometric environment is six-coordinate with four oxygen and two fluorine atoms forming trigonally distorted geometry which is similar to the central octahedral unit. However, the Mn-X (X = O, F) bonds involved in bridging to the adjacent octahedron are longer, with an average distance of 2.239 Å

compared to 2.097 Å for the others. The Mn cation in this octahedron shares a face with the central Mn centred octahedron in the triplet and is presumably repelled and resulting in shift of the terminal Mn ion towards the unshared faces. The polyhedra triplet found within compound **VI** is very similar to that of hematite α-Fe_2O_3.[11] Bond valence sums of the two Mn atoms in MnO_4F_2 are 2.004 Å and 2.039 Å. These values are consistent with the oxidation states for all Mn centres of +2.

Table 4.16: *Crystal and diffraction information for compound VI*

Empirical formula	$Mn_3F_6P_3O_8NH_4$
Formula weight ($gmol^{-1}$)	517.76
Temperature (K)	280
Appearance	Pale pink column
Crystal size (mm)	0.15 × 0.09 × 0.05
Crystal system	Monoclinic
Space group	*C2/c*
Unit cell dimensions	a=20.428(1) Å, b=7.633(4) Å c=7.783(4) Å, β=103.5(10)^o
λ/Å	0.71073 Å (Mo K_α)
Volume ($Å^3$)	1180.01(2)
Z	4
Density (gcm^{-3})	2.892
Reflections collected	7904
Unique reflections	2351
R_1 (all)	0.0227
wR_2 (all)	0.0733
GooF	0.98

Table 4.17: *Bond lengths between selected atoms*

Bond	Bond length (Å)	Bond	Bond length (Å)
Mn1-O1	2.222(2)	Mn2-F3	2.139(1) × 2
Mn1-O2	2.104(2)	P1-O4	1.485(2)
Mn1-O3	2.217(2)	P1-F2	1.577(2)
Mn1-O4	2.083(2)	P2-O1	1.514(2)
Mn1-F3	2.279(2) × 2	P2-O2	1.506(2)
Mn2-O1	2.136(2) × 2	P2-O3	1.514(2)
Mn2-O3	2.185(2) × 2	P2-F1	1.573(2)

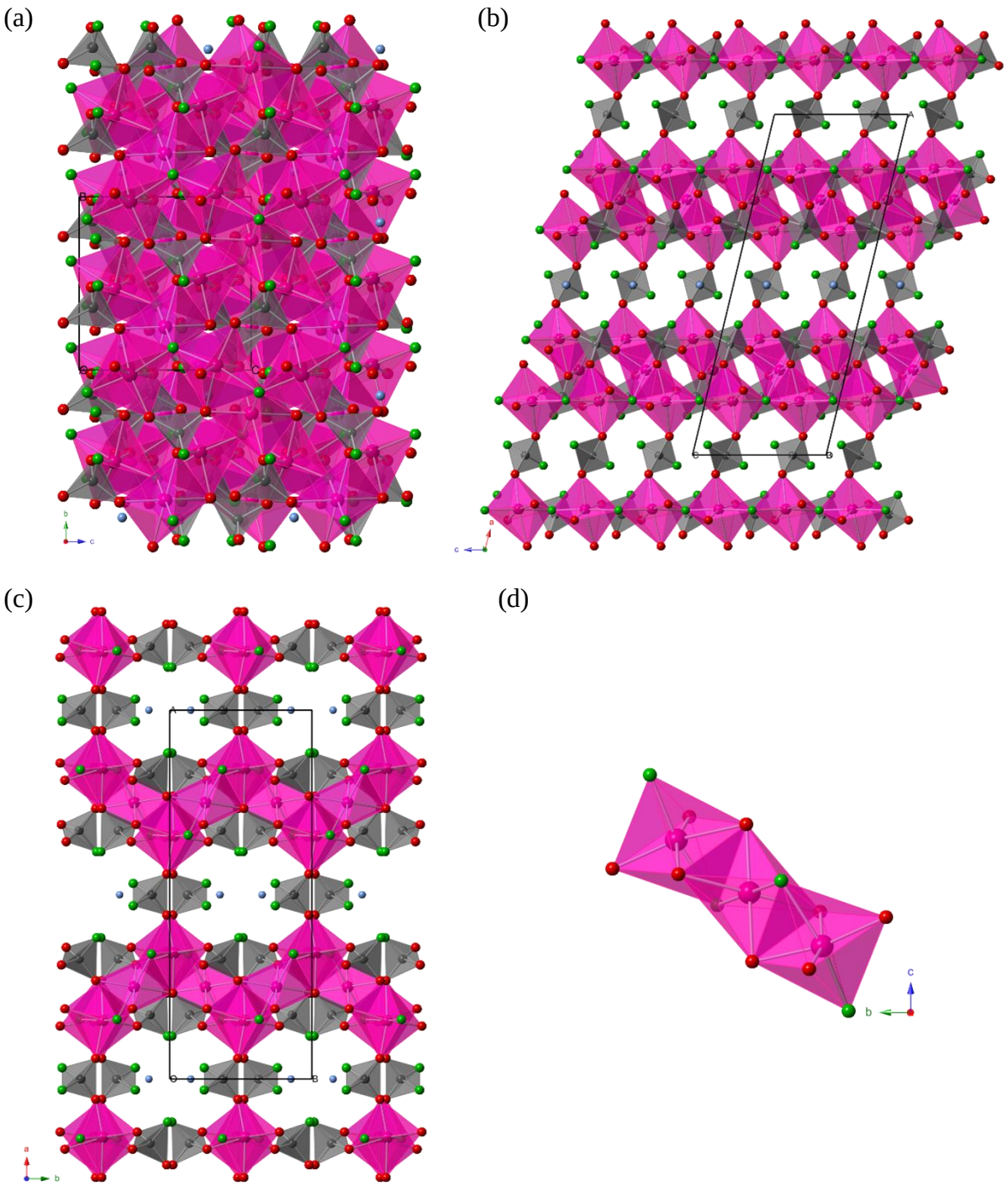

Figure 4.11: *The structure of $(NH_4)Mn_3(PO_3F)_2(PO_2F_2)F_2$ viewed down the (a) a-, (b) b-, (c) c-crystallographic axes, with the manganese octahedra are shown in pink, phosphate tetrahedra in grey, oxygen in red, fluorine in green, nitrogen in sky blue, hydrogen in pale pink. (d) Shows the manganese octahedral triplet within the structure*

Table 4.18: *Bond valence calculations for selected atoms*

Atom label	Bond valence	Atom label	Bond valence
O1	1.95 -	F2	0.85 -
O2	1.74 -	F3	0.90 -
O3	1.93 -	Mn1	2.00 +
O4	1.79 -	Mn2	2.04 +
F1	0.87 -		

The two distinct phosphate tetrahedra within compound **VI** are PO_3F and PO_2F_2. The PO_3F tetrahedra are connected to the neighbouring manganese triplets through vertex-sharing of two μ^2-bridging oxygen and one μ^3-bridging oxygen to form the two-dimensional layer, the fourth vertex within the tetrahedra is terminal and assigned as a fluoride group, this was determined by comparing the ADP values of this terminal site to the bridging oxygen as when assigned as fluoride it produces a similar ADP value to all other anion sites, this was further confirmed by BV calculations. The two-dimensional polyhedra layers are cross-linked by the second tetrahedra through sharing of two apical oxygen atoms, the third and fourth vertexes within the tetrahedra are terminal and confirmed to be fluoride groups. The PO_2F_2 tetrahedra are orientated such that the fluoride groups are pointed to the open space of the pores. From the key bond lengths list in Table 4.17, the P-F bonds in both tetrahedra are found to be elongated at 1.573(2) Å for PO_3F tetrahedron and 1.577(2) Å for PO_2F_2 tetrahedron. The P-O bonds within PO_3F tetrahedron have similar lengths (1.506(2)-1.514(2) Å). The PO_2F_2 tetrahedra have two P-O bonds involved in bridging to the manganese octahedra and have the same length of 1.487 Å(2).

The two-dimensional layers are cross-linked by PO_2F_2 tetrahedra to form the 3-dimensional framework consisting of pores along the *bc*-plane, and these pores are filled with ammonium cations. It was not possible to locate the hydrogen positions partly because the diffraction study of compound **VI** was carried out at room temperature and the ammonium ions likely to be subject to large torsional displacement units. Therefore nitrogen atoms were used to represent the ammonium cations for clarity. The ammonium cations found in the pores are held in place by forming hydrogen bonding interactions with the polyhedral oxygen atoms of the framework as shown in Figure 4.12. The distances found for O…N and F…N donor-acceptor are around 3.0 Å, which are reasonable lengths for N-H…O and N-H…F interactions. This suggests that

hydrogen-bonding interactions are present between the anionic inorganic framework and the ammonium cations.

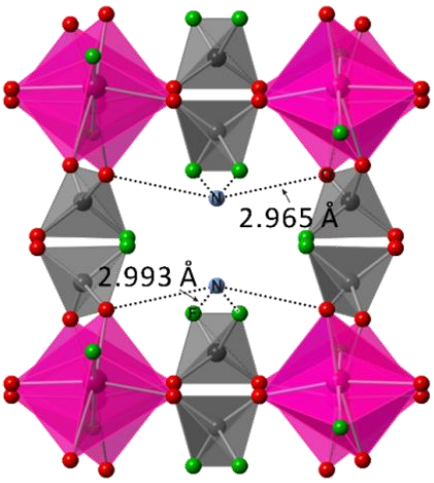

Figure 4.12: *Hydrogen bonding in compound VI for the ammonium cations in pores.*

The IR spectrum (Appendix 2) of compound **VI** shows a broad absorption band at 3500-2900 cm^{-1}, due to the stretching mode of the N-H bonds within the ammonium cations, though this occurs at a relatively low energy because of the weak hydrogen bonding. The TGA data of compound **VI** is depicted in Figure 4.13. The sample was heated in air in a temperature range of 25-700 ^{o}C. A gradual mass loss is observed (4 %) within the temperature range 100 – 300 ^{o}C, this was considered to be due to 1 mole of ammonium being lost from crystal structure, the mass loss percentage is comparable to the calculated 3.5 %. A further rapid mass loss is observed on heating over 300 ^{o}C, which was attributed to the departure of fluorine containing species, and is consistent with structural collapse. The DTA trace shows exothermic peaks after 450 ^{o}C, suggesting structural changes occur. An SEM image of a single crystal was recorded and is displayed in Figure 4.14.

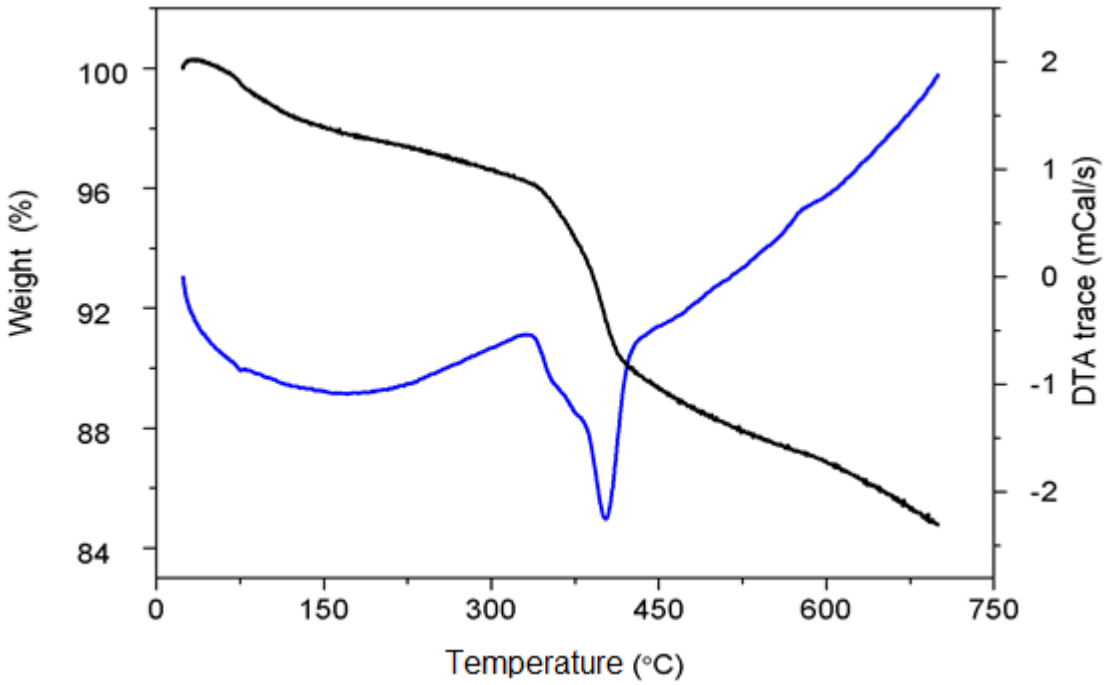

Figure 4.13: *TGA plot for the thermal decomposition of VI. Black and blue lines represented the TGA and DTA data as a function of temperature respectively.*

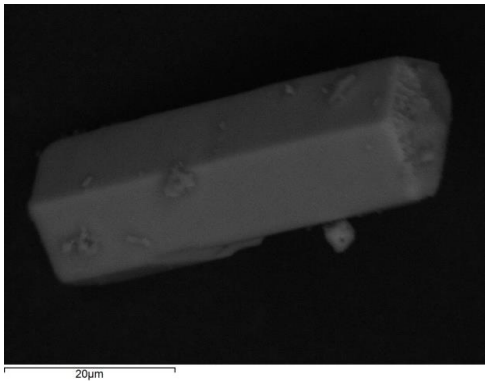

Figure 4.14: *SEM image of $(NH_4)Mn_3(PO_3F)_2(PO_2F_2)F_2$ single crystal*

4.7 Compound VII: $Li_5(VOF)_3(PO_4)_3 \cdot 4H_2O$

Compound **VII** crystallised as dark green platy crystals. One suitable crystal was selected for a single crystal X-ray diffraction study and data were collected at 120 K, with the resulting crystallographic information summarised in Table 4.19. The compound possesses a triclinic unit cell with space group $P2_1/c$ and forms a two-dimensional layered structure, which is based on the vanadium octahedra and phosphate tetrahedra. Key bond lengths are summarised in Table 4.20.

The crystal structure of compound **VII** is depicted from three different viewpoints in Figure 4.15. The structure is formed by layers of alternating VO_5F octahedra and PO_4 tetrahedra linked together to form a square network. A similar polyhedral layer in the form of a square network has been previously reported,[12] but instead the vanadium site is five-coordinate as VO_5 in a square pyramidal environment. Within the structure of the title compound, each vanadium centre is coordinated with five oxygen atoms and one fluorine atom to form a strongly distorted octahedron. The octahedra are repeatedly connected in the *bc*-plane by phosphate tetrahedra via corner-sharing of four oxygen atoms in each of the PO_4 tetrahedron thereby constructing a square network polyhedral layer. These alternating connected polyhedra form four-membered rings, which consist of two VO_5F octahedra and two PO_4 tetrahedra. The separation distance between each layer is approximately 4.4 Å, and the space is occupied by Li^+ cations and the non-bonded water molecules.

The structure of compound **VII** shows the features of mixed valence vanadium, and three crystallographically independent vanadium environments (V1, V2 and V3) are found; all form similar distorted octahedra VO_5F. Within each octahedron, the four oxygen atoms at equatorial positions are bridging to the neighbouring phosphate groups, the bond lengths between the vanadium centres and equatorial oxygen are regular, with V-O bonds lengths ranging from 1.910(2) Å to 2.036(3) Å. The average V-O length are V1 = 1.939 Å, V2 = 2.022 Å and V3 = 2.015 Å respectively. The vanadium centred octahedra are significantly distorted; the vanadium atom in the octahedron is displaced towards one of the oxygen atoms. This leads to the formation of a characteristic short terminal vanadyl bond, the lengths of the V=O bonds are given for all three vanadium octahedra as: 1.587(3) Å for V1, 1.609(3) Å for V2 and 1.603(3) Å for V3, these are typical vanadyl bond lengths and agree with those reported previously in the literature.[13]

The V-F bond is at the opposite side of the vanadyl bond and is usually very long (2.110(2) Å for V1, 2.108(2) Å for V2, 2.114(2) for V3). The vanadium polyhedron appears as a strongly distorted octahedron derived from a square pyramid, with additional fluorine atom in the *trans* position to the double-bonded oxygen in square pyramid forming a relatively weak V-F bond. The trend of the bond lengths in VO_5F octahedron is very similar to that found in VO_6 octahedron reported previously.[13,14] The structural characteristics of vanadium leads to the construction of a layered structure. The distorted VO_5F octahedra share their coplanar oxygen with the PO_4 tetrahedra. The vanadyl groups alternate up and down, where the octahedral fluorine atoms are always terminal, and are oriented toward the inter-layer space. The obtained oxidation states for V2 and V3 are +4, and +5 for V1, these were supported by the BV calculations (Table 4.21)

Table 4.19: *Crystal and diffraction information of compound VII*

Empirical formula	$Li_5V_3F_3P_3O_{18}H_6$
Formula weight ($gmol^{-1}$)	631.48
Temperature (K)	120
Appearance	Dark green plate
Crystal size (mm^3)	0.5 × 0.05 × 0.025
Crystal system	Triclinic
Space group	$P\bar{1}$
Unit cell dimensions	a=7.778(6) Å, b= 8.953(7) Å, c=11.824 (9) Å α=99.2(7)°, β=90.03(6)°, γ=109.32(8)°
λ/Å	0.71073 Å (Mo K_α)
Volume ($Å^3$)	765.53
Z	1
Density (gcm^{-3})	2.15
Reflections collected	6884
Unique reflections	3456
R_1 (all)	0.0351
wR_2 (all)	0.1031
GooF	1.008

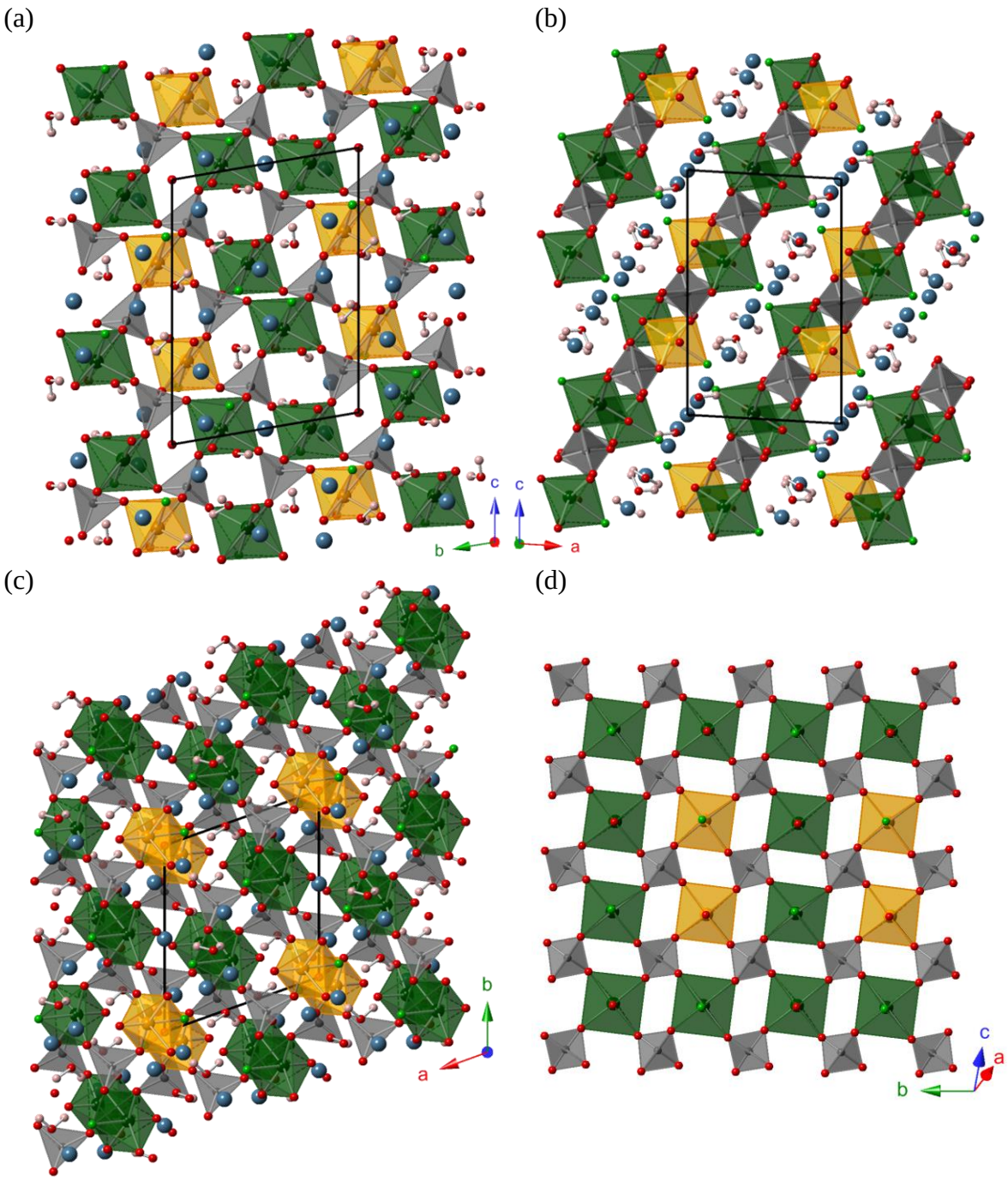

Figure 4.15: *Structure of $Li_5(VOF)_3(PO_4)_3{\cdot}4H_2O$ viewed down the (a) a-, (b) b-, (c) c-crystallographic axes, with the V^V octahedra in yellow-orange, V^{IV} octahedra in dark green, phosphate tetrahedra in dark grey, oxygen in red, fluorine in green and lithium in sky blue, oxygen for water molecule in purple for charily and hydrogen in pale pink. (d) shows a square network of alternating connected VO_5F and PO_4 polyhedra*

Table 4.20: *Bond lengths between selected atoms*

Bond	Bond length (Å)	Bond	Bond length (Å)	Bond	Bond length (Å)
V1-O4	1.930(2)	V2-O15	1.609(3)	P1-O9	1.523(3)
V1-O6	1.910(2)	V2-F1	2.108(2)	P1-O12	1.539(3)
V1-O8	1.979(3)	V3-O2	2.017(2)	P2-O7	1.529(3)
V1-O11	1.935(3)	V3-O5	2.010(3)	P2-O8	1.552(3)
V1-O14	1.587(3)	V3-O9	2.010(2)	P2-O10	1.526(3)
V1-F3	2.110(2)	V3-O12	2.024(3)	P2-O11	1.550(3)
V2-O1	2.007(3)	V3-O13	1.603(3)	P3-O2	1.533(3)
V2-O3	2.018(2)	V3-F2	2.114(2)	P3-O3	1.536(3)
V2-O7	2.026(3)	P1-O1	1.528(3)	P3-O4	1.565(3)
V2-O10	2.036(3)	P1-O6	1.560(3)	P3-O5	1.525(3)

Table 4.21: *Bond valence calculations for selected atoms*

Atom label	Bond valence	Atom label	Bond valence
O1	2.11 -	O12	1.95 -
O2	2.12 -	O13	1.66 -
O3	1.97 -	O14	1.74 -
O4	2.05 -	O15	1.62 -
O5	2.12 -	F1	0.60 -
O6	2.14 -	F2	0.59 -
O7	2.13 -	F3	0.57 -
O8	1.97 -	V1	4.78 +
O9	2.07 -	V2	4.25 +
O10	2.10 -	V3	4.30 +
O11	2.12 -		

Three crystallographically distinct phosphate tetrahedral environments were found within the structure. Each PO_4 tetrahedron bridges four VO_5F octahedra by sharing its four corners with the octahedra. These polyhedra then alternate to form a square network layer running parallel to the *b*-axis. Since the PO_4 units are fully coordinated, all O atoms are involved in bonding to vanadium centres. The bond lengths within the three PO_4 tetrahedra are quite similar, with P-O bond lengths ranging between 1.523(3) and 1.560(3) Å.

There are five lithium coordination sites represented as Li1, Li2, Li3, Li4 and Li5. Three lithium sites are six-coordinate and form irregular octahedra while two lithium sites are five-coordinate and form trigonal bipyramids. For Li1, Li2, Li5 sites, their

coordinations are formed by sharing two oxygen atoms with neighbouring water molecules, and two oxygen and two fluorine atoms with VO_5F octahedra, the Li-O and Li-F bond distances are between ~1.89 Å and ~2.26 Å, which applies for all lithium sites. The Li3 and Li4 are five-coordinate with three oxide ligands and two fluoride ligands shared with VO_5F octahedra and PO_4 tetrahedra along the polyhedral layer.

The material contains water molecules. The oxygen atoms of the water molecules were located directly from SXD data, however, the hydrogen positions were only assigned partly though the single crystal refinement, due to their weak scattering power. BV calculations show the terminal fluorine atoms within each VO_5F octahedron have low bond valence values, which are ascribed to the hydrogen bonding interactions gain from the water molecules and the octahedral terminal sites. The characteristic distances found for F…O donor-acceptor are in the range of ~2.53-2.86 Å. which are reasonable lengths for O-H…F bonds. This suggests relatively strong N-H…F hydrogen bonds are present within the structure.

4.8 General summary

A range of new transition metal fluorophosphate materials have been prepared directly from the hydrothermal method in fluoride-rich media, and resulted in successful incorporation of fluoride into the their structures as exemplified by seven new compounds presented in this chapter. All compounds were primarily characterised by single crystal X-ray diffraction and structures were fully solved. Materials were further characterised through IR spectroscopy, EDS analysis showed the existence of specific species within the material and TGA analysis was used to investigate the thermal stability of the material studied.

As concluded from the details given in Table 4.1, all synthesis were carried out under mild hydrothermal conditions. In order for single crystals to form, reaction temperatures of around 175 ^{o}C with period of 48 hours were generally required. The produced materials with structural dimensionalities included the one-dimensional chain structure (**II**), two-dimensional layered structures (**I**/**III**/**VII**) and three-dimensional frameworks (**IV**/**V**/**VI**). The new material structures incorporating fluoride have several features in common, the phosphate coordinations generally form tetrahedral environments with four oxygen or mixed anion sites (OH, F) present as part of the tetrahedra. The transition metals are found in octahedral coordinations with formula of $M(O,F)_6$ (M=V, Fe, Mn) for all the material structures presented in this chapter. The synthetic method previously used to prepare fluoride incorporated material usually employed HF solution as a fluoride ion source, but due to the extremely dangerous nature of HF, substitutions, such as the use of MF_3 (M=V, Fe, Mn), were chosen to provide a large quantity of fluorine in the reaction mixture. Additional HF may be used in some reactions for the purpose of increasing ion mobility without inclusion of unnecessary ions, but only at a low level (<0.05 mL). Oxide ions are often replaced by fluoride ions and incorporated as terminal species on metal polyhedra or phosphate tetrahedra to form the M-F or P-F bonds; due to such terminating effect, this breaks up the structures of further connection, thus lowering the structural dimensionality.[3] A similar behaviour was noticed in the earlier reported metal fluoride frameworks.[15] For the novel structures presented in this chapter, fluoride acting as terminal sites can be found in the seven new structures, and forms prevalent PO_3F units within the compounds **I**-**VI**, or more rarely the PO_2F_2 unit, as in compound **VI**. These tetrahedra form part of the connected polyhedral structures, with oxygen typically acting as

bridging units to metal ion sites and fluorine in a terminal position. Previously reported materials contain fluorophosphate tetrahedra within the structures are only known in a relatively few cases.[16, 17] The fluoride in metal octahedra is not just incorporated as terminal sites, but also acted as bridging species and generally located at *trans*-positions forming M-F-M linkages (M = transition metal ions), this can be seen in compounds **I** and **V**. Fluoride ions at bridging sites are normally μ^2, but more rarely μ^3-bridging fluoride have been reported.[18] The fluoride ions occupying terminal sites in the polyhedra units within the structures were generally found to be oriented toward open region and may form ionic interactions to counter-cations, for example as in compound **III**. The terminal fluoride ion carries lower charge compared to oxide ion within the framework, thus the ionic bonds created between terminal fluoride and counter-cation are expected to show relatively weak interactions. Therefore structures with channels or interlayer space lined by fluorides may provide facile pathways for small ion mobility, e.g. Li^+ or Na^+. The terminal fluoride may also form hydrogen bonds to protons on counter-cation such as NH_4^+, as in compound **VI**. In PO_3F tetrahedra, the terminal P-F bonds are significantly longer than the bridging P-O bonds to the metal ion sites.

The metal ion coordinations within structures across the seven new compounds are found to adopt the common octahedral environments. Most of these octahedra are distorted from the regular octahedron. Typically for the manganese centred octahedral units with an oxidation state of +3. The distortions of the manganese centred octahedra are often caused by the Jahn-Teller effect. This can be observed in compounds **VI** and **III**, where the manganese centred octahedra forms a triplet building unit, and typically each of them is subject to Jahn-Teller distortion. The distorted geometry caused by such effect typically shows an elongation of the axial Mn-O/F bond lengths, in contrast with the equatorial bonds in the octahedron. For example, in compound **III** the average axial Mn-O bond is 2.168 Å, compared with 1.886 Å of equatorial Mn-O/F bonds gives a difference of 0.28 Å. It can be noted in the same octahedron, the average Mn-O bonds are slightly longer than the Mn-F bonds, and this attributed to the smaller ionic radius of F^- compared to O^{2-}. However, this is not always the case. In compound **I**, the Mn-F bond occupied at axial positions which being elongated due to the Jahn-Teller effect, whereas the equatorial Mn-O bonds appears of shorter length. An elongated axial Mn-F bond in a Mn^{3+} coordination is less frequently observed, in comparison with the more preferred equatorial positions. In compound **V**, although one of the octahedra is centred

on manganese in a +3 oxidation state, its coordination geometry is almost regular octahedron with all six bonds close in length. This may arise from low spin d^4 manganese. There is one example which has been reported in the literature with the low spin d^4 manganese in an regular octahedron is the $K_4Mn(CN)_6$, where the average of six Mn-C bond length is 1.98 Å.[19]

The structure of compound **IV** is based on the alternating iron-centred octahedra and fluorophosphate tetrahedra, resulting in a ladder topology of three-dimensional framework. The iron centre adopting the +3 oxidation state and forming octahedral coordination with similar Fe-O bond lengths. The fluoride ions are again found to adopt the terminal sites on the phosphate unit.

Compound **VII** contains vanadium centred octahedra and PO_4 tetrahedra linked to produce a layered structure. The vanadium-centred octahedra were found to be very different from the manganese centred or iron centred octahedra, due to the short terminal vanadyl V=O bond formed; this especially has been observed previously in numerous compounds.[14, 20, 21] The vanadyl bond within the VO_5F octahedron has a bond length around 1.6 Å, and the opposite terminal V-F bond significantly longer than other bonds within the octahedron, at between 2.1-2.6 Å.[14] These structural characteristics of vanadium lead to the formation of many layered structures with layers composition of VOF (**VII)**. The co-planar oxygen atoms in the VO_5F octahedra are μ^2-bridging species. Compound **VII** shows at least one vanadium ion has an oxidation state of +5, where the other two remain as +4. Although they form similar coordinations, closer examination of V^VO_5F octahedron shows the bond lengths formed between metal centre and co-planar oxygen are slighter shorter than the V-O bonds within the V^{IV}O5F octahedra. Similar compounds with characteristic layered structure with Li^+ existing in the inter-layer space have not been reported previously in the literature. The related $Na_3(VO)_2(PO_4)_2F$ has been reported and studied as the positive-electrode for Na-ion battery and shows good electrochemical property with a potential voltage plateaux at 3.6-4.1 V *vs*. Na/Na^+.[22]

4.9 Conclusion

Seven new transition metal fluorophosphate have been produced directly through utilising hydrothermal route in fluoride-rich media. All compounds were characterised by SXD. The produced structures show the fluoride was successfully incorporated.

Notable structural features include that the fluoride was preferred as the terminal species or as bridging units between multiple metal centres. Other features of the fluorophosphates presented in this chapter are relevant to their possible applications. Studies in respect of optomagnetic properties would be of interest on Mn^{III} compounds, e.g. compound **I** can be used for energy storage application, compounds **III** and **VII** can be regarded as being possible positive-electrode materials, due to the formed layered structures with space between layers filled with Li^+ cations. It would be possible for Li^+ intercalation/deintercalation through electrochemical reactions in battery to produce Mn^{II} and Mn^{IV} (**III**) or V^{II}, V^{III} and V^{V} (**VII**) derivatives, similar to those that occur in Li_2MnPO_4F[2] and $LiVPO_4F$.[23] Further production and purification could be carried out on compound **VII,** and several of these compounds will be studied and tested in other research groups in the future.

4.10 References

1. B. Xu, D. N. Qian, Z. Y. Wang and Y. S. L. Meng, *Mater. Sci. Eng. R-Rep.*, 2012, **73**, 51-65.
2. B. L. Ellis, W. R. M. Makahnouk, W. N. Rowan-Weetaluktuk, D. H. Ryan and L. F. Nazar, *Chem. Mater.*, 2010, **22**, 1059-1070.
3. J. Rouse and M. T. Weller, *Dalton Trans.*, 2009, 10330-10337.
4. J. A. Armstrong, E. R. Williams and M. T. Weller, *J. Am. Chem. Soc.*, 2011, **133**, 8252-8263.
5. F. C. Hawthorne, *TMPM Tschermaks Petr. Mitt.*, 1983, **31**, 121-135.
6. M. Cavellec, D. Riou and G. Ferey, *J. Solid State Chem.*, 1994, **112**, 441-442.
7. F. C. Hawthorne, S. Krivovichev, V. and P. Burns, C., *Rev. Mineral. Geochem.*, 2000, **40**.
8. A. C. Keates, J. A. Armstrong and M. T. Weller, *Dalton Trans.*, 2013, **42**, 10715-10724.
9. J. A. Armstrong, E. R. Williams and M. T. Weller, *Dalton Trans.*, 2013, **42**, 2302-2308.
10. R. D. Shannon and C. T. Prewitt, *Acta Crystallogr. Sect. B*, 1969, **B25**, 925-946.
11. U. S. Rochelle M. Cornell, *The Iron Oxides: Structure, Properties, Reactions, Occurrences and Uses*, John Wiley & Sons, 2006.
12. A. A. Tsirlin and H. Rosner, *Phys Rev. B*, 2009, **79**.
13. P. Y. Zavali and M. S. Whittingham, *Acta Crystallogr., Sect. B: Struct. Sci*, 1999, **55**, 627-663.
14. N. A. Chernova, M. Roppol, A. C. Dillon and M. S. Whittingham, *J. Mater. Chem.*, 2009, **19**, 2526-2552.
15. K. Adil, M. Leblanc, V. Maisonneuve and P. Lightfoot, *Dalton Trans.*, 2010, **39**, 5983-5993.
16. M. Berraho, C. Rkha, A. Vegas and M. Rafiq, *Acta Crystallogr., Sect. C: Cryst. Struct. Commun.*, 1992, **48**, 1350-1352.
17. M. Berraho, A. Vegas, M. Martinezripoll and M. Rafiq, *Acta Crystallogr., Sect. C: Cryst. Struct. Commun.*, 1994, **50**, 666-668.
18. E. R. Williams, S. A. Morris and M. T. Weller, *Dalton Trans.*, 2012, **41**, 10845-10853.

19. C. E. Housecroft and A. G. Sharpe, *Inorganic Chemistry*, Second edition edn., Pearson Education Limited, Essex, 2005.
20. Y. U. Park, D. H. Seo, B. Kim, K. P. Hong, H. Kim, S. Lee, R. A. Shakoor, K. Miyasaka, J. M. Tarascon and K. Kang, *Sci. Rep.*, 2012, **2**.
21. E. Kotsapa and M. T. Weller, *Chem. Commun.*, 2011, **47**, 6132-6134.
22. P. Serras, V. Palomares, A. Goni, I. G. de Muro, P. Kubiak, L. Lezama and T. Rojo, *J. Mater. Chem.*, 2012, **22**, 22301-22308.
23. J. Barker, M. Y. Saidi and J. L. Swoyer, *J. Electrochem. Soc.*, 2003, **150**, A1394-A1398.

CHAPTER FIVE: TRANSITION METAL SULFATE/FLUOROSULFATES

5.0 Introduction

Previous chapters have described the results of studies of the metal fluorophosphate materials resulting from incorporating fluoride into the reaction pathway, leading to the formation of novel structures showing many new features. This chapter presents the results of further synthetic work on new fluoride-incorporated structures, but focused on a different polyanionic system. In the search for new battery electrode materials, structures built on transition metals and polyanions ($TO_4^{3-/2-}$) have become very attractive, particularly since the discovery of the electrochemically active $LiFePO_4$.[1] The positive attributes of polyanion groups, such as PO_4, thus have gained much attention.[2] Many phosphates/fluorophosphates materials have been explored in order to investigate the high electrode potentials that result from the inductive effect of $TO_4^{3-/2-}$ and the electron-withdrawing character of the F^- ion.[3] However, by substituting the phosphate anion for the more electron-withdrawing sulfate anion within the structure, it was found that the electrode potential could be further improved.[4] This is attributed to the inductive effect of sulfate ion and the greater electronegativity of sulphur than phosphorus. Moreover, by incorporating fluoride within the structures, such improvements can be further reinforced.

Many previously reported metal sulfate structures have been produced under extreme conditions or via very complex routes. However, the syntheses within this work were accomplished through using the direct hydrothermal route to produce new mid-first row transition metal sulfate/fluorosulfate materials. Compared to the synthesis of metal fluorophosphate structures, using phosphoric acid as source for phosphorus and oxygen, for the work described in this chapter, sulfuric acid was employed in the reactions. Metal fluorides were used as the metal and fluorine sources. Hydroxides or fluorides such as LiOH, NaOH or KF *etc* were employed in the reactions to provide countercations. In a typical reaction, all starting materials were combined in a 23 mL Teflon lined hydrothermal autoclave and heated to the desired temperature. Products were collected by filtration under vacuum, washed with distilled water and air dried.

Table 5.1 summarises the reaction conditions of the new produced metal sulfate/fluorosulfate structures, including the starting materials, reaction temperatures and times, in addition to any observations of the final products. A wide range of reaction conditions were investigated during the research work, with more than 500

experiments carried out. Many of the materials were obtained as crystalline phases, but due to the insufficient size of crystals, they could not be characterised by the SXD technique. Other materials produced that were not listed in the table, were known samples, amorphous materials or non-reacted starting materials.

Table 5.1: *Synthetic conditions for all transition metal sulfate/fluorosulfate materials*

Starting regents	**Temp (^{o}C)**	**Time (hours)**	**Crystal morphology and purity**	**Product(s)**	**Thesis section**
$FeSO_4 \cdot 7H_2O$ (0.719 mmol , 0.2 g); HF (0.719 mmol, 0.0278 ml); NaF (1.079 mmol, 0.0453 g)	175	48	Yellow plate Multi-phases	$Na_2FeF_3SO_4$	5.1 (VIII)
FeC_2O_4 (0.37 mmol, 0.0532 g); H_2SO_4 (1.479 mmol, 0.0804 ml); KF (1.479 mmol, 0.0859 g)	175	48	Yellow column Single phase	$K_2FeF_3SO_4$	5.2 (IX)
FeF_3 (0.599 mmol, 0.1 g); H_2SO_4 (1.198 mmol, 0.0652 ml); $LiOH \cdot H_2O$ (1.797 mmol, 0.0776 g)	175	48	Yellow-green needle Single phase	$Li_3FeF_2(SO_4)_2 \cdot H_2O$	5.3 (X)
VF_3 (0.4 mmol, 0.0432 g); H_2SO_4 (0.8 mmol, 0.435 ml); NaOH (1.2 mmol, 0.0634 mL)	175	48	Dark green plate Single phase	$Na_3VF_2(SO_4)_2$	5.4 (XI)
MnF_3 (0.475 mmol, 0.0532 g); H_2SO_4 (0.951 mmol, 0.0517 ml); NaOH (1.426 mmol, 0.0753 ml);	175	48	Dark brown fragment Multi-phases	$Na_3MnF_2(SO_4)_2$	5.4 (XI)
FeF_3 (0.599 mmol, 0.1 g); H_2SO_4 (1.198 mmol, 0.0652 ml); NaOH (1.797 mmol, 0.0949 ml)	175	48	Pale pink column Single phase	$Na_3FeF_2(SO_4)_2$	5.4 (XI)
FeF_3 (0.599 mmol, 0.1 g); H_2SO_4 (1.198 mmol, 0.0652 ml); $LiOH \cdot H_2O$ (1.797 mmol, 0.0754 g)	175	48	Yellow needle Multi-phase	$Li_{0.5}Fe(O_{0.5}F_{0.5})SO_4$	5.5 (XII)
MnF_3 (0.772 mmol, 0.0864 g); H_2SO_4 (1.544 mmol, 0.084 ml); NaF (2.316 mmol, 0.0972 ml);	175	48	Dark brown plate Single phase	$Na_5Mn_3F_4(SO_4)_4$	5.6 (XIII)

Starting regents	Temp (^{o}C)	Time (hours)	Crystal morphology and purity	Product(s)	Thesis section
MnF_2 (0.753 mmol, 0.07 g); H_2SO_4 (1.506 mmol, 0.0819 ml); NaF (2.259 mmol, 0.0949 g);	180	72	Dark brown fragments Multi-phases	$Na_{12}Mn_3F_8(SO_4)_6$	5.7 (XIV)
MnF_3 (0.912 mmol, 0.1021 g); $(NH_4)_2SO_4$ (1.824 mmol, 0.1206 g); $LiOH{\cdot}H_2O$ (2.736 mmol, 0.1148 g)	175	48	Pale pink plates Single phase	$(NH_4)LiMn(SO_4)_2$	5.8 (XV)

5.1 Compound VIII: $Na_2FeF_3SO_4$

The product crystallised as yellow platy crystals. A suitable crystal was selected for a single crystal X-ray diffraction study on a Rigaku FR-E+ UHF Diffractometer at University of Southampton, data were collected at 120 K, and the resulting crystallographic information summarised in Table 5.2. The structure of the title compound possesses a monoclinic unit cell, with space group $P2_1/m$, and forms a one-dimensional chain structure, which consists of iron octahedra and sulfate tetrahedra (Figure 5.1). Key bond lengths are summarised in Table 5.3.

The structure of compound **VIII** consists of one-dimensional *zig-zag* chains running parallel to the *b*-axis, which are built from corner-sharing FeO_2F_4 octahedra, linked via *trans*-fluoride in each octahedron (Figure 5.1). The linear chain, based on the -Fe-F-Fe-F- backbone has a Fe-F-Fe angle of 139.16°. This is an analogue of the butlerite-type chain.[5] This type of chain backbone is also found in other inorganic fluoride materials.[6] The corner-linked *zig-zag* chains have pairs of adjacent FeO_2F_4 octahedra bridged symmetrically by SO_4 tetrahedra, through two μ^2-bridging oxygen atoms within the SO_4 tetrahedron, and each FeO_2F_4 octahedron is connected with two SO_4 tetrahedra through two *trans*-oxygen atoms within each octahedron. The corner-shared FeO_2F_4 octahedra and SO_4 tetrahedra form three-membered rings, based on two Fe- and one S-centred polyhedra, where the sulfate tetrahedra positions alternate on either side along the *zig-zag* chain and each has two terminal oxygen atoms. The *trans*-fluoride and oxygen atoms within the FeO_2F_4 octahedron are involved in bridging, the other pair of *trans*-fluoride atoms within the octahedron are terminal and are orientated toward the inter-chain space in the *ab*-plane. Adjacent chains interleave sulfate group positions in the *bc*-plane are separated by Na^+ cations which are held by ionic bonds formed between the cations and the anionic species, O and F, from the main chain. The observed linear chain in compound **VIII** is also found within other compounds such as $Na_2MnF_3(PO_3(OH,F))_2$ and $[H_2N(CH_2)_4NH_2]MF_3(SO_4)$ (M = V, Fe).[7-9]

EDX data confirmed the presence of fluorine within the material structure. The deduction of the position of fluorine within the structure during the refinement is generally based on the determination of atomic displacement parameter (ADP) values (provide in cif),

as when oxygen sites yielded non-positive or very small ADP values, reassignment of these sites as fluoride produces an ADP value that is similar to all other anion sites, correct assignment also leads to a reduction in data fitting residual values. Further bond valence calculations and the overall charge-balancing of the structure also provides judgement of whether a fluoride site has been assigned correctly, where the bond valance value for an oxygen atom should be approximately 2, or for fluorine approximately 1. The BV values are given in Table 5.4.

Table 5.2: *Crystal and diffraction information of compound VIII*

Empirical formula	$Na_3FeF_3SO_4$
Formula weight ($gmol^{-1}$)	254.88
Temperature (K)	120
Appearance	Yellow plate
Crystal size (mm)	0.21 × 0.09 × 0.05
Crystal system	Monoclinic
Space group	$P2_1/m$
Unit cell dimensions	a=5.654(6) Å, b=7.357(8) Å c=6.888(8) Å, β=109.11(2)^o
λ/Å	0.71073 Å (Mo K_α)
Volume ($Å^3$)	270.7(5)
Z	2
Density (gcm^{-3})	1.79
Reflections collected	1436
Unique reflections	665
R_1 (all data)	0.0762
wR_2 (all data)	0.1893
GooF	1.23

Table 5.3: *Bond lengths between selected atoms*

Bond	Bond length (Å)	Bond	Bond length (Å)
Fe1-O1	1.997(5)	S1-O1	1.496(4) × 2
Fe1-F1	1.912(2)	S1-O2	1.454(6)
Fe1-F2	1.963(3)	S1-O3	1.447(6)

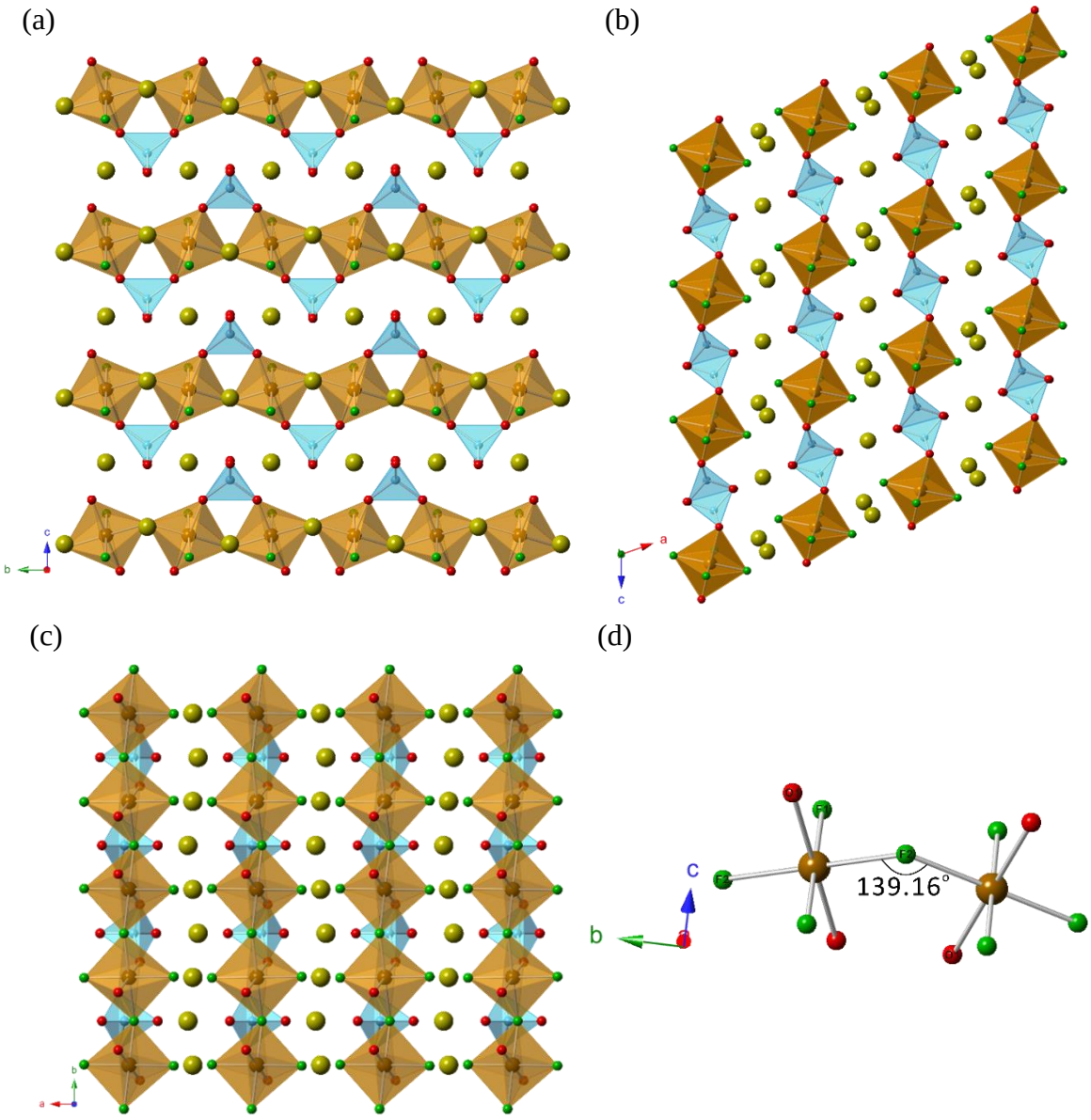

Figure 5.1: *The structure of $Na_3FeF_3SO_4$ viewed down the (a) a-, (b) b-, (c) c-crystallographic axes, with the Fe octahedra are shown in yellow-brown, sulfate tetrahedra in aqua blue, oxygen atoms in red, fluorine in green and sodium cations in yellow (d) shows the repeating octahedral unit among the Fe-chain*

One crystallographically unique iron octahedral environment is present within the structure. Each FeO_2F_4 octahedron is six-coordinate, with *trans*-fluoride connections between octahedra building up the Fe-chain, and *trans*-oxygens are bridging to the SO_4 tetrahedra. The remaining *trans*-fluorides are terminal. The bond lengths within the FeO_2F_4 octahedron are given in Table 5.3. The bonds involved in bridging have very similar bond

distances, with 2 × (Fe-O) bonds at 1.997(5) Å and 2 × (Fe-F2) at 1.963(3) Å respectively, but the terminal Fe-F1 bond is slightly shorter with distance of 1.912(2) Å. This is comparable to the bond lengths of the octahedron in $Na_2Mn^{III}F_3(PO_3(OH,F))_2$, which also shows a shorter terminal Mn-O with length of 1.854 Å, other bonds include 2 × (Mn-O) at 1.904 Å and 2 × (Mn-O) at 2.097 Å respectively. The BV calculation (Fe1 = 3.02) supports the oxidation state of Fe as +3.

The structure of compound **VIII** contains one crystallographically unique sulfate group (S1). The bond lengths summarised in Table 5.3 show the four S-O bonds in the SO_4 tetrahedron are close in length, but with the bridging bonds to iron longer than the terminal bonds. The average length of the four S-O bonds was found to be 1.466 Å. The O-S-O bond angles within the tetrahedron are in the range of ~107.9-110^o, compared to the standard 109.5^o in an ideal tetrahedron, the difference observed is less than 2^o. During the single crystal refinement, the ADPs (provided in cif) show similar values for all anion sites within the sulfate unit, indicating that no fluoride was incorporated. BV calculations for oxygen anions all showed the expected values close to 2, and the overall charge balanced structure also confirmed the formation of $[SO_4]^{2-}$ anionic group within the compound structure.

Table 5.4: *Bond valence calculations of selected atoms*

Atom label	Bond valence	Atom label	Bond valence
O1	2.07 -	F1	0.98 -
O2	1.98 -	F2	1.14 -
O3	1.92 -	Fe1	3.02 +

The sodium cations are found to exhibit two distinct crystallographic environments within the structure, and these two sodium sites have very different anion coordinations (Na-X < 3.00 Å). One of the sodium sites is eight-fold with five short Na-F and three long Na-O bond distances, the other one is an almost regular octahedral NaO_4F_2. The shortest Na-Na separation distance is 3.62 Å.

EDS analysis showed the presence of Na (17.1%), Fe (9 %), S (9.4%), F (30.5%) and O (34 %), with an experimental atomic ratio of 1.88:1:1.04:3.37:3.76, that is approximately in

agreement with the theoretical ratio of 2:1:1:3:4. An SEM image of the compound **VIII** crystals was recorded and is shown in Figure 5.2.

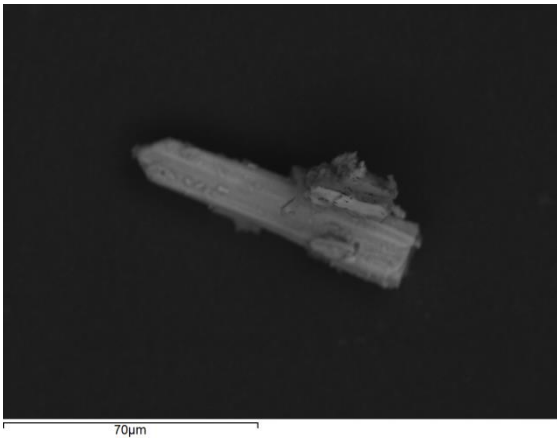

Figure 5.2: *SEM image of $Na_3FeF_3SO_4$ single crystal, with a small amount of unidentified matrix.*

5.2 Compound IX: $K_2FeF_3SO_4$

The product crystallised as yellow columnar crystals. A suitable crystal was selected for a single crystal X-ray diffraction study. Data were collected at 120 K, and resulting crystallographic information summarised in Table 5.5. The structure of the title compound possesses an orthorhombic unit cell with the space group *Pbcn* and forms a one-dimensional chain structure, consisting of iron centred octahedra and sulfate tetrahedra (Figure 5.3). Key bond lengths are summarised in Table 5.6.

The structure of compound **IX** is similar in form to compound **VIII,** consisting of linear chains separated by K^+ cations. Compound **IX** is isostructural to $A_2MnF_3SO_4$ (A=K, Cs, Rb, NH_4)[10, 11] and $(NH_4)_2MF_3SO_4$ (M=Fe, V). The polyhedral chains are again built up of corner-linked FeO_2F_4 octahedra. The shared corners are μ^2-bridging fluoride, occupying the *trans*-position of each octahedron; this behaviour is very similar to the chains found in compound **VIII**. The chain, based on the –F-Fe-F-Fe- backbone, can also be found in many other reported metal fluoride frameworks.[12] The observed Fe-F-Fe angle along the linear chain is about ~129.3^o which is significantly smaller than in compound **VIII** (~139.2^o). Although the Fe based chains formed within the two compounds are identical, however the arrangements of the chains in three dimensional space are very different. The chains in compound **IX** run parallel to the *c*-axis, and are staggered from each other, whilst the chains in compound **VIII** are aligned and run parallel to each other and the *b*-axis.

As in compound **VIII**, the iron cation within compound **IX** only has a single unique crystallographic environment. The iron site has an octahedral coordination environment, with two terminal fluorine atoms, two bridging fluorine atoms, and two oxygen atoms from bridging sulfate units. By consideration of the bond lengths summarised in Table 5.6, it can be seen that the terminal Fe1-F1 bond is 1.887(7) Å, whilst the bridging Fe1-F2 and Fe1-O2 bonds are 1.980(6) Å and 2.006(5) Å, (the terminal bond is noticeably shorter than the bridging bonds). This gives an arrangement of two short and four (approximately equal) long bonds in the octahedron. The Fe cation within the octahedron was suggested by BV calculation to adopt an oxidation state of +3. However the Fe^{III} octahedron with such a strongly distorted coordination arrangement is uncommon, and is comparable to the Mn^{III} octahedron within the isostructural $K_2MnF_3SO_4$, whose coordination shows similar bonding

arrangement of two short and four long bonds. However, as reported in the paper, this is likely to be caused by the Jahn-Teller effect of high spin d^4 manganese, thus leading to an octahedron with a tetragonal compression.[10] An iron site with a +3 oxidation should not be subject to the Jahn-Teller effect, therefore this cannot explain the Fe^{III} coordination within compound **IX**. Presumably, the distortion of the Fe^{III} site can be considered to be forced by the double bridge-system in the infinite chain anion,[11] and the expectation that the terminal Fe-F interaction would be stronger than the bridging Fe-F bonds.

Table 5.5: *Crystal and diffraction information of compound IX*

Empirical formula	$K_2FeF_3SO_4$
Formula weight ($gmol^{-1}$)	287.09
Temperature (K)	120
Appearance	Yellow column
Crystal size (mm)	0.17 ×0.11 × 0.051
Crystal system	Orthorhombic
Space group	*Pbcn*
Unit cell dimensions	a=10.9902(4) Å, b=8.4234(3) Å c=7.1570(3) Å, $\alpha=\beta=\gamma=90^o$
λ/Å	0.71073 Å (Mo K_α)
Volume ($Å^3$)	662.56(4)
Z	4
Density (gcm^{-3})	2.44
Reflections collected	6135
Unique reflections	1339
R_1 (all data)	0.033
wR_2 (all data)	0.0817
GooF	1.08

Table 5.6: *Bond lengths between selected atoms*

Bond	Bond length (Å)	Bond	Bond length (Å)
Fe1-O2	2.006(5) × 4	S1-O1	1.447(3) × 2
Fe1-F1	1.887(7)	S1-O2	1.503(3) × 2
Fe1-F2	1.980(6)		

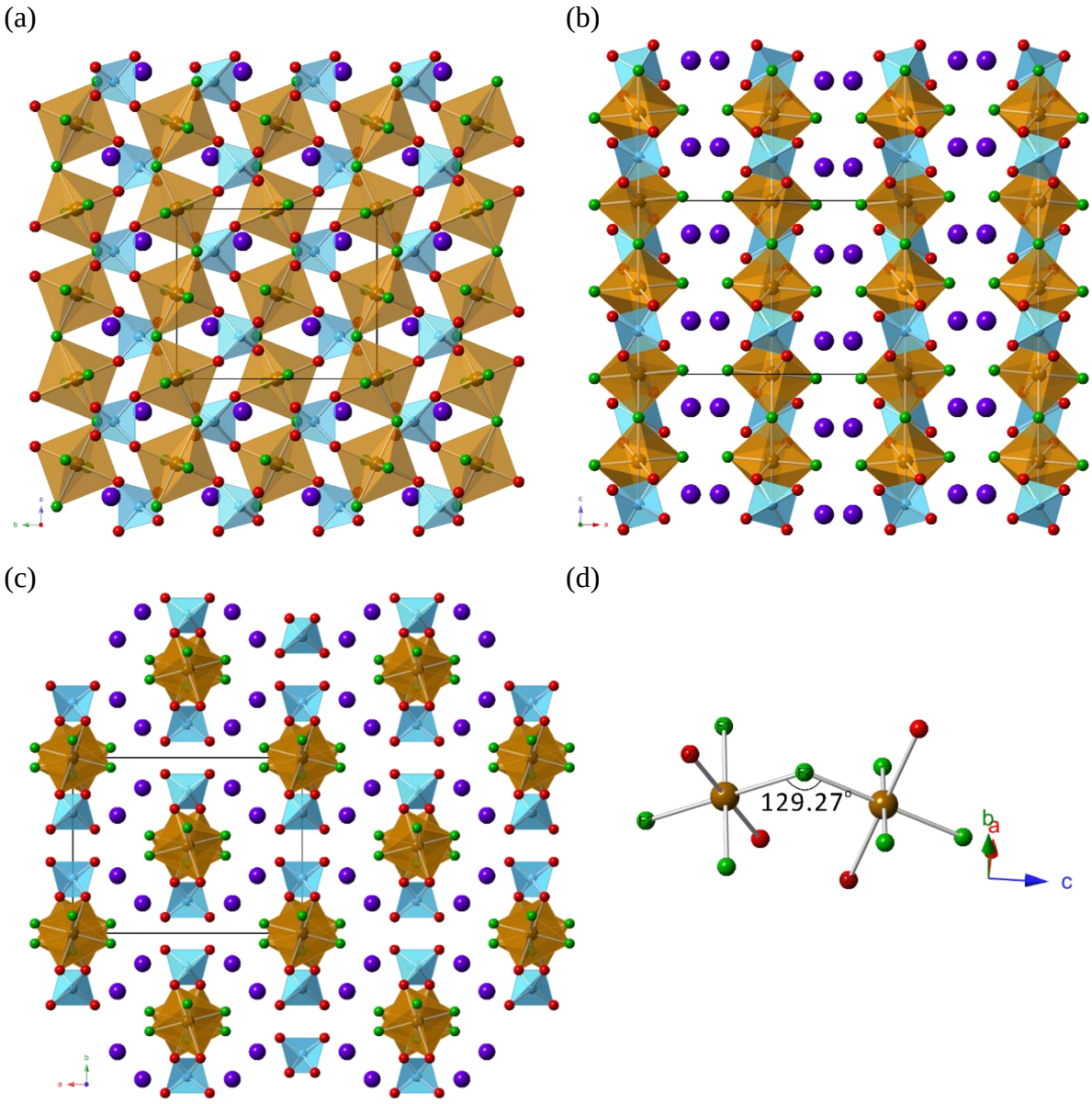

Figure 5.3*: The structure of $K_2FeF_3SO_4$ viewed down the (a) a-, (b) b-, (c) c-crystallographic axes, with the Fe octahedra are shown in yellow-brown, sulfate tetrahedra in aqua blue, oxygen atoms in red, fluorine in green and sodium cations in yellow. (d) shows the repeating octahedral units among the Fe-chain*

A similar double bridge-system, as seen in the infinite chains of this compound, has also be seen in the compounds **V** (chapter 4) and **VIII**. The sulfate group within compound **IX** only possesses one crystallographically unique tetrahedral environment. As described previously, the sulfate groups bridge adjacent octahedra along the Fe-chain, a possible effect of bridging sulfate groups is a decrease in the angle at the bridging fluoride. It can be

seen from Table 5.6 that the effect of the bridging interaction accounts for a significant lengthening of the S-O bond, with length of 1.503(3) Å.. The terminal S-O bond is relatively shorter with a length of 1.447(3) Å, the shorter S-O bonds can be considered to be modified by some multiple-bond character.[11] The most distorted O-S-O angle from the tetrahedral value is ~114.5 ^{o}, this can be explained as a result of greater repulsion between the two terminal bonds, with multiple-bond character, than between the bridging bonds.[10] BV calculations of the individual atoms are given in Table 5.7.

Table 5.7: *Bond valence calculations of selected atoms*

Atom label	Bond valence	Atom label	Bond valence
O1	1.85 -	F2	1.06 -
O2	2.08 -	Fe1	3.02 +
F1	0.89 -		

The K^{+} cations, residing in the space between the chains, form buckled sheets perpendicular to the *c*-axis. Each potassium atom forms an irregular coordination with five oxygen and three fluorine atoms from main framework chain. The distances of the K-X (X = O, F) interactions are in the range of ~2.6 - 2.9 Å. An SEM image of the compound **IX** crystals was recorded and is shown in Figure 5.4. The EDS analysis also confirmed presence of fluorine within the material. EDS data confirms the presence of K (18.3%), Fe (8.1%), S (8.4%), F (32.1%) and O (33.2%), with an experimental ratio of 2.25:1:1.03:3.9:4.1, that is approximately in agreement with the theoretical ratio of 2:1:1:3:4.

Figure 5.4: *SEM image of a $K_2FeF_3SO_4$ single crystal*

5.3 Compound X: $Li_3FeF_2(SO_4)_2 \cdot H_2O$

The product crystallised as yellow needle shaped crystals. A suitable crystal was selected for a single crystal X-ray diffraction study. Data were collected at 120 K, with the resulting crystallographic information summarised in Table 5.8. The structure of the title compound possesses a monoclinic unit cell with space group $P2_1/n$ and forms a one-dimensional chain structure, which consists of iron centred octahedra and sulfate tetrahedra (Figure 5.5). Key bond are lengths summarised in Table 5.9.

The structure of compound **X** consists of chains similar to those found in compound **II** (chapter 4), but differs in the arrangement of the structural components, as the linear chain in compound **X** consists of iron centred octahedra and sulfate tetrahedra, linked alternately through corner-sharing via μ^2-bridging oxygen atoms. Each pair of adjacent Fe-octahedra is bridged by two sulfate tetrahedra, along the chain, forming four-membered polyhedral rings. The chains are aligned parallel to the *a*-axis, and interleave sulfate group positions in the *ac*-plane. Adjacent chains are separated by Li^+ cations, whilst water molecules are also present within the material.

Only one independent iron coordination environment exists in compound **X.** The iron site is six-coordinate, with four bridging oxygen atoms to sulfate groups occupying equatorial positions, and two terminal fluoride at axial positions, which also form part of the lithium coordination environment. The bond lengths summarised in Table 5.9, show all six bonds of the octahedral environment are close in length, but with bridging Fe-O bonds slightly longer. The average length of the four Fe-O bonds is 2.004 Å, and for terminal Fe-F bonds the average length is 1.923 Å. The shorter Fe-F bonds reflect the slightly smaller ionic radius of F^-, previously observed in related compounds.[13] The BV calculation (Fe1 = 3.08) indicates that the Fe centre adopts an oxidation state of +3.

Sulfate groups bridge the iron centred octahedra and are found in two distinct tetrahedral environments. Each sulfate tetrahedron bridges two adjacent Fe-tetrahedra through two μ^2-bridging oxygen atoms, and the remaining two oxygen atoms in the sulfate group being terminal and orientated into the inter-chain space. The bond lengths, summarised in Table 5.9, show bridging S-O bonds within the two sulfate tetrahedra are all

elongated compared to a free sulfate ion. The average length of the bridging S-O bonds within the two tetrahedral environments is 1.492 Å for the S1 unit and 1.502 Å for the S2 unit. The shorter terminal S-O bonds show multiple-bond character and are very similar in length, in the range of 1.453(3)-1.467(3) Å among the two sulfate tetrahedra. Similar behaviour is found in compound **VIII** and **IX**, where distortion of angles was also observed within the two sulfate units from an ideal tetrahedron. The multiple-bond character of the terminal S-O bonds causes the O-S-O angle to increase due to the repulsion between the multiple-bond and the bridging oxygen. Observed angles are ~112.1^{o} and ~112.3^{o} for S1 and S2 units respectively.

Table 5.8: *Crystal and diffraction information of compound X*

Empirical formula	$Li_3FeF_2S_2O_8H_2O$
Formula weight ($gmol^{-1}$)	324.89
Temperature (K)	120
Appearance	Yellow needle
Crystal size (mm)	0.11 × 0.051 × 0.09
Crystal system	Monoclinic
Space group	$P2_1/n$
Unit cell dimensions	a=5.1726(27) Å, b=12.5921(52) Å c=12.2734(49) Å, β=91.647(9)^{o}
λ/Å	0.71073 Å (Mo K_α)
Volume ($Å^3$)	799.08(6)
Z	4
Density (gcm^{-3})	1.85
Reflections collected	10503
Unique reflections	3166
R_1 (all data)	0.0717
wR_2 (all data)	0.1905
GooF	1.086

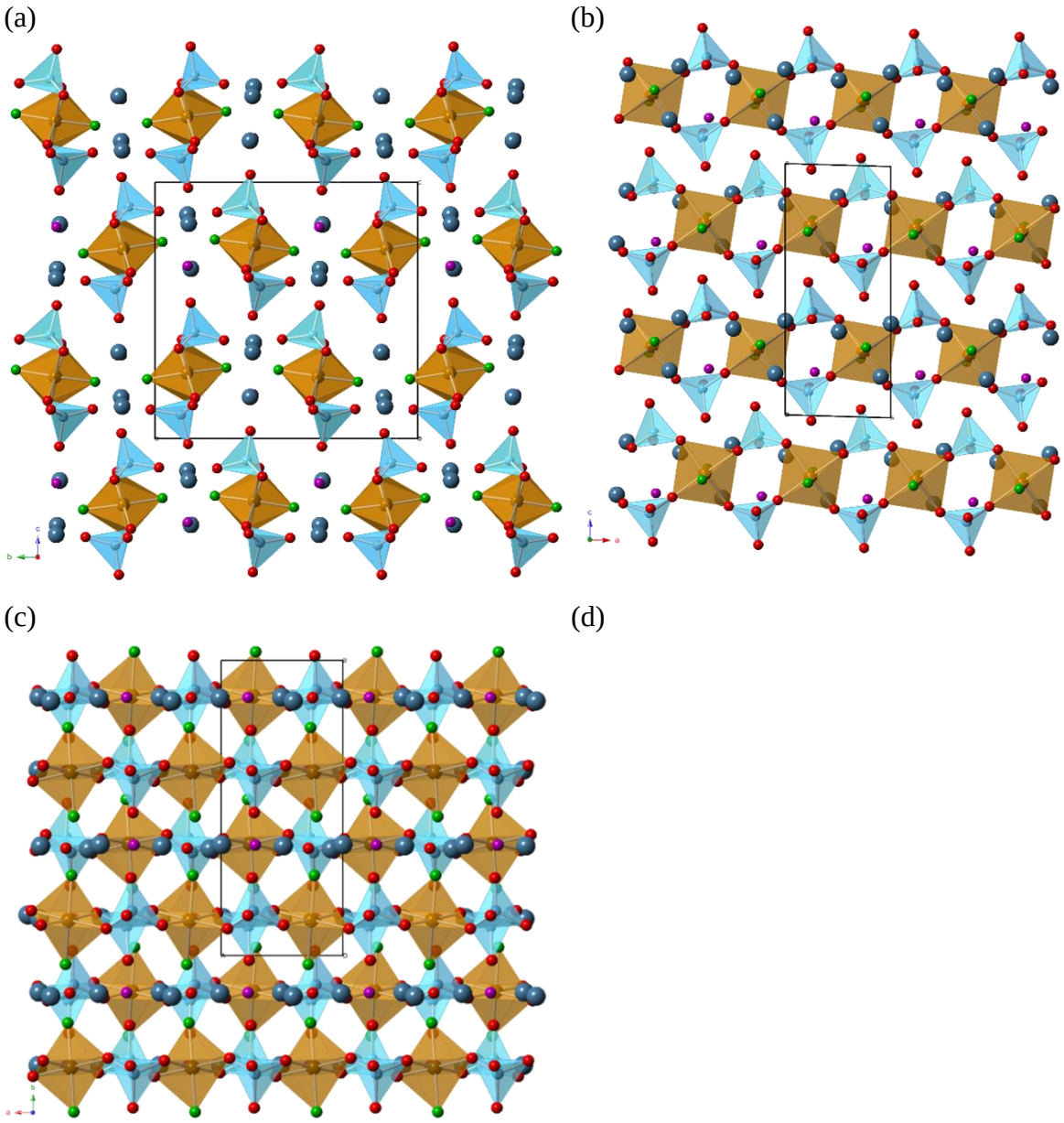

Figure 5.5*: The structure of $Li_3FeF_2(SO_4)\cdot H_2O$ viewed down the (a) a-, (b) b-, (c) c-crystallographic axes, with the Fe octahedra are shown in yellow-brown, sulfate tetrahedra in aqua blue, oxygen atoms in red, fluorine in green and Lithium cations in yellow, water molecule in pink for clarity.(d) show the repeating unit of the Fe chain*

Table 5.9: *Bond lengths between selected atoms*

Bond	Bond length (Å)	Bond	Bond length (Å)
Fe1-O1	2.007(3)	S1-O4	1.467(3)
Fe1-O2	1.997(3)	S1-O7	1.496(3)
Fe1-O5	2.004(3)	S1-O9	1.463(3)
Fe1-O7	2.010(3)	S2-O2	1.508(3)
Fe1-F1	1.923(2)	S2-O3	1.453(3)
Fe1-F2	1.923(3)	S2-O5	1.496(3)
S1-O1	1.498(3)	S2-O8	1.461(3)

Table 5.10: *Bond valence calculations for selected atoms*

Atom label	Bond valence	Atom label	Bond valence	Atom label	Bond valence
O1	1.97 -	O7	1.99 -	Li1	1.12 +
O2	1.93 -	O8	2.01 -	Li2	1.10 +
O3	1.83 -	O9	1.98 -	Li3	1.01 +
O4	1.98 -	F1	1.01 -		
O5	1.96 -	F2	0.97 -		
O6	0.44 -	Fe1	3.08 +		

Lithium cations occupy the inter-chain spaces present in the structure, adopting three different anion coordination environments: $Li(1)O_3F_2$, $Li(2)O_4F_2$ and $Li(3)O_2F_2$, and the separations between these cations (Li-Li) are just above ~2.5 Å. BV calculations (Table 5.10) for the Li^+ cations show values close to 1. Water molecules also reside in the space between chains, with likely hydrogen-bonding interactions between the water molecules and the framework oxygen or fluorine atoms. However, it was not possible to locate any of the hydrogen atoms through the SXD study, therefore O6 shows lack of bond valency.

Further investigations were carried out on this sample. Figure 5.6 shows the analysis of compound **X** by TGA and DTA. A 16.395 mg sample was heated in air from room temperature to 500 ℃. The TGA curve reveals a three-step weight loss. An initial weight loss was observed at around 100 ^oC, and is attributed to the elimination of a small amount of water absorbed on the compound surface. Then a second gradual weight loss (~5.2 %) was observed within the temperature range 130-270 ^oC, which is considered to be the departure of 1 mole of lattice water from the structure, the value is comparable to the

calculated value of 5.5 %. The further weight loss after 270 ^{o}C is ascribed the loss of fluorine, possibly as HF gas from structure. A DTA endothermic peak is observed at 250 ^{o}C, further evidencing the removal of the lattice water and the resulting structural change. A brown mixture obtained after TGA was characterised by PXD, showed multiple phases include Li_2SO_4, Fe_2O_3 and $FeSO_4$. An SEM image of the compound crystal was recorded and is displayed in Figure 5.7.

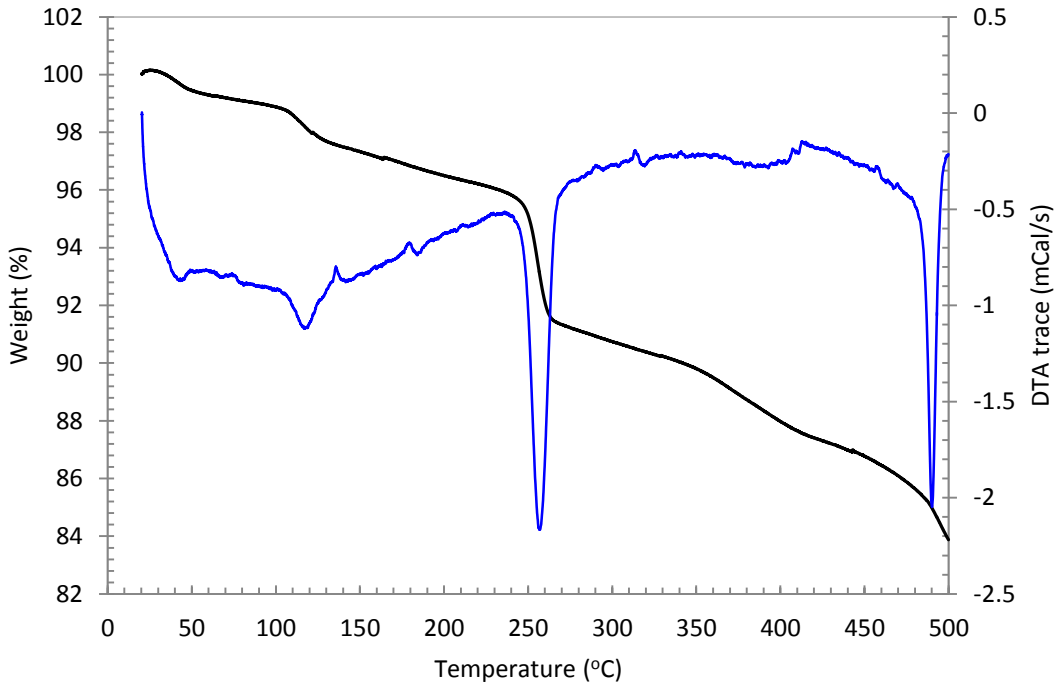

Figure 5.6: *TGA plot for the thermal decomposition of $Li_3FeF_2(SO_4)\cdot H_2O$. Black and green lines represented the TGA and DTA data as a function of temperature respectively*

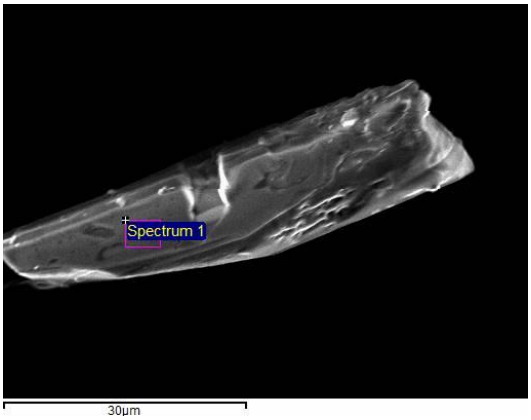

Figure 5.7: *SEM image of $Li_3FeF_2(SO_4)\cdot H_2O$ single crystal*

5.4 Compound XI: $Na_3MF_2(SO_4)_2$ (M = V, Mn, Fe)

A SXD study was undertaken on the three isostructural compounds, $Na_3MF_2(SO_4)_2$ (M = V, Mn, Fe) on a Rigaku FR-E+ UHF Diffractometer. The SXD data for all three compounds were collected at 120 K, with the resulting crystallographic information summarised in Table 5.11. The structure of the three isostructural compounds has an orthorhombic unit cell with space group *Pbcn*, and forms a two-dimensional layered structure. The layers within the three compounds all consist of linked metal octahedra and sulfate tetrahedra, as shown in Figure 5.8, with key bond lengths for the three compounds summarised in Table 5.12.

$Na_3MF_2(SO_4)_2$ (M = Fe) crystallised as pale pink needle crystals. Its structure can be described as comprising two-dimensional layers, each layer consisting of linked iron octahedra and sulfate tetrahedra running parallel to *a*- and *c*-axis. Each iron octahedron within the layer shares all four oxygen atoms with four sulfate units, whilst each sulfate tetrahedron bridges two neighbouring iron octahedra through corner sharing of two μ^2-bridging oxygen atoms. The remaining two oxygen atoms within the sulfate tetrahedron are terminal and orientate towards the inter-layer space. The layers can also be seen as made up of eight-membered polyhedral rings, based on four Fe-centred and four S-centred polyhedra. The layers are separated by Na^+ cations with an inter layer distance above 4 Å between the terminal fluorides of opposing Fe octahedra.

$Na_3MF_2(SO_4)_2$ (M = Mn) crystallised as brown plate crystals. Its structure is based on manganese octahedra and sulfate tetrahedra. The manganese centred octahedra found within this structure are strongly distorted as they are subject to the Jahn-Teller effect. Such distortions are well known in other manganese octahedral coordination environments with high spin Mn d^4 configurations.

$Na_3MF_2(SO_4)_2$ (M = V) crystallised as dark green plate crystals. The arrangement of the structure is identical to the above two compounds, consisting of two-dimensional layers based on vanadium octahedra and sulfate tetrahedra. Through the isostructures of the three compounds, the major differences arise from their unique octahedra building units, a comparison of the three octahedra is shown in Figure 5.8 (d).

EDS data confirmed the presence of fluorine within the three materials. As previously introduced, the deduction of the presence of fluorine within the structures relies on the comparison of ADP values (provided in cifs). Correct assignments of possible fluoride sites result in ADP values similar to all other anion sites, as well as a reduction in data fitting residual values. BV calculations for selected atoms, shown in Table 5.13, show that all BV values for fluorine atoms are comparable to the standard value of 1, whilst the BV sums for oxygen atoms are approximately 2.

Table 5.11: *Crystal and diffraction information of compound XI*

Empirical formula	$Na_3VF_2S_2O_8$	$Na_3MnF_2S_2O_8$	$Na_3FeF_2S_2O_8$
Formula weight ($gmol^{-1}$)	349.81	353.81	354.81
Temperature (K)	120	120	120
Appearance	Green plate	Brown plate	Pink column
Crystal size (mm)	0.34 × 0.08 × 0.05	0.45 × 0.21 × 0.05	0.5 × 0.07 × 0.05
Crystal system	Orthorhombic	Orthorhombic	Orthorhombic
Space group	*Pbcn*	*Pbcn*	*Pbcn*
a (Å)	a = 8.827(4)	a = 8.9311(11)	a = 8.911(4)
b (Å)	b = 13.878(7)	b = 13.5739(17)	b = 13.9953(10)
c (Å)	c = 6.610(3)	c = 6.6991(8)	c = 6.6332(3)
α (°), *β* (°), *γ* (°)	*90, 90, 90*	*90, 90, 90*	*90, 90, 90*
λ/Å	0.71073 Å (Mo $K_α$)	0.71073 Å (Mo $K_α$)	0.71073 Å (Mo $K_α$)
Volume ($Å^3$)	809.8(7)	812.1(2)	818.0(1)
Z	4	4	4
Density (gcm^{-3})	2.02	2.03	2.19
Reflections collected	1878	7930	4360
Unique reflections	922	937	945
R_1 (all)	0.020	0.049	0.023
wR_2 (all)	0.053	0.116	0.088
GooF	0.606	1.092	1.037

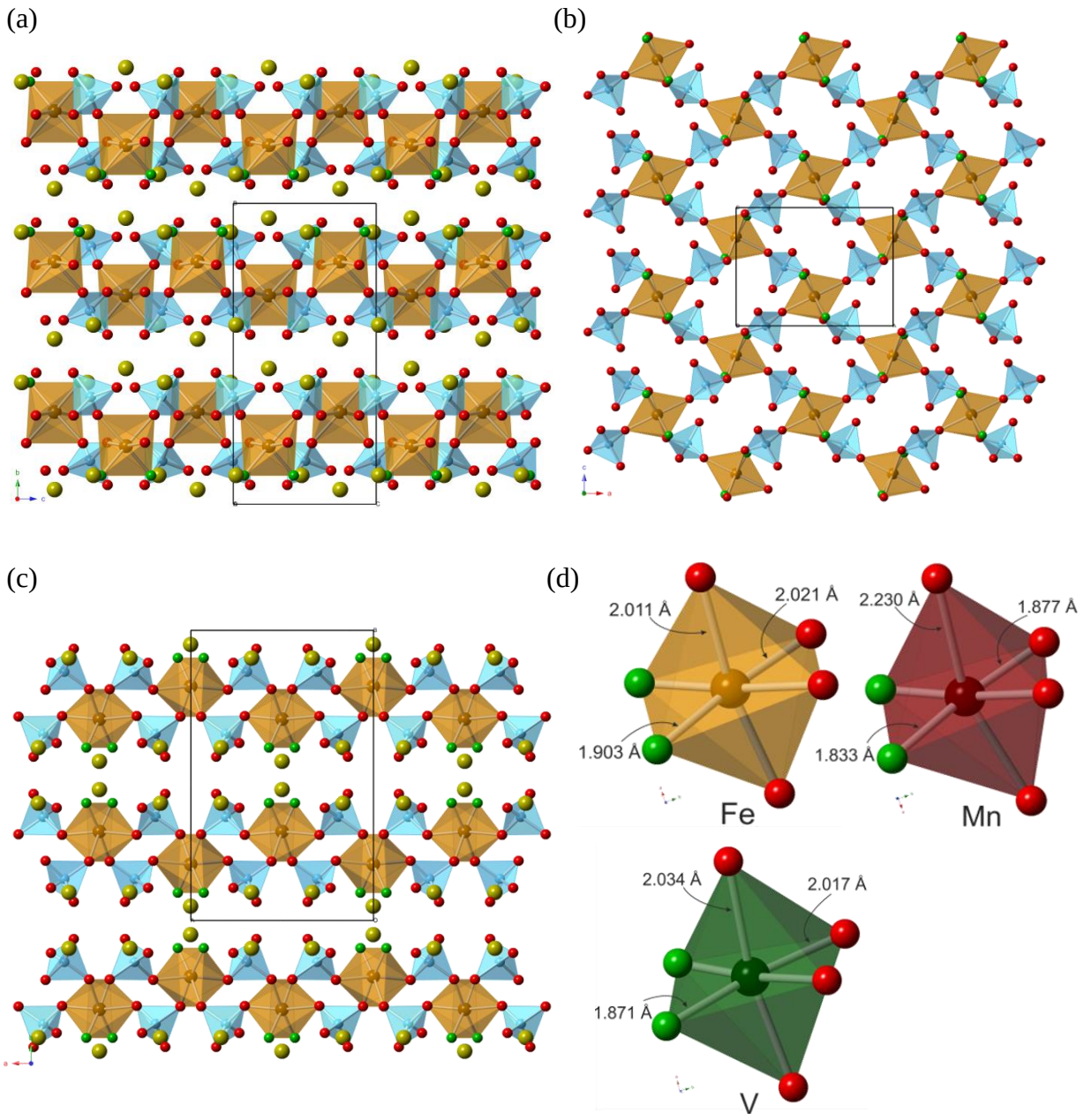

Figure 5.8: *The structure of $Na_3MF_2(SO_4)_2$ (M = V, Mn, Fe), (a) View along the layers at a crystallographic axis. (b) A single layer without Na^+ present view at b-axis. (c) View along the layers at c-axis. Key: gold octahedra – M, blue tetrahedra – S, red sphere – O, green sphere – F, yellow sphere – Na^+ cation. (d) shows the changes in the MO_4F_2 octahedron geometry for Fe, Mn, and V.*

Table 5.12: *Bond lengths between selected atoms*

Bond	Bond length (Å)	Bond	Bond length (Å)	Bond	Bond length (Å)
V1-O1	2.017(1) × 2	Mn1-O1	1.877(9) × 2	Fe1-O1	2.021(1) × 2
V1-O4	2.034(1) × 2	Mn1-O4	2.230(1) × 2	Fe1-O4	2.001(1) × 2
V1-F1	1.872(1) × 2	Mn1-F1	1.833(6) × 2	Fe1-F1	1.903(1) × 2
S1-O1	1.500(2)	S1-O1	1.516(1)	S1-O1	1.493(1)
S1-O2	1.449(2)	S1-O2	1.428(9)	S1-O2	1.449(2)
S1-O3	1.457(2)	S1-O3	1.444(1)	S1-O3	1.453(2)
S1-O4	1.483(2)	S1-O4	1.457(1)	S1-O4	1.490(2)

Within the isostructural series of compounds $Na_3MF_2(SO_4)_2$ (M = V, Mn, Fe), the metal ion sites show the coordination environments expected for these ions with high spin d^3, d^4, and d^6 electronic configurations. Each of the compounds only contains one unique transition metal ion octahedral coordination environment. All the metal ion sites within the different compounds are six-coordinate, with four bridging oxygen to four sulfate groups, and two terminal fluorides occupying the *cis*-positions. Bond lengths, given in Table 5.12, show that the FeO_4F_2 octahedron is the least distorted compared to the VO_4F_2 and MnO_4F_2 octahedra. The bridging Fe-O bonds within the FeO_4F_2 octahedron are similar in length with an average distance of 2.016 Å, whilst the terminal Fe-F bonds are significantly shorter, with distance of 1.903 Å. The shorter terminal bonds have been observed in many other metal ion sites, and due to the smaller ionic radius of F^- compare to O^{2-}. Similar bond arrangements can also be found within the VO_4F_2 octahedron. The bridging V-O bonds are ~0.155 Å longer than the terminal V-F bonds. The manganese ion site has the most distorted octahedral coordination environment. Due to the high spin d^4 configuration of the Mn ion within its coordination sphere, it shows the Jahn-Teller effect, manifested as a strong tetragonal distortion. The bond lengths in MnO_4F_2 octahedron demonstrate a noticeable elongation of the axial Mn-O bond with length of 2.230(1) Å, in contrast with the equatorial Mn-O and Mn-F bonds, yielding $r_{axial}/r_{equatorial}$ = 1.20. The average M-X (X=O, F)show only small variations, V → Mn → Fe with values of 1.974, 1.980 and 1.978 Å respectively, reflecting the expected ionic radii of these species.[14]

There is one crystallographically unique tetrahedral sulfate coordination environment present within each of the three compounds. Similar to previously observed SO_4 units, the

bond lengths show that the bridging S-O bonds are longer than the terminal bonds, and the most distorted O-S-O angles are between terminal oxygen atoms. For $Na_3M^{III}F_2(SO_4)_2$ when M = V, the average terminal S-O bond length in the sulfate unit is 1.453 Å, and for M = Fe the terminal S-O has an average length of 1.451 Å, These values are comparable to previously reported S-O distances.[15] Consideration of the bond lengths for the SO_4 unit within $Na_3Mn^{III}F_2(SO_4)_2$, show that there is one bond S1-O1, with length of 1.516(1) Å, which is noticeably different from the other S-O bonds. The crystal structure of this compound shows that O1 and O4 are both acting as bridging species, where O1 occupies the equatorial site of Mn-octahedron, and O4 occupies an axial site. Due to the Jahn-Teller distortion of Mn-octahedron, the elongated axial and equatorial Mn-O bonds lead to the bridging S-O bonds being stretched. The most distorted O-S-O angles within the sulfate tetrahedra for the three compounds M = V, Mn, and Fe, are ~112^o, ~115.2^o and ~112.4^o respectively, the high value for Mn again being a manifestation of the Jahn-Teller effect.

Table 5.13: *Bond valence calculations of selected atoms*

Atom label	Bond valence	Atom label	Bond valence	Atom label	Bond valence
O1	2.06 -	O1	2.17 -	O1	2.08 -
O2	2.05 -	O2	2.13 -	O2	2.03 -
O3	1.99 -	O3	2.03 -	O3	1.97 -
O4	2.05 -	O4	2.00 -	O4	2.06 -
F1	1.00 -	F1	0.99 -	F1	0.96 -
V1	3.13 +	Mn1	3.16 +	Fe1	3.05 +

The inter-layer space is filled by Na^+ cations, in two environments, with coordination to the terminal fluorine atoms on the transition metal ion sites and the oxygen atoms of the sulfate groups; one Na(F_4O_2) site has near trigonal prismatic geometry, whilst the other is irregular and seven-fold, Na(O_6F). The shortest Na…Na separations for M=V, Mn, Fe are and 3.50, 3.76 and 3.51 Å respectively.

EDS analysis were carried on two samples. For $Na_3VF_2(SO_4)_2$, the data shows the presence of Na (16.1%), V (5.2%), S (14.2%), F (9.1%) and O (55.3%), with an experimental atomic ratio of 3.12:1:2.75:1.77:10.75, approximately in agreement with the

theoretical ratio of 3:1:2:2:8. For $Na_3FeF_2(SO_4)_2$, the analysis indicates the presence of Na (15.7%), Fe (6.1%), S (11.9%), F (15.2%) and O (51.1%), with atomic ratio of 2.59:1:1.96:2.49:8.42 which matches approximately with the theoretical ratio of 3:1:2:2:8,. SEM images of the two compounds were recorded and shown in below (Figure 5.9).

(a)

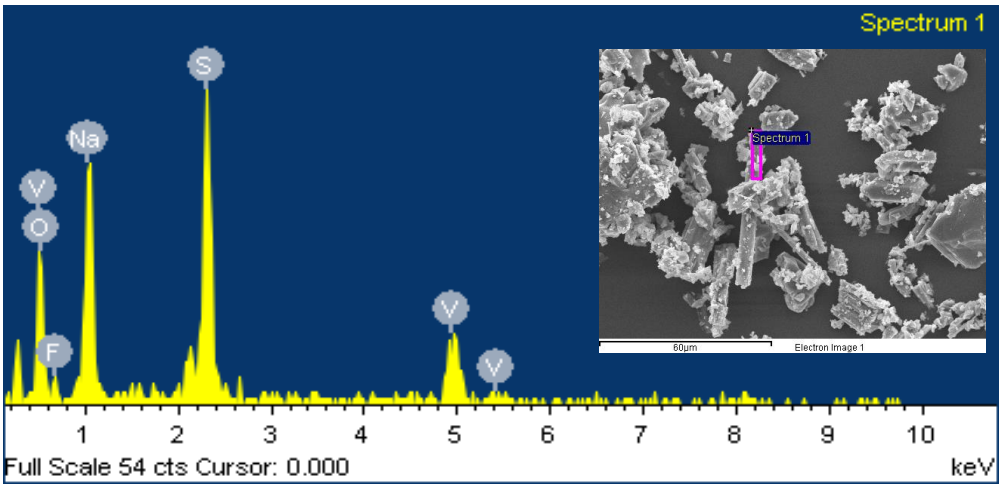

(b)

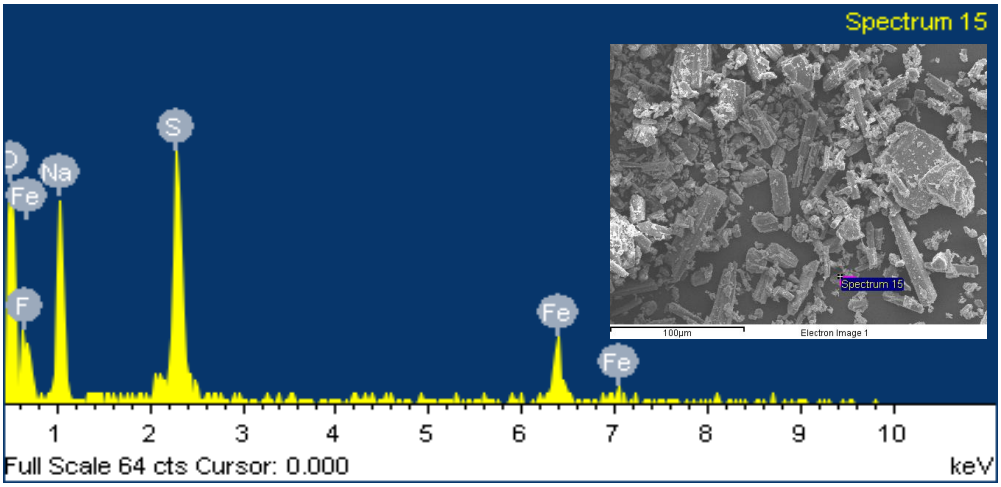

Figure 5.9: *(a) shows the SEM image of crystalline $Na_3V^{III}F_2(SO_4)_2$, and EDS data of the sample. (b) shows the SEM image of crystalline $Na_3Fe^{III}F_2(SO_4)_2$, and EDS data of the sample.*

The isostructural compounds of the $Na_3MF_2(SO_4)_2$ (M = V, Mn, Fe) series consists of layers and Na^+ cations, suggesting they may be used as good potential cathode materials for Na-ion batteries. Attempts to produce pure phases showed that only two of them could be

produced under stoichiometric reaction ratios. PXD studies on $Na_3MF_2(SO_4)_2$ (M = V, Fe) showed minor impurities were present within the materials (Figure 5.10).

(a)

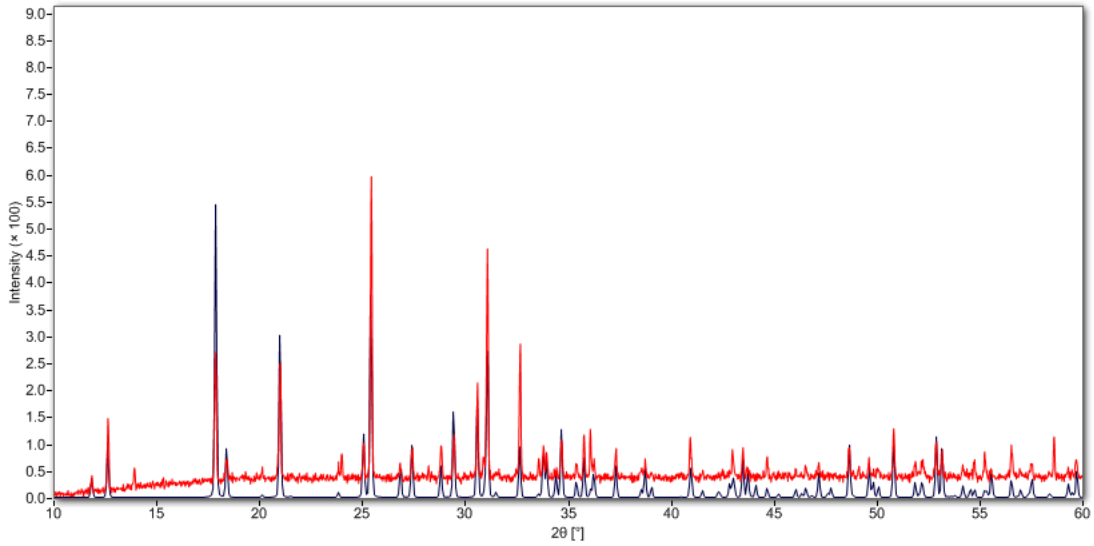

(b)

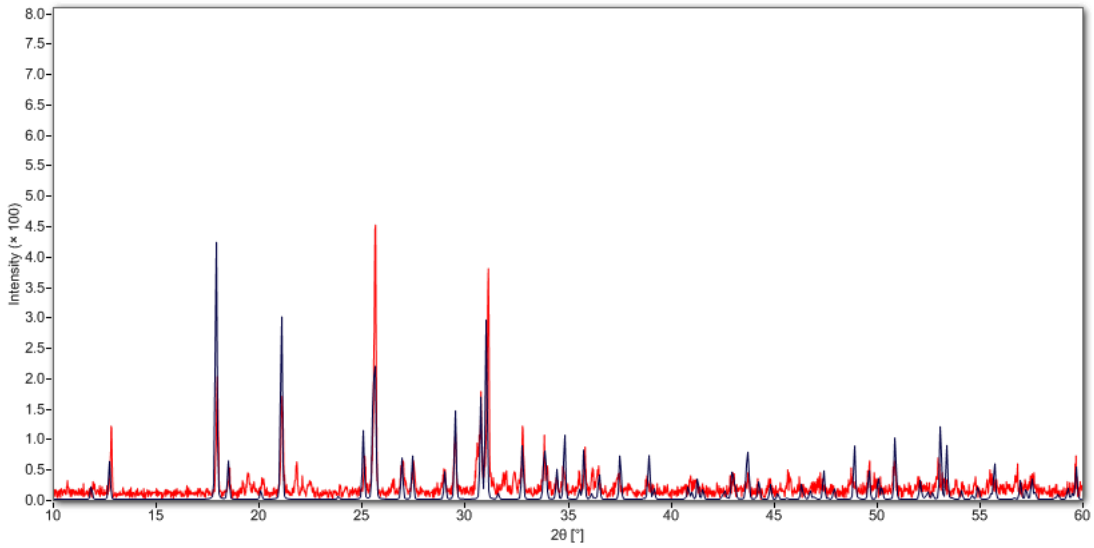

Figure 5.10: *PXD patterns for $Na_3FeF_2(SO_4)_2$ (a), $Na_3VF_2(SO_4)_2$ (b). Minor impurities were present within both compounds. Experimental data shown in red vs. calculated data shown in dark blue*

5.4.1 Electrochemical tests on $Na_3MF_2(SO_4)_2$ (M = V, Fe)

- Experimental details (Work carried out by Alex Madsen in John R. Owen group[16])

$Na_3VF_2(SO_4)_2$ and $Na_3FeF_2(SO_4)_2$ were used as the active materials for electrochemical sodium insertion/extraction experiments and were initially ground using a ball mill (particle size ~20 mm). The active material (75% wt) was combined with dry acetylene black (20% wt) in a pestle and mortar and ground until a homogenous mixture was formed. Dry PTFE (5% wt) was then added to the mixture, and worked into a single solid piece. The cathode material was then calendared using a rolling mill to produce an 80 μm thick uniform film. Cathode pellets, of thickness 8mm, were produced from the film using a punch and dried under vacuum at 120 ºC overnight.

Electrochemical testing of the resulting material was carried out using PFA Swagelok type cells with 1.0 M $NaPF_6$ in PC soaked glass fibre separators and sodium foil negative electrodes assembled under an inert argon atmosphere. The water content of the electrolyte, tested using the Karl Fischer technique, was found to contain less than 10 ppm of moisture. A potentiostat was used to cycle the cells under constant current conditions at a C-rate of 0.1 assuming one e^- transfer per formula unit of active material.

- Results and discussion

The open circuit of 2.88 V vs. Na metal was measured for pristine $Na_3FeF_2(SO_4)_2$. Figure 5.11 shows the results of the cell cycled twice under galvanostatic conditions. During the first anodic half cycle, the upper potential limit was set at 4.0 V to avoid any possible electrolyte decomposition. A plateau near 3.5 V, leading to a significant rise to the limiting potential after passage of 65 mAh g^{-1}, suggests the Fe^{III} has been oxidised to Fe^{IV}, with a theoretical capacity of 75 mAh g^{-1} for the extraction of one electron and one sodium ion per structural unit. However, during the cathodic half cycle a low capacity of 3 mAh g^{-1} showed a strong resistance to any re-insertion as the potential reduced to the negative limit of 2.0 V, presumably due to the structural change occurred during the extraction of sodium cations, that blocked the sodium ion diffusion pathways.

The potential limit was raised to 4.5 V on the second cycle, due to further oxidation of iron, which resulted in the expanding of the potential window to investigate reactions at higher potential. On the second charge, the voltage increases sharply to 4.2 V, where a further irreversible oxidation process occurs. Since it has recently been shown that $NaPF_6$ can be stable above 4.5 V vs. Na in this solvent, the observed current is attributed to further oxidation of the sample by extraction of sodium. However, oxidation of Fe^{IV} to Fe^{V} is unlikely, and therefore the evolution of oxygen, as previously demonstrated for high voltage lithium cathodes such as $LiMn_{0.5}Ni_{0.5}O_2$ is a more likely explanation.

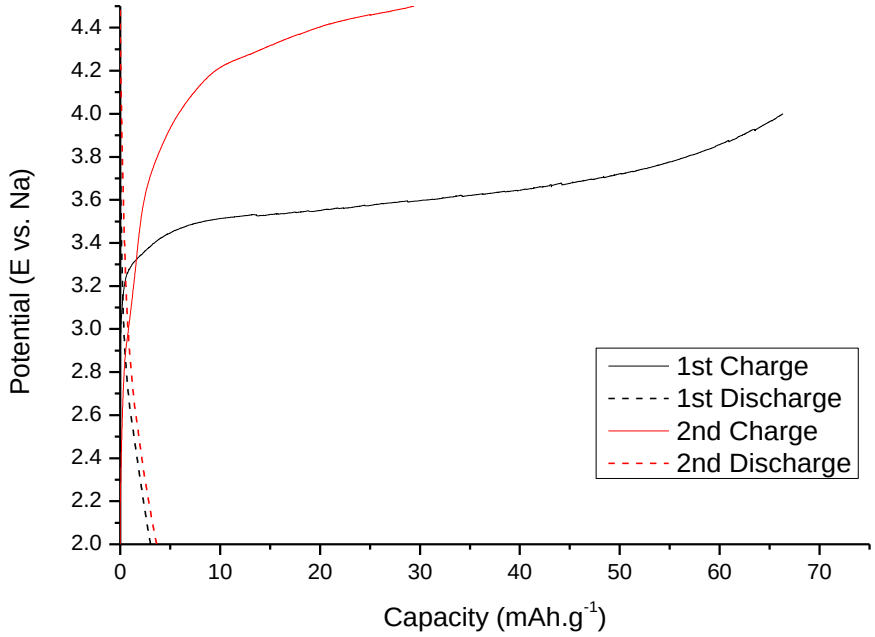

Figure 5.11: *Galvanostatic cycling of $Na_3FeF_2(SO_4)_2$ vs. Na metal with 1.0 M $NaPF_6$ in PC at 7.6 mA g^{-1}, i.e. approximately 0.1 C assuming a theoretical capacity of 76 mAh g^{-1}.*

The results for the $Na_3VF_2(SO_4)_2$ positive electrode material, tested in the same way as $Na_3FeF_2(SO_4)_2$, are shown in Figure 5.12. The open circuit of the pristine cell was measured at 2.68 V vs. Na metal. A gradual rise in potential from 3.3 V to 4.0 V after the passage of the oxidation 101 mAh g^1 (c.f. 77 mAh g^{-1} for a one-electron transfer) suggests the occurrence of rather more than a single oxidation from V^{III} to V^{IV}, and more than one sodium atom extracted, with the possibility of some V^{V} being produced. The cathodic half-cycle showed a value of 6.5 mAh g^{-1}, which is possibly evidence for the re-insertion of sodium, to a small extent.

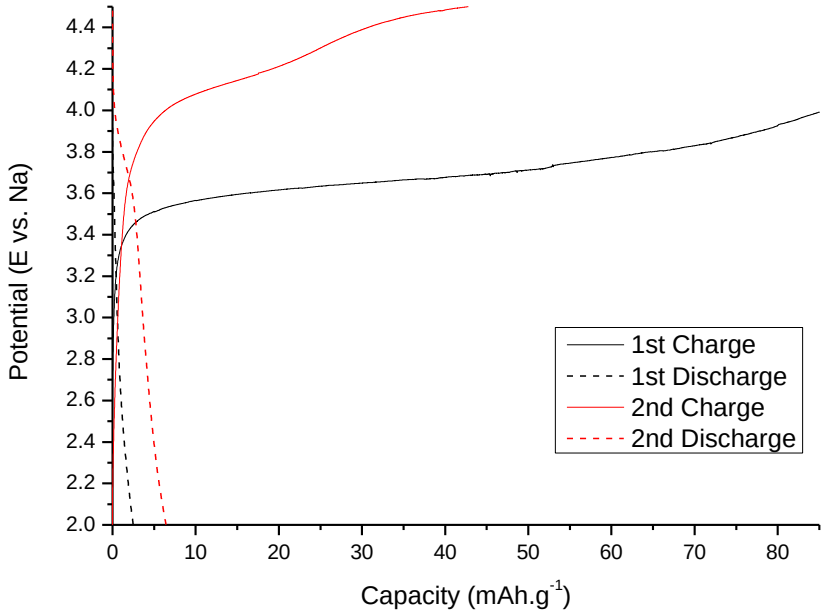

Figure 5.12: *Galvanostatic cycling of $Na_3VF_2(SO_4)_2$ vs. Na metal with 1.0 M $NaPF_6$ in PC at 7.7 mA g^{-1}, i.e. approximately 0.1 C assuming a theoretical capacity of 77 mAh g^{-1}.*

- Result conclusion

The electrochemical results indicate that sodium may be oxidatively extracted from both polycrystalline $Na_3FeF_2(SO_4)_2$ and $Na_3VF_2(SO_4)_2$ at voltages of 3.5 and 3.6 V, *versus* sodium metal, respectively. The voltage for the oxidation of the Fe^{3+} compound is significantly higher than those found for $Na_2FeP_2O_7$ (3.0 V)[17] and Na_2FePO_4F (3.0 V)[3] for sodium insertion and reduction of Fe^{3+} to Fe^{2+}. Cycling of the cells shows the reverse process of sodium re-intercalation is not facile. However, all materials were studied as made and not optimised in terms of, for example, particle size and further work will be required before we can establish whether or not these materials form suitable (de-) insertion materials for room temperature sodium cells. As well as nanostructuring and coating the materials, further potential studies include appropriate doping (of both framework metal and anion) with the aim of introducing defects and improving sodium ion mobility.

5.5 Compound XII: $Li_{0.5}Fe(O_{0.5}F_{0.5})SO_4$

The product crystallised as yellow needle crystals. A suitable crystal was selected for a single crystal X-ray diffraction study. The data were collected at 120 K, with the resulting crystallographic information summarised in Table 5.14. The structure of the titled compound has an orthorhombic unit cell with space group *Pnma* and forms a three-dimensional framework with channels running down the *a*-axis. The structure is comprised of iron centred octahedra and sulfate tetrahedra (Figure 5.13). Key bond lengths are shown in Table 5.15.

The structure of compound **XII** consists of one-dimensional chains, further linked by sulfate tetrahedra to build up a three-dimensional network. The polyhedral chain consists of corner-sharing Fe-octahedra, resulting in a -$O_{0.5}F_{0.5}$-Fe-$O_{0.5}F_{0.5}$–Fe- backbone. Such a chain system was found within previously described compounds **V**, **VIII**, and **IX**. The angle between Fe sites within the chain is around 135.9^o. Each pair of adjacent Fe-octahedra is bridged by a SO_4 group through the sharing of two μ^2-bridging oxygen atoms, resulting in the formation of three-membered polyhedral ring. Unlike the sulfate groups within the previously described compounds which possess two terminal S-O bonds, the sulfate groups within compound **XII** are fully connected, bridging pairs of Fe-octahedra from different polyhedral chains, therefore resulting in the formation of a three-dimensional framework. Four-membered rings are formed from alternating connected sulfate and iron polyhedra, based on two of each sulfate and iron units, and creating a channel running down the *a*-axis, with diameter of 3.71 Å. The channel is of a suitable size for occupancy by Li^+ ions.

Only one unique iron coordination environment was found within the structure. The iron site is six-coordinate and forms an octahedral coordination with six bridging atoms. During the single crystal refinement, the bridging anion site (O, F) between the Fe-octahedra was refined as mixed oxygen and fluorine; this is likely due to the substitutional disorder within the structure. Since the site could be refined as fully occupied of 1.0, for charge balance needed, the site was refined as mixed anions of half occupied oxygen and fluorine (occupancy 0.5 for each) rather than all O or F. This anion site occupies the *trans*-position of the octahedron and is responsible for bridging between adjacent octahedra. The four equatorial oxygen atoms within the Fe-octahedron bridge to four sulfate groups. The

bond lengths given in Table 5.15 shows that the six bonds within the Fe-octahedron are very similar in length, with the average length of the six bonds is 2.01 Å, which is in good agreement with the sums of the Shannon crystal radii (Fe-O = 1.95 Å).[14]

Table 5.14: *Crystal and diffraction information of compound XII*

Empirical formula	$Li_{0.5}FeO_{0.5}F_{0.5}SO_4$
Formula weight ($gmol^{-1}$)	172.88
Temperature (K)	120
Appearance	Yellow needle
Crystal size (mm)	0.2 × 0.068 × 0.036
Crystal system	Orthorhombic
Space group	*Pnma*
Unit cell dimensions	a=7.3914(2) Å, b= 6.3771(2) Å c=7.1956(2) Å, $\alpha=\beta=\gamma=90^o$
λ/Å	0.71073 Å (Mo K_α)
Volume ($Å^3$)	339.17(1)
Z	4
Density (gcm^{-3})	3.48
Reflections collected	3056
Unique reflections	425
R_1 (all)	0.0811
wR_2 (all)	0.2556
GooF	1.167

Table 5.15: *Bond lengths between selected atoms*

Bond	Bond length (Å)	Bond	Bond length (Å)
Fe1-O2	2.031(7)	S1-O2	1.478(7)
Fe1-O3	1.987(6) × 2	S1-O3	1.483(7) × 2
$Fe1\text{-}O1_{0.5}F1_{0.5}$	2.033(7) × 2	S1-O4	1.490(6)
Fe1-O4	1.988(7)		

Table 5.16: *Bond valence calculations of selected atoms*

Atom label	Bond valence	Atom label	Bond valence
O1	n/a	F1	n/a
O2	2.21 -	Fe	2.95 +
O3	2.19 -	Li	1.02 +
O4	2.08 -		

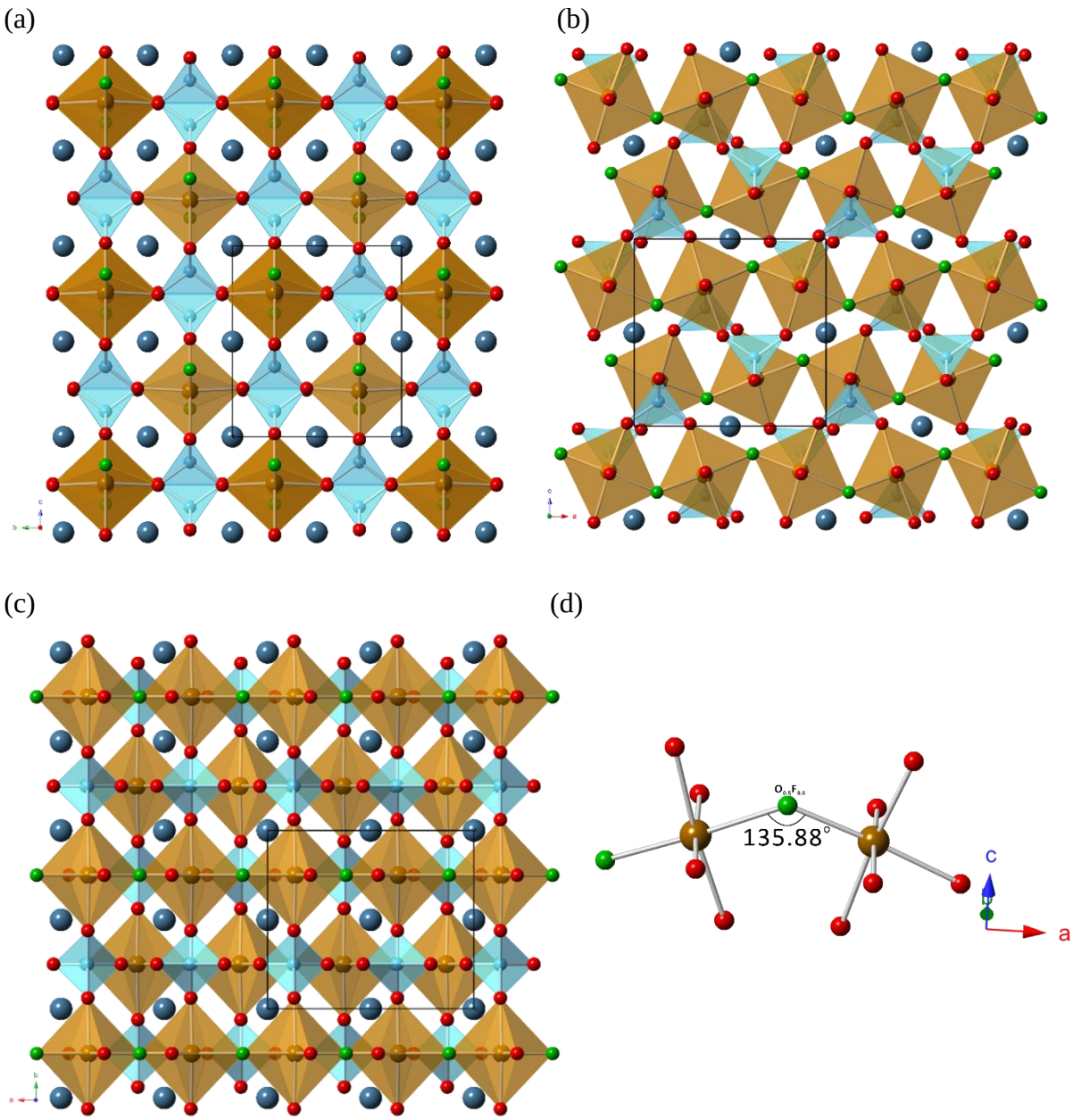

Figure 5.13*: The structure of $Li_{0.5}Fe(O_{0.5}F_{0.5})SO_4$ viewed down the (a) a-, (b) b-, (c) c-crystallographic axes, with the Fe octahedra are shown in yellow-brown, sulfate tetrahedra in aqua blue, oxygen atoms in red, fluorine in green and Lithium cations in blue. (d) shows the Fe-chain connected through sharing of half occupied $O_{0.5}F_{0.5}$.*

There is one crystallographically unique coordination environment of sulfate present within the structure. The sulfate unit adopts a tetrahedral coordination with four apical oxygen atoms shared with four Fe-octahedra. Since all four S-O bonds are involved in bridging, the observed bonds lengths are quite similar. The average length of the four S-O

bonds is 1.484 Å, this in good agreement with the sums of Shannon crystal radii (S-O = 1.5 Å).[14] The O-S-O angles within the tetrahedron are in the narrow range of 108.3-110.05°.

The lithium cation residing in the channel has a single coordination environment, forming almost regular octahedra, LiO_4F_2. The material is compositionally similar to $LiFeSO_4F$, which also has a three-dimensional structure with Li^+ cations filled in channels, and has been proved to be a possible cathode material for use in Li-ion batteries. By introducing fluorine and the more electron-withdrawing sulfate groups within the structure, an electronic potential of 3.6 vs. Li metal has been reported for this compound, which is slightly higher than $LiFePO_4$.[4] The crystal structure characteristics of cathode materials directly influence the Li^+ ion intercalation/extraction processes in electrochemical performance. Hence, in terms of structure, $Li_{0.5}Fe(O_{0.5}F_{0.5})SO_4$ with channels filled with Li^+ ions running along three crystallographic axes may make a good alternative cathode, and with a greater number of Li^+ sites within the structure, compared to that in $LiFeSO_4F$, the Fe^{III} would oxidise to Fe^{IV} in the electrochemical process. However, the material could not be produced in large quantities, thus further characterisation methods were limited.

5.6 Compound XIII: $Na_5Mn_3F_4(SO_4)_4$

The product crystallised as brown platy crystals. A suitable crystal was selected for a single crystal X-ray diffraction study. Data were collected at 120 K, with the resulting crystallographic information summarised in Table 5.17. The structure of the title compound adopts a triclinic unit cell with space group $P\bar{1}$ and exhibits a three-dimensional framework with channels down both the *a*- and *b*-axes. The structure is comprised of manganese centred octahedra and sulfate tetrahedra (Figure 5.14). Key bond lengths are listed in Table 5.18.

The structure of $Na_5Mn_3F_4(SO_4)_4$ contains mixed valence manganese sites; *trans*-$Mn^{III}O_2F_4$ and $Mn^{II}O_5F$ octahedra linked to form a triplet in which two $Mn^{II}O_5F$ octahedra corner-share through F atoms at *trans*-position of a $Mn^{III}O_2F_4$ octahedron. The observed Mn-F-Mn angle within the triplet is around 131.3°. Each *trans*-$Mn^{III}O_2F_4$ is also linked to two SO_4 tetrahedral units through μ^2-bridging oxygen atoms and another *trans*-fluoride is terminal as can be seen in Figure 5.11 (d). Each $Mn^{II}O_5F$ octahedra is linked to five SO_4 tetrahedra with one of these sulfate groups connected to the *trans*-$Mn^{III}O_2F_4$ octahedron, producing a three-membered ring. Each SO_4 tetrahedra is connected with three $Mn^{II}O_5F$ octahedra or two $Mn^{II}O_5F$ octahedra and a *trans*-$Mn^{III}O_2F_4$ octahedron to form a three-dimensional network with channels in the *ac* plane containing Na^+ cations.

EDS data confirmed, semi-quantitatively, the presence of fluorine within compound **VIII**. During the single crystal structure refinement, all fluorine sites within the Mn-coordination spheres were confirmed to be assigned correctly, as they produced ADP values that were similar to other anion species (provided in cif). The final charge balanced structure also proved this. BV calculations were completed for all anions within the materials, and the obtained values were all close to the expected values, where for fluorine the value is approximately 1, and for oxygen the value is 2. All values are shown in Table 5.19.

Table 5.17: *Crystal and diffraction information of compound XIII*

Empirical formula	$Na_5Mn_3F_4S_4O_{16}$
Formula weight ($gmol^{-1}$)	739.56
Temperature (K)	120
Appearance	Brown plate
Crystal size (mm)	$0.23 \times 0.17 \times 0.041$
Crystal system	Triclinic
Space group	$P\bar{1}$
Unit cell dimensions	a=6.6183(5) Å, b=6.6718(5) Å c=8.9410(7) Å, α=94.58(1)^o, β=96.81(2)^o, γ=92.38(1)^o
λ/Å	0.71073 Å (Mo K_α)
Volume ($Å^3$)	390.25(2)
Z	1
Density (gcm^{-3})	1.43
Reflections collected	3963
Unique reflections	2208
R_1 (all)	0.030
wR_2 (all)	0.058
GooF	0.926

There are two crystallographically distinct manganese octahedral environments present within the material; $Mn^{III}O_2F_4$ and $Mn^{II}O_5F$. Within the Mn^{III} octahedron, two fluorine and two oxygen atoms form bridges to neighbouring Mn^{II} and sulfur centres, and the other two fluorine atoms are terminal. For the $Mn^{II}O_5F$ octahedron, all five oxygen atoms within the coordination are bridging to five sulfate units, and the fluorine is shared with the $Mn^{III}O_2F_4$ octahedron. The bond lengths summarised in Table 5.18 show that , in the $Mn^{III}O_2F_4$ octahedron, the bridging Mn-F bond is clearly elongated with a length of 2.113(2) Å, due to tetragonal distortion of the octahedron caused by Jahn-Teller effect. The equatorial Mn-O bonds bridged to the sulfate units show a shorter length of 1.939(2) Å, and the terminal Mn-F bond is the shortest with a length of 1.839(2) Å. The observed bonds within the $Mn^{II}O_5F$ octahedron all display similar lengths; and the average of the six bonds is 2.159 Å. The BV sums (Mn1 = 2.97, Mn2 = 2.10) support the oxidation state of Mn1 is +3 and Mn2 is +2 respectively.

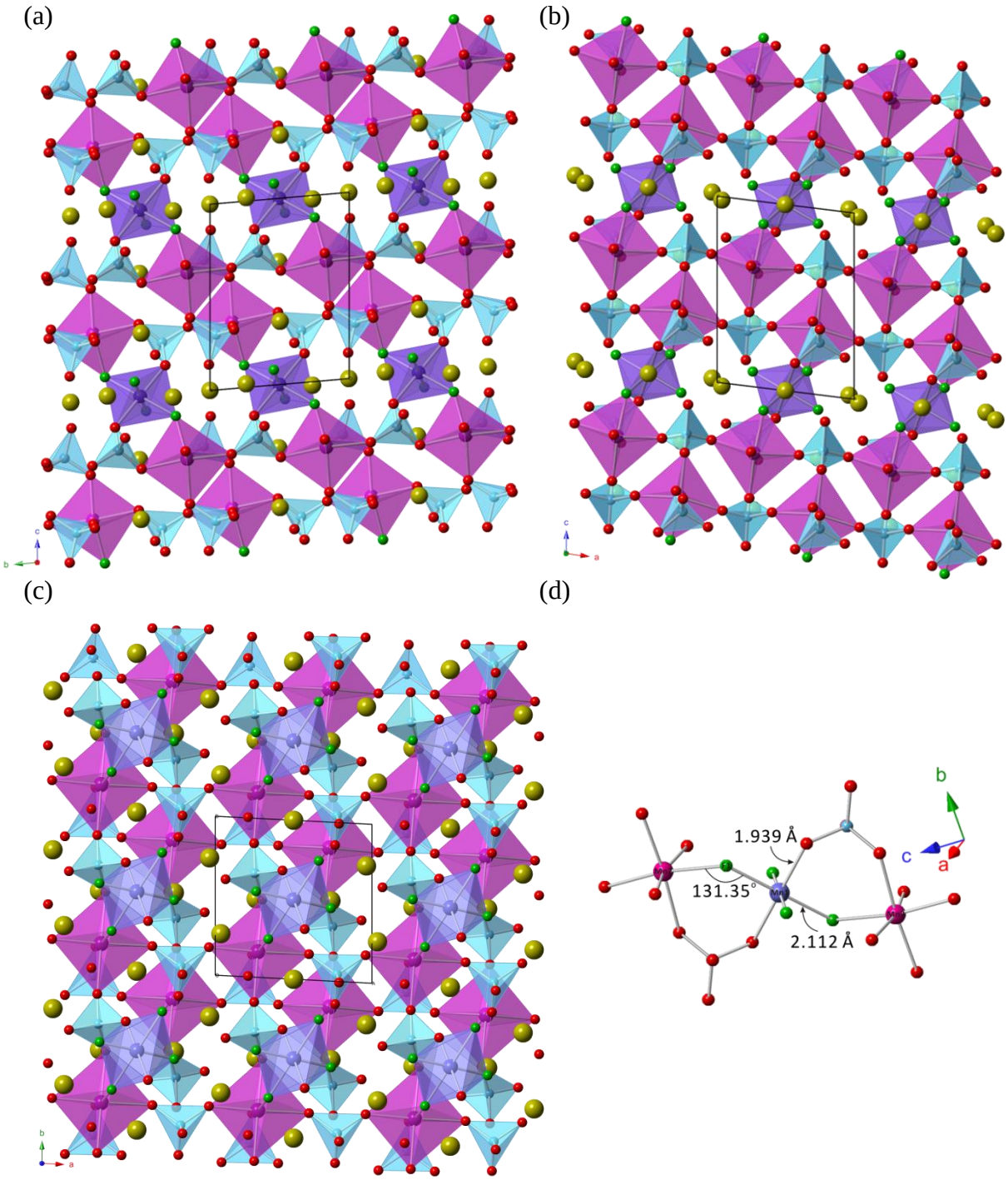

Figure 5.11*: The structure of $Na_5Mn_3F_4(SO_4)_4$ viewed down the (a) a-, (b) b-, (c) c-crystallographic axes, with the Mn^{II} octahedra are shown in pink, Mn^{III} are shown in purple, sulfate tetrahedra in light blue, oxygen atoms in red, fluorine atoms in green and Na^+ cations in gold yellow. (d) shows the manganese triplets with the manganese octahedra bridged by sulfate units.*

Table 5.18: *Bond lengths between selected atoms*

Bond	Bond length (Å)	Bond	Bond length (Å)
Mn1-O6	1.939(2) × 2	S1-O2	1.486(8)
Mn1-F1	2.113(3) × 2	S1-O3	1.477(9)
Mn1-F2	1.839(2) × 2	S1-O4	1.477(9)
Mn2-O1	2.153(2)	S1-O5	1.473(4)
Mn2-O2	2.232(2)	S2-O1	1.453(7)
Mn2-O3	2.150(2)	S2-O5	1.449(1)
Mn2-O4	2.129(2)	S2-O6	1.521(1)
Mn2-O5	2.148(2)	S2-O7	1.483(1)
Mn2-F1	2.139(2)		

Table 5.19: *Bond valence calculations of selected atoms*

Atom label	Bond valence	Atom label	Bond valence
O1	2.01 -	O7	1.99 -
O2	2.01 -	O8	2.04 -
O3	2.02 -	Mn1	2.97 +
O4	2.03 -	Mn2	2.10 +
O5	2.05 -	F1	1.04 -
O6	2.13 -	F2	1.01 -

There are two crystallographically independent sulfate tetrahedra (S1 and S2) present within the compound **VIII** structure. The S2 tetrahedron is connected to two $Mn^{III}O_2F_4$ octahedra and one $Mn^{II}O_5F$ octahedron through corner-sharing of three oxygen atoms, the fourth oxygen atoms is found to be terminal. The S1 tetrahedron is vertex-shared with three $Mn^{II}O_5F$ octahedra, *via* three μ^2-bridging oxygen atoms, whereas the fourth oxygen atom is the terminal site. Both terminal oxygen atoms within the two distinct sulfate units are aligned into the open region of the framework. By consideration of the bond lengths summarised in Table 5.15, it can be seen that the four S-O bonds within the S1 tetrahedron have similar lengths with an average of 1.489 Å. The O-S-O angles do not deviate substantially from the expected tetrahedral value of 109.28°, with all angles found in the range of ~106.3-111.2°. The S2 tetrahedron consists of two long and two short S-O bonds. The two long bonds involved in bridging to the MnF_4O_2 and MnO_5F octahedra form a three-membered ring, with lengths of 1.521(1) Å and 1.483(1) Å respectively. For the two short bonds, S2-O1 is a terminal bond but is slightly longer than the bridging S2-O5 bond.

However, this does not follow the trend of previously described sulfate units, where the bringing bonds are commonly found have longer lengths due to their specific bond orders. In fact it seems that the bond and angle variations in sulfate units strongly depend on the nature of the surrounding units.

The sodium cations reside in the channels, with three different coordination environments present (Na-X < 3.00 Å): $Na(1)O_7F$, $Na(2)O_4F_2$ and $Na(3)O_4F_3$. Two form irregular geometries and one forms an octahedron. The Na-O and Na-F bond distances were determined to be between ~2.265- 2.991 Å, and sodium ion separations are at 3.21 and 3.55-3.6 Å respectively.

EDS data confirms the presence of Na (12.3%), Mn (7.3%), S (11.2%), F (20.9%) and O (48.4%), with an experimental ratio of 1.69:1:1.55:2.87:6.67, approximately in agreement with the theoretical ratio of 1.67:1:1.33:1.33:5.33. An SEM image of a single crystal of compound **XIII** was recorded and is shown in Figure 5.12.

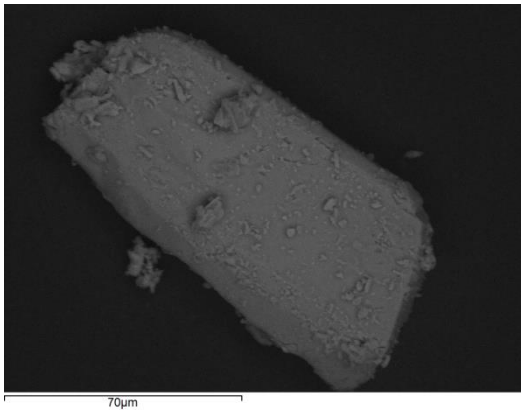

Figure 5.12: *SEM of a $Na_5Mn^{III}Mn^{II}{}_2F_4(SO_4)_4$ crystal*

5.7 Compound XIV: $Na_{12}Mn_3F_8(SO_4)_6$

The product crystallised as brown platy crystals. A suitable crystal was selected for a single crystal X-ray diffraction study. Data were collected at 120 K, with the resulting crystallographic information summarised in Table 5.20. The structure of the title compound exhibits a triclinic unit cell with space group $P\bar{1}$ and has a three-dimensional framework with open channels. The structure is comprised of manganese centred octahedra and sulfate tetrahedra (Figure 5.13). Key bond lengths are listed in Table 5.21.

The structure of compound **XIV** also displays the features of mixed valence manganese, similar to that of compound **XIII**. The structure consists of alternating connected Mn centred octahedra and SO_4 tetrahedra which form the three-dimensional framework with channels containing Na^+ cations running along all three lattice directions.

Three crystallographically distinct manganese coordination environments (Mn1, Mn2 and Mn3) are observed within the compound **XIV** structure; all the manganese ions are six-coordinate, forming octahedral-type geometries. For MnO_2F_4 (two sites Mn1 and Mn2), two axial oxygen atoms are found to bridge between the Mn- and S-centres, whilst the four fluorine atoms at equatorial positions are all terminal, which is uncommon. The MnO_6 (Mn 3) octahedron shares three oxygen atoms with six sulfate tetrahedral units through μ^2-bridging oxygen atoms. Table 5.20 shows all bond lengths within the Mn- and S-based polyhedra. Within the two MnO_2F_4 octahedra, two Mn-O bonds were observed to be elongated with length of 2.11 Å for Mn1 site, and 2.075 Å for Mn2 site. The equatorial Mn-F within the two Mn-sites are very similar, with the average Mn-F bond lengths for Mn1 and Mn2 sites being 1.891 Å and 1.866 Å respectively. The observed distortions of the two Mn-sites are subjected to the strong Jahn-Teller effect. Within the MnO_6 octahedron, the determined Mn-O bonds are in the range of 2.075-2.218 Å, which is comparable to Mn-O lengths in MnO_6 octahedra previously reported.[18] BV analysis has been carried out on the Mn cations as shown in Table 5.22, the calculated values for Mn1, Mn2 and Mn3 reflected their oxidation states of +3, +3 and +2 respectively.

Table 5.20: *Crystal and diffraction information of compound XIV*

Empirical formula	$Na_{12}Mn_3F_8S_6O_{24}$
Formula weight ($gmol^{-1}$)	1169.05
Temperature (K)	120
Appearance	Brown plate
Crystal size (mm)	0.22 × 0.15 × 0.05
Crystal system	Triclinic
Space group	$P\bar{1}$
Unit cell dimensions	a=9.5075(4) Å, b=9.5470(5) Å c=9.6386(5) Å, α=113.8(7)°, β=105.154(4)°, γ=108.954(1)°
λ/Å	0.71073 Å (Mo K_α)
Volume ($Å^3$)	674.72(2)
Z	1
Density (gcm^{-3})	2.14
Reflections collected	6303
Unique reflections	3086
R_1 (all)	0.035
wR_2 (all)	0.057
GooF	0.905

Table 5.21: *Bond lengths between selected atoms*

Bond	Bond length (Å)	Bond	Bond length (Å)	Bond	Bond length (Å)
Mn1-O10	2.110(4) × 2	Mn3-O7	2.218(5) × 2	S2-O2	1.480(5)
Mn1-F1	1.909(2) × 2	Mn3-O11	2.189(4) × 2	S2-O5	1.470(4)
Mn1-F3	2.873(3) × 2	S1-O3	1.466(3)	S2-O6	1.457(5)
Mn2-O12	2.142(6) × 2	S1-O7	1.465(5)	S3-O4	1.467(9)
Mn2-F2	1.867(3) × 2	S1-O9	1.457(1)	S3-O8	1.466(4)
Mn2-F4	1.866(8) × 2	S1-O10	1.486(5)	S3-O11	1.472(4)
Mn3-O2	2.075(3) × 2	S2-O1	1.469(4)	S3-O12	1.481(7)

Table 5.22: *Bond valence calculations of selected atoms*

Atom label	Bond valence	Atom label	Bond valence	Atom label	Bond valence
O1	2.10 -	O7	2.08 -	Mn1	2.89 +
O2	2.13 -	O8	1.99 -	Mn2	2.95 +
O3	2.01 -	O9	2.03 -	Mn3	2.20 +
O4	1.95 -	O10	2.03 -	F1	0.94 -
O5	2.10 -	O11	2.06 -	F2	0.96 -
O6	2.03 -	O12	2.08 -	F3	0.97 -

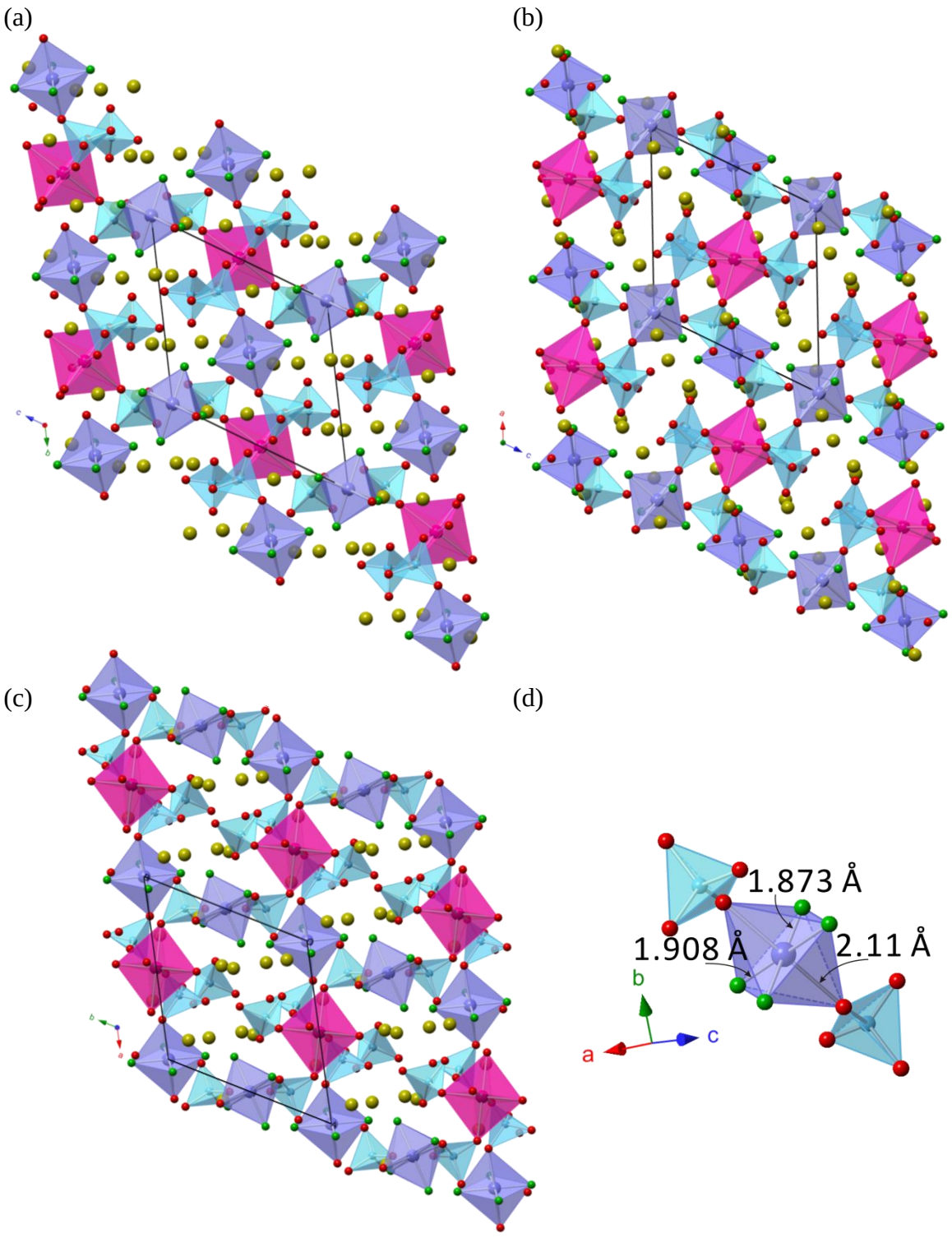

Figure 5.13: *The structure of $Na_{12}Mn_3F_8(SO_4)_6$ viewed down the (a) a-, (b) b-, (c) c-crystallographic axes, with the Mn^{II} octahedra are shown in pink, Mn^{III} are shown in purple, sulfate tetrahedra in light blue, oxygen atoms in red, fluorine atoms in green and Na^+ cations in gold yellow. (d) shows the unusual Mn1 site with four terminal fluorine*

There are three crystallographically distinct sulfate coordination environments (S1, S2 and S3) present within compound **XIV**. For the S1 and S3 tetrahedra, each of them is linked with two Fe centred octahedra through vertex-sharing of two μ^2-bridging oxygen atoms, and the two remaining oxygen atoms within each of the two tetrahedra are terminal and orientated towards the channels. In the S2 tetrahedral unit, three terminal sites are observed, and the single bridging oxygen atom is connected between the tetrahedron and the MnO_6 octahedron. Through consideration of the bond lengths summarised in Table 5.21, within the S1 tetrahedron, it can be seen that the S1-O10 bond is noticeably longer than other S-O bonds, where the O10 is found linked to form part of the MnO_2F_4 octahedron which exhibits strong Jahn-Teller distortion, whilst the other three S-O bonds (including one bridging bond) are quite similar. The observation is also found in previously described compounds, where the sulfate units are connected with an Mn^{III} species. Similarly, the S3 tetrahedron contains one long and three short S-O bonds, where the longer S3-O12 bond is linked to the $Mn^{III}O_2F_4$ octahedron with observed length of 1.481 Å, the S3-O11 bond which shows a slightly shorter length of 1.472(4) Å is connected to the $Mn^{II}O_6$ octahedron, and the two terminal bonds are again the shortest with an average length of 1.476 Å. For S2 tetrahedron, the bridging S2-O2 exhibits the longest distance of 1.480(5) Å, and the lengths of the three terminal S-O bonds are lying in the range of ~1.45-1.47 Å. The BV calculations have been carried out for all anions; as values given in Table 5.22 directly reflect the oxidation number of each anion, where the expected value for oxygen is 2, and for fluorine the expected value is 1.

The sodium cations reside in the channels, with six different coordination environments present (Na-X $<$ 3.00 Å), including NaF_2O_3, NaF_2O_4 and NaF_2O_5. They all form irregular geometries. The Na-F and Na-O bond distances were determined to be between ~2.3 Å and ~3.0 Å, and the separations between sodium cations are just above 3.37 Å.

5.8 Compound XV: $(NH_4)LiMn(SO_4)_2$

The product crystallised as pale pink platy crystals. A suitable crystal was selected for a single crystal X-ray diffraction study. Data were collected at 120 K, with the resulting crystallographic information summarised in Table 5.23. The structure of compound **XV** possesses a monoclinic unit cell with space group $P2_1/n$ forms a three-dimensional framework consisting of channels down the *c*-axis. The structure is comprised of manganese centred octahedra and sulfate tetrahedra (Figure 5.14). Key bond lengths are listed in Table 5.24.

The structure of compound **XV** consists of alternating Mn centred octahedra and sulfate tetrahedra, connected by sharing corners to build up the three-dimensional framework. Each Mn-octahedron is linked with six sulfate tetrahedra, and each sulfate tetrahedron is connected with three Mn-octahedra. Two different polyhedral rings are observed; the four-membered rings are produced based on two Mn- and two S- centred polyhedral units. Whereas the channels are formed based on eight-membered rings running down to the *c*-axis, which is occupied by both Li^+ and NH_4^+ cations. Single crystal refinement suggested that no fluorine was incorporated in the structures, and further confirmed through EDS analysis. Since MnF_3 was used in the reaction, it was suggested that fluoride acted as a mineraliser, aiding the reaction mechanism in the formation of the framework but is not incorporated into the structure.

One distinct manganese coordination environment is found within the structure. The Mn ion centre coordinates with six oxygen atoms form a MO_6 octahedron. BV calculation (Mn = 2.08) indicates that the oxidation states of Mn centre within the MnO_6 octahedron is +2, as shown in Table 5.25. Within the MnO_6 octahedron, all six oxygen form bridges to the six neighbouring sulfate groups. By consideration of the bond lengths summarised in Table 5.24, all six Mn-O bridging bonds display similar length, the average of the six bonds is 2.171 Å, which is in good agreement with the sums of Shannon crystal radii (Mn^{II}-O = 2.23 Å).[14]

Table 5.23: *Crystal and diffraction information of compound XV*

Empirical formula	$LiMnS_2O_8NH_4$
Formula weight ($gmol^{-1}$)	272.04
Temperature (K)	120
Appearance	Pale pink plate
Crystal size (mm)	0.12 × 0.09 × 0.03
Crystal system	Monoclinic
Space group	$P2_1/n$
Unit cell dimensions	a=8.0686(3) Å, b=10.1669(3) Å c=9.1528(4) Å, β=114.667(9)^o
λ/Å	0.71073 Å (Mo K_α)
Volume ($Å^3$)	682.31(3)
Z	4
Density (gcm^{-3})	2.10
Reflections collected	9321
Unique reflections	2715
R_1 (all)	0.0287
wR_2 (all)	0.0976
GooF	1.379

Table 5.24: *Bond lengths between selected atoms*

Bond	Bond length (Å)	Bond	Bond length (Å)
Mn1-O1	2.193(7)	S1-O2	1.487(7)
Mn1-O2	2.164(7)	S1-O3	1.476(2)
Mn1-O3	2.221(1)	S1-O4	1.457(4)
Mn1-O6	2.153(7)	S2-O5	1.479(9)
Mn1-O7	2.148(8)	S2-O6	1.486(1)
Mn1-O8	2.146(6)	S2-O7	1.467(9)
S1-O1	1.492(6)	S2-O8	1.477(9)

Table 5.25: *Bond valence calculations of selected atoms*

Atom label	Bond valence	Atom label	Bond valence
O1	1.98 -	O6	1.94 -
O2	1.98 -	O7	1.93 -
O3	1.91 -	O8	1.95 -
O4	1.88 -	Mn1	2.08 +
O5	1.97 -	Li1	1.09 +

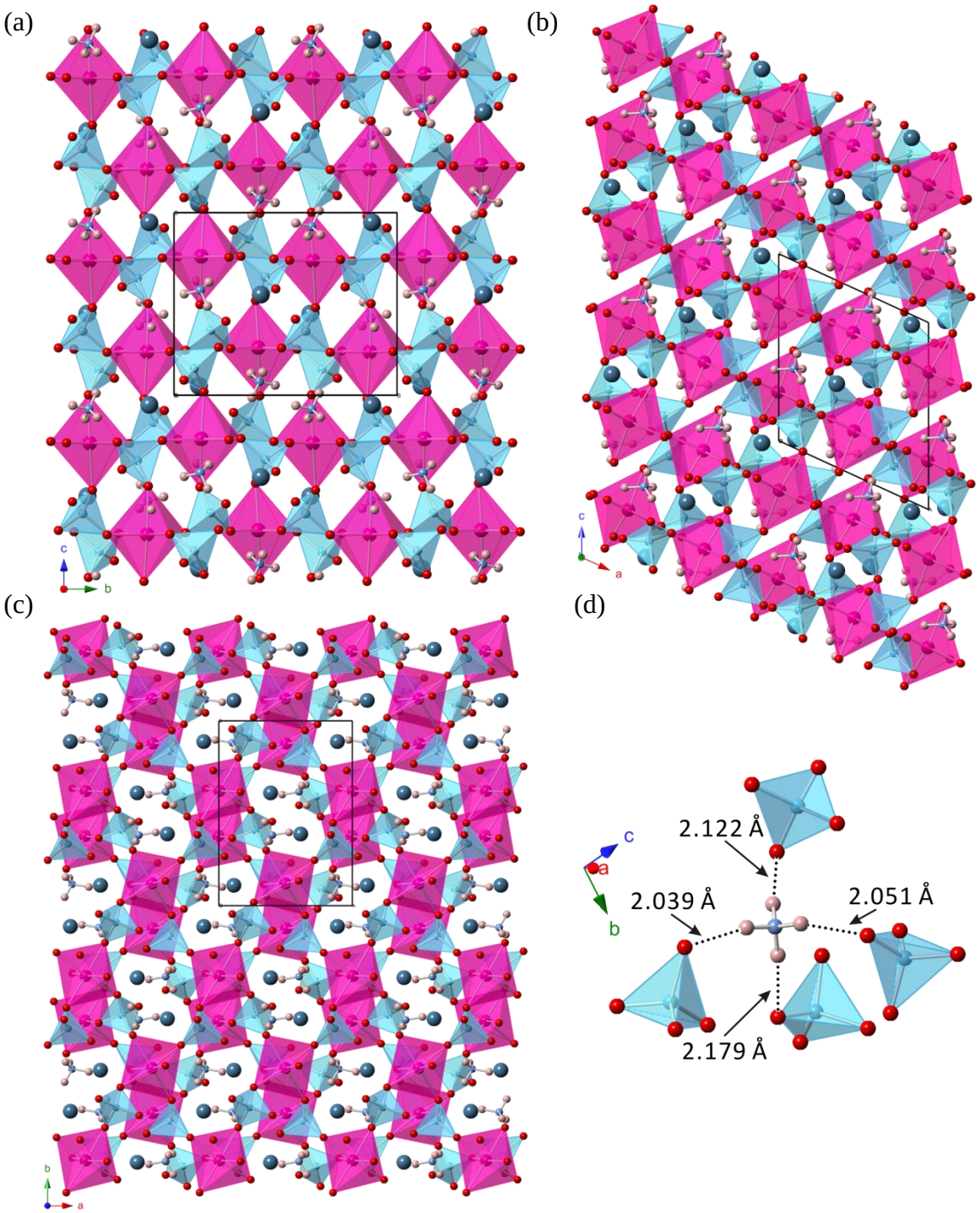

Figure 5.14*: The structure of $(NH_4)LiMn(SO_4)_2$ viewed down the (a) a-, (b) b-, (c) c-crystallographic axes, with the Mn^{II} octahedra are shown in pink, sulfate tetrahedra in light blue, oxygen atoms in red, Li^+ cations in sky blue, ammonia tetrahedra in purple. (d) shows the hydrogen bonding between the NH_4 cations and framework oxygen atoms. Hydrogen bonding is represented by black dashed lines.*

Two distinct sulfate tetrahedral environments are found within the structure, S1 and S2 are used to represent the two tetrahedral units. Both tetrahedra are connected with three adjacent Mn-octahedra through vertex-sharing of three μ^2-bridging oxygen atoms in each of the tetrahedral group, where the fourth oxygen is terminal and orientated toward the channels. The bond lengths summarised in Table 5.24 shows the three bridging S-O bonds within the S1 tetrahedral unit are significantly longer than the terminal bond and lie in the range of ~1.47-1.50 Å, and the terminal bond displays a relatively short length of 1.457(4) Å. The observed bond distances in S2 tetrahedral units are slightly different, where all four S-O bonds are very similar in length, with the average length of the four bonds being 1.477 Å. The O-S-O angles within the S1 tetrahedron are found in the range of ~104-111.5^o. The resulting small O-S-O angle may be attributed to the multi-bond character of S-O bond to the bridging oxygen.[10] For the S2 unit, the O-S-O angles are very close to the 109.5^o value of a regular tetrahedron, the observed angles are being between 108.42^o and 111.76^o, with a mean O-S-O angle of 109.46^o.

There are two different types of cations present within the material structure, NH_4^+ and Li^+. The ammonium hydrogen atoms within the NH_4^+ cation were found directly from the SXD data. These ammonium cations reside in the channels forming hydrogen bonds to the framework oxygen anions, as shown in Figure 5.14 (d). The observed distances for the hydrogen bond NH…O are in the range of ~2.04-2.18 Å.

Li^+ cations also reside in the channels along the *c*-axis, and adopt a single coordination environment. The Li centre coordinates with five oxygen atoms forms a five-fold irregular coordination with distances lying between ~1.95 Å and 2.24 Å, which is in agreement with the Shannon crystal radii.[14] The Li-Li separation distance within the structure is ~2.79 Å. The BV calculation shows a sum of 1.09 for Li^+ in agreement with the oxidation number on lithium cation.

The IR spectrum of compound **XV** (Appendix 4) shows a broad absorption band at 3480-2831 cm^{-1}, which is expected for the stretching mode of N-H within the ammonium cations, and a peak observed at 1409.94 cm^{-1} is attributed to the N-H bend. This supported the presence of ammonium within the structure. The thermal stability of compound **XV** was also studied by TGA, and the data are shown in Figure 5.15. A sample of 16.617 mg

was heated in air from room temperature to 500 ℃. There was a significant weight loss observed within the temperature range from 300 ^{o}C to 485 ^{o}C. The rapid drop in weight was assumed to be due to the NH_4^+ cations being removed from structure. However the percentage weight lost within this temperature range is greater than the corresponding ammonium content within the structure, presumably due to the structural collapse plus HF loss that resulted by removing the ammonium cations at such temperature. The DTA trace shows an exothermic peak within this temperature range, which also indicated the collapse of the framework structure.

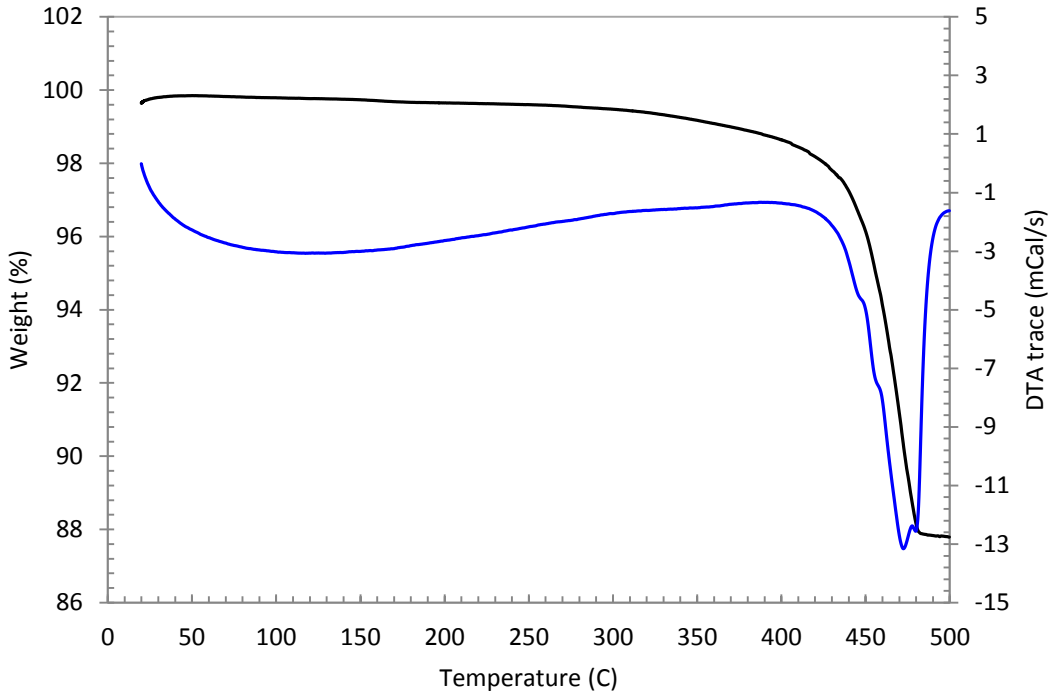

Figure 5.15: *TGA plot for the thermal decomposition of $(NH_4)LiMn(SO_4)_2$. Black and green lines represented the TGA and DTA data as a function of temperature respectively.*

5.9 General summary

A range of novel transition metal sulfate materials have been prepared using the hydrofluorothermal method. All reactions were undertaken in fluoride-rich media, in similar conditions to those used for the synthesis of transition metal phosphates materials. Most of the produced compounds show that their structures have successfully incorporated fluoride, with the exception of compound **XV**. The structures presented herein were obtained from the SXD. PXD, EDS, IR as well as TGA were also used to further characterise the compounds.

Table 5.1 showed the reaction conditions of the new synthesised compounds. All reactions were completed under mild hydrothermal conditions, with a reaction temperature of 175 ^{o}C used. The prepared compounds present a number of different structural dimensionalities, ranging from one-dimensional chains to three-dimensional frameworks, which are similar to the previously produced phosphate structures in chapter four. The choice of sulfate instead of phosphate was due to their similar chemical properties, and similar atomic radii with the adoption of tetrahedral coordination.[19] Since all reactions were undertaken in fluoride-rich media, it was possible to produce metal sulfate structures that incorporated fluoride and show new structural features. Synthesis of metal sulfate structures employed H_2SO_4 as the sulfate source; other starting materials used include MnF_3, FeF_3 and counter-cation sources such as LiOH, NaOH, KOH or NH_4OH.

Compared to the phosphate tetrahedra, the sulfate tetrahedra found within the metal sulfate structures are noticeably different. Despite both adopting tetrahedral geometries, fluoride can be incorporated into the phosphate tetrahedron to form PO_3F anions. The compounds presented in this chapter all consist of SO_4 anions, without the incorporation of fluoride. The SO_4 anion is isoelectronic with the PO_3F anion, with the latter commonly found within the previously studied metal phosphate frameworks. For the metal sulfate structures, the fluoride ions were more frequently incorporated to the metal ion polyhedra in the form of $[MO_nF_{6-n}]^{m-}$ and acted as either bridging sites or terminal sites, for example, within the structures of **VIII**, **IX** and **XIII**. More rarely, e.g. within the structure of **XIV**, the manganese octahedron contained four co-planar fluorides that were all terminal and pointed into the channels. The oxygen atoms within the SO_4 tetrahedra were not always

involved in bridging, in fact one or more oxygen atom were typically terminal, and consistently point into inter-framework, -layer or-chain spaces, forming ionic interactions with the charge balancing counter cations. The behaviour of the terminal oxygen within the SO_4 is identical to the fluoride within the PO_3F tetrahedron, acting to break the connectivity of the polyhedra, resulting in a reduction of structural dimensionality. The bond lengths among the sulfate tetrahedra are regular, where the bridging S-O bonds are generally longer than the terminal bonds, and the O-S-O angles between the terminal bonds are greater. This is likely due to the multiple-bond character of S-O bonds in SO_4 anions.[11]

Examination of the metal coordination environments found within the metal sulfate structures indicated the formation of prevalently octahedral geometries with a variety of distortions. For Mn^{III} species, distortions were expected to be caused by the Jahn-Teller effect, with a noticeable elongation of bond observed for octahedra environments. The average length of the elongated bonds for all Mn^{III} octahedra among the structures is 2.148 Å, compared to the equatorial bonds with a mean of 1.875 Å. For compound **XI**, the JT-distortion for Mn-octahedra is the strongest, with $r_{axial}/r_{equatorial}$ = 1.20, as mentioned previously. For other structures the $r_{axial}/r_{equatorial}$ of Mn^{III} octahedra are: 1.12 for **XIII**, 1.12 (Mn1) and 1.15 (Mn2) for **XIV** respectively. For other metal octahedral coordination spheres such as Fe and V, the bond lengths indicate that the observed terminal bonds are significantly shorter than the bridging bonds. Similar to the terminal bonds, the M-F bonds are usually slightly shorter than comparable M-O bonds; this is due to the smaller ionic radius of F^- than the O^{2-}. For the Mn^{II} species, all six bonds within the octahedral coordinations are above or close to 2.1 Å, this is comparable to those reported in $MnSO_4$.[20]

Other features of the metal sulfate structures produced and presented in this chapter are the relevant possible applications. Recent research on metal sulfate materials is very focused on searching for new potential electrodes for either Li-ion or Na-ion batteries.[21-24] Although $LiFePO_4$ has emerged as promising candidate,[1] such a material shows intrinsically low ionic and electronic transport. However, these issues could in principle be solved by incorporating fluoride and more electron-withdrawing SO_4 anions into the structures.[4] In addition, the mixed SO_4^{2-} and F^- anions system generates candidate materials which exhibit higher cell potentials, through the inductive effect of SO_4, as the greater

electronegativity of sulphur, compared to phosphorus, weakens the M-O bonds.[2, 3] As a consequence, $LiFeSO_4F$ shows a potential of 3.9 V.[25] The research work present here has made some progress on seeking new possible electrode material for Na-ion batteries.[24] Compound **XI**, the isostructural $Na_3M^{III}F_2(SO_4)_2$ (M = V, Mn, Fe) has been prepared directly through the hydrofluorothermal route by using MF_3 (M = V, Mn, Fe), H_3PO_4 and NaOH as starting materials. These compounds, having layered structures with Na^+ cations residing in between the layers, are seen as possible positive-electrodes for Na-ion batteries. Electrochemical tests were carried on $Na_3M^{III}F_2(SO_4)_2$ (M = V, Fe), and the results indicate that the voltages for metal cations oxidation within the two materials *versus* sodium metal are correspondingly higher than many other reported materials. The drawback is likely to arise from the poor conductivities of these two materials, due to the lack of direct M-M or M-X-M (X = O, F) interactions within the structures. However, these might be improved by further coating with carbon as well as nanostructuring. Through consideration of all structures present herein, compound **VIII** and **XII** can also be considered as potential candidates.

Thermal investigations were carried out on compounds **X** and **XV** through TGA. The results indicate that removing the water molecules and ammonium cations within the two compounds destabilised the overall structures and resulted in structural collapse.

5.10 Conclusion

Nine new metal fluorosulfates and one metal sulfate compounds have been produced via the hydrofluorothermal method. Through using metal fluorides as fluorine providers, nine structures were produced successfully incorporating fluoride anions. By introducing polyanionic SO_4 within the material structures, some of the materials may have potential use in making high voltage rechargeable batteries, due to the greater inductive effect of SO_4 ions over PO_4 ions and the highly electronegative fluoride within the structures.

5.11 Reference

1. A. K. Padhi, K. S. Nanjundaswamy and J. B. Goodenough, *J. Electrochem. Soc.*, 1997, **144**, 1188-1194.
2. C. Masquelier and L. Croguennec, *Chem. Rev.*, 2013, **113**, 6552-6591.
3. B. L. Ellis, W. R. M. Makahnouk, W. N. Rowan-Weetaluktuk, D. H. Ryan and L. F. Nazar, *Chem. Mater.*, 2010, **22**, 1059-1070.
4. N. Recham, J. N. Chotard, L. Dupont, C. Delacourt, W. Walker, M. Armand and J. M. Tarascon, *Nat. Mater.*, 2010, **9**, 68-74.
5. L. Fanfani, A. Nunzi and P. F. Zanazzi, *Am. Mineral.*, 1971, **56**, 751-&.
6. K. Adil, M. Leblanc, V. Maisonneuve and P. Lightfoot, *Dalton Trans.*, 2010, **39**, 5983-5993.
7. J. A. Armstrong, E. R. Williams and M. T. Weller, *J. Am. Chem. Soc.*, 2011, **133**, 8252-8263.
8. G. Paul, A. Choudhury, R. Nagarajan and C. N. R. Rao, *Inorg. Chem.*, 2003, **42**, 2004-2013.
9. G. Paul, A. Choudhury and C. N. R. Rao, *Chem. Mater.*, 2003, **15**, 1174-1180.
10. U. Klein, F. Hahn, W. Massa and J. Pebler, *Z. Anorg. Allg. Chem.*, 2005, **631**, 1785-1792.
11. A. J. Edwards, *J. Chem. Soc. A*, 1971, 3074-&.
12. D. R. Sears and J. L. Hoard, *J. Chem. Phys*, 1969, **50**, 1066-&.
13. J. A. Armstrong, E. R. Williams and M. T. Weller, *Dalton Trans.*, 2013, **42**, 2302-2308.
14. R. D. Shannon and C. T. Prewitt, *Acta Crystallogr. Sect. B*, 1969, **B25**, 925-946.
15. P. G. Jonsson and I. Olovsson, *Acta Crystallogr. Sect. B*, 1968, **B 24**, 559-&.
16. Q. Wang, A. Madsen, J. R. Owen and M. T. Weller, *Chem. Commun.*, 2013, **49**, 2121-2123.
17. P. Barpanda, T. Ye, S. Nishimura, S. C. Chung, Y. Yamada, M. Okubo, H. S. Zhou and A. Yamada, *Electrochem. Commun.*, 2012, **24**, 116-119.
18. A. Larranaga, J. L. Mesa, J. L. Pizarro, L. Lezama, J. P. Chapman, M. I. Arriortua and T. Rojo, *Dalton Trans.*, 2005, 1727-1733.
19. L. Willy, *Nature.*, 1930, **126**, 916.

20. G. Will, B. C. Frazer and B. C. Cox, *Acta Crystallogr., Sect. A: Found. Crystallogr.*, 1965, **19**, 854-&.

21. M. Ramzan, S. Lebegue and R. Ahuja, *Phys. Rev. B: Condens. Matter Mater. Phys.*, 2010, **82**, 5.

22. P. Barpanda, M. Ati, B. C. Melot, G. Rousse, J. N. Chotard, M. L. Doublet, M. T. Sougrati, S. A. Corr, J. C. Jumas and J. M. Tarascon, *Nat Mater*, 2011, **10**, 772-779.

23. M. Ati, M. T. Sougrati, N. Recham, P. Barpanda, M. Reynaud, C. Delacourt, M. Armand, J. C. Jumas and J. M. Tarascon, *Batteries and Energy Technology (General)- 219th Ecs Meeting*, 2011, **35**, 57-63.

24. Q. L. Wang, A. Madsen, J. R. Owen and M. T. Weller, *Chem. Commun.*, 2013, **49**, 2121-2123.

25. P. Barpanda, M. Ati, B. C. Melot, G. Rousse, J. N. Chotard, M. L. Doublet, M. T. Sougrati, S. A. Corr, J. C. Jumas and J. M. Tarascon, *Nat. Mater.*, 2011, **10**, 772-779.

CHAPTER SIX: TEMPLATED TRANSITION METAL SULFATES/FLUOROSULFATES

6.0 Introduction

Templating agents have been used widely in hydrothermal reactions for the preparation of new framework materials. The major interest in templating agents arises from their structure directing abilities, used for the formation of many functional materials, such as zeolitic materials and mesoporous silicates. The sizes and shapes of the templating reagents can significantly influence the structural features of these materials. Initially templated syntheses were aimed at the production of materials whose structures consist of TO_4 (T = Al, P, Si) tetrahedra as the primary building units, such as aluminosilicate and aluminophosphate zeolites. However, other templated structures formed from different tetrahedral units have also been targeted, including arsenates[1], selenates[2] and sulfates[3].

Within a templated reaction, the structure of the material can be directed by the templating agent through hydrogen bonding and electrostatic interactions. The latter is considered as the driving force for the structure condensing, whilst the hydrogen bonding is expected to cause changes in crystal packing.[4] The structure directing agents employed for templating reactions are commonly amines, which are often protonated and become positively charged due to acidic reaction conditions, thereby also making them counter cations to charge balance a negatively charged framework. This behaviour is similar to that performed by other monovalent and divalent cations in the metal phosphate/sulfate structures (chapter four and five).

Different amine templates were trialled, and reaction temperature and time for the different synthesises were also varied. Table 6.1 summarises the reaction conditions used for any newly produced templated metal sulfate structures; including starting materials, reaction temperature and time, in addition to the observations on the final products. The typical hydrofluorothermal reactions were carried out in 23 mL Teflon-lined Parr autoclaves. The resulting crystalline materials were primarily analysed *via* SXD, with supporting techniques such as IR, EDS and TGA also completed on the products to characterise them where possible. Successful reactions resulting in the production of new phases are discussed in detail in this chapter.

Table 6.1: *Synthetic conditions for template metal sulfate/fluorosulfate structures*

Starting regents	Temp (^{o}C)	Time (hours)	Crystal morphology and purity	Product(s)	Thesis section
MnF_3 (0.475 mmol , 0.0532 g); H_2SO_4 (1.9 mmol, 0.1034 ml); *trans*-1,4-diaminocyclohexane (0.95 mmol, 0.1085 g)	150	48	Pale pink rod Single phase	$[H_2\text{-}(C_6H_{16}N_2)]Mn_2(SO_4)_2F_2$	6.1 (XVI)
MnF_3 (0.536 mmol, 0.0532 g); H_2SO_4 (1.9 mmol, 0.1034 ml); Hydrazine (0.95 mmol, 0.0942 ml)	150	96	Pale pink ellipse Single phase	$[H_2\text{-}(N_2H_6)]_5Mn(SO_4)_6$	6.2 (XVII)
VF_3 (0.4 mmol, 0.0432 g); H_2SO_4 (1.9 mmol, 0.0871 ml); *trans*-1,4-diaminocyclohexane (0.95 mmol, 0.0914 g)	175	48	Dark green needle Single phase	$[H_2\text{-}(C_6H_{16}N_2)]V(SO_4)_2F$	6.3 (XVIII)
FeF_2 (0.714 mmol, 0.067 g); H_2SO_4 (2.856 mmol, 0.1553 ml); *trans*-1,4-diaminocyclohexane (1.42 mmol, 0.1631 g)	175	48	Dark brown needle Single phase	$[H_2\text{-}(C_6H_{16}N_2)]Fe(SO_4)_2F$	6.3 (XVIII)
FeF_3 (0.599 mmol, 0.1 g); H_2SO_4 (1.198 mmol, 0.0562 ml); Ethylenediamine (0.599 mmol, 0.04 ml)	150	48	Green rod Single phase	$[H_2\text{-}(C_2H_8N_2)](NH_4)Fe(SO_4)_3$	6.4 (XIX)

6.1 Compound XVI: [H_2-*trans*-1,4-diaminocyclohexane]$Mn_2F_2(SO_4)_2$

The product crystallised as pale pink rod shaped crystals. A suitable crystal was selected for a single crystal X-ray diffraction study. All data were collected at 120 K, with the resulting crystallographic information summarised in Table 6.2. The structure of compound **XVI** has a monoclinic unit cell, with space group *P*2/*c*, and forms a two-dimensional structure. The structure is comprised of manganese centred octahedra and sulfate tetrahedra (Figure 6.1). Key bond lengths are listed in Table 6.3.

Within compound **XVI**, each identical layer is formed from manganese triplets as the basic building unit, which are further connected by sulfate tetrahedra along the *c*-axis. Adjacent layers are parallel to each other and are orientated perpendicular to the *a*-axis. Within each polyhedral layer, the manganese centred octahedral triplets alternate in orientation and are linked end to end by sulfate tetrahedra to form undulating polyhedral chains. These chains are aligned parallel to each other and are further cross-linked by additional sulfate tetrahedra, resulting in the polyhedral layer (Figure 6.1 a). Within the Mn-octahedra triplet building unit, the three Mn centred octahedra are connected through sharing *trans* F-Mn-O edges of a central Mn-octahedron. The two Mn-octahedra on either side of the triplet are identical. The Mn-O-Mn and Mn-F-Mn angles found between the connected Mn centres are 95.55^o and 109.62^o respectively. The O atoms among the *trans* F-Mn-O edges further bridge to two sulfate tetrahedra, *via* μ^3-bridging, and alternate along the manganese triplet. In addition, the adjacent Mn-octahedra within the triplet are bridged by sulfate tetrahedra through μ^2-bridging oxygens occupying the axial sites of the Mn-octahedra and producing three-membered rings. The two-dimensional layers are separated, with the inter-layer spacing occupied by diprotonated *trans*-1,4-diaminocyclohexane cations, $[H_3N\text{-}C_6H_{10}\text{-}NH_3]^{2+}$.

There are two distinct manganese coordination environments Mn1 and Mn2 present within the structure. Each Mn centre coordinates with four oxygen and two fluorine atoms, forming a MnO_4F_2 octahedron. The EDS analysis confirms the presence of fluorine within compound **XVI**. During the single crystal refinement, the two fluoride sites in the MnO_4F_2 octahedron were initially assigned as oxide anions, however the resulting ADP values were smaller than other anion sites. Reassignments of these two sites as fluoride resulted in improved ADP values, similar to other anions, and the data

fitting residual values also being reduced. The two fluoride sites were further examined through BV calculations which are given in Table 6.4.

Table 6.2: *Crystal and diffraction information of compound XVI*

Empirical formula	$N_2C_6H_{14}Mn_2S_2O_8F_2$
Formula weight ($gmol^{-1}$)	454.19
Temperature (K)	120
Appearance	Pale pink rod
Crystal size (mm^3)	0.2 × 0.11 × 0.05
Crystal system	Monoclinic
Space group	*P*2/*c*
Unit cell dimensions	a=12.032(3) Å, b=5.672(1) Å c=20.430(4) Å, β=90.502(5)^o
λ/Å	0.71073 Å (Mo K_α)
Volume ($Å^3$)	1394.17
Z	2
Density (gcm^{-3})	2.13
Reflections collected	12680
Unique reflections	5421
R_1 (all data)	0.0492
wR_2 (all data)	0.1662
GooF	1.164

The fluoride anions occupy on the Mn-octahedra sites at *trans*-positions and act as bridging or terminal species. The six anionic sites within the Mn2 octahedron are all involved in bridging. Within the Mn1 octahedron, five anionic sites bridge to neighbouring units, including edge-sharing (O-Mn-F edge) with the Mn2 octahedron and corner-sharing (μ^2- or μ^3-bridging oxygen) with different sulfate groups. The sixth site is terminated by a fluoride anion. Key bond lengths for the Mn-octahedra are given in Table 6.3. As mentioned earlier, the Mn-octahedra form a triplet through the sharing of an O-Mn-F edge, and this edge-sharing of octahedra may result in geometric distortions from the ideal packing geometry. For the Mn1 site, the bond created between the Mn centre and the μ^3-bridging oxygen has a length of 2.319(6) Å, which is longer than the other bridging bonds (created between the Mn-centre to μ^2-brigding sites) with a mean length of 2.133 Å. The terminal Mn-F bond is slightly shorter (2.122(7) Å). The observed X-Mn-X (X = O, F) angles are in the range of ~74.3-98.9^o, compare to the idealised 90^o for a regular octahedron; therefore the Mn1 site is strongly distorted.

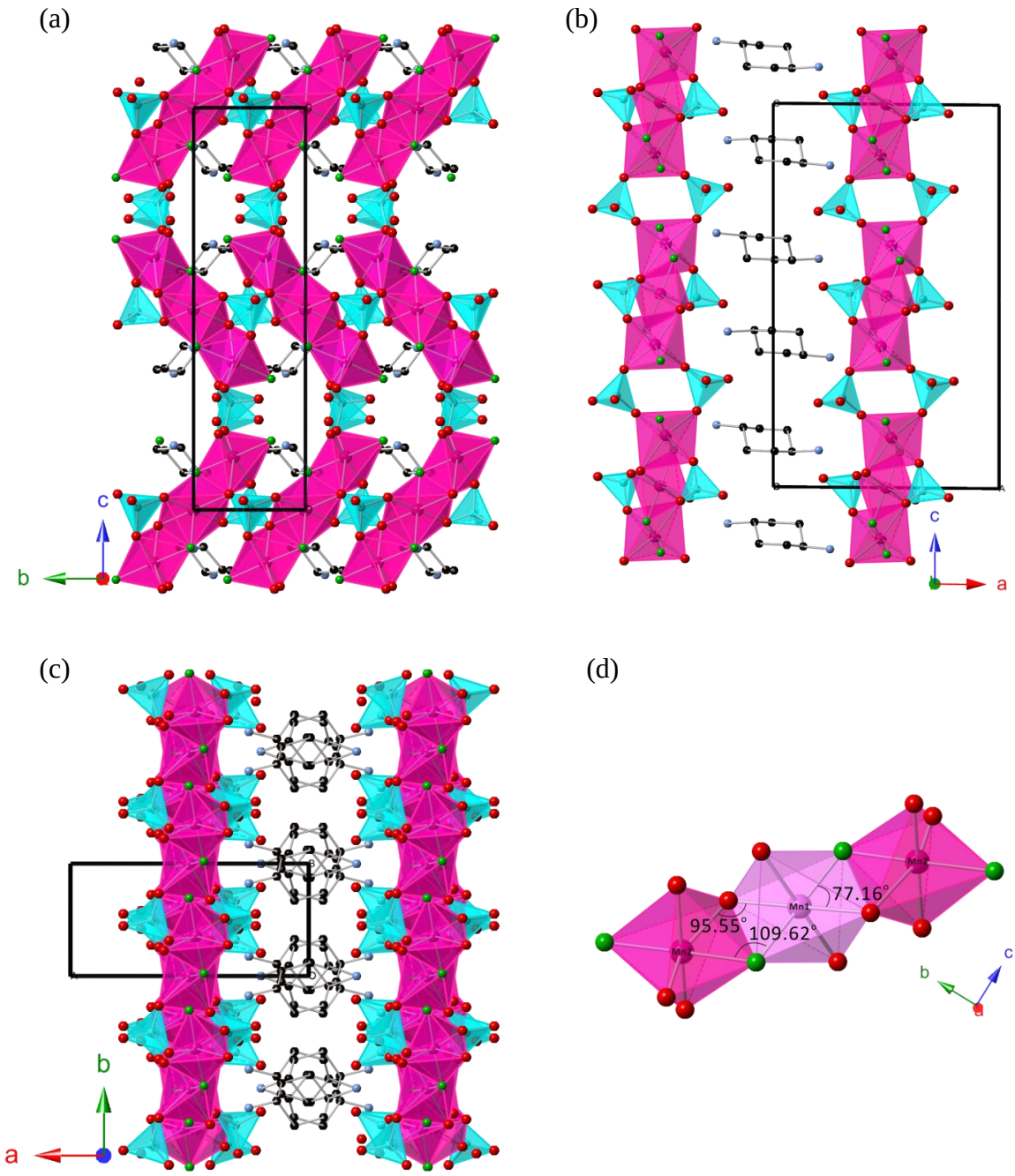

Figure 6.1: *The structure of [H_2-trans-1,4-diaminocyclohexane]$Mn_2F_2(SO_4)_2$ viewed down the (a) a-, (b) b-, (c) c-crystallographic axes, where the Mn^{II} octahedra are shown in pink, sulfate tetrahedra in sky blue, oxygen atoms in red, fluorine in green, nitrogen in blue, hydrogen in pale pink and carbon in black. (d) shows the edge-sharing MnF_2O_4 octahedra unit in the structure*

For the Mn2 octahedron, the bridging Mn-O bonds are all have similar lengths. The bonds created between the Mn-centre to the μ^2- and μ^3-briding oxygen have lengths of 2.261(2) Å and 2.246(2) Å respectively. However, the bridging Mn-F, with a length of 2.036(3) Å, is clearly shorter than the Mn-O bonds, thus making the Mn2 site more like a 'compressed' octahedron. The observed X-Mn-X (X = O, F) angles within the Mn2

octahedron lie between ~84.1^{o} and ~95.9^{o}. The oxidation states of the Mn cations within the structure were established by consideration of the bond lengths and BV calculations. The Mn cations were suggested to adopt + 2 oxidation states, as the determined bond lengths within the two Mn-octahedra are comparable to the reported Mn^{II} complexes.[5] These were further confirmed by the BV calculations, where the BV sums for the two manganese centres (Mn1 and Mn2) are 1.98 and 1.96 respectively. The low BV values of the oxygen atoms are due to the hydrogen bonding, which are not included in calculations, where the expected BV value for oxygen atoms is approximately 2.

Table 6.3: *Bond lengths between selected atoms*

Bond	Bond length (Å)	Bond	Bond length (Å)
Mn1-O1	2.211(5)	S1-O3	1.469(1)
Mn1-O2	2.319(6)	S1-O4	1.495(2)
Mn1-O4	2.161(5)	S1-O6	1.478(3)
Mn1-O8	2.127(4)	S1-O8	1.483(3)
Mn1-F1	2.122(7)	S2-O1	1.481(1)
Mn1-F2	2.101(9)	S2-O2	1.505(2)
Mn2-O2	2.246(2) × 2	S2-O5	1.483(7)
Mn2-O5	2.261(2) × 2	S2-O7	1.461(2)
Mn2-F2	2.036(3) × 2		

Compound **XVI** contains two crystallographically distinct sulfate tetrahedral units, S1 and S2, within its structure. The S1 units bridges between the manganese triplets through bridging two Mn2 octahedra (*via* vertex-sharing of two μ^2-briding oxygen per S1 tetrahedral unit) on either side of the triplets, creating four-membered rings based on two Mn- and two S-centred polyhedral units. The other two vertices within the S1 tetrahedron are terminal and oriented towards the inter-layer space. Bond lengths given in Table 6.3 show the bridging S-O bonds within the S1 unit are slightly longer than the terminal S-O bonds, due to the effect of the bridging interaction within the sulfate group.[6] The average lengths of the bridging and terminal bonds are 1.489 Å and 1.473 Å respectively, which are comparable to the S-O lengths described in the literature.[7] The shorter S-O bonds are considered to be modified by multiple-bond character, which is similar to that found in other compounds such as **IX** (chapter five). The observed O-S-O angles within the S1 unit are in the range of ~108.8^{o}-110.9^{o}, therefore, the S1 tetrahedron is regarded as almost regular. For the S2 tetrahedral unit, the three bridging S-O bonds can be seen to have longer distances, in particular the bond created between

the sulfur centre and the μ^3-bridging oxygen. The mean length of the three bridging S-O bonds is 1.490 Å, 0.04 Å greater than the shorter terminal S-O bond. The O-S-O angles within the S2 unit lie between ~108.4° and ~110.7°. Similarly to other metal sulfate structures, no fluoride was found to be incorporated in the sulfur coordination geometries.

Table 6.4: *Bond valence calculations of selected atoms*

Atom label	Bond valence	Atom label	Bond valence
O1	1.89 -	O7	1.70 -
O2	1.85 -	O8	1.84 -
O3	1.73 -	F1	0.71 -
O4	1.88 -	F2	0.82 -
O5	1.84 -	Mn1	1.98 +
O6	1.86 -	Mn2	1.96 +

As mentioned previously, $[H_3N\text{-}C_6H_{10}\text{-}NH_3]^{2+}$ cations reside between the layers. The arrangement of the template molecules is such that the cyclohexane rings reside in the centre of the inter-layer spaces, and NH_3^+ groups attached to carbon at the 1, 4 positions in the cyclohexane ring are orientated towards the layers. During the structure refinement, the positions of nitrogen and carbon atoms were located directly from SXD data. After refinement of the $[Mn_2F_2(SO_4)_2]^{2-}$ layers, it was suggested that the template unit must be described as being diprotonated, in order for correct charge-balance, thus giving $[H_3N\text{-}C_6H_{10}\text{-}NH_3]^{2+}$. Location of the hydrogen atoms of the template unit from Fourier maps was impractical and therefore hydrogen positions were assigned using a riding model. Hydrogen bonds were noted between NH_3^+ groups and the oxygen of the sulfate tetrahedra. Figure 6.2 shows the likely hydrogen bonding interactions. The distances of the observed NH…O hydrogen bonding were in the ~1.90-2.09 Å range.

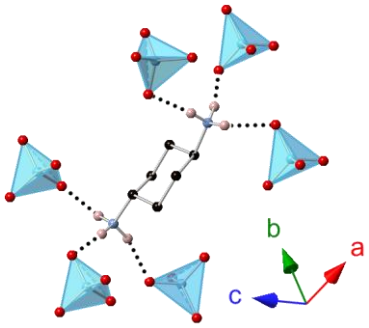

Figure 6.2: *Hydrogen bonding interactions between the NH_3^+ groups of the trans-1,4-diaminocyclohexane cations and framework oxygen atoms. Hydrogen bonding is represented by black dashed lines.*

The IR spectrum (Appendix 5) showed a broad band within the range of 3500-2500 cm^{-1}. The absorption peak at 3311 cm^{-1} associated with the stretching mode of N-H within the $-NH_3^+$ groups. The peak at around 1526.67 cm^{-1} was considered to be the N-H bend, Peaks observed within the 1500-1300 cm^{-1} region were correlated to the C-N and C-C stretching modes as well as the C-H bending mode. Strong peaks observed at around 1000 cm^{-1} belong to the vibration mode of S-O bonds.[8] The thermal behaviour of compound **XVI** was investigated and shown in Figure 6.3. The TGA shows an initial weight loss (3 %) at 100 ^oC was due to the elimination of water absorbed from the surface. The TGA curve indicates that compound **XVI** is very stable up to 350 ^oC. Then a significant weight loss of 35 % was observed within the temperature range of 380-480 ^oC corresponding to the loss of diaminocyclohexane and possible fluorine containing species from the structure, and is comparable to the calculated 33.7 %. A further weight loss (19 %) was observed after 480 ^oC and was attributed to the departure of SO_4 in conversion to SO_3 gas, the value is close to the calculated 21.2 %. The white powder obtained after the TGA experiment was identified by PXD as $MnSO_4$. Similar thermal behaviours can be seen in other templated transition metal sulfate frameworks.[9] An SEM image was recorded for compound **XVI**, and is depicted in Figure 6.4.

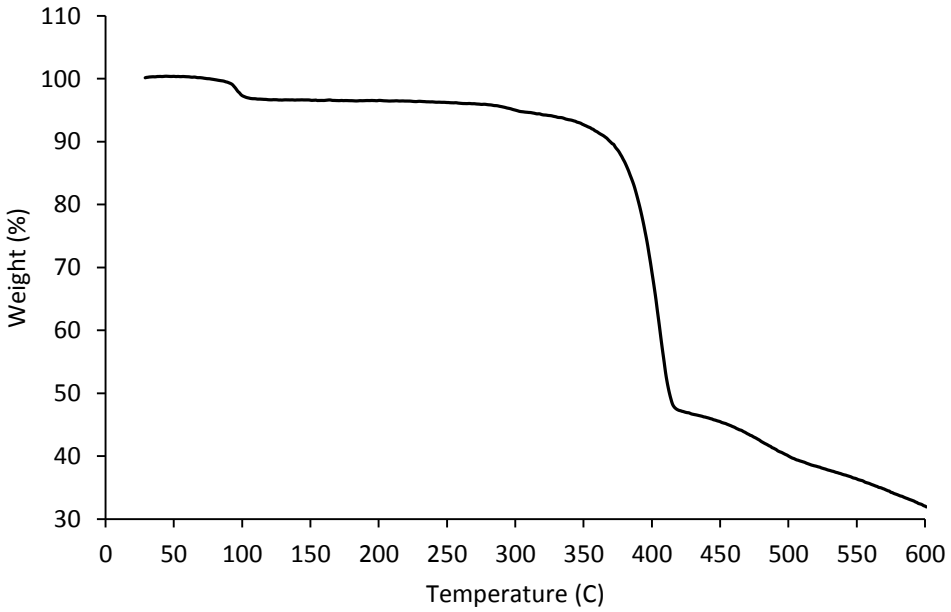

Figure 6.3: *TGA plot for the thermal decomposition of* $[H_2\text{-}(C_6H_{16}N_2)]Mn_2(SO_4)_2F_2$. *Black and green lines represented the TGA*

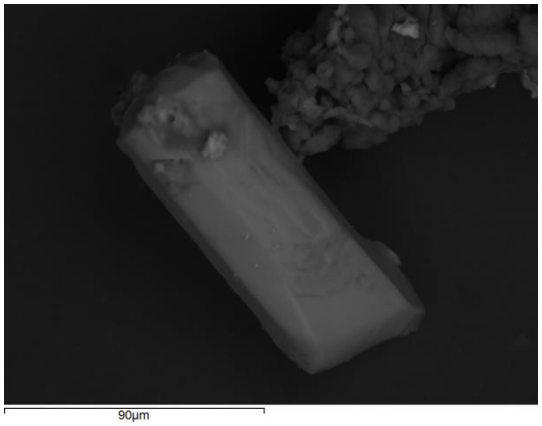

Figure 6.4: *SEM image of a [H_2-trans-1,4-diaminocyclohexane]$Mn_2F_2(SO_4)_2$ single crystal*

6.2 Compound XVII: $[H_2\text{-hydrazinum}]_5Mn(SO_4)_6$

The product crystallised as very pale pink ellipsoid crystals. A suitable crystal was selected for a single crystal X-ray diffraction study. Data were collected at 120 K, and the resulting crystallographic information is summarised in Table 6.5. The structure of compound **XVII** possesses a monoclinic unit cell, with space group *C*2/*c*, and forms a one-dimensional structure consisting of chains. These chains are comprised of manganese centred octahedra and sulfate tetrahedra (Figure 6.5). Key bond lengths are listed in Table 6.6.

The structure of compound **XVII** consists of one-dimensional chains, which are formed of alternating connected manganese centred octahedra and sulfate tetrahedra, linked through vertex-sharing of two μ^2-bridging oxygen atoms per sulfate unit. Within the chain, adjacent Mn octahedra are bridged by two sulfate tetrahedra, producing a four-membered ring. Each Mn-octahedron coordinates with six sulfate tetrahedra, with two terminal sulfate groups oriented toward the inter-chain space. The chains, built up by the alternating connected polyhedra, are aligned parallel to the *c*-axis. The inter-chain space along the *ac*-plane is occupied by hydrazinium cations, whilst the space along the *bc*-plane is filled with both hydrazinium cations and non-coordinated sulfate anions SO_4^{2-}. EDS analysis confirmed no fluoride was present within compound **XVII**.

One crystallographically independent manganese coordination environment was found within the structure. This Mn centre coordinates with six oxygen atoms to form a MnO_6 octahedron. Within the MnO_6 octahedron, all six oxygen atoms bridge to form part of the sulfate groups. Bond lengths summarised in Table 6.05, show that all six M-O bonds lie in the range of 2.174(2)-2.263(2) Å. The Mn cation adopts a oxidation state of +2, due to the consideration of Mn-O bonds which are comparable to reported Mn^{II} species,[5] as well as being in good agreement with the Shannon crystal radii of Mn-O in Mn^{II} octahedron.[10] BV calculation on the Mn cation gave a sum of 1.95, which also indicates the 2+ charge on the Mn ion. BV calculations are given in Table 6.7.

Table 6.5: *Crystal and diffraction information of compound XVII*

Empirical formula	$N_{10}H_{30}MnS_6O_{24}$
Formula weight ($gmol^{-1}$)	801.82
Temperature (K)	120
Appearance	Pale pink ellipse
Crystal size (mm)	0.2 × 0.2 × 0.1
Crystal system	Monoclinic
Space group	*C2/c*
Unit cell dimensions	a=15.217(3) Å, b=15.996(3) Å c=9.978(2) Å, β=100.982(4)^o
λ/Å	0.71073 Å (Mo K_α)
Volume ($Å^3$)	2384.20(2)
Z	2
Density (gcm^{-3})	2.29
Reflections collected	16635
Unique reflections	4825
R_1 (all data)	0.0337
wR_2 (all data)	0.0769
GooF	1.04

Table 6.6: *Bond lengths between selected atoms*

Bond	Bond length (Å)	Bond	Bond length (Å)	Bond	Bond length (Å)
Mn1-O1	2.263(2) × 2	S1-O4	1.483(2)	S2-O8	1.477(2)
Mn1-O2	2.193(2) × 2	S1-O6	1.459(2)	S3-O9	1.478(2)
Mn1-O4	2.174(2) × 2	S2-O3	1.472(2)	S3-O10	1.465(3)
S1-O1	1.486(2)	S2-O5	1.480(2)	S3-O11	1.478(2)
S1-O2	1.478(2)	S2-O7	1.468(2)	S3-O12	1.464(3)

Table 6.7: *Bond valence calculations of selected atoms*

Atom label	Bond valence	Atom label	Bond valence
O1	1.77 -	O8	1.46 -
O2	1.79 -	O9	1.46 -
O3	1.52 -	O10	1.50 -
O4	1.45 -	O11	1.46 -
O5	1.79 -	O12	1.51 -
O6	1.61 -	Mn1	1.95 +
O7	1.50 -		

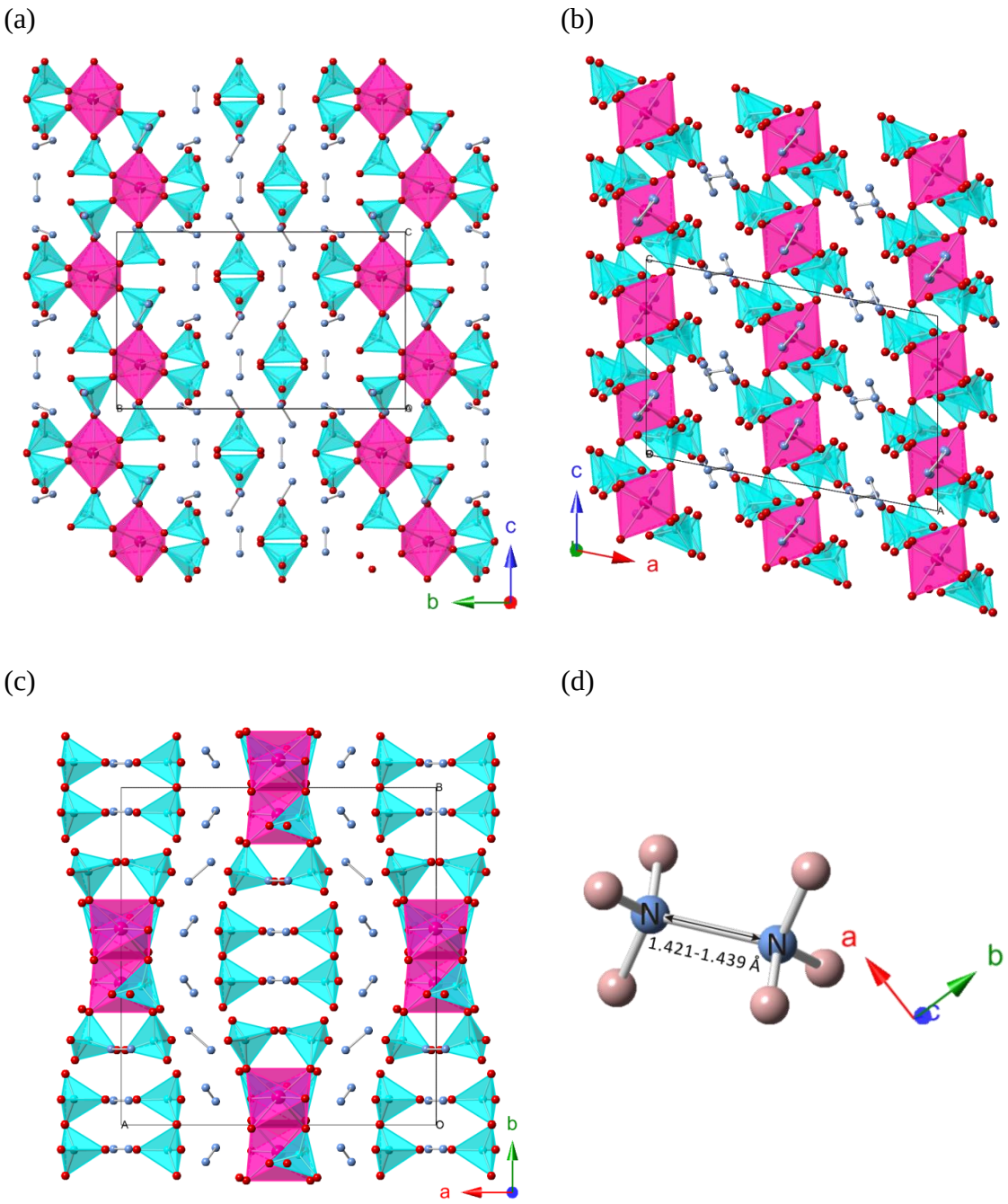

Figure 6.5*: The structure of $[H_2\text{-}N_2H_6]_5Mn(SO_4)_6$ viewed down the (a) a-, (b) b-, (c) c-crystallographic axes, with the Mn^{II} octahedra are shown in pink, sulfate tetrahedra in sky blue, oxygen atoms in red, nitrogen in blue, hydrogen in pale pink and carbon in black. (d) shows a hydrazinium cation with represented N-N distances*

The sulfate groups present within the structure exhibit three crystallographically distinct environments. Each of the sulphur centres coordinate with four oxygen atoms to form the tetrahedral units S1, S2 and S3. The S1 unit bridges a pair of manganese octahedra through the vertex-sharing of two μ^2-bridging oxygen along the chain. The remaining two vertices within the S1 tetrahedron are terminal and orientated towards

inter-chain spaces. The bond lengths given in Table 6.6 show three long S-O bonds and one short bond, clearly the S1-O6 bond, with a shorter length of 1.459(2) Å, is the terminal bond. Three long bonds S1-O1, S1-O2 and S1-O4 have lengths of 1.486(2) Å, 1.478(2) Å and 1.483(2) Å respectively. Closer examination of the S1 tetrahedron indicates the former two S-O bonds are involved in bridging between the Mn centres, whilst the S1-O4 bond is terminal. The similar length of this terminal bond, compared to the bridging bonds, can be explained due to its hydrogen bonding interaction to the hydrazinium cation. The observed O-S-O angles lie in the range of ~108.2-110.8^{o}, which are very close to the 109.5^{o} of an ideal tetrahedron. The S2 tetrahedra coordinate to the MO_6 octahedra *via* the vertex-sharing of a μ^2-bridging oxygen per S2 unit with other three vertices terminated by oxide groups and oriented toward the inter-chain spaces. One S-O bond with length of 1.480(2) Å is considered as the bridging bond, the other three terminal bonds are similar in length with an average length of 1.472 Å. The observed O-S-O angles within the S2 unit are in between of ~108.9-109.8^{o}. Hence, the S2 tetrahedron can be regarded as almost regular. The S3 tetrahedral units are located in the space between the polyhedral chains. The suggestion is that these independent anion groups are held in place by the hydrogen bonding interactions. The S3 tetrahedron consists of two long S-O bonds with an average length of 1.478 Å, and two slightly shorter bonds with an average length of 1.465 Å. The shorter S-O bonds can be considered to have partial multiple-bond character. All O-S-O bonds found within the S3 unit are close to the ideal tetrahedral value; with the mean of the six angles being 109.47^{o}.

The $[N_2H_6]^{2+}$ cations are located between the chains within the structure, and are present in four crystallographically distinct environments. The nitrogen atoms were simply assigned from the SXD data, with the hydrogen positions also located directly. For charge balance purpose, the counter-cation must be described as having two protons in order to charge-balance the negatively charged inorganic framework. Since hydrazine was used as starting material, it can be suggested that the hydrazine molecules have been protonated and formed the hydrazinium bivalent cation, $[N_2H_6]^{2+}$. The $[N_2H_6]^{2+}$ cations exist in a staggered configuration, with determined N-N distances in the range of 1.421-1.439 Å, comparable to those found in other hydrazinium (2+) compounds.[11] Hydrogen bonding interactions are also exhibited within the structure. The independent sulfate anions and the cations are held in place by hydrogen bonding. Possible hydrogen

bonding interactions of the NH_3^+ terminal groups to the oxyanions are displayed in Figure 6.6; these were based on the appropriate distances over which hydrogen bonding commonly occurs. The observed N-H…O distances are lying in the ~1.8-2.2 Å range. The shortness of the hydrogen bonding indicates the strong bond within the structure. The relatively low BV values of oxygen atoms again are due to the hydrogen bonding.

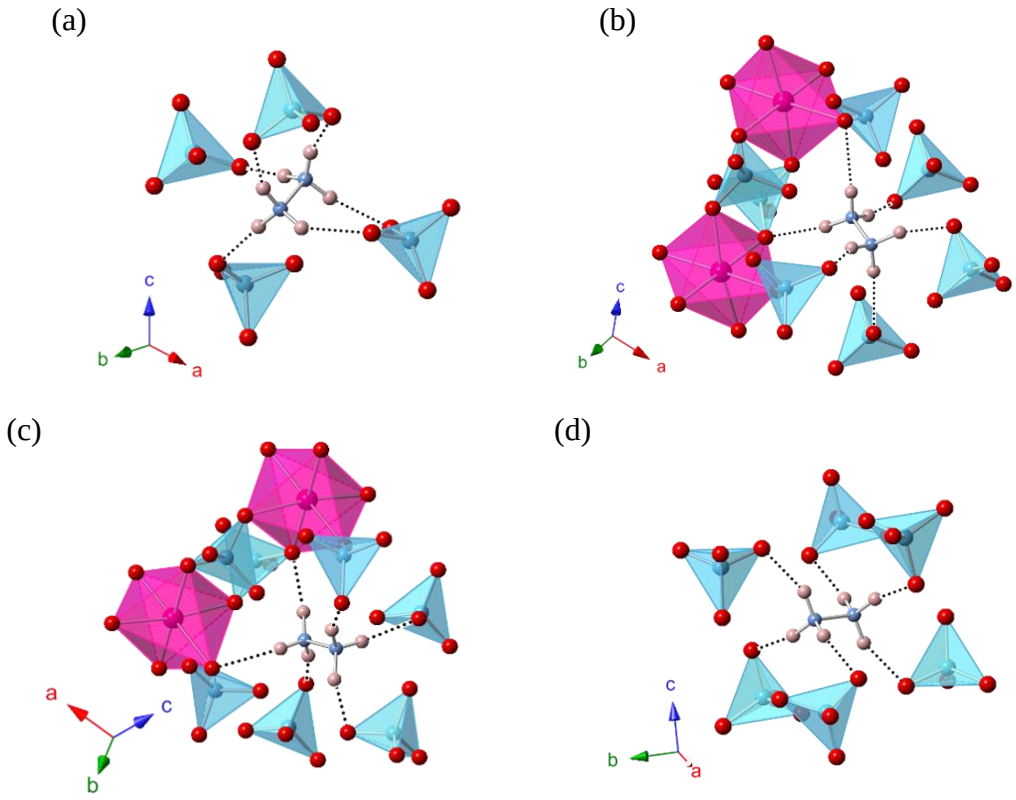

Figure 6.6*: The hydrogen bonding between the amine groups in hydrazinium cations and framework oxygen atoms. Hydrogen bonding is represented by black dash lines.*

FT-IR spectroscopy (Appendix 6) displays a broad absorption band at 3225-2600 cm^{-1}, with the absorption band at around 3100 cm^{-1} is associated with the stretching mode of N-H of $-NH_3^+$. A peak observed at 1509.8 cm^{-1} is considered to be due to the N-H bending of $-NH_3^+$. Strong peaks observed at around 1056.3 cm^{-1} were related to the N-N stretching. These peaks are evidence for the presence of hydrazinium within **XVII**. Similar IR spectra can be found for other inorganic hydrazine derivatives.[12]

Figure 6.7 illustrates the weight loss upon heating in air for compound **XVII**. The TGA curve reveals a two-step weight loss, a rapid weight loss in the temperature range 255-280 ^oC corresponding to the loss of 5 mole of hydrazinium along with the 2 moles of independent sulfate within the structure, the observed weight loss percentage is

around 46 % and is comparable to the calculated value of 45.2 %. A sharp peak was seen at 280 ^{o}C is probably due to the decomposition of hydrazinium leading to the collapse of structure, which is very exothermic in the DTA trace, which also indicates evidence of the structural changes. The second observed gradual weight loss between 280-460 ^{o}C is likely attributed to the further decomposition of sulfate from the main framework, and resulted in a 22 % weight loss which is similar to the calculated 24 %. The decomposed white compound was further studied by PXD, but the sample diffracted weakly, the pattern obtained can be attributed to the anhydrous $MnSO_4$.

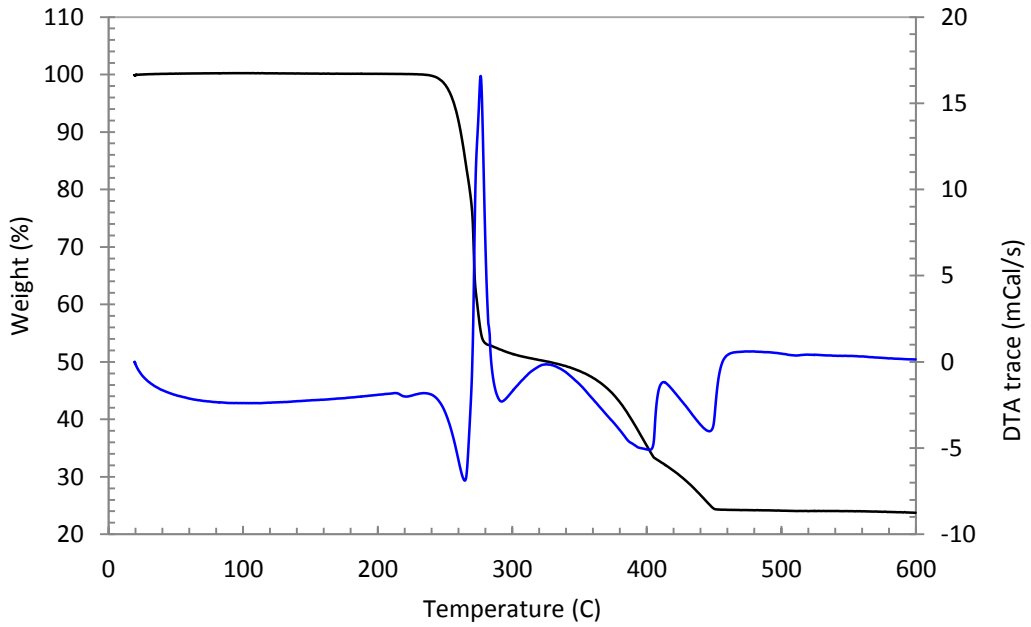

Figure 6.7: *TGA plot for the thermal decomposition of XVII. Black and green lines represented the TGA and DTA data as a function of temperature respectively.*

6.3 Compound XVIII: [H_2-*trans*-1,4-diaminocyclohexane]$MF(SO_4)_2$ (M = V, Fe)

Both products (M = V, Fe) crystallised as needle crystals, with dark brown colour for M = Fe, and dark green colour for M = V. One suitable crystal of each of these two compounds was selected for a single crystal X-ray diffraction study. Data were collected at 120 K, and the resulting crystallographic information is summarised in Table 6.8. Both structures possess a monoclinic unit cell with the same space group, $P2_1/c$, and consist of one-dimensional polyhedral chains. Key bond lengths are listed in Table 6.9.

The structure of [H_2-*trans*-1,4-diaminocyclohexane]$MF(SO_4)_2$ (M = V, Fe), viewed along three different directions, is depicted in Figure 6.8. Within the two structures, each metal ion centre is coordinated by four oxygen atoms and two fluorine atoms arranged into an almost regular octahedron. The MO_4F_2 octahedra are bound together at their corners through F atom sharing at the *trans*-position to produce a linear *zig-zag* chain, with a –F-M-F-M- backbone running along the *c*-axis. The resulting M-F-M angles along the chains of both compounds are quite similar, ~126^o. Each pair of adjacent MO_4F_2 octahedra along the chain are bridged by two sulfate tetrahedra through sharing two corner oxygen atoms within the octahedra; this produces three-membered rings based on two M- and one S-centred polyhedra, and four-membered rings based on two of each, these alternate in orientation along the chain direction. This chain is also noted as forming a tancoite type topology.[13] The adjacent chains are arranged parallel to each other along the *bc*-plane as shown in Figure 6.7 (a) and are separated by diprotonated *trans*-1,4-diaminocyclohexane molecules, $[H_3N(C_6H_{10})NH_3]^{2+}$. These chains are held together by hydrogen bonds formed between the *trans*-1,4-diaminocyclohexane and the oxo-polyhedra oxygen atoms of the chains. This structure type is also observed in open-framework metal phosphates[14] as well as in sulfate[15] and the phosphate minerals[13].

Both of the compounds contain one unique metal coordination environment within their structures. Each metal centre is six-coordinate, with four oxide ligands and two fluoride ligands per metal ion, as mentioned above. The bond lengths in the FeO_4F_2 octahedron are very similar, four Fe-O bonds at equatorial positions have distances of Fe-O3 = 1.986(3) Å, Fe-O4 = 1.965(3) Å, Fe-O5 = 1.955(3) and Fe-O7 = 1.972(3) Å,

the average Fe-O distance is 1.970 Å. Two Fe-F bonds involved in bridging between metal centres at axial positions have the similar lengths of 1.969(4) Å. The bond angles between the metal centre and the ligands are very close to 90° lying in the ~87.9°-92.5° range. All bond lengths are given in Table 6.9. Similarly to the iron site, the vanadium centre is also six-coordinate, with the bond lengths observed in each VO_6F_2 octahedron also very similar in length. The average length for the four bridging V-O bonds is 1.972 Å, and two V-F bonds have the same length of 1.967(4) Å. The bond angles within the VO_6F_2 octahedron are very close to those of a regular octahedron. Both metal cations adopt oxidation states of +3, this was confirmed through examination of the bond valence calculations for each metal centre, as given in Table 6.10.

Table 6.8: *Crystal and diffraction information of compound XVIII*

Empirical formula	$N_2C_6H_{12}FeS_2O_8F$	$N_2C_6H_{12}VS_2O_8F$
Formula weight ($gmol^{-1}$)	383.2	374.24
Temperature (K)	120	120
Appearance	Dark brown needle	Dark green needle
Crystal size (mm)	0.2 × 0.05 × 0.02	0.2 × 0.05 × 0.02
Crystal system	Monoclinic	Monoclinic
Space group	$P2_1/c$	$P2_1/c$
Unit cell dimensions	a=10.254(2) Å, b=17.758(4) Å c=7.050(2) Å, β=93.96°	a=10.262(2) Å, b=17.761(4) Å c=7.052(2) Å, β=93.94°
λ/Å	0.71073 Å (Mo K_α)	0.71073 Å (Mo K_α)
Volume ($Å^3$)	1280.70(8)	1282.24(8)
Z	4	4
Density (gcm^{-3})	2.14	2.07
Reflections collected	17794	17460
Unique reflections	5137	5115
R_1 (all)	0.067	0.0661
wR_2 (all)	0.2059	0.1858
GooF	1.073	0.959

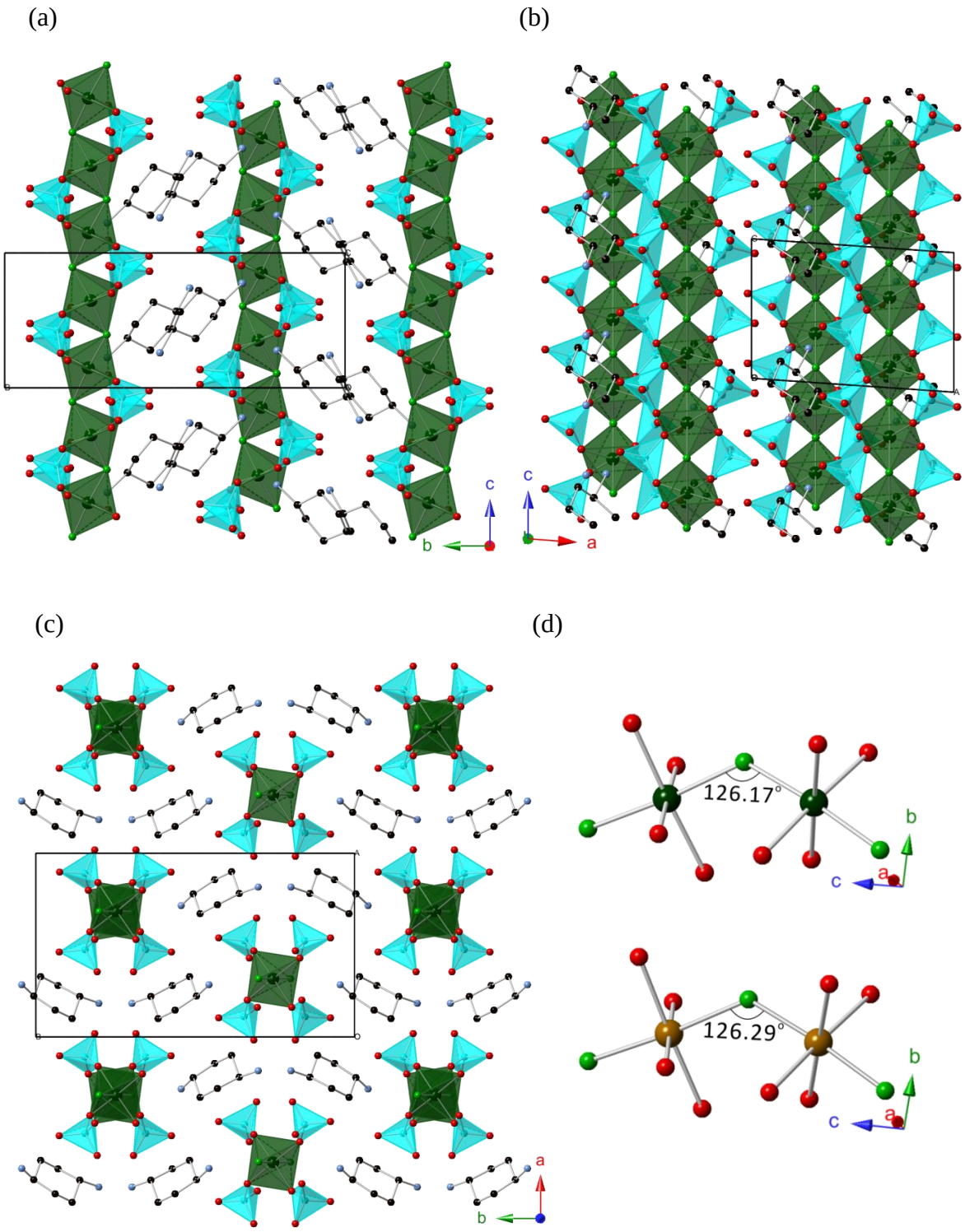

Figure 6.8: *The structure of $(N_2C_6H_{14})MFSO_4$ (M=V, Fe) viewed down the (a) a-, (b) b-, (c) c-crystallographic axes, where the Fe octahedra are shown in yellow-brown, V in dark green, sulfate tetrahedra in aqua blue, oxygen atoms in red, fluorine in green and nitrogen in sky blue, carbon in black and hydrogen in pale pink. (d) shows a single chain consisting of vanadium octahedra and sulfate tetrahedra*

Table 6.9: *Bond lengths between selected atoms*

Bond	Bond length (Å)	Bond	Bond length(Å)
Fe1-O3	1.986(3)	V1-O2	1.966(3)
Fe1-O4	1.965(3)	V1-O4	1.986(3)
Fe1-O5	1.955(3)	V1-O7	1.978(3)
Fe1-O7	1.972(3)	V1-O8	1.960(3)
Fe1-F1	1.969(4) × 2	V1-F1	1.967(4) × 2
S1-O5	1.506(2)	S1-O5	1.449(2)
S1-O6	1.447(1)	S1-O6	1.448(3)
S1-O7	1.503(3)	S1-O7	1.502(2)
S1-O8	1.449(2)	S1-O8	1.504(2)
S2-O1	1.456(3)	S2-O1	1.448(3)
S2-O2	1.450(2)	S2-O2	1.506(2)
S2-O3	1.491(3)	S2-O3	1.453(3)
S2-O4	1.506(2)	S2-O4	1.492(2)

Table 6.10: *Bond valence calculations of selected atoms*

Atom label (M=Fe)	Bond valence	Atom label (M=V)	Bond valence
O1	1.52 -	O1	1.73 -
O2	1.53 -	O2	1.97 -
O3	1.95 -	O3	1.80 -
O4	1.93 -	O4	1.97 -
O5	1.93 -	O5	1.76 -
O6	1.55 -	O6	1.76 -
O7	1.94 -	O7	1.98 -
O8	1.55 -	O8	1.95 -
F1	0.93 -	F1	1.02 -
Fe1	3.12 +	V1	3.03 +

There are two crystallographically non-equivalent sulfate groups present in each of the two isostructural compounds. The sulphur centres are coordinated with four oxygen atoms to form tetrahedral units. The sulfate tetrahedra are bridged between adjacent metal octahedra through the sharing of two vertices per tetrahedral unit, whilst the other two vertices within each of the sulfate tetrahedron are terminal, and orientate toward the inter-chain space. The observed bond lengths within the sulfate tetrahedra of the two isostructural compounds indicate the bridging bonds to the metal sites are always longer than the terminal bonds. More specifically, for the two isostructural compounds when M = Fe, and the S1 and S2 represent the two non-equivalent sulfate environments, the bridging S-O bonds to the iron site within the two sulfate units are very close in length,

the average lengths of the bridging S-O bonds are 1.505 Å for S1 unit and 1.498 Å for S2 unit. The terminal S-O bonds are relatively shorter with mean length of 1.488 Å for S1 and 1.453 Å for S2. The most distorted O-S-O angle within the S1 unit, from the ideal tetrahedral value, is ~113.6^{o} between the terminal oxygen atoms, and for S2 unit a corresponding value of ~112.7^{o} was observed. These distortions are likely to be attributed to the greater repulsion between the two terminal bonds with multiple-bond character than the bridging bonds.[16] The O-S-O angles within the two tetrahedral units lie in the range of ~108.4^{o}-113.6^{o} for S1 tetrahedron, and ~107.8^{o}-112.7^{o} for S2 tetrahedron. Similar observations of sulfate tetrahedral units were also found within the isostructural compound when M = V. The average lengths of the bridging S-O bonds for S1 and S2 units are 1.503 Å and 1.499 Å respectively, while for terminal bonds, these lengths are 1.448(3) Å and 1.450(2) Å. The O-S-O angles observed within the tetrahedra are in the range of ~107.4^{o}-113.3^{o} for S1, and ~107.8^{o}-112.4^{o} for S2.

As previously stated, the *trans*-1,4-diaminocyclohexane molecules reside in the inter-chain space, and the possible hydrogen bonding interactions depicted in Figure 6.9. For the two isostructural compounds, each of them contains two crystallographically distinct $[H_3N(C_6H_{10})NH_3]^{2+}$ cations, both in the chair-conformation. Each molecule forms six hydrogen bonds to the oxo-polyhedra oxygen and fluorine atoms through two NH_3^+ groups. The observed NH…O distances within the structure (M = Fe) are in the ~1.9-2.1 Å range, and NH…F bonds have distance of ~2.2 Å. For the structure M = V, the NH…O distances within the ~1.9-2.2 Å range, and NH…F bonds have distance of ~2.2 Å. The low BV values of those oxygen atoms are due to the hydrogen bonding, which are not involved in calculations.

(a) (b)

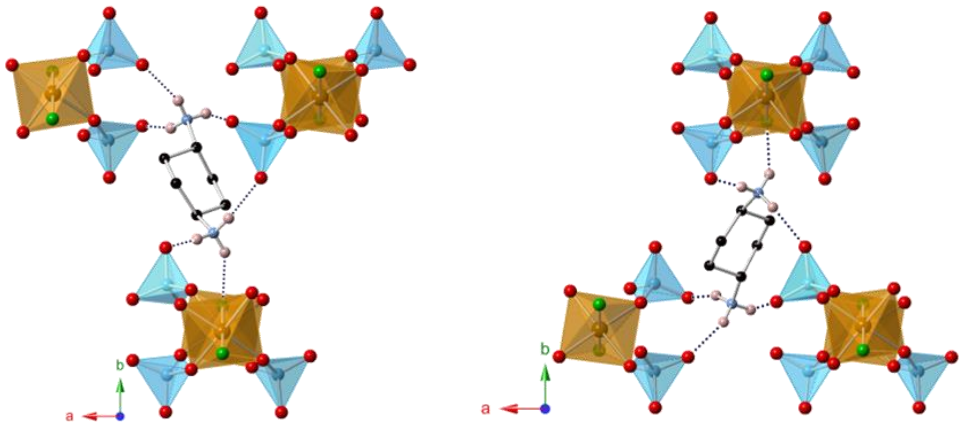

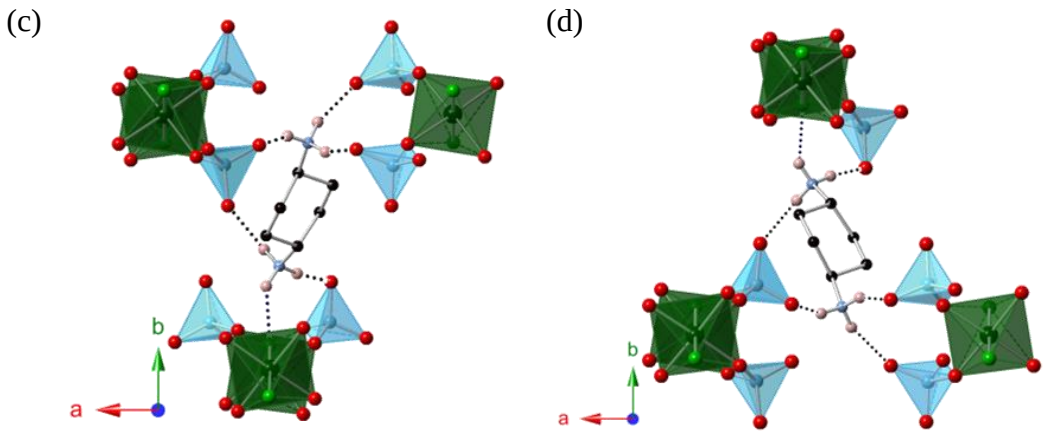

Figure 6.9: *The hydrogen bonding interactions within the isostructural compounds, upper M=Fe, lower M=V. Hydrogen bonding is represented by black dash lines*

The compound was further studied by TGA. However, pure stoichiometric products of the two isostructural compounds could not be obtained in large quantities. The TGA displayed in Figure 6.10 is based on the compound M = Fe, isolated from impurities but only tiny amount (0.208 mg) has been studied. The TGA of compound M = Fe only provides the general information of its thermal behaviour, analysed by flowing O_2 gas within the temperature range of 25-600 ^{o}C. The TGA curve indicates the compound is stable below 200 ^{o}C. A first gradual weight loss was starting at 225 ^{o}C until 380 ^{o}C, with observed ~40 % considered to be the departure of diaminocyclohexane and possible fluorine from the structures; this is reasonably close to the calculated from composition of 34.2 %. The second weight loss (~20 %) was observed between 380-450 ^{o}C and corresponds to the sulfate decomposition, this roughly agrees with the calculated value from composition of 25.1%. SEM micrographs of the two compounds have been recorded while collecting EDS data and are shown in Figure 6.11.

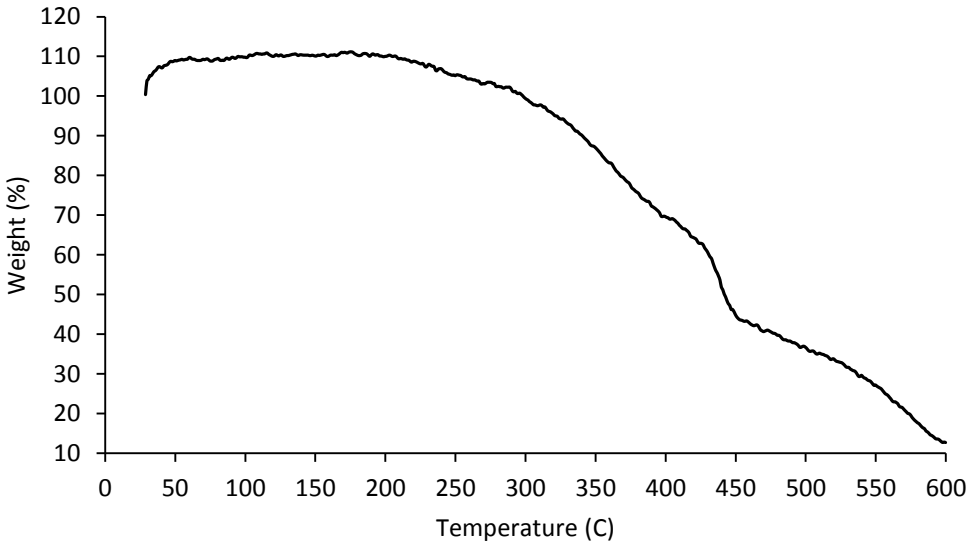

Figure 6.10: *TGA plot for the thermal decomposition of [H_2-trans-1,4-diaminocyclohexane]FeF(SO_4)$_2$.*

(a) (b)

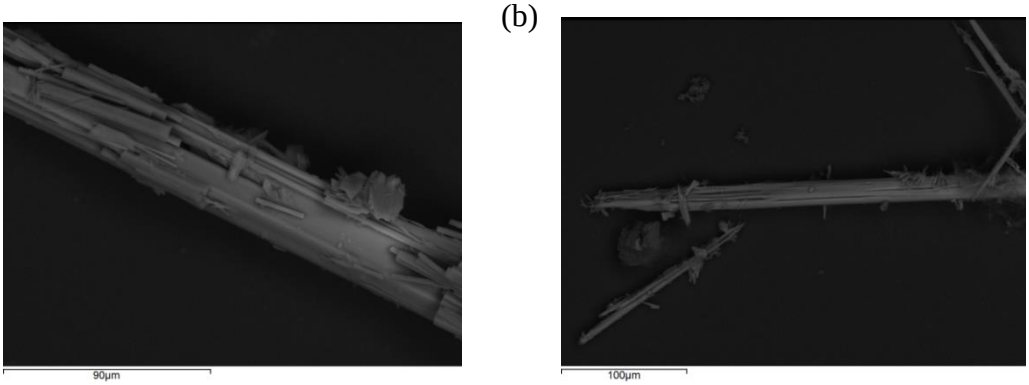

Figure 6.11: *SEM images of the isostructural compounds ($N_2C_6H_{14}$)$MFSO_4$, (a) M = V, (b) M = Fe single crystals*

6.4 Compound XIX: $[H_2$-ethylenediamine$](NH_4)Fe(SO_4)_3$

The product crystallised as green rod shaped crystals. A suitable crystal was selected for a single crystal X-ray diffraction study. Data were collected at 120 K, with the resulting crystallographic information summarised in Table 6.11. The structure of compound **XVII** possesses a monoclinic unit cell with space group *C2/c,* and forms a one-dimensional structure consisting of chains. The structure is comprised of iron centred octahedra and sulfate tetrahedra (Figure 6.11). Key bond lengths are listed in Table 6.12.

Compound **XIX** is structurally related to the ferrinatrite $Na_3Fe(SO_4)_{3,}$[17] with both structures consisting of one-dimensional chains, which are built up from alternating connected iron centred octahedra and sulfate tetrahedra. The chains within compound **XIX** run parallel to the *a*-axis and perpendicular to the *c*-axis. Within the polyhedral chain, each pair of neighbouring iron centred octahedra are bridged by three sulfate tetrahedra through the corner-sharing of two μ^2-bridging oxygen atoms, producing four-membered rings based on two Fe- and two S- based polyhedral units. The inter-chain space is filled by the diprotonated ethylenediamine (EDA) and ammonium cations. The polyhedral chains are held in position by hydrogen bonds.

There are two crystallographically non-equivalent iron sites, Fe1 and Fe2, present within the structure. Each of the iron centres coordinates to six oxygen atoms, forming the common octahedral environments, bridging to six sulfate tetrahedra. The bond lengths summarised in Table 6.12 indicate that the Fe-O bonds found within the Fe1 site are all similar in length. The mean length of the six Fe-O bonds is 1.998 Å. The observed Fe-O bonds within the Fe2 site are also very close in length, lying in the range of 1.986(1)-2.019(4) Å with an average of 1.994 Å. The iron centres within the two sites were assumed to adopt the oxidation state of +3, This was further confirmed through the BV calculations on the iron cations, given in Table 6.13. EDS analysis shows no fluoride was incorporated within the compound **XIX**.

Table 6.11: *Crystal and diffraction information of compound XIX*

Empirical formula	$N_3C_2H_{14}FeS_3O_{12}$
Formula weight ($gmol^{-1}$)	424.19
Temperature (K)	120
Appearance	Green rod
Crystal size (mm)	0.15 × 0.09 × 0.03
Crystal system	Monoclinic
Space group	$P2_1/n$
Unit cell dimensions	a=8.671(3) Å, b=14.441(6) Å c=10.760(3) Å, β=109.089(12)^o
λ/Å	0.71073 Å (Mo K_α)
Volume ($Å^3$)	1273.25(56)
Z	4
Density (gcm^{-3})	2.15
Reflections collected	20830
Unique reflections	5157
R_1 (all data)	0.0776
wR_2 (all data)	0.2148
GooF	1.281

Table 6.12: *Bond lengths between selected atoms*

Bond	Bond length (Å)	Bond	Bond length (Å)	Bond	Bond length (Å)
Fe1-O1	1.976(5) × 2	S1-O5	1.484(4)	S2-O3	1.473(2)
Fe1-O6	2.004(9) × 2	S1-O6	1.483(1)	S2-O4	1.490(2)
Fe1-O10	2.014(5) × 2	S1-O7	1.473(2)	S3-O9	1.493(4)
Fe2-O4	1.986(1) × 2	S1-O8	1.443(2)	S3-O10	1.492(4)
Fe2-O5	1.976(5) × 2	S2-O1	1.483(4)	S3-O11	1.478(7)
Fe2-O9	2.019(4) × 2	S2-O2	1.446(2)	S3-O12	1.446(9)

Table 6.13: *Bond valence calculations of selected atoms*

Atom label	Bond valence	Atom label	Bond valence
O1	2.01 -	O8	1.57 -
O2	1.57 -	O9	1.94 -
O3	1.47 -	O10	1.94 -
O4	1.97 -	O11	1.45 -
O5	2.01 -	O12	1.56 -
O6	1.94 -	Fe1	3.13 +
O7	1.48 -	Fe2	3.16 +

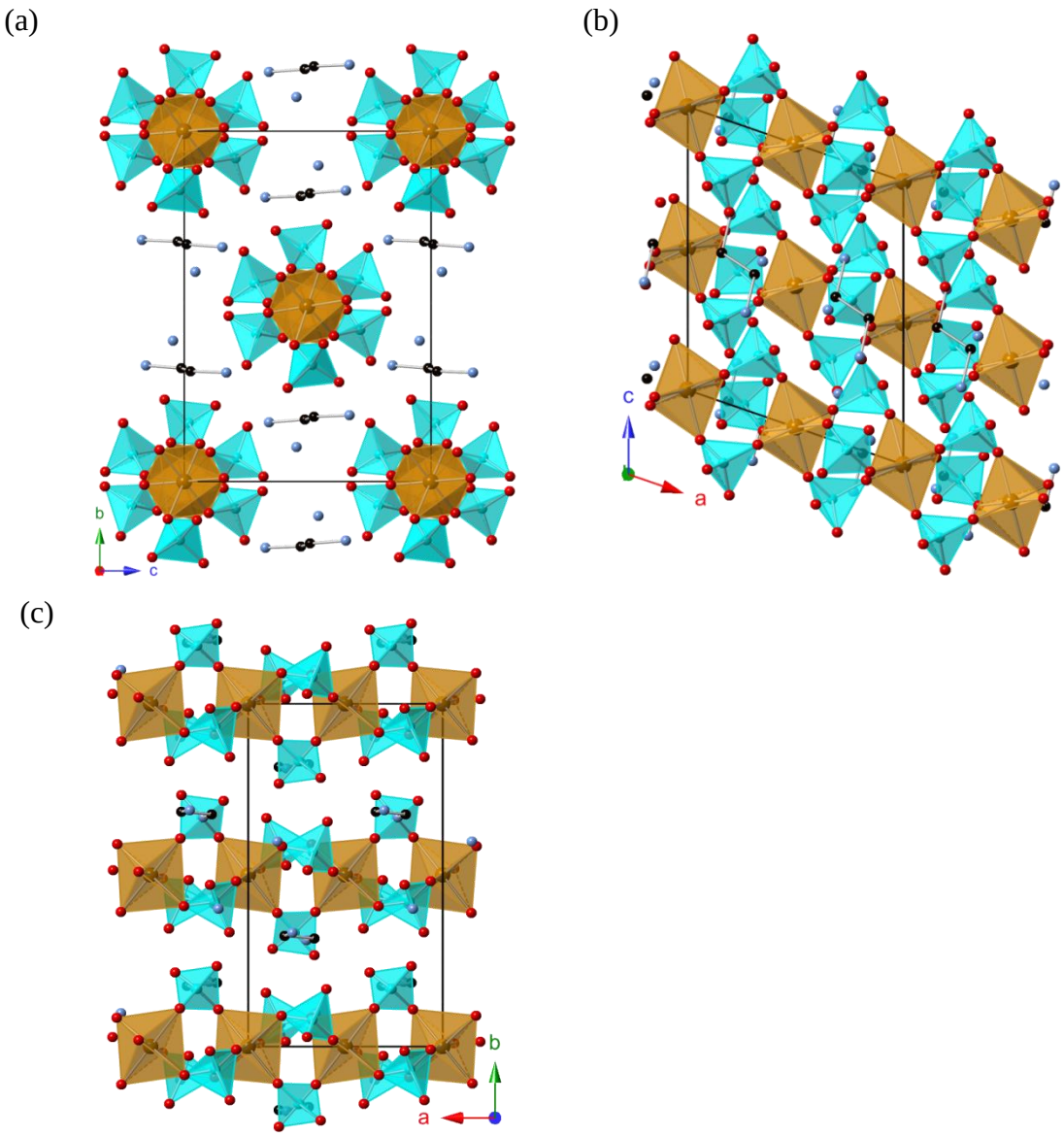

Figure 6.11: *The structure of $(N_2C_2H_6)(NH_4)Fe(SO_4)_3$ viewed down the (a) a-, (b) b-, (c) c-crystallographic axes, with the Fe octahedra are shown in yellow-brown, sulfate tetrahedra in aqua blue, oxygen atoms in red and nitrogen in sky blue, carbon in black.*

Three crystallographically distinct sulfate tetrahedral environments were found within the structure, represented as S1, S2 and S3. Each sulfate group bridges two Fe-octahedra *via* vertex-sharing of two oxygen atoms, the remaining two vertices within the three sulfate tetrahedra are terminated, and directed toward the inter-chain space. Bond lengths summarised in Table 6.12 indicate each sulfate tetrahedral unit contains two long bridging and two short terminal bonds. The average bridging S-O bonds to the iron centres within the three sulfate units are 1.483 Å for S1, 1.487 Å for S2 and 1.492 Å for S3. The shortest terminal S-O bonds are in the range of 1.443(2)-1.446(2) Å. Like other sulfate tetrahedra described previously which possess two terminal S-O bonds, the

most distorted O-S-O angles in these three sulfate units are found between two terminal oxygen, ranging from ~112.2°-111.2° due to the greater repulsion of multiple terminal S-O bonds.[6]

Two different cations are present within the structure. The ethylenediamine molecules were found to be present as the diprotonated $[H_3N(C_2H_4)NH_3]^{2+}$ cations, which, together with the NH_4^+ cations, balance the negatively charged $[Fe(SO_4)_3]^{3-}$ polyhedral chains. In a number of amine templated inorganic materials, the template molecules act as cations that counter-balance the structure and also donate electron density to the nearest O/F anions.[18] During the single crystal refinement, locating of hydrogen atoms of the template unit was impractical for this compound; the hydrogen positions were calculated using a riding model and is included in the structure refinement. Hydrogen bonding was formed between oxide anions and the hydrogen ions attached to the ethylenediamine and ammonium cations. The oxide anions appear to interact with four hydrogen atoms present in the ammonium cations. However, these hydrogen positions were not located due to their weak scattering power. The possible hydrogen bonding interactions are depicted as dashed lines between nitrogen atom and the terminal oxygen to aid clarity. The observed O…N donor-acceptor distances are in the ~2.5-2.6 Å range. These relatively short donor-acceptor distances indicate strong hydrogen bonding may be present between ammonium cations and the oxo-polyhedral oxygen. For the protonated EDA cations, two possible hydrogen bonding interactions were found; with NH…O distances of ~1.9-2.0 Å. Hydrogen bonding interactions are shown in Figure 6.12. As described before, the low BV values of some oxygen atoms are due to the hydrogen bonding, which are not included in calculations.

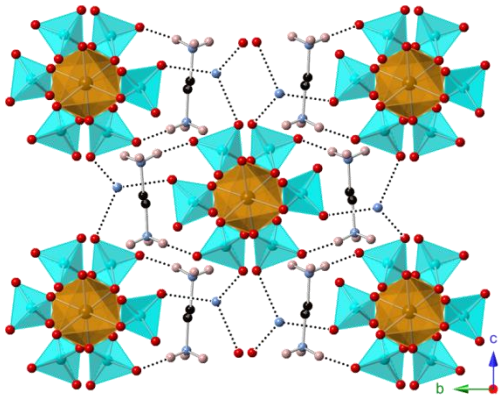

Figure 6.12: *Hydrogen bonding associated with terminal oxide anions and protonated EDA and ammonium cations. The hydrogen bonding interactions are represented as black dashed lines.*

The IR spectrum (Appendix 7) of compound **XIX** exhibits a broad absorption region in the 3300-2800 cm^{-1} range, which are expected for the stretching modes of N-H and C-H associated the ethylenediamine and ammonium cations. The observed peak at 1485 cm^{-1} is due to the N-H bend, whilst the peak at around 1202 cm^{-1} is likely to be caused by C-H bends within the EDA. Peaks observed at around 1011 cm^{-1} are due to the S-O stretches.[8] The absorption frequencies associated with N-H stretches are shifted marginally, compared to reference frequencies; this difference was attributed to hydrogen bonding interactions between the cations and the framework. The characteristic absorption bands were accounted for by the presence of organic species within compound **XIX**. The TGA data (Figure 6.13) shows a gradual weight loss of 39 % observed in the 250-480 ^{o}C range corresponding to the loss of ethylenediamine, ammonium and SO_3 gas converted from SO_4, which is comparable to the calculated 37.76 %. The thermal behaviour is also observed of other organically templated iron sulfate frameworks.[19] An SEM image of a compound XIX crystal was recorded and is shown in Figure 6.14.

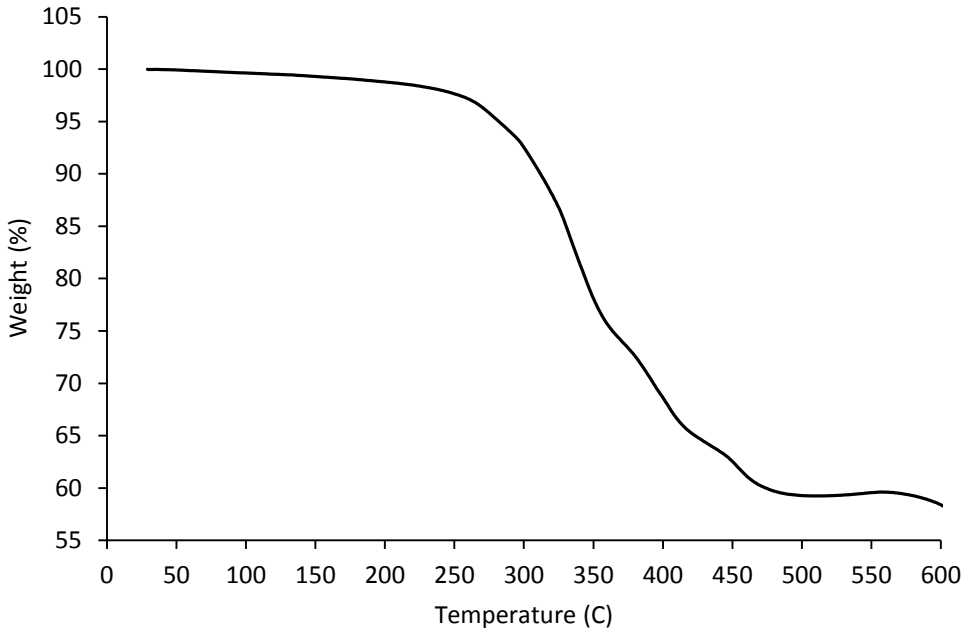

Figure 6.13: *TGA plot for the thermal decomposition of [H_2-ethylenediamine](NH_4)Fe^{III}(SO_4)$_3$.*

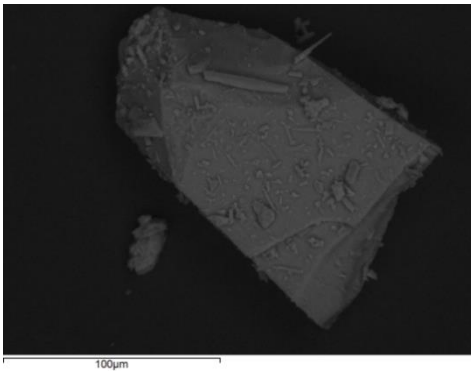

Figure 6.14: *SEM image of a [H_2-ethylenediamine](NH_4)Fe(SO_4)$_3$ crystal*

6.5 General summary

As with the compounds described in the previous chapters, all synthesises were carried out using a hydrothermal method in fluoride-rich medium. Fluoride anions were successfully incorporated into three structures, and all amine molecules were suggested as the counter cations as well as the structure directing agents. The five new structures present here contribute to the extension of the family of organically templated metal sulfate structures.

There are several noteworthy features observed in the structures. Compound **XVI** forms a two-dimensional layered structure containing an edge-shared Mn-octahedral triplet linked through the F-atom which seems to be the only structure for an organically templated manganese fluorosulfate extended frameworks. Compound **XVII** displays a one-dimensional chain structure motif assembled from corner-sharing MnO_6 and SO_4 polyhedra. The type of chain can be seen as double-stranded based on four-membered rings, also found in phosphate-based structures, the main difference being, the Mn-octahedron coordinates to six sulfate tetrahedra with two of them having the unusual feature of three terminal oxygen atoms. Compound **XVIII** possesses tancoite-type typology which occurs in many sulfate and phosphate minerals, such as the sideronatrite $Na_2[Fe(OH)(SO_4)_2]\cdot(H_2O)_3$ and the tancoite $Na_2LiH[Al(PO_4)_2(OH)]$.[13, 20] Synthetically produced structures obtained using hydrothermal methods with the similar topologies have also been reported.[9, 21, 22] Thus the tancoite chain built up from MO_6 and TO_4 polyhedra can be seen as the fundamental building units for open-framework materials and it is possible to transform the tancoite-type chain to two- and three-dimensional structures via mild hydrothermal treatment.[23] Compound **XIX** possesses linear topological structure commonly found in ferrinatrite minerals. The characteristic chain is formed by the adjacent metal octahedra bridged by three TO_4 tetrahedra by sharing-corners. This linear topology can also be found in arsenate frameworks,[1] where the synthetic structures are all held by hydrogen bonding interactions to form a three-dimensional assembly.

Closer examination of the five metal sulfate structures, found that the sulfate tetrahedra exhibit two short S-O bonds which were always terminal. This results in the preparation of sulfate extended structures with two and three dimensional cross linking being very difficult, as explained in Chapter One. As with metal sulfate structures

described in Chapter Five, no fluoride was found to be incorporated as part of the sulfate groups. This is explained as sulphur bonds to four oxygen atoms form a very stable coordination.

The transition metal sites again adopt exclusively octahedral geometries. The fluoride anions were found to be incorporated on the metal ions as either terminal sites or as bridges between metal cations, such as in compound **XVI**. All manganese cations adopt a valence state of +2, and the observed Mn-X (X = O, F) bond lengths within the octahedral site are above 2.1 Å. For the isostructural compound **XVIII**, the vanadium and iron centres adopt octahedral coordination geometries very close to regular. All bonds were found to be of similar in length, and fluoride anions were incorporated at *trans*-positions of the metal octahedra, and act as bridging sites between metal centres.

Template molecules within these compounds were found to be protonated due to the acidic reaction conditions. The template molecules occupy the space in between layers (**XVI**) or chains (**XVIII**, **XIX**) and act as counter cations and structure directing agents. They form hydrogen bonds to the framework anions, and, therefore, direct the formation of the structures. The average distance of the observed hydrogen bonds across the compounds is 2.02 Å (NH…O). The thermal behaviours of all templated structures were studied. The TGA data shows the structure of compound **XVI** is stable up to 350 ^{o}C, whilst the structures of compounds **XVII**, **XVIII**, **XIX** decompose above 250 ^{o}C, 220 ^{o}C and 280 ^{o}C respectively. This suggests the two-dimensional structure of the compound **XVI** exhibits higher thermostability than other one-dimensional chain structures. The higher decomposition temperatures of compound **XIX** may also indicate that the presence of different types of cations requires more energy for complete structural rearrangement.

6.6 Conclusions

One novel two-dimensional (**XVI**) and four one-dimensional (**XVII**, **XVIII**, **XIX**) templated structures have been synthesised. Some reactions were carried out at lower temperature to avoid the possible decompositions of organic species. Fluoride anions were successfully incorporated into compounds **XVI** and **XVIII**.

6.7 Reference

1. S. Ekambaram and S. C. Sevov, *Inorg. Chem.*, 2000, **39**, 2405-2410.
2. C. N. Rao, J. N. Behera and M. Dan, *Chem Soc Rev*, 2006, **35**, 375-387.
3. D. ben Hassan, W. Rekik, H. Naili and T. Mhiri, *Chemical Papers*, 2014, **68**, 210-216.
4. S. Li, Q. Li, K. Wang, X. Tan, M. Zhou, B. Li, B. Liu, G. Zou and B. Zou, *J Phys Chem B*, 2011, **115**, 11816-11822.
5. G. Will, B. C. Frazer and B. C. Cox, *Acta Crystallogr., Sect. A: Found. Crystallogr.*, 1965, **19**, 854-&.
6. A. J. Edwards, *J. Chem. Soc. A*, 1971, 3074-&.
7. G. D. Andreetti, L. Cavalca and A. Musatti, *Acta Crystallographica, Section A: Foundations of Crystallography*, 1968, **B**, 683.
8. G. Socrates, *Infrared and Raman Characteristic Group Frequencies: Talbes and Charts*, 3 edn., Wiley, 2006.
9. G. Paul, A. Choudhury and C. N. R. Rao, *Chem. Mater.*, 2003, **15**, 1174-1180.
10. R. D. Shannon and C. T. Prewitt, *Acta Crystallogr. Sect. B*, 1969, **B25**, 925-946.
11. T. S. Cameron, O. Knop and L. A. Macdonald, *Can. J. Chem.*, 1983, **61**, 184-188.
12. K. C. Patil and T. M. Rattan, *Inorganic Hydrazine Derivatives: Synthesis, Properties and Applications*, John Wiley & Sons, Ltd, United Kingdom, 2014.
13. F. C. Hawthorne, *TMPM Tschermaks Petr. Mitt.*, 1983, **31**, 121-135.
14. F. Bonhomme, S. G. Thoma and T. M. Nenoff, *J. Mater. Chem.*, 2001, **11**, 2559-2563.
15. Y. Fu, Z. Xu, J. Ren, H. Wu and R. Yuan, *Inorg. Chem.*, 2006, **45**, 8452-8458.
16. U. Klein, F. Hahn, W. Massa and J. Pebler, *Z. Anorg. Allg. Chem.*, 2005, **631**, 1785-1792.
17. K. Mereiter, *TMPM Tschermaks Petr. Mitt.*, 1976, **23**, 317-327.
18. Y. N. Zhao, G. S. Zhu, X. L. Jiao, W. Liu and W. Q. Pang, *J. Mater. Chem.*, 2000, **10**, 463-467.
19. L. Ma, D. Li, Y. Xing, X. C. Liu and G. J. Li, *Z. Anorg. Allg. Chem.*, 2010, **636**, 2681-2685.
20. F. C. Hawthorne, S. Krivovichev, V. and P. Burns, C., *Rev. Mineral. Geochem.*, 2000, **40**.

21. S. Mahesh, M. A. Green and S. Natarajan, *J. Solid State Chem.*, 2002, **165**, 334-344.

22. K. H. Lii and Y. F. Huang, *Chem. Commun.*, 1997, 1311-1312.

23. C. Livage, F. Millange, R. I. Walton, T. Loiseau, N. Simon, D. O'Hare and G. Ferey, *Chem. Commun.*, 2001, 994-995.

CHAPTER SEVEN: CONCLUSIONS AND FUTURE WORK

7.0 Overall conclusions and future work

- Inorganic materials with solar near infrared absorbing properties

The research on NIR absorbing materials as part of the project was mainly focused on developing inorganic materials with strong NIR absorbing properties. As described in Chapter Three, a series of copper phosphate based inorganic materials have been studied. Despite being previously reported materials, many of them exhibited useful optical properties that had been poorly investigated previously. In particular those which can absorb specific portions of the electromagnetic spectrum of sunlight are in demand for many industrial or architectural applications.

In undertaking the research presented herein, many synthetic techniques were exploited. The materials produced, through the various synthetic methods, were mainly characterised using powder X-ray diffraction and materials exhibiting the desired structural features were investigated further in respect of their NIR absorbing properties. As the mechanism for absorption of NIR radiation in the materials investigated derives from *d-d* electronic transitions, which may be restricted by the Laporte selection rules, many compounds produced were targeted with structures that would relax the effects of such rules. The study of the series of compounds $ACuP_2O_7$ (A = Li, Na, K) demonstrated that the absorbance can be affected strongly by the copper coordination geometry. Copper in a non-centrosymmetric coordination environment resulted in breakdown of Laporte selection rule leading to the electronic transitions being less "forbidden". The absorbance coefficient was found to be further enhanced by introducing fluoride into the copper-based materials; in Cu_2PO_4F the copper atoms adopt highly irregular coordination environments and this compound displays a very strong absorption spectrum in the NIR region,. Fluorides coordinated to a metal centres act as strong π-donor ligands, reducing the energy separation of the *d* orbitals (a very weak field ligand) and thus reducing the energy required for *d-d* transitions. As a consequence, fluoride-containing materials absorb strongly in the NIR region, but absorb weakly, or do not absorb in the visible part of the spectrum. Although many copper-based materials are known as being intensely coloured, it is possible to modify their structures and compositions so that they only absorb in the NIR region.

Further work in this area of research could be carried out with the aim of further improving the NIR absorbing properties of transition metal compounds while

minimising absorption in the visible region. Other complex copper phosphate materials containing non-centrosymmetric coordinations of copper centres are an obvious target – for example calcium or magnesium derivatives. Materials containing transition metals other than copper may also exhibit strong absorption in the NIR region; one example is Fe^{2+} as in $K_2FeP_2O_7$ where the spectrum is almost totally within the NIR region. A common aspect of the chemistries of iron and copper ions, in the +2 oxidation state, is that their coordination spheres often form similar environments and may be subject to the Jahn-Teller effect (octahedral Cu^{2+}, $t_{2g}^6e_g^3$; tetrahedral high spin Fe^{2+}, $e^3t_2^3$). Moreover, in terms of sustainability issues materials based on iron and copper are non-toxic. However, the preparation of iron(II) compounds requires reducing conditions, due to the easier oxidation from Fe^{2+} to Fe^{3+}.

While phosphate based transition metal compounds have appropriate properties for developing commercial NIR absorbers, other materials based on different anionic systems may also be potential candidates. For example, transition metal compounds containing silicate and sulfate as ligands, as these species are likely to generate very weak ligand fields; they may also encourage the formation of the tetrahedral coordination environments for the transition metal. Furthermore transition metal compounds containing the metal centres cross-linked by simple anions, such as oxide and fluoride, and oxoanions, such as phosphate, silicate and sulfate, usually exhibit very stable structures that resist thermal decomposition and chemical attack. Such stability would be beneficial for commercial applications, allowing their long term use.

- Inorganic framework materials

A major part of the project was to synthesise new transition metal phosphate / sulfate materials through hydrothermal methods. The materials produced in this study were all synthesised in fluoride-rich hydrothermal conditions, with the aim of incorporating fluoride anions into the final material compositions, often in combination with other anionic species giving mixed-anion phases. These mixed-anion, transition metal compounds were expected to show new structural features resulting from the incorporation of fluoride, as opposed to those of the well-studied and reported transition metal oxo- compounds. In this work nineteen new materials were produced, indicating the successful incorporation of fluoride within their structures, including seven phosphate-based, and twelve sulfate-containing new compounds. Three new compounds

produced under these synthesis conditions were not found to contain fluoride anions. Consequently the use of metal fluorides as starting materials offers an alternative, safer way to prepare F-containing compositions without introducing HF directly into the reaction mixture; HF has previously been commonly used in preparation of similar compounds in solvothermal synthesis.

Seven new phosphate based structures were described in Chapter 4. Their structures were all found to be constructed from various connected octahedral and tetrahedral units, where the octahedral units were centred on a transition metal, such as manganese, iron and vanadium, surrounded by oxygen and fluorine atoms, whilst the tetrahedral groups were phosphate units. Although many transition metal phosphate-based structures are known, very few fluoride-containing, mixed transition metal structures have been reported previously. Particularly notable among these phases were those containing manganese in the +3 oxidation state. The mixed fluoride-phosphate structures display a number of interesting and unusual structural features: fluoride anions were often found to adopt the bridging sites between metal centres, or the terminal sites of the metal coordination sphere. Fluoride ions were also found to adopt terminal sites within the phosphate tetrahedra, i.e. produce the PO_3F unit; where these PO_3F units were found in the structure, the terminal fluoride was found to always be directed towards extra-framework or layer spaces. The inclusion of fluorides anions was also found to lower the structural dimensionality of the materials produced,, mainly due to the terminal positions adopted by fluoride anions within polyhedra.

Further studies of these phosphate materials could focus on their potential applications. For example layered structures with interleaved cations may exhibit good ion mobility, and those containing lithium or sodium ions may have applications as battery cathode or anode materials. The ammonium containing structures may also be of interest in their ion exchange properties, where the ammonium could be removed and replaced with other cations, or through partial decomposition with ammonia evolution and proton transfer to the framework. As all of these structures are based on transition metals, which exhibit many different oxidations states, they offer a wide range of functionalities in respect of, for example, optical absorption spectra, catalysis and magnetic properties; however, these would need to be investigated further.

Compared to the phosphate materials, there is a scarcity of analogous sulfate materials reported in the literature. Chapter 5 describes ten new transition metal sulfate structures, which were all produced via the hydrofluorothermal method. Similar to the synthesis of phosphate materials, metal fluorides were also used as starting materials in preparation of sulfate materials, with the aim of introducing fluoride anions to the products and avoiding the use of HF. Nine of the new structures were found to contain fluoride anions. As found with the phosphate materials discussed previously, the fluoride anions tend to adopt bridging, between metal sites, and terminal sites in the metal coordinations, but sulfate tetrahedral units showed no fluoride ion incorporation. This behaviour is likely to be due to the sulfur centres in the +6 oxidation sate needing to bond to four oxygen -2 ions to form a stable coordination; the lower charge of fluoride and inability to form double bonds mitigates against its incorporation in the sulphur coordination environment. The layered structures produced, which also incorporated sodium ions, were suggested as potential secondary battery cathode materials, and their electrochemical properties were studied; the cell potentials obtained, for the materials investigated, were significantly higher than those found previously for comparable materials. Other lithium or sodium containing structures, including the three-dimensional structures with cations in channels, may also be of interest in respect of their electrochemical properties, and therefore as potential cathode materials for either Na-ion or Li-ion rechargeable batteries. The materials studied in this work were not optimised in terms of, for example, particle size, and further work of this type will be required to fully determine the potential of this new class of compounds for energy storage applications.

The intention of the synthetic work on templated sulfate structures described in Chapter 6 was to extend the range of known structures, in particular those containing mixed anions. i.e. transition metal sulfate-fluoride compositions. The rarity of sulfate containing, connected structures (compared with the prevalence of phosphates) originates in several factors but is mainly a result of the high oxidation of sulphur, requiring double bonds to oxygen to satisfy its valence, which then act to terminate the structures. Sulfate is therefore often found as a bridging ligand between just two transition metal centres – rather than connecting three of more units into a two or three dimensional network. As a result, of the five new structures produced, four of them possessed one dimensional chains, and only one exhibited a two dimensional layered

structure. Three of them showed the incorporation of fluoride anions within their structures, acting as either bridging or terminal species. Hydrogen bonds were created between the templating molecules and the inorganic frameworks. Thermal investigations indicated that once the templates had been removed, the material structures became unstable and decomposed.

As has been discussed above, a number of novel structures have been synthesised employing the newly developed hydrofluorothermal method, involving the introduction of fluoride ions into the reaction medium from transition metal fluoride sources. The products have been primarily characterised by SXD, assisted with other techniques, such as PXD, EDS and IR. The range of known framework species has been extended, especially materials with frameworks formed by combining transition metals with polyoxoanions and fluorides. Within this research work, several materials have been produced which possess properties of potential interest for various applications. The synthetic techniques explored and the new materials discovered should provide the basis for future research in this field.

APPENDIX

CHAPTER FOUR:

A.1: IR spectrum of compound I: $Ba_2Mn_2F_5(PO_4)(PO_3F)\cdot 2H_2O$

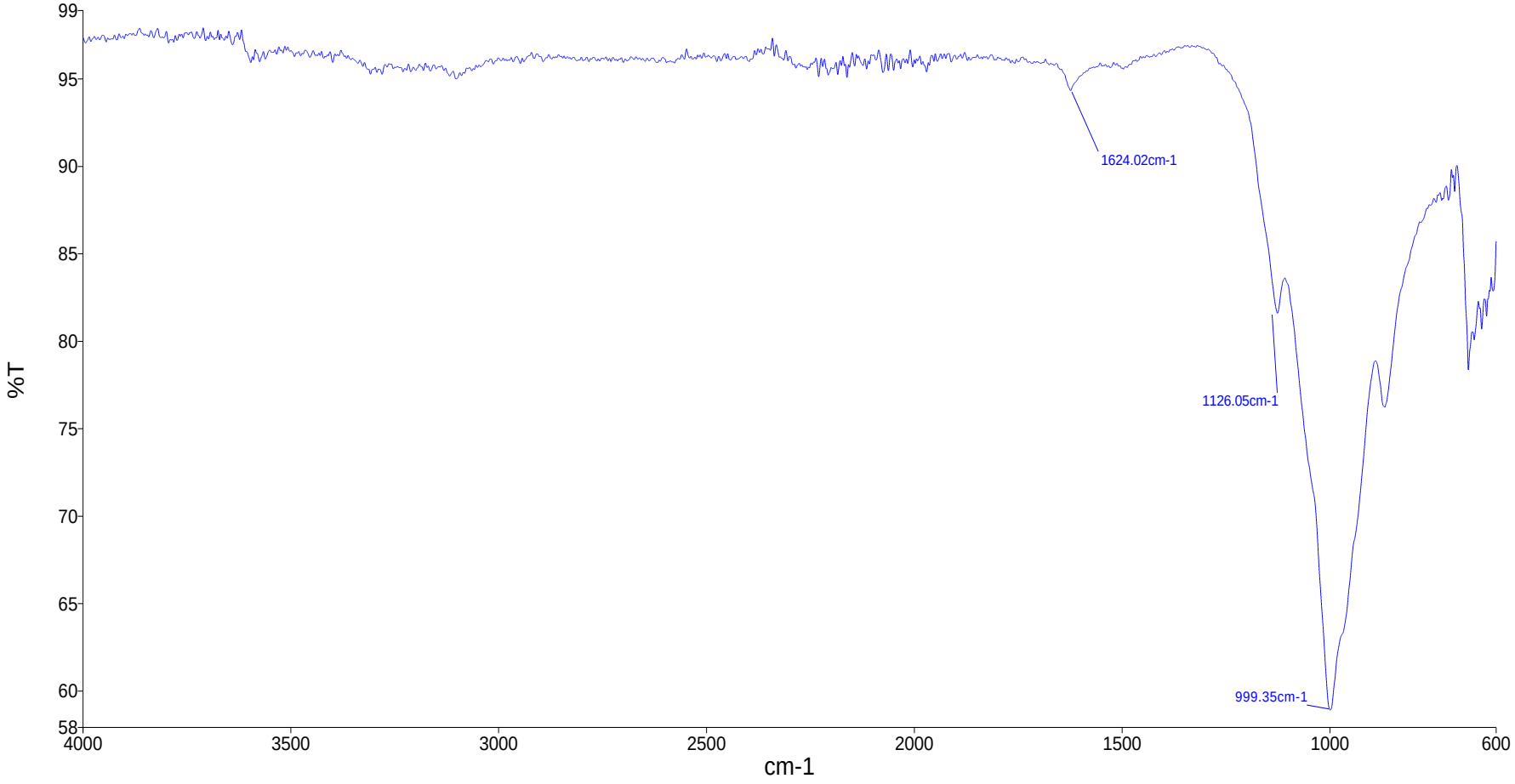

A.2: IR spectrum of Compound VI: $(NH_4)Mn_3(PO_3F)_2(PO_2F_2)F_2$

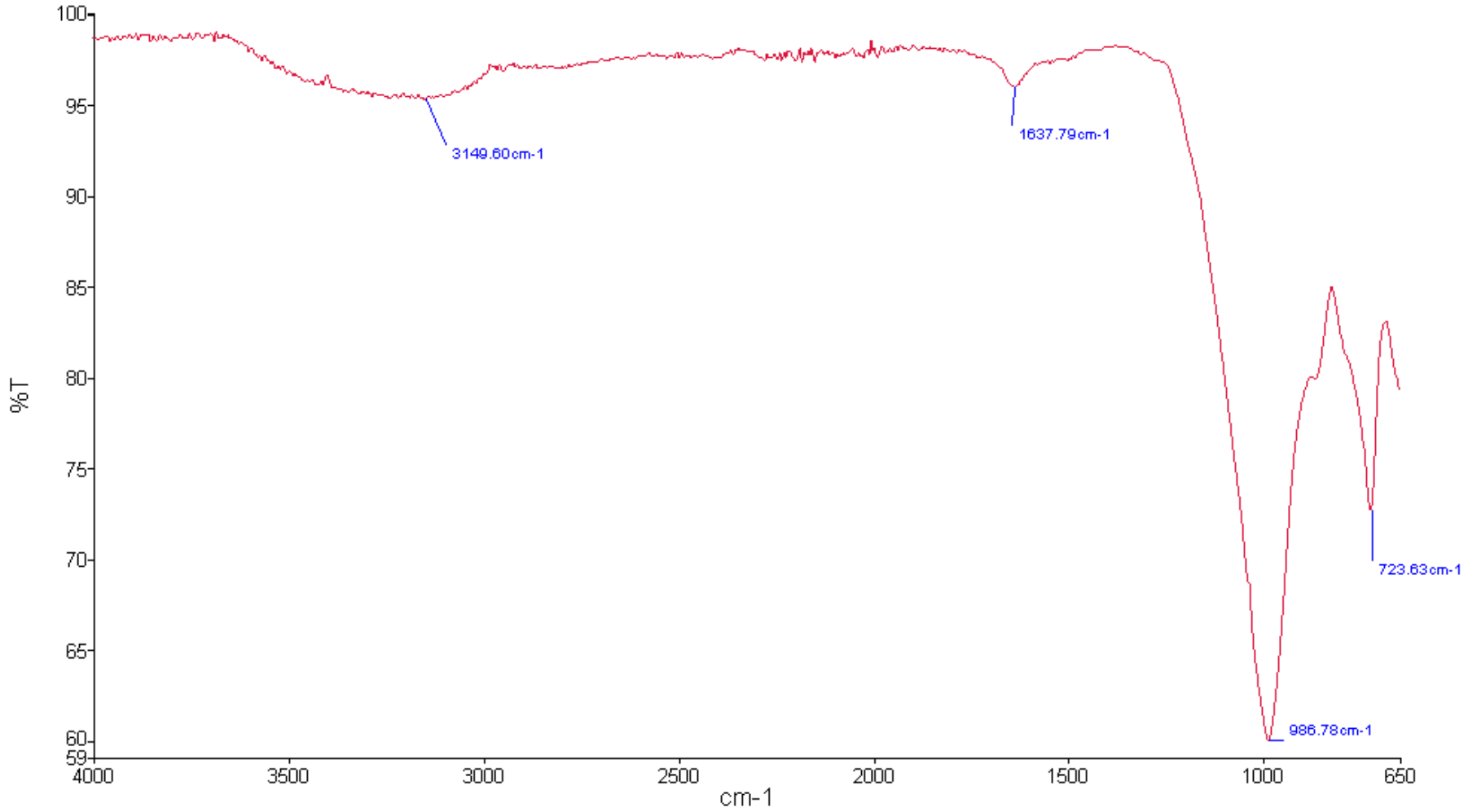

CHAPTER FIVE:

A.3: IR spectrum of Compound X: $Li_3FeF_2(SO_4)_2 \cdot H_2O$

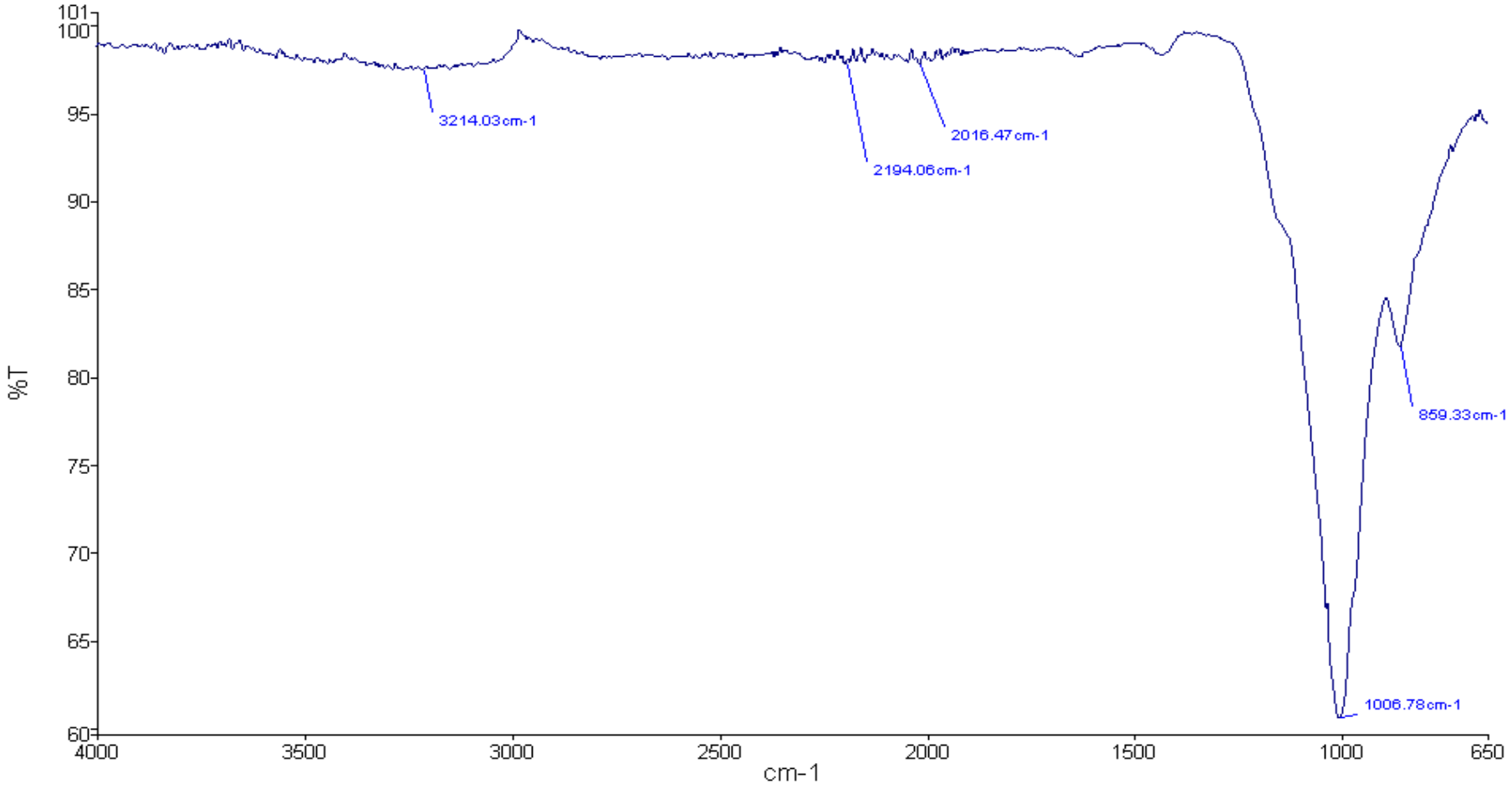

A.4: IR spectrum of Compound XV: $(NH_4)LiMn(SO_4)_2$

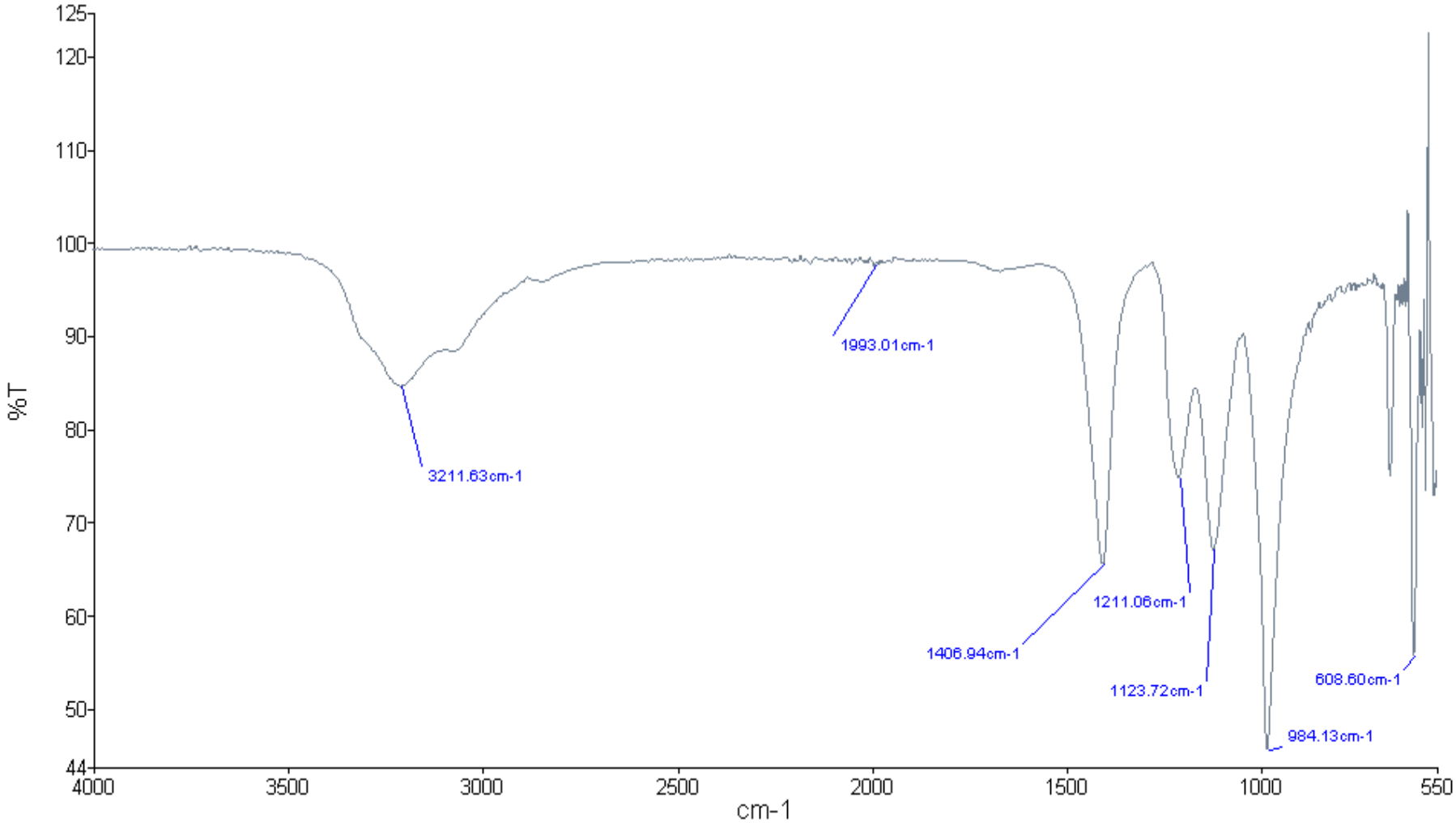

A.5: IR spectrum of Compound XVI: $[H_2\text{-}(C_6H_{16}N_2)]Mn_2(SO_4)_2F_2$

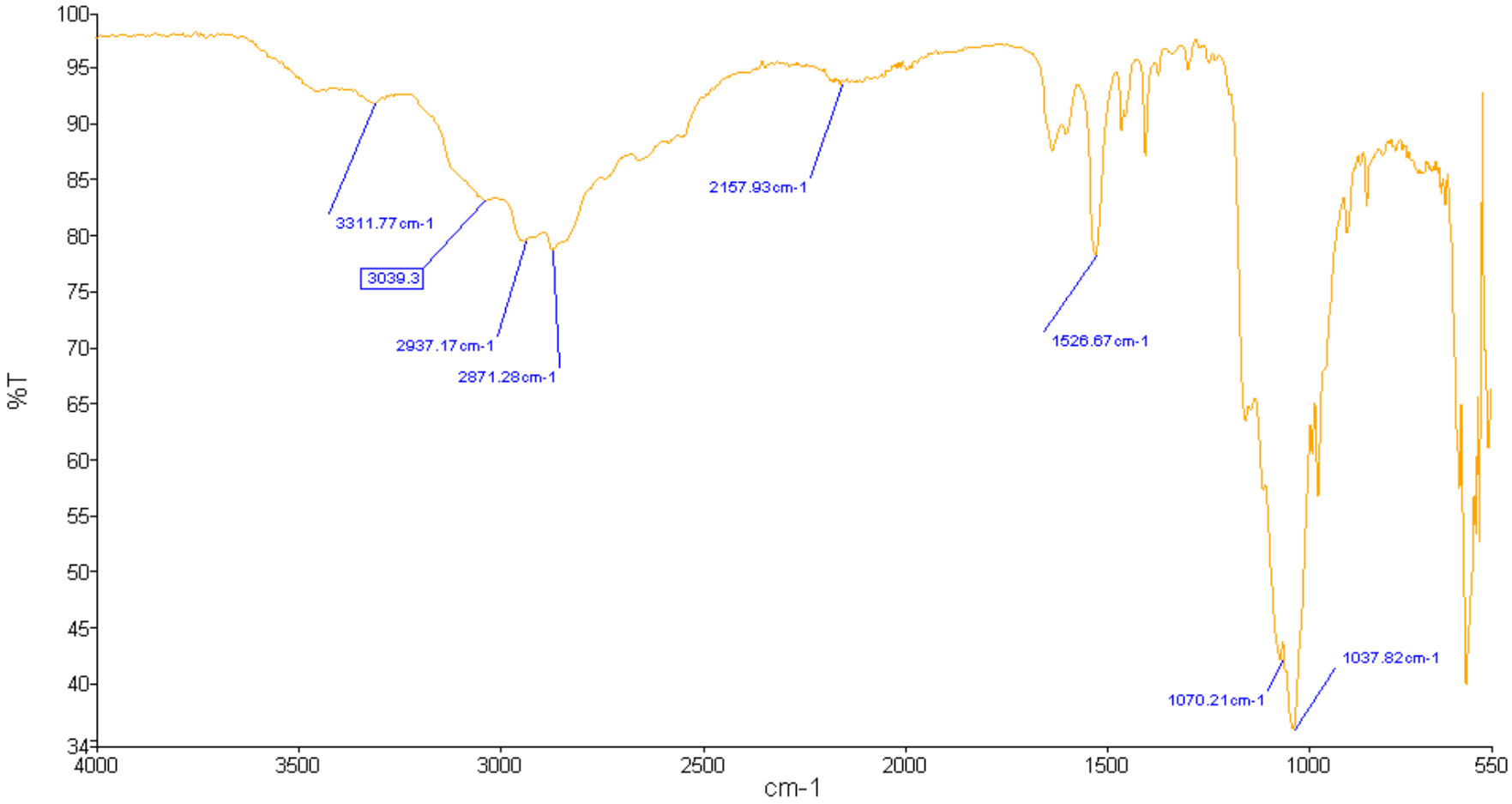

A.6: IR spectrum of Compound XVII: $[H_2\text{-}(N_2H_6)]_5Mn(SO_4)_6$

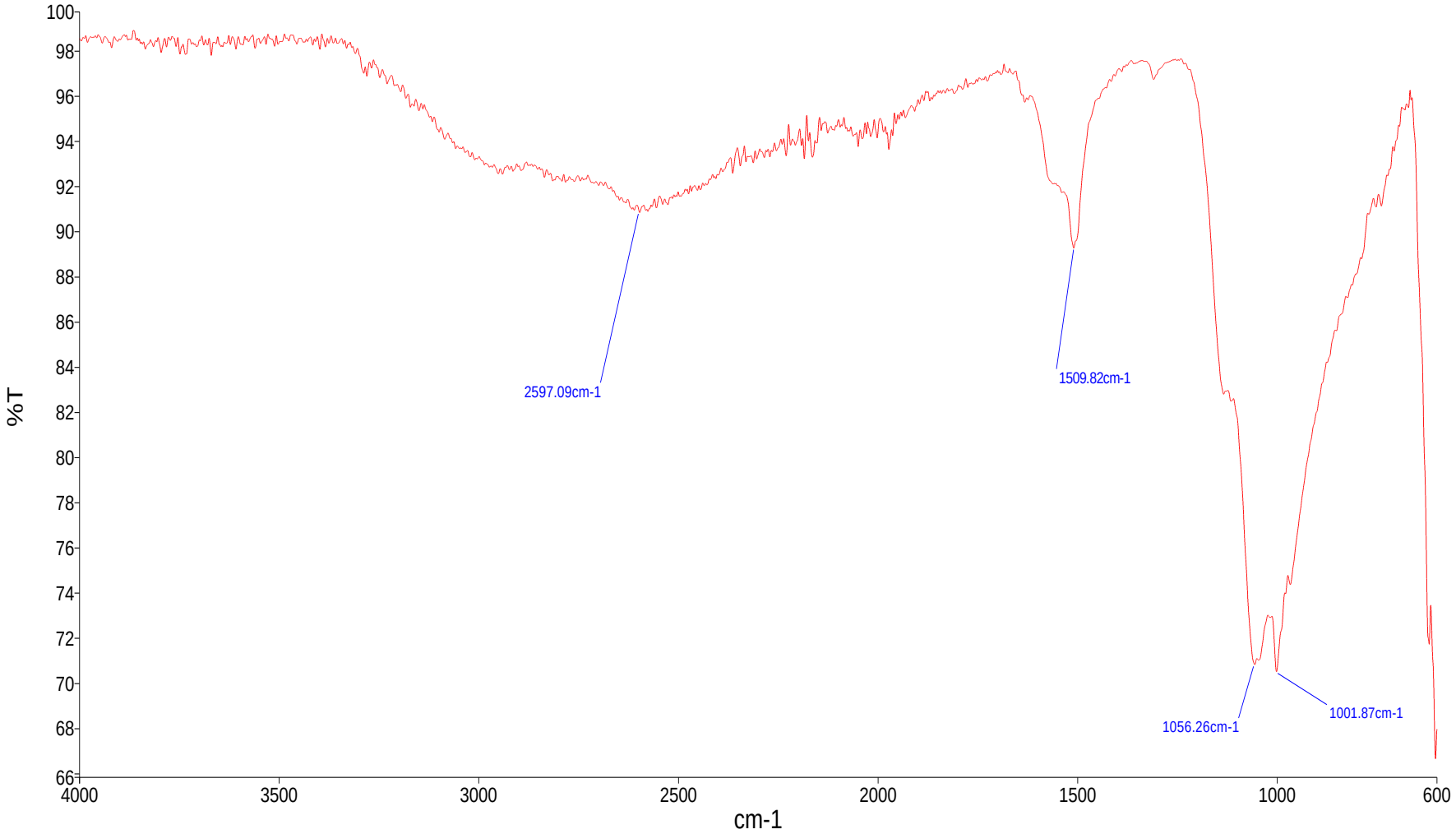

A.7: IR spectrum of Compound XIX: $[H_2\text{-}(C_2H_8N_2)](NH_4)Fe(SO_4)_3$